MONITORING GAS EMISSIONS OF ACTIVE VOLCANOES

Identification of natural degassing variations and combination of volcano monitoring techniques

DISSERTATION

ZUR ERLANGUNG DES DOKTORGRADES

AN DER MATHEMATISCH-NATURWISSENSCHAFTLICHEN

FAKULTÄT DER CHRISTIAN-ALBRECHTS-UNIVERSITÄT ZU KIEL

VORGELEGT VON
STEFAN BREDEMEYER
KIEL, 2016

Erste/r Gutachter/in: PD Dr. T.H Hansteen

Zweite/r Gutachter/in: Prof. Dr. C. Devey

Tag der mündlichen Prüfung: 20. Februar 2017

Zum Druck genehmigt: 20. Februar 2017

Hiermit erkläre ich, dass ich die vorliegende Doktorarbeit selbständig und ohne Zuhilfenahme unerlaubter Hilfsmittel erstellt habe. Weder diese noch eine ähnliche Arbeit wurde an einer anderen Hochschule im Rahmen eines Prüfungsverfahrens vorgelegt, veröffentlicht oder zur Veröffentlichung vorgelegt. Ferner versichere ich, dass die Arbeit unter Einhaltung der Regeln guter wissenschaftlicher Praxis der Deutschen Forschungsgemeinschaft entstanden ist.

Kiel, Dezember 2016

Stefan Bredemeyer

. . . consider the notion of periodicity. The general recurrences of things are very obvious in our ordinary experience. Days recur, lunar phases recur, the seasons of the year recur, rotating bodies recur to their old positions, beats of the heart recur, breathing recurs. On every side, we are met by recurrence. Apart from recurrence, knowledge would be impossible; for nothing could be referred to our past experience. Also, apart from some regularity of recurrence, measurement would be impossible. In our experience, as we gain the idea of exactness, recurrence is fundamental.

In the sixteenth and seventeenth centuries, the theory of periodicity took a fundamental place in science. Kepler devined a law connecting the major axes of the planetary orbits with the periods in which.the planets respectively described their orbits: Galileo observed the periodic vibrations of pendulums: Newton explained sound as being due to the disturbance of air by the passage through it of periodic waves of condensation and rarefaction: . . . The birth of modern physics depended upon the application of the abstract idea of periodicity to a variety of concrete instances.

Alfred North Whitehead (1925)

IV

PREFACE

This cumulative thesis is based on five manuscripts, which are complemented by an introduction to the overarching topic *volcano monitoring*, including a short overview of volcano surveillance methods used in the presented interdisciplinary studies (Chapter I). Four of the manuscripts have been published in peer-reviewed scientific journals (Chapters II-V), while the last one still is in preparation for submission (Chapter VI). Each of these Chapters thus contains its own abstract, introduction, description of the geological setting of the working area, presentation of results, discussion of the results, and conclusions. The contributions of the authors, which were involved in the preparation of the manuscripts, are indicated below along with short summaries of the methods applied in Chapters II-VI. Details on the acquisition, evaluation and processing of the gas monitoring data recorded in the framework of this thesis are appended to this thesis (Appendix).

Chapter II **Synchronous degassing patterns of the neighbouring volcanoes Llaima and Villarrica in south central Chile: the influence of tidal forces.** (*published 2014 in the International Journal of Earth Sciences (Geologische Rundschau)*)

Bredemeyer, S., T. H. Hansteen

Chapter II examines periodically recurrent variations in the sulphur dioxide (SO_2) degassing rates of Villarrica and Llaima volcanoes in south central Chile and aims at assigning the observed cyclical variations to their likely causes. Continuous long-term measurements of SO_2 emission rates were conducted at Villarrica and Llaima by means of permanent stationary scan-DOAS (Differential Optical Absorption Spectroscopy) instruments and weather hindcasts of the Global Forecast System (GFS). The resulting time series were statistically examined in tandem with Earth tide related vertical ground surface displacements and compared to the local variations in barometric pressure. The analysis of the time series revealed diurnal, weekly, and fortnightly periodicities in degassing activity, which were attributed to changes in barometric pressure and tidal oscillations of Earth's crust. These results were used to develop a conceptual magma degassing model, in order to explain the observed degassing variations.

Contributions: Stefan Bredemeyer and Thor H. Hansteen prepared the paper, which considerably benefited from discussions of the subject with Armin Freundt. Evaluation of SO_2 emission rates and statistical analysis of the gas emission data in conjunction with corresponding weather and Earth tides data was conducted by Stefan Bredemeyer. Development of the conceptual magma degassing model was completed by Stefan Bredemeyer.

Chapter III **SO_2 degassing from Turrialba Volcano linked to seismic signatures during the period 2008–2012.** (*published 2013 in the International Journal of Earth Sciences (Geologische Rundschau)*)

Conde, V., **S. Bredemeyer**, E. Duarte, Javier F. Pacheco, Sebastian Miranda, Bo Galle, Thor H. Hansteen

Chapter III is a rather classical volcano monitoring paper, in which the insights from monitoring data of different proxies for volcanic activity were combined with information from the eruption history and petrological data of Turrialba volcano in Costa Rica. SO_2 emission rates from Turrialba were compared to seismicity time series in order to describe and interpret the temporal evolution of the activity during the first five years of a new period of volcanic unrest. The seismicity time series used in this study comprise Real-time Seismic Amplitude Measurements (RSAM), and simple event statistics of different volcanic earthquake types including the number of occurrences of long period (LP), very long period (VLP) and volcano tectonic (VT) earthquakes, as well as the duration of periods with volcanic tremor. Results from the combined statistical analysis of these time series and hypocenter distribution of hybrid earthquakes were used to infer the development of the volcanic activity and locate related processes in the magmatic system. A magma supply rate was deduced from SO_2-fluxes and sulphur contents in matrix glass and melt inclusions in phenocrysts of Turrialba tephras, measured by electron microprobe analysis.

Contributions: Vladimir Conde and Stefan Bredemeyer authored the paper and were supervised by Bo Galle and Thor H. Hansteen in the process of writing. Evaluation of the SO_2-fluxes and statistical analysis of the gas emission data in conjunction with complementary seismic data was performed by Vladimir Conde. Eliecer Duarte, Javier F. Pacheco, and Sebastian Miranda provided the complementary seismic data and first-hand observations of the volcanic activity. Electron microprobe analysis was conducted by Heidi Wehrmann. Volcanological interpretation of the data was largely completed by Stefan Bredemeyer.

Chapter IV **Linking SO_2 emission rates and seismicity by continuous wavelet transform: implications for volcanic surveillance at San Cristóbal volcano, Nicaragua.** (*published 2014 in the International Journal of Earth Sciences (Geologische Rundschau)*)

Conde, V., **S. Bredemeyer**, J. A. Saballos, Bo Galle, T. H. Hansteen

Chapter IV explores the merits and limitations of Continuous and Cross Wavelet Transforms (CWT & XWT) as tools for eruption prediction by means of combined analysis of different volcanic activity proxies, using the example of SO_2 emission rates and Real-time Seismic Amplitude Measurements (RSAM) from San Cristóbal volcano in Nicaragua. Results from the individual CWT analyses and the combined XWT analysis of the time series were then used to infer the development of the volcanic activity and related magmatic processes at depth.

Contributions: Vladimir Conde wrote much of the manuscript and was assisted by Stefan Bredemeyer,·J. Armando Saballos,·Bo Galle,·and Thor H. Hansteen. Vladimir Conde evaluated the SO_2 emission rates and Armando Saballos provided the RSAM data. Vladimir Conde carried out the statistical analysis and was supported by Stefan Bredemeyer regarding the volcanological interpretation of the data.

Chapter V **Gas emissions from five volcanoes in northern Chile and implications for the volatiles budget of the Central Volcanic Zone.** (*published 2014 in Geophysical Research Letters*)

Tamburello, G., T. H. Hansteen, **S. Bredemeyer**, A. Aiuppa, F. Tassi

Chapter V is a classical gas monitoring paper prospecting the gas compositions and SO_2 emission rates from five volcanoes in Northern Chile (Láscar, Lastarria, Putana, Ollagüe, and San Pedro), which were used to calculate the total volatiles output of these volcanoes. These results were in turn used to estimate the along arc volatiles budget of the Central Volcanic Zone and compared to the gas chemistry and volatiles output of the Southern Volcanic Zone in Southern Chile.

Contributions: Giancarlo Tamburello authored the paper and was supported in the process of writing by the co-authors Thor H. Hansteen, Stefan Bredemeyer, Alessandro Aiuppa, and Franco Tassi. Giancarlo Tamburello performed gas composition measurements using Multi-GAS and filter packs at Láscar and Lastarria volcano, and conducted SO_2-flux and wind speed measurements at Putana and Láscar volcanoes by means of a UV camera. Stefan Bredemeyer and Thor H. Hansteen conducted scan-DOAS surveys at Láscar, Lastarria, Putana, San Pedro, and Ollagüe volcanoes in order to measure SO_2-fluxes. Evaluation of SO_2-fluxes from all five volcanoes was completed by Stefan Bredemeyer. Franco Tassi provided gas composition data from a direct sampling survey at Ollagüe volcano. The volatiles budget of the Central Volcanic Zone was assessed by Giancarlo Tamburello.

Chapter VI **Radar path delay effects in volcanic gas plumes: The case of Láscar volcano, Northern Chile.** (*manuscript in preparation*)

Bredemeyer, S., F.-G. Ulmer, T. H. Hansteen, E. De Zeeuw van Dalfsen, N. Richter, T. Walter

Chapter VI is a methodological manuscript, in which ground-based measurements of gas compositions and SO_2 slant column densities in crosswind profiles of the volcanic gas plume of Láscar volcano were combined with satellite-based synthetic aperture radar (SAR) data in order to quantify the radar path delays

caused by volcanic water vapour emissions in interferometric displacement measurements. For this purpose a method was developed, which enables to map the areas of a volcano, in which the radar path was repeatedly delayed by enhanced water vapour contents in the volcanic gas plume during subsequent satellite radar observations. Water vapour contents in the volcanic gas plume and the background atmosphere were determined from a combination of scan-DOAS and multi-GAS measurements, and modeled weather hindcasts of the Global Forecast System (GFS), respectively. The gas plume related water vapour estimates were then used as an a priori information, which was integrated into the Cinderella algorithm, along with surface temperatures, barometric pressure, relative humidity, spatial and temporal baselines, in order to estimate the different SAR delay contributions in the examined time series of differential interferometric synthetic aperture radar (DInSAR) measurements.

Contributions: Stefan Bredemeyer wrote 90% of the manuscript together with Franz-Georg Ulmer, and was supported by valuable comments of the co-authors Thor H. Hansteen, Elske De Zeeuw van Dalfsen, Nicole Richter, and Thomas Walter. Thor.H Hansteen significantly improved the structure and organization of the manuscript. Stefan Bredemeyer & Franz-Georg Ulmer developed the analytical method. Evaluation and statistical analysis of the gas emission and weather data, as well as estimation of precipitable water vapour contents in the volcanic gas plume and the background atmosphere was performed by Stefan Bredemeyer. DInSAR analysis, WRF simulations, development of the Cinderella algorithm, and SAR delay estimation by means of the Cinderella algorithm was done by Franz-Georg Ulmer. Wind field analysis based on hindcasts of atmospheric soundings from the GFS and onsite observations was done by Stefan Bredemeyer, and complemented by a 3-dimensional wind field analysis obtained from the Weather Research and Forecasting Model (WRF), which was conducted by Franz-Georg Ulmer.

MONITORING GAS EMISSIONS OF ACTIVE VOLCANOES

Identification of natural degassing variations and combination of volcano monitoring techniques

STEFAN BREDEMEYER

ABSTRACT

Degassing of magmatic volatiles is an important driving force of magma ascent inside Earth's crust and thus plays a crucial role in the evolution of volcanic systems. Emission rates of magmatic gases are commonly used as a proxy for the magma supply rate of a volcano enabling to assess the amount of magma moving through the subsurface of a volcano during both, periods of quiescent and eruptive volcanic activity. Strong increases or decreases in gas emission rates and pronounced changes in the composition of gas emissions are often among the first precursory signs of an eruption and comparison of the gas emission rates with the volumes and volatile contents of erupted magma allows inferring the amount of endogenously degassing magma stored within the magma reservoir of a volcano. Endogenous magma degassing moreover is responsible for the generation of several deep-sourced precursory signals of possibly impending eruptions, which may manifest as enhanced seismic activity at depth, or surface deformation of the volcanic edifice. Determination of the time lag between the occurrence of such deep-seated precursory signals and observations of changes in fluxes of magmatic gas escaping at the surface of the volcano enables to deduce the depth and ascent velocity of the degassing magma. Continuous surveillance of gas emissions from active volcanoes thus provides valuable information about the state of volcanic activity, and can help to improve our understanding of the underlying magmatic processes and associated eruption dynamics.

This thesis is a contribution to the interdisciplinary field of applied volcanology and focuses on the study of volcanic gas emissions by means of ground-based spectroscopic remote sensing techniques. Furthermore it aims at fostering the routine use and integration of such measurements into existing multi-parameter volcano surveillance networks of the involved local volcano observatories. For this purpose continuous long-term monitoring of sulphur dioxide (SO_2) emission rates was performed using permanent networks of fully-automated scanning ultraviolet (UV) spectrometers at some of the most active and persistently degassing stratovolcanoes in the volcanic arcs of Chile, Costa Rica and Nicaragua. These measurements yielded detailed time series of SO_2 emission rates, which were calculated using differential optical absorption spectroscopy (DOAS) in conjunction with wind transport directions and velocities derived from weather hindcasts of the Global Forecast System (GFS), and delivered insights into the degassing behaviour of the monitored volcanoes.

Chapter II of this work investigates the periodic degassing behaviour of Villarrica and Llaima volcanoes in South-Central Chile and the influence of external forces on volcanic degassing. Statistical analysis of the hourly averaged degassing time series from Villarrica and Llaima volcanoes revealed systematic cyclic variations of SO_2 emission rates at diurnal, weekly, fortnightly, monthly and annual time scales, which synchronously occur on both volcanoes, and which persisted regardless of the state of activity, i.e. they were retained during periods of quiescent and eruptive degassing. The synchronicity of the degassing variations observed at both volcanoes strongly suggests that external factors play a role in modulating the degassing efficiency of the volcanoes. Combined analysis of the SO_2-fluxes from both volcanoes and corresponding time series from weather and Earth tide models enabled to attribute these degassing cycles to changes in barometric pressure and Earth tide induced pressure fluctuations.

Chapters III and IV address the difficulties related to the interpretation of gas emission data used as an indicator of upcoming volcanic unrest and explore the merits and limitations of different statistical methods for the individual and combined analysis of time series records of proxies for volcanic activity. Eruption

forecasting can significantly be improved by means of a combined analysis of SO_2 emission rates with complementary volcano monitoring data, such as time series from event statistics of the occurrence of volcanic earthquakes, or Real-time Seismic Amplitude Measurements (RSAM). Our results show that SO_2 emission data are often difficult to interpret without further knowledge of the activity state of the volcano, due to the ambiguity of decreasing emission rates, which may either indicate that the probability of an eruption is diminishing because the magma retreats and/or further magma supply is stalling, or the decrease indicates that the gas is being trapped and accumulating at depth, which potentially increases the threat of an imminent eruption. In order to obtain a more complete and clearer image of the processes occurring at depth, the SO_2 emission data from Turrialba volcano in Costa Rica (Chapter III) and San Cristóbal volcano in Nicaragua (Chapter IV) were thus complemented with seismic data. Statistical analysis of the combined datasets enabled us to reconstruct the medium-term evolution of the volcanic activities encountered at both volcanoes, and revealed recurrent features in the measured signals, which may be used to identify eruptive activity. Cross Wavelet Transform (XWT) analysis was applied to daily averaged SO_2 flux and Real-time Seismic Amplitude Measurement (RSAM) time series of San Cristóbal and proved to be a valuable tool to detect explosive events, since the wavelet coefficients of both parameters show a pronounced correlation during the periods with explosive activity, which were generally preceded by periods of several days to weeks in which the correlation considerably increased. In addition, a Fast Fourier Transform (FFT) analysis of the daily averaged SO_2-flux, RSAM, and volcanic tremor duration time series from Turrialba yielded weekly and fortnightly cyclic variations as in the case of Villarrica and Llaima volcanoes, thus supporting the hypothesis of an external influence on degassing activity as proposed in Chapter II.

Chapter V focuses on gas composition and SO_2-flux measurements from five volcanoes in Northern Chile (Lastarria, Láscar, Putana, San Pedro, Ollagüe), which were combined to calculate the degassing rates of different major components (H_2O, CO_2, H_2, HCl, HF, and HBr) of the volcanic gases emitted from these volcanoes. These gas fluxes were used to assess the volatiles budget of the Chilean part of the Central Volcanic Zone (CVZ). Gas compositions from Láscar and Lastarria volcanoes are similar to those of the volcanoes from the Southern Volcanic Zone (SVZ) suggesting the presence of a uniform magmatic gas fingerprint throughout the Chilean arc.

Chapter VI presents a method, which enables the quantification of the water vapour related radar path delays in the volcanic gas plume of Láscar volcano in Northern Chile by means of integrating gas emission measurements and information from the Global Forecast System weather model into the analysis of radar interferometric measurements obtained from the synthetic aperture radar (InSAR) on the TerraSAR-X satellite. The method requires at least 3 radar acquisitions and approximately contemporary gas emission measurements, in order to map and quantify recurrent gas plume related radar path delays that influence interferometric displacement measurements, which in turn can be used for the improvement of ground deformation measurements at strongly degassing volcanoes.

_____

KURZFASSUNG

Die Entgasung magmatischer Volatile ist die treibende Kraft für den Magmenaufstieg in der Erdkruste und spielt somit eine entscheidene Rolle in der Entwicklung vulkanischer Systeme. Emissionsraten magmatischer Gase werden für gewöhnlich als Anzeiger für die Magmenfördermenge eines Vulkans verwendet und ermöglichen somit sowohl in Zeiträumen ruhiger als auch eruptiver Vulkanaktivität die Abschätzung der Magmenmengen, die sich im Untergrund eines Vulkans bewegen. Eine starke Zu- oder Abnahme der Gasemissionsraten, sowie deutliche Veränderungen der chemischen Zusammensetzung der Gase gehören häufig zu den ersten Anzeichen eines bevorstehenden Vulkanausbruchs. Der Vergleich von Gasemissionsraten mit dem Volumen und Volatilengehalt von eruptiertem Magma erlaubt es Rückschlüsse auf die Menge der im Magmenreservoir eines Vulkans gespeicherten endogen entgasenden Magmen zu ziehen. Die endogene Entgasung von Magma ist darüber hinaus für die Erzeugung von verschiedenen Vorläufersignalen von möglicherweise bevorstehenden Vulkanausbrüchen verantwortlich, die ihren Ursprung in größerer Tiefe des Vulkans haben, und welche sich zum Beispiel in Form von erhöhter seismischer Aktivität oder der Deformation des Vulkangebäudes äußern. Die Ermittlung der Zeitabstände zwischen solchen tiefsitzenden Signalen und den Beobachtungen von Veränderungen der Flüsse von den an der Oberfläche des Vulkans entweichenden magmatischen Gasen ermöglicht die Herleitung der Tiefe und Aufstiegsgeschwindigkeit der entgasenden Magmen. Eine kontinuierliche Überwachung von vulkanischen Gasemissionen liefert daher wertvolle Informationen über den Aktivitätszustand eines Vulkans und kann somit dabei helfen unser Verständnis von den damit verbundenen magmatischen Prozessen und der Dynamik von Vulkanausbrüchen zu verbessern.

Diese Dissertation ist ein Beitrag zum weitläufigen interdisziplinären Feld der angewandten Vulkanologie und der Studie von vulkanischen Gasemissionen unter der Verwendung von bodengebundenen spektroskopischen Fernerkundungstechniken. Desweiteren zielt sie darauf ab, die routinierte Benutzung und die Integrierung solcher Messungen in die bereits existierenden Multi-Parameter Vulkanüberwachungsnetzwerke der involvierten Vulkanobservatorien zu fördern. Für diese Zwecke wurde an einigen der aktivsten und dauerhaft entgasenden Stratovulkane in Chile, Costa Rica und Nicaragua eine kontinuierliche Langzeitüberwachung von Schwefeldioxid (SO_2)-Emissionsraten mittels permanent installierter Netzwerke aus voll-automatischen ultraviolett (UV)–Spektrometer Stationen mit eingebauter Abtastvorrichtung durchgeführt. Diese Messungen lieferten detaillierte Zeitreihen von SO_2 – Emissionsraten, die mittels differentieller optischer Absorptionsspektroskopie (DOAS) in Verbindung mit Windrichtungen und Windgeschwindigkeiten aus Rückberechnungen des Global Forecast Systems (GFS) berechnet wurden, und gaben somit Einblicke in das Entgasungsverhalten der überwachten Vulkane und ermöglichten darüber hinaus die gemeinsame Analyse mit komplementären seismischen Überwachungsdaten.

Kapitel II dieser Arbeit untersucht das periodische Entgasungsverhalten der Vulkane Villarrica und Llaima im Mittleren Süden Chiles und den Einfluß externer Kräfte auf die Vulkanentgasung. Statistische Analysen der stündlich gemittelten Entgasungszeitreihen ergaben, dass die SO_2-Emissionsraten der beiden untersuchten Vulkane zeitgleich auftretenden periodisch wiederkehrenden Schwankungen unterliegen, die sich auf unterschiedlichen Zeitskalen von Tagen, Wochen, Monaten und Jahren abspielen. Diese zyklischen Variationen bestehen unabhängig vom Zustand der vulkanischen Aktivität, sowohl in Zeiträumen ruhiger als auch eruptiver Entgasung und werden nur dann unterbrochen, wenn die Entgasung durch eine Blockierung der oberflächlichen Entgasungswege verhindert wird. Das an beiden Vulkanen zeitgleiche Auftreten dieser Entgasungsvariationen legt nahe, daß externe Faktoren die Vulkanentgasung beeinflußen. Die kombinierte statistische Analyse von SO_2-Emissionsraten und zugehörigen Informationen aus Wetter- und Erdgezeitenmodellen ermöglichte es, diese Entgasungszyklen auf Veränderungen des Luftdrucks und auf durch Erdgezeiten induzierte Druckschwankungen zurückzuführen.

Die Kapitel III und IV befassen sich mit der Problematik der Interpretation von Gasemissionsdaten als Indikator für das Einsetzen und die Entwicklung vulkanischer Unruhephasen und untersuchen den Nutzen verschiedener statistischer Methoden für die Analyse von Proxy-Signalen bzw. indirekten Anzeigern für Vulkanaktivität. Die Vorhersage von Eruptionen anhand von Gasemissionsdaten kann deutlich verbessert werden, wenn sie in Kombination mit anderen geeigneten Vulkanüberwachungsdaten analysiert werden.

Unsere Ergebnisse zeigen, daß SO_2-Emissionsdaten aufgrund der Mehrdeutigkeit, die eine Abnahme der Entgasungsraten mit sich bringt, häufig schwierig zu interpretieren sind, ohne weitere Kenntnis über den Aktivitätszustand des Vulkans zu haben. Eine Abnahme der Emissionsraten kann entweder darauf hindeuten, dass die Wahrscheinlichkeit eines Vulkanausbruchs abnimmt, weil das Magma sich zurückzieht und/oder die weitere Versorgung mit neuem Magma ins Stocken geraten ist, oder sie kann bedeuten, dass das Gas in der Tiefe zurückgehalten wird und sich dort ansammelt, was möglicherweise die Gefahr eines bevorstehenden Ausbruchs erhöht. Um ein vollständigeres und klareres Bild der in der Tiefe auftretenden Vorgänge zu erhalten, wurden die SO_2-Emissionsdaten der Vulkane Turrialba in Costa Rica (Kapitel III) und San Cristóbal in Nicaragua (Kapitel IV) zusammen mit komplementären seismischen Daten ausgewertet. Die kombinierte statistische Analyse der Datensätze ermöglichte die Rekonstruktion der zeitlichen Entwicklung der Aktivität beider Vulkane, und offenbarte wiederkehrende Muster in den Messsignalen, welche dazu verwendet werden können das Einsetzen eruptiver Aktivität zu erkennen. Eine Cross-Wavelet-Transformations (XWT) Analyse wurde auf die täglich gemittelten SO_2-Flüsse und die Echtzeit-Messung seismischer Amplituden (RSAM) von San Cristóbal angewandt und erwies sich als ein wertvolles Werkzeug, um das Einsetzen explosiver Vulkanaktivität zu detektieren, da die Waveletkoeffizienten der beiden Parameter an Tagen mit explosiver Aktivität eine ausgeprägte Korrelation gezeigt haben, denen im allgemeinen kurze Perioden von mehreren Tagen bis Wochen mit einer deutlichen Zunahme der Korrelation vorausgegangen sind. Darüber hinaus ergaben die Fourier-Analysen an den Zeitreihen von tagesdurchschnittlichen SO_2 Flüssen, sowie von Echtzeitmessungen der seismischen Amplituden (RSAM) und von der Dauer des vulkanischen Tremors von Turrialba wöchentliche und zweiwöchige zyklische Schwankungen, wie im Fall von Villarica und Llaima. Dieses Ergebnis unterstützt somit die in Kapitel II aufgestellte Hypothese, daß die Entgasungsaktivität von Vulkanen durch externe Kräfte beeinflusst wird.

Kapitel V legt das Hauptaugenmerk auf die Messung von Gaszusammensetzungen und SO_2-Flüssen von fünf Vulkanen in Nord-Chile (Lastarria, Láscar, Putana, San Pedro, Ollagüe), die miteinander kombiniert wurden, um die Entgasungsraten der verschiedenen Hauptbestandteile (H_2O, CO_2, H_2, HCl, HF, and HBr) der austretenden vulkanischen Gase zu bestimmen. Anhand dieser Gas-Flüsse wurde ein Volatilenbudget für den chilenischen Teil der Zentralen Vulkanzone Südamerikas erstellt. Die chemische Zusammensetzung der Gasemissionen von Láscar und Lastarria ist vergleichbar mit der Zusammensetzung von den Gasen der Vulkane in der Südlichen Vulkanzone, was auf die Anwesenheit eines durchgängig einheitlichen magmatischen Gas Fingerabdrucks im gesamten Chilenischen Vulkanbogen schliessen läßt.

Kapitel VI beschreibt eine Methode, in welcher Gasemissionsmessungen und Informationen aus dem Global Forecast System (GFS Wettermodell) mit den radar-interferometrischen Messungen von TerraSAR-X, einem satellitengestützten Radar mit synthetischer Apertur (InSAR) kombiniert werden, um die durch vulkanischen Wasserdampf hervorgerufenen Laufzeitverzögerungen von Radarechos in der vulkanischen Gasfahne vom Vulkan Láscar in Nord-Chile zu quantifizieren. Das Verfahren erfordert mindestens 3 Radar-Akquisitionen und annähernd zeitgleiche Gasemissionsmessungen, um die Laufzeitverzögerungen zu quantifizieren, die wiederum zur Verbesserung von Bodenverformungsmessungen an stark entgasenden Vulkanen verwendet werden können.

CONTENTS

CHAPTER I

Introduction

Introduction

1. The role of volatiles and magma degassing in volcanism

The mantle is Earth's largest volatile reservoir, which steadily supplies its crust, secondary atmosphere and Oceans with material by means of of volcanism and intrusion processes, which thus play a major role in the differentiation of our planet (Rubey, 1956). The major volatile components dissolved in the magma, which ascends through the crust prior to an eruption are in the order of their abundance: water (H_2O), carbon dioxide (CO_2), sulfur compounds (mainly SO_2 and H_2S), and halogen compounds (e.g. hydrogenated halogens such as HCl and HBr). These volatile components, though constituting only a minor fraction of a magma, provide the driving force of volcanism from the initiation of magma formation deep below Earth's crust to the dynamics of their release in the form of multi-component gas mixtures at the Earth's surface. Most volcanic activity on Earth occurs at the divergent and convergent margins of tectonic plates and is intimately linked to the movement of these plates, but a considerable number of volcanoes also occurs within the plates, of which some are located above so-called hot-spots, which are zones of upwelling hot mantle material. Magma generation at Mid-Ocean Ridges, Continental Rifts and hot-spot volcanoes is caused by decompression melting of volatile-bearing hot mantle material, which ascends below a thin lithosphere in response to plate divergence and crustal extension, respectively due to buoyancy differences of mantle plumes to their surroundings (Langmuir & Foresyth, 2007; Thybo & Nielsen 2009; Smith, 2003; Lee & Grand, 2012). Melt formation beneath volcanic arcs in contrast is related to the dehydration of the subducted oceanic plate during its descent into the hot asthenosphere (Harry & Green 1999). The influx of additional water and other volatiles dramatically lowers the melting temperature of the peridotitic mantle above the downgoing plate by 100s of degrees, and thus induces the generation of partial melts with basaltic composition (Peacock, 1996). Basaltic melts are typically less dense than the surrounding solid peridotitic mantle due to thermal and petrological differences, causing them to buoyantly ascend to the base of the overlying crust, which they intrude along crustal-scale faults.

As magma propagates through the crust towards the surface, the dissolved volatiles exert a strong influence on the ascent velocity, evolution, and eruption of magma (Wilson & Head III, 1981). Most of the basaltic magma intruding into the crust however never reaches Earth's surface and solidifies in large plutonic bodies, or dyke intrusions which stagnate deep within the crust (Rubin, 1993; Huppert & Sparks; 1988; McNutt et al., 1975), or is being stored in magma chambers at shallower crustal levels beneath the volcanic edifice (Francis et al., 1993; Pinel & Jaupart, 2004). A large fraction of the gas emitted to the atmosphere is supplied by endogenous degassing of such non-erupted basaltic magma in the sub-volcanic storage system (Allard 1997).

The process of magma degassing is largely controlled by the different solubility of the major volatile constituents H_2O, CO_2, sulfur and halogen species, which strongly depend on the confining pressure and the chemical composition of the magma (Holloway & Jakobsson, 1986). Solubility of these volatiles generally decreases with decreasing magma pressure, and thus the magma gradually gets saturated in volatiles as it decompresses during its ascent, resulting in exsolution of a given volatile constituent and the formation of bubbles, when the melt becomes oversaturated in the respective volatile. CO_2 is much less soluble in magma than most other volatiles and may already start to degas at crustal depths of several tens of kilometers, whereas sulfur species, H_2O and halogens remain dissolved until the magma nears the surface in the upper part of the volcano's conduit (e.g. Wallace, 2005). Nucleation of bubbles significantly decreases the bulk density of the degassing magma resulting in an increase of its buoyancy, which in turn increases the ascent velocity of the magma (Sparks, 1978). Magma degassing thus promotes magma convection, providing a self-sustaining mechanism that is required to keep a volcano in an active state and maintain its mass- and energy balance (Kazahaya et al., 2002). Bubbles grow in size during the ascent of the magma due to further decompression and diffusion of volatiles into the bubbles (Proussevitch & Sahagian, 1996). When the magma nears the surface, and as soon as the bubble density in the magma is large enough, bubbles accumulate and grow by coalescence with adjacent bubbles forming gas slugs, which in particular in low viscositiy magmas and at low magma ascent rates separate from the magma and rise faster than the

surrounding melt (Wilson, 1980). Magma ascent velocity significantly influences the bubble growth rate, which in turn controls whether the magma erupts effusively or explosively. Bubbles grow quickly at high decompression rates, i.e. when the magma rises rapidly leading to fragmentation of the magma and explosive eruption. At low magma ascent rates in contrast the bubbles grow much slower which results in effusive eruption of the magma.

2. The purpose of volcano surveillance

Eruption forecasting is one of the most important goals of volcanology, and is targeting to answer the critical questions when, where and how a volcano will erupt. Eruption predictions are generally based on insights obtained from statistical assessment of volcano monitoring data and from detailed studies of the eruption history of the volcano. Global historical eruption records and documentations of the accompanying changes in volcanic activity show that volcanic eruptions are almost always preceded by periods of anomalous volcanic unrest, which may last hours to months and which may follow a recognizable pattern, and thus enable to forecast eruptions, if the premonitory signs are perceived in time and interpreted correctly.

   Volcano surveillance in general has the purpose to identify these precursory signs of possibly impending eruptions by means of observing changes in proxy indicators for volcanic activity, i.e. parameters, which enable to describe the activity state of a volcano and which can be used to derive mathematical models of volcano structure and eruption mechanisms. Increasing seismicity and gas emission rates, along with changes in gas and magma composition, surface temperatures and deformation of the volcanic edifice, are often the earliest detectable precursors of an imminent eruption. Continuous monitoring of these proxy indicators can help to detect the intrusion and ascent of magma in a volcano, and at best to find out whether and how much magma will reach Earth's surface during a period of unrest, and thus provides powerful tools for eruption forecasting and hazard assessment.

3. Volcano surveillance methods

Various methods and technologies are used to monitor volcanic activity. Direct sampling methods and on-site observations are in principle very valuable for the purpose of identifying changes in volcanic activity, however they are generally often impracticable, since they require accessing the potentially hazardous crater areas of a volcano on a regular basis. Deployment of automated in-situ sensors and the application of remote sensing methods offer convenient alternatives to collect data of such dangerous and/or inaccessible areas from a safe distance, which is in particular crucial for the surveillance of remote volcanoes, where frequent on-site observations are in general not possible. Measurements obtained from remote sensing techniques are due to their remoteness however often influenced by dynamic changes in the medium between sensor and monitored object that the measurement signal has to propagate through, making it difficult to assign the observed changes in the remotely sensed signal to exclusively one cause that is exclusively related to the target. Most remote sensing applications thus demand elaborate corrections of path effects, in some cases involving the acquisition of additional independent parameters, which allow correction of the biased remotely sensed signal, in order to obtain the fraction of the signal that is related to changes in the monitored object, which in turn enables coherent interpretation of the data.

   In Chapters III to VI of this thesis, the time series of remotely sensed SO_2 emission rates from persistently degassing volcanoes were statistically examined and used in combination with the information obtained from several volcano monitoring techniques, comprising geochemical methods such as direct sampling of volcanic gases and in-situ measurements of gas compositions (Chapters V and VI), as well as seismic measurements (Chapters III and IV) and geodetic remote sensing methods (Chapter VI). The following section intends to give a "short overview" of the different volcano monitoring methods used in this thesis, which is in particular addressed to those who are not familiar with the topic volcano monitoring.

3.1 Monitoring volcanic gas emissions

Variations in composition and concentration of volatile mixtures discharged from magma have long been recognized as important indicators of magmatic processes occurring at depth (e.g. Daly, 1911). Gas emissions of nearly all volcanoes are dominated by magmatic water vapour (H_2O), which in particular at arc volcanoes often accounts for more than 90% of the discharged gas (Fischer et al., 2008). Minor gas components comprise carbon dioxide (CO_2) and sulphur compounds (mainly SO_2 and H_2S), which typically account for only a few % each, followed by even smaller amounts of hydrogen (H_2), hydrogen halides (HCl, HF, HBr, HI), noble gases like helium and argon (Symonds et al., 1994; Oppenheimer et al., 2014), and a large variety of more complex organic compounds, such as hydrocarbons and halogenated hydrocarbons (Tassi et al., 2011; Frische et al., 2006).

Emission rates of magmatic gases are commonly used as a proxy for the magma supply rate of a volcano during periods of both, quiescent and eruptive volcanic activity and thus allow inferring the amount of endogenously degassing magma stored at depth within the magmatic plumbing system of a volcano by means of comparison with the volumes and volatile contents of erupted magma. Eruptions of persistently degassing volcanoes are very often preceded by anomalous changes in the amount and composition of gas emissions (Hirabayashi et al., 1982; Aiuppa, 2007). Endogenous magma degassing moreover is responsible for the generation of several precursory signals of an impending eruption, which may manifest as triggered seismic activity at depth (Chiodini et al., 2003; Pino et al., 2011), or surface deformation of the volcanic edifice due to the accumulation and release of gas from hydrothermal systems (Samsonov et al., 2014; Ruch et al., 2009). Determination of the time lag between such deep-seated precursory signals and observations of changes in fluxes and compositions of magmatic gas escaping at the surface of the volcano provides information about the depth and ascent velocity of the degassing magma (e.g. Burton et al., 2007). Continuous monitoring of the abundance and fluxes of volatile components from volcanoes thus plays a key role in forecasting changes in volcanic activity and provide an insight into the dynamics and movement of degassing magma.

3.1.1 Direct gas sampling and in-situ measurements

The collection of volcanic gas samples at their various points of escape to the atmosphere, and subsequent analysis of these samples in the laboratory by elaborate dry and wet chemistry and gas chromatography methods, has long been the only means to measure chemical and isotopic compositions of volcanic gas emissions (e.g. Giggenbach, 1975; Sutton & Elias 2014). Analysis of the volcanic gas samples enables to determine both, major and trace gas components with high accuracy, and can yield a very detailed picture of the magmatic gas composition, provided that the collected gas was not contaminated prior to, or during the process of sampling (e.g. Gerlach & Casedevall, 1986; Symonds et al., 1992).

Gas samples obtained from fumaroles and bubbling hydrothermal springs however tend to be strongly altered by secondary processes, which occur as the magmatic gas rises through the fracture system in the subsurface of the volcano edifice (Nordlie, 1971). Such secondary processes involve the removal of magmatic gas by wall rock interactions, or the addition of gas from non-magmatic sources, such as mixing with atmospheric gases and mixing with H_2O vapour boiled off from deep hydrothermal systems and shallow meteoric water, which leads to dilution, respectively contamination of the magmatic gas composition already before the gas mixture escapes to the atmosphere. Similarly the acidic magmatic gas components and in particular SO_2 and hydrogen halides may be scrubbed from the upward percolating gas, when the gas has to permeate ground or surface water, in which they dissolve and thus get diluted, which may mask the intrusion of new magma especially during early stages of volcanic unrest (Symonds et al., 2001).

The degree of contamination of the magmatic gas by secondary processes prior to sampling strongly varies in time and depending on the location of the sampling site, respectively the distance from the degassing magma. Gas emissions from fumaroles thus merely represent very localized instantaneous snapshots of the gas compositions, which generally do not reflect the bulk gas composition emitted from the

volcano. Volcanic gas emissions obtained from domes and the immediate proximity of open magma surfaces are generally less affected by these secondary processes, and thus more likely yield gas samples representative of the primary composition of the magmatic gas, which is why volcanologists typically try to obtain their gas samples as close as possible to the degassing magma, and from fumaroles with the highest outlet temperatures (Tazieff, 1970; Le Guern et al., 1979). Direct sampling of volcanic gases thus often is extremely dangerous, especially during periods of enhanced volcanic activity, and not practicable due to the common inaccessibility of the crater areas of many volcanoes, which hinders maintaining a high frequency of sampling.

In order to yield more representative gas composition measurements than those obtained from fumaroles, several methods were developed during the past three decades, which enable to measure the concentration of selected gas components in the bulk volcanic gas plume. The filter-pack methodology was designed to collect ash, aerosols and acidic gases such as SO_2, HCl, and HF from volcanic gas plumes by means of pumping ambient air through a series of base-impregnated filters, which are preceded by a particle filter in order to prevent particles such as ash and aerosols to contaminate the impregnated filters (Finnegan et al., 1989). In the laboratory, the absorbed volatiles and dust samples are leached out of the filters and analysed by instrumental neutron activation analysis (INAA) and/or ion chromatography (IC), yielding concentrations of the respective gas species. The recurrent sampling of gas and ash by means of filter-packs in the downwind portion of the volcanic plume thus enables to deduce magma degassing depths from gas composition variations based on the different solubility of the volatile species in magma (Aiuppa et al., 2004a). This method may be less dangerous in comparison to the on-site collection of fumarolic gases, provided that the morphology of the volcano edifice is truncated enough, that it allows staying at a safe distance and at the same time still capturing the gas plume.

Filter-packs are often used in combination with so-called multi-GAS instruments (multi-component Gas Analyzer Systems; e.g. Aiuppa et al., 2005; Shinohara, 2005), which allow conducting continuous measurements of the four most abundant gas constituents (H_2O, CO_2, SO_2, H_2S) in volcanic gas plumes at a high frequency. Multi-GAS instruments typically consist of a suite of electrochemical sensors specific to SO_2 and H_2S, and a non-dispersive infrared closed-path spectrometer for the detection of H_2O and CO_2 , which are supplied with ambient air by means of a pump. Such sensors are the only means to conduct geochemical in-situ measurements in real-time, and have widely been used as mobile units for the purpose of ground-based geochemical mapping of fumarolic fields (Aiuppa et al., 2005), or mapping of volcanic gas plumes by means of airborne traverses (Gerlach et al. 1998), or as fully automated telemetric gas monitoring stations, which were deployed immediately downwind of the emission source, in order to capture variations of the gas composition and temperature of the volcanic gas plume in the long term (Aiuppa et al., 2007).

3.1.2 Remote sensing of gas emissions

Gas emission rates from volcanoes typically are retrieved using optical spectroscopic methods, as these are the only means to capture the gas concentration in the whole extent of the volcanic gas plume, which is necessary to obtain the mass flux of the emitted gas. Spectroscopic remote sensing methods are generally based on multi-spectral measurements of light, which has transited through, and partially been absorbed by the volcanic gases contained in the volcanic gas plume. Due to their unique molecular structures, each of the gases in the plume absorbs light at characteristic wavelengths in the UV or IR regions of the electromagnetic spectrum, resulting in distinct broad and narrow band optical absorption structures, which are superimposed on each other in the measured light spectra, and thus reflect the composition of the light absorbing gas mixture. Analysis of the positions and amplitudes in particular of the narrow band absorption structures provides information on the presence and concentration of the gases contained in the optical path of the spectrometer.

Apart from being much safer than monitoring by direct sampling methods, gas emission monitoring by means of spectroscopic remote sensing techniques has the major advantage that these methods generally allow for automated acquisition of gas measurements and real-time data analysis, however they typically

only allow for the quantification of selected major gas components. Despite the abundance of H_2O and CO_2 in magmatic gas emissions, their quantification by means of remote sensing methods is exceedingly difficult, since they are also present in the ambient atmosphere in significant amounts (e.g. Francis & Rothery, 2000). Remote measurements of magmatic volatiles have thus strongly focussed on SO_2 , which in contrast to H_2O and CO_2 is readily detectable by ultraviolet and infrared spectroscopic methods, due to its strong absorption in distinctive narrow band wavelength ranges of the electromagnetic spectrum, and since its abundance in the volcanic gas plume is high compared to the negligible atmospheric concentrations (Fischer 2008). SO_2 emission rates are generally obtained from spectroscopic measurements of crosswind gas concentration profiles through volcanic gas plumes in combination with transport velocities derived from weather data provided by wind models or weather stations. Combining such SO_2 emission rate measurements with simultaneous in-situ plume gas composition measurements allows for the estimation of fluxes of other gas constituents, by means of multiplying the SO_2 fluxes with molar mixing ratios determined from concentration measurements of other gas constituents in the volcanic gas plume (Edmonds et al., 2010).

The Ultraviolet Correlation Spectrometer (COSPEC), which has been introduced to volcanological community in the early 1970s (Stoiber & Jepsen, 1973), has long been the primary tool for remote measurements of SO_2 emissions from volcanoes and was used for the first assessments of global volcanogenic volatile fluxes to the atmosphere (Andres & Kasgnoc, 1998; Halmer et al., 2002). COSPEC to date is still being used for SO_2-flux monitoring on a number of volcanoes around the world, such as Soufrière Hills (Montserrat), Kilauea (Hawaii), Mijakejima volcano and Mount Asama in Japan (Young et al., 1998; Sutton et al., 2001; Kazahaya et al., 2004; Owahda et al., 2013), though nearly all of the measurements by means of COSPEC were performed rather sporadically and mainly covered periods of volcanic crisis, as they strongly relied on labour-intense field campaigns, since this bulky instrument is not suited for automated acquisition of data.

COSPEC has thus in many places been gradually been displaced by easily operated instruments based on robust lightweight miniature UV spectrometers, such as mini-DOAS (miniature DOAS; Galle et al., 2003), FLYSPEC (Horton et al., 2006), MAX-DOAS (Multi-Axis DOAS; Bobrowski et al., 2003), and scan-DOAS (Galle et al., 2010), which allow fully automated acquisition of data at a relatively high temporal rate of several minutes per measurement and are thus used on an increasing number of volcanoes to permanently monitor SO_2 emission rates, enabling to effortlessly study long-term degassing variations including periods of quiescence (e.g. Nicholson et al., 2013). The UV spectrometers utilize linear CCD sensors combined with a diffraction grating, and thus provide one-dimensional hyperspectral measurements, which can in principle be used to simultaneously also quantify other light absorbing trace gases than SO_2 , such as bromine monoxide (BrO; Bobrowski et al., 2003; Lübcke et al., 2013), or chlorine monoxide (ClO; Lee et al., 2005).

Spectroscopic imaging systems, such as IDOAS (Imaging DOAS; Bobrowski et al, 2006) and UV cameras (Mori & Burton, 2006) are the most recent advancements in the field of ground-based SO_2 emission monitoring, which enabled two-dimensional visualization of gas dispersion and observation of short term variations in degassing behaviour at a high temporal resolution of down to 1 Hz (Oppenheimer et al., 2009; Boichu et al., 2010; Tamburello et al., 2013; Nadeau et al., 2015). Tracking of the gas plume in such highly resolved image sequences furthermore allows determination of accurate plume speeds, which in this work have been used to calculate SO_2-fluxes from scan-DOAS measurements at Láscar volcano (Chapter V: Tamburello et al., 2014). Efforts have been made during the past decade to automate processing of the vast amounts of data which such cameras record within a short period of time, in order to provide the possibility to conduct continuous long term monitoring in real-time (Burton et al., 2015; Kern et al., 2015).

Satellite-based nadir looking UV and IR sensors allow to globally measure SO_2 emissions from volcanoes on a regular basis (Flower et al., 2016), however at a rather low frequency depending on the revisit times of the satellites, and were used to map and track volcanic gas plumes, since the first detection of SO_2 in the volcanic eruption cloud of El Chichón volcano by means of the Total Ozone Mapping Spectrometer on the Nimbus-7 satellite in 1982 (Krueger et al., 1983). While early space-based optical sensors were still restricted to monitoring eruption clouds and high altitude gas emissions from very strong

sources, technological advances in multispectral sensors onboard of satellites have recently lead to an improved spatial and spectral resolution, which significantly reduced the detection limits of SO_2, and thus offer the opportunity to monitor non-eruptive SO_2 emissions from quiescently degassing volcanoes. The development of more sophisticated retrieval algorithms now enable to monitor the trajectories of SO_2 and ash emissions from volcanoes, which is valuable in particular for aviation safety (Corradini et al., 2010).

Open-path Fourier transform infrared (OP-FTIR) spectroscopy has on several volcanoes successfully been applied to the study of the chemical composition of gas emissions (Notsu et al., 1993; Mori & Notsu, 1997; Oppenheimer et al., 1998) and gas emission rates of selected gas species (Duffell et al., 2001). OP-FTIR measurements can be performed at a high frequency and permit to simultaneously sense multiple gas species including H_2O, CO_2, CO, OCS, SO_2, HCl, HF and SiF_4. Reliable retrievals of H_2O and CO_2 concentrations are however not straight forward to obtain and require very short path lengths, i.e. the instrument has to be deployed relatively close to the emission source in order to avoid interference with the background atmosphere (e.g. Burton et al., 2000; La Spina et al., 2013).

3.2 Monitoring volcano seismicity

The investigation of volcano related seismic signals is arguably the most common and reliable volcano monitoring method used by volcano observatories worldwide, which probably can be attributed to the long history of volcano seismology and the benefits related to the experiences gained through over a century of scientific observations. Pioneering work was conducted by Fusakichi Omori, who examined the seismic signals related to the 1910 eruptions of Usu-san and Asama-yama volcanoes in Japan, and found that volcanic eruptions typically are preceded and accompanied by earthquakes and ground vibrations, which he related to magma movement and fracturing of the surrounding bedrocks (Omori, 1911; Omori, 1912).

Volcanic activity produces a variety of seismic signals, which have specific waveform characteristics that can be used to infer the associated processes occurring at depth and the surface of the volcanic edifice. The occurrence of volcano related seismicity heralding an eruption often tends to be very localized and to cluster in the regions of magma emplacement, resulting in so-called earthquake swarms. Sufficiently dense networks of seismometer sensors deployed on volcanoes allow for the determination of hypocenters of single events, which in turn enables to locate and track magma movement and associated deep-seated changes in activity.

Classification of seismic signals from volcanoes is commonly based on the dominant frequency content and shape of the waveform in particular in the region of the onset of individual signals (e.g. Lahr et al., 1994). Four main types of volcano related seismic signals are generally distinguished: Volcano-tectonic (VT) earthquakes, long-period (LP) earthquakes, volcanic tremor, and explosion earthquakes.

The occurrence of volcano-tectonic earthquake swarms is often one of the first signs of magma intrusion at depth. Volcano-tectonic earthquakes are high-frequency events, which typically contain prevalent frequencies in the range of 2-50 Hz, and are thought to originate from shear fracture of solidified magma and/or surrounding bedrocks associated to dike propagation and the emplacement of fresh magma (Roman & Cashman, 2006). The waveforms of volcano-tectonic events are characterized by clearly distinguishable impulsive onsets of pressure- and shear-wave arrivals, and thus contain information on the orientation of the local stresses exerted during rupture. Such volcano-tectonic events are thus very similar to and cannot be distinguished from general shallow tectonic earthquakes.

Low-frequency seismicity occurring at volcanoes is commonly interpreted as a sign for magma movement and degassing processes, and comprises long-period events, continuous volcanic tremor, and very long-period events. Long-period events typically resemble small tectonic earthquakes in duration, but their waveforms show no shear-wave arrivals and are characterized by a very emergent onset of a low frequency waveform, which is commonly restricted to the frequency range between 1 and 5 Hz. The source regions of long-period events are generally located in the upper part of the volcanic conduit, and their occurrence is commonly interpreted as a resonant response of fluid-filled cracks or conduit walls to short-term pressure perturbations caused by fluid or gas flow, or magma movement (Chouet, 1996).

Volcanic tremor is a continuous seismic low frequency signal, which typically occurs at persistently degassing volcanoes during phases of vigorous degassing, and accompanies virtually all volcanic eruptions (McNutt & Nishimura, 2008). The spectral characteristics of volcanic tremor are very similar to those of long-period events, though they are generally denoted by much narrower frequency ranges and may significantly differ in duration of the waveform, which can last for minutes to days with sustained amplitude following the emergent onset of the pressure-wave. Duration and amplitude of such signals are good indicators for the activity state of a volcano, their occurrence, however, superimposes on and thus hinders the detection and identification of the above described signals.

Volcanic explosions often produce very long period (VLP) signals, which are characterized by waveforms with periods ranging from 3 to 100s of seconds. The very long period signals are followed within few seconds by short-period signals characterized by frequency contents above 1 Hz, which accompany the eruption of pyroclastics (Nishimura, 1995; Chouet et al., 1997). Very long period events generally originate from small shallow seated source regions in the upper part of the volcanic conduit, and were ascribed to gas bubble bursting during strombolian explosions (Chouet et al., 2003) and degassing bursts from obstructed volcanic vents (Chouet et al., 2005).

Yet another earthquake type frequently occurring on volcanoes is the hybrid earthquake. Hybrid events share the characteristics of volcano-tectonic and long-period events, and have high frequency onsets followed by low-frequency oscillations, suggesting the contemporary occurrence of volcano-tectonic and long-period seismicity related processes. Hybrid events are accordingly commonly ascribed to brittle failure of solidified magma and the wall rocks of the magma plumbing system, in combination with resonance of the fluid-filled conduit, due to magma movement (e.g. Tuffen et al., 2003), but may also be related to low rupture velocities combined with strong path effects as a result from a shallow source location (e.g. Harrington & Brodsky, 2007).

This list of the above described volcano related seismic signals is, however, by far not exhaustive, even if it would be supplemented by all the signals resulting from processes occurring on the surface of the volcano edifice. Such superficial seismic signals comprise continuous signals resembling tremor, which are related to landslides, lahars, rockfalls and pyroclastic flows, and short-duration events related to icequakes, which are an important feature on glaciated volcanoes.

The physical meaning of the different seismic signals, in particular of the low-frequency events and their relation to magma movement is, however, not yet well understood, and explanation of source mechanisms, in particular of those signals related to deep-seated processes is still subject of the recent research (McNutt, 2005). The physical processes underlying the generation of seismic signals, which manifest at the surface of the volcanic edifice are in contrast a bit better constrained, as these processes typically can be observed and measured by other monitoring methods, e.g. by means of recordings from infrasonic pressure sensors, which in many places are used to complement seismic networks (e.g. Johnson et al., 2004). The attribution of these superficially occurring signals to their likely causes often merely demands visual observation of the event, respectively observations of the changes related to the event by comparison of the conditions encountered before and after the event.

The requirement to evaluate a large abundance and variety of volcano related seismic signals, in order to identify precursory signs of an impending eruption, calls for automatic detection and classification of seismic events. Automated identification of the different classes of events in continuous seismic records by means of pattern recognition is however very challenging, since signals of each seismic event appear to be different at different stations and event classes may partially overlap in certain waveform characteristics used for classification (Curilem et al., 2009; Curilem et al., 2016). In addition, various individual signals may temporarily overlap especially during periods of enhanced volcanic activity, or in the aftermath of large intraplate earthquakes, when the frequent occurrence of aftershocks obscures the volcanic events (Mora et al., 2012). Moreover, the spectral and wave field features used for the classification of events tend to change during eruptions, due to migration of source locations of the individual events (Cannata et al., 2009), hampering the automated discrimination of the different volcano seismic events.

For early warning purposes, the development of volcanic activity often can already sufficiently well be deduced from time series based on simple seismic event statistics, such as counts of the number of different event type occurrences per hour or day, changes in the duration of tremor signals, or even better by

monitoring their hypocenter distributions. Interpretation of such data is however significantly facilitated, when seismic time series data is used in combination with time series of other proxies of volcanic activity, such as SO_2-flux measurements, as shown in Chapter III of this thesis (Conde et al., 2013).

In order to be able to assess the volcanic hazard in a timely manner during volcanic crisis, volcano observatories generally routinely measure the level of seismic activity by means of so-called Real-time seismic amplitude measurements (RSAM). RSAM is calculated from raw seismometer data (Endo & Murray, 1991), and yields a time series of the time-averaged seismic energy release during an episode of volcanic activity. Such measurements thus readily can be down sampled to the temporal resolution of other available volcano monitoring data, facilitating comparison and combined analysis as demonstrated in Chapters III and IV (Conde et al., 2013 and Conde et al., 2014). One major drawback of RSAM is that such measurements may also contain significant contributions of non-volcanic sources, such as weather-related or anthropogenic noise, and distant tectonic earthquakes.

3.3 Monitoring volcano deformation

The eruptions of many volcanoes are preceded by periods of inflation of the ground surface as a result of the accumulation of ascending magma in shallow seated magma chambers, or as a result of dike propagation, when the magma establishes new pathways towards the surface, and are accompanied and followed by the deflation of the surface as a result of magma eruption and magma retreat respectively (Segall 2013). Repeated measurements of such ground surface deformations in conjunction with appropriate numerical deformation models provide information on the changes of the shape and size of the inflating or deflating magma reservoir (Mogi, 1958; Okada 2006), and allow assessing the stability of the flanks of the volcanic edifice (Voight et al., 2002; Lundgren et al., 2003). Standard techniques, which are commonly used in combination to measure volcano deformation, include several ground-based geodetic methods, such as repeated precise leveling and triangulation surveys, electronic distance measurements (EDM) using reflected laser or infrared light, occasional use of temporary global positioning systems (GPS) (e.g. Tryggvason, 1994). All of these methods require establishment of dense networks of benchmarks which cover the whole volcanic area in order to resolve the surface deformation pattern with respect to the surrounding non-deforming ground. Furthermore such measurements generally require the repeated realization of labor and time intense measurement campaigns, and thus often are restricted to less frequent occasional measurements of vertical and lateral displacements between marked points on and around the volcanic edifice, which generally are conducted prior to and after eruptions and thus often lack information during eruptive periods. Borehole sensors, such as tilt meters and strain meters provide continuous measurements of the inclination and strain of the flanks of the monitored volcano, the latter of which are however only used on a few volcanoes such as Hekla and Soufrière Hills (Linde et al., 1993; Hautmann et al., 2013). The development of more advanced continuous global positioning systems (GPS) and in particular the invention of interferometric synthetic aperture radar (InSAR) techniques has in the past three decades led to a growing wealth of available volcano deformation data. InSAR measurements utilize the phase difference of radar reflections of the ground surface, which were recorded during different satellite overpasses to measure changes in the position of reflection points with a high spatial resolution. Satellite based InSAR provides long term observations of surface deformations with global coverage, but is limited to observe slow deformation processes, due to the rather sparse frequency of satellite overpasses.

References

Aiuppa, A., M. Burton, F. Mure`, and S. Inguaggiato (2004b), Intercomparison of volcanic gas monitoring methodologies performed on Vulcano Island, Italy. *Geophys. Res. Lett.*, 31, L02610, doi:10.1029/2003GL018651.

Aiuppa, A., Federico, C., Giudice, G., Gurrieri, S., Paonita, A., & Valenza, M. (2004a). Plume chemistry provides insights into mechanisms of sulfur and halogen degassing in basaltic volcanoes. *Earth and Planetary Science Letters*, 222(2), 469-483. DOI:10.1016/j.epsl.2004.03.020

Aiuppa, A., C. Federico, G. Giudice, and S. Gurrieri (2005), Chemical mapping of a fumarolic field: La Fossa Crater, Vulcano Island (Aeolian Islands, Italy). *Geophys. Res. Lett.*, 32, L13309. doi:10.1029/2005GL023207.

Aiuppa, A., Moretti, R., Federico, C., Giudice, G., Gurrieri, S., Liuzzo, M., Papale, P., Shinohara, H., & Valenza, M. (2007). Forecasting Etna eruptions by real-time observation of volcanic gas composition. *Geology*, 35(12), 1115-1118. doi: 10.1130/G24149A.1

Allard, P. (1997). Endogenous magma degassing and storage at Mount Etna. *Geophysical Research Letters*, 24(17), 2219-2222. DOI: 10.1029/97GL02101

Andres, R. J., & Kasgnoc, A. D. (1998). A time-averaged inventory of subaerial volcanic sulfur emissions. *Journal of Geophysical Research: Atmospheres*, 103(D19), 25251-25261. DOI: 10.1029/98JD02091

Bobrowski, N., Hönninger, G., Lohberger, F., & Platt, U. (2006). IDOAS: A new monitoring technique to study the 2D distribution of volcanic gas emissions. *Journal of volcanology and geothermal research*, 150(4), 329-338. DOI:10.1016/j.jvolgeores.2005.05.004

Bobrowski, N., Hönninger, G., Galle, B., & Platt, U. (2003). Detection of bromine monoxide in a volcanic plume. *Nature*, 423(6937), 273-276. doi:10.1038/nature01625

Boichu, M., Oppenheimer, C., Tsanev, V., & Kyle, P. R. (2010). High temporal resolution SO_2 flux measurements at Erebus volcano, Antarctica. Journal of Volcanology and Geothermal Research, 190(3), 325-336.na example, *Geophys. Res. Lett.*, 40, 4818–4822, doi:10.1002/grl.50924.

Bredemeyer S, Hansteen T (2014) Synchronous degassing patterns of the neighbouring volcanoes Llaima and Villarrica in southcentral Chile: the influence of tidal forces. *Int J Earth Sci (Geol Rundsch)* 103(7):1999–2012. doi:10.1007/s00531-014-1029-2

Burton, M. R., Oppenheimer, C., Horrocks, L. A., & Francis, P. W. (2000). Remote sensing of CO_2 and H_2O emission rates from Masaya volcano, Nicaragua. *Geology*, 28(10), 915-918. DOI:10.1130/0091-7613(2000)28<915:RSOCAH>2.0.CO;2

Burton, M., Allard, P., Muré, F., & La Spina, A. (2007). Magmatic gas composition reveals the source depth of slug-driven Strombolian explosive activity. *Science*, 317(5835), 227-230. DOI: 10.1126/science.1141900

Burton, M. R., Salerno, G. G., D'Auria, L., Caltabiano, T., Murè, F., & Maugeri, R. (2015). SO_2 flux monitoring at Stromboli with the new permanent INGV SO_2 camera system: A comparison with the FLAME network and seismological data. *Journal of Volcanology and Geothermal Research*, 300, 95-102. DOI: 10.1016/j.jvolgeores.2015.02.006

Cannata, A., Hellweg, M., Di Grazia, G., Ford, S., Alparone, S., Gresta, S., Montalto, P. & Patanè, D. (2009). Long period and very long period events at Mt. Etna volcano: Characteristics, variability and causality, and implications for their sources. *Journal of Volcanology and Geothermal Research*, 187(3), 227-249. DOI:10.1016/j.jvolgeores.2009.09.007

Chouet, B. A. (1996). Long-period volcano seismicity: its source and use in eruption forecasting. *Nature*, 380(6572), 309-316. doi:10.1038/380309a0

Chouet, B., Dawson, P., Ohminato, T., Martini, M., Saccorotti, G., Giudicepietro, F., De Luca, G., Milana, G., Scarpa, R. (2003). Source mechanisms of explosions at Stromboli Volcano, Italy, determined from moment-tensor inversions of very-long-period data. *Journal of Geophysical Research: Solid Earth*, 108(B1). DOI: 10.1029/2002JB001919

Chouet, B., Dawson, P., & Arciniega-Ceballos, A. (2005). Source mechanism of Vulcanian degassing at Popocatépetl Volcano, Mexico, determined from waveform inversions of very long period signals. *Journal of Geophysical Research: Solid Earth*, 110(B7). DOI: 10.1029/2004JB003524

Conde, V., **S. Bredemeyer**, E. Duarte, Javier F. Pacheco, Sebastian Miranda, Bo Galle, Thor H. Hansteen (2013). SO_2 degassing from Turrialba Volcano linked to seismic signatures during the period 2008–2012. *Int J Earth Sci (Geol Rundsch)*, Volume 103, Issue 7, pp 1983-1998. DOI 10.1007/s00531-013-0958-5

Conde, V., **S. Bredemeyer**, J. A. Saballos, Bo Galle, T. H. Hansteen (2014). Linking SO_2 emission rates and seismicity by continuous wavelet transform: implications for volcanic surveillance at San Cristóbal volcano, Nicaragua. *Int J Earth Sci (Geol Rundsch)*, pp 1-13. DOI 10.1007/s00531-015-1264-1

Corradini, S., Merucci, L., Prata, A. J., & Piscini, A. (2010). Volcanic ash and SO_2 in the 2008 Kasatochi eruption: Retrievals comparison from different IR satellite sensors. *Journal of Geophysical Research: Atmospheres*, 115(D2). DOI: 10.1029/2009JD013634

Curilem, G., Vergara, J., Fuentealba, G., Acuña, G., & Chacón, M. (2009). Classification of seismic signals at Villarrica volcano (Chile) using neural networks and genetic algorithms. *Journal of volcanology and geothermal research*, 180(1), 1-8. DOI:10.1016/j.jvolgeores.2008.12.002

Curilem, M., Huenupan, F., Beltrán, D., San Martin, C., Fuentealba, G., Franco, L., Cardona, C., Acuña, G., Chacón, M., Khan, M. S., Becerra Yoma, N. B. (2016). Pattern recognition applied to seismic signals of Llaima volcano (Chile): An evaluation of station-dependent classifiers. *Journal of Volcanology and Geothermal Research*, 315, 15-27. DOI:10.1016/j.jvolgeores.2016.02.006

Daly, R. A. (1911, June). The nature of volcanic action. In *Proceedings of the American Academy of Arts and Sciences* (Vol. 47, No. 3, pp. 47-122). American Academy of Arts & Sciences. DOI: 10.2307/20022712

Duffell, H., Oppenheimer, C., & Burton, M. (2001). Volcanic gas emission rates measured by solar occultation spectroscopy. *Geophysical research letters*, 28(16), 3131-3134. DOI: 10.1029/2000GL012425

Edmonds, M., Aiuppa, A., Humphreys, M., Moretti, R., Giudice, G., Martin, R. S., Herd, R. A., Christopher, T. (2010). Excess volatiles supplied by mingling of mafic magma at an andesite arc volcano. *Geochemistry, Geophysics, Geosystems*, 11(4).DOI:10.1029/2009GC002781

Endo, E. T., & Murray, T. (1991). Real-time seismic amplitude measurement (RSAM): a volcano monitoring and prediction tool. *Bulletin of Volcanology*, 53(7), 533-545. DOI: 10.1007/BF00298154

Finnegan, D. L., Kotra, J. P., Hermann, D. M., & Zoller, W. H. (1989). The use of [7]LiOH-impregnated filters for the collection of acidic gases and analysis by instrumental neutron activation analysis. *Bulletin of volcanology*, 51(2), 83-87. DOI: 10.1007/BF01081977

Fischer T.P. (2008). Fluxes of volatiles (H_2O, CO_2, N_2, Cl, F) from arc volcanoes. *Geochemical Journal*, Vol. 42, pp. 21 to 38, 2008. DOI:10.2343/geochemj.42.21

Flower, V. J., Oommen, T., & Carn, S. A. Improving automated global detection of volcanic SO_2 plumes using the Ozone Monitoring Instrument (OMI). doi:10.5194/amt-2016-206

Francis P.W. and Rothery D.A. (2000). Remote sensing of active volcanoes. *Annu. Rev. Earth Planet. Sci.* 2000. Vol.28:81–106. DOI: 10.1146/annurev.earth.28.1.81

Francis, P., Oppenheimer, C., & Stevenson, D. (1993). Endogenous growth of persistently active volcanoes. *Nature*, 366(6455), 554-557. DOI:10.1038/366554a0

Frische, M., Garofalo, K., Hansteen, T. H., & Borchers, R. (2006). Fluxes and origin of halogenated organic trace gases from Momotombo volcano (Nicaragua). *Geochemistry, Geophysics, Geosystems*, 7(5). DOI: 10.1029/2005GC001162

Galle, B., Oppenheimer, C., Geyer, A., McGonigle, A. J., Edmonds, M., & Horrocks, L. (2003). A miniaturised ultraviolet spectrometer for remote sensing of SO_2 fluxes: a new tool for volcano surveillance. *Journal of Volcanology and Geothermal Research*, 119(1), 241-254. DOI:10.1016/S0377-0273(02)00356-6

Galle B., Johansson M., Rivera C., Zhang Y., Kihlman M., Kern C., Lehmann T., Platt U., Arellano S., Hidalgo S. (2010) Network for observation of volcanic and atmospheric change (NOVAC)—a global network for volcanic gas monitoring: network layout and instrument description. *J Geophys Res* 115:D05304. doi:10.102 9/2009JD011823

Gerlach, T. M., & Casadevall, T. J. (1986). Evaluation of gas data from high-temperature fumaroles at Mount St. Helens, 1980–1982. *Journal of volcanology and geothermal research*, 28(1), 107-140. doi:10.1016/0377-0273(86)90008-9

Gerlach, T. M., McGee, K. A., Sutton, A. J., & Elias, T. (1998). Rates of volcanic CO_2 degassing from airborne determinations of SO_2 emission rates and plume CO_2/SO_2: test study at Puʹ uʹ Oʹ o Cone, Kilauea Volcano, Hawaii. *Geophysical research letters*, 25(14), 2675-2678. DOI: 10.1029/98GL02030

Giggenbach, W. F. (1975). A simple method for the collection and analysis of volcanic gas samples. *Bulletin volcanologique*, 39(1), 132-145. DOI: 10.1007/BF02596953

Le Guern, F., Carbonnelle, J. and Tazieff, H., 1979. Erta' Ale lava lake: heat and gas transfer to the atmosphere. *J. Volcanol. Geotherm. Res.*, 6: 27--48. doi:10.1016/0377-0273(79)90045-3

Halmer, M. M., Schmincke, H. U., & Graf, H. F. (2002). The annual volcanic gas input into the atmosphere, in particular into the stratosphere: a global data set for the past 100 years. *Journal of Volcanology and Geothermal Research*, 115(3), 511-528. DOI: 10.1016/S0377-0273(01)00318-3

Harrington, R. M., & Brodsky, E. E. (2007). Volcanic hybrid earthquakes that are brittle-failure events. *Geophysical Research Letters*, 34(6).DOI: 10.1029/2006GL028714

Harry, D. L., & Green, N. L. (1999). Slab dehydration and basalt petrogenesis in subduction systems involving very young oceanic lithosphere. *Chemical Geology*, 160(4), 309-333. DOI:10.1016/S0009-2541(99)00105-9

Hautmann, S., Hidayat, D., Fournier, N., Linde, A. T., Sacks, I. S., & Williams, C. P. (2013). Pressure changes in the magmatic system during the December 2008/January 2009 extrusion event at Soufrière Hills Volcano, Montserrat (WI), derived from strain data analysis. *Journal of Volcanology and Geothermal Research*, 250, 34-41. DOI:10.1016/j.jvolgeores.2012.10.006

Hirabayashi, J. I., Ossaka, J., & Ozawa, T. (1982). Relationship between volcanic activity and chemical composition of volcanic gases-A case study on the Sakurajima Volcano. *Geochemical Journal*, 16(1), 11-21. DOI:10.2343/geochemj.16.11

Holloway, J. R., & Jakobsson, S. (1986). Volatile solubilities in magmas: Transport of volatiles from mantles to planet surfaces. In *Lunar and Planetary Science Conference Proceedings* (Vol. 16).

Hooper, A., Prata, F., & Sigmundsson, F. (2012). Remote sensing of volcanic hazards and their precursors. *Proceedings of the IEEE*, 100(10), 2908-2930. DOI:10.1109/JPROC.2012.2199269

Horton, K. A., Williams-Jones, G., Garbeil, H., Elias, T., Sutton, A. J., Mouginis-Mark, P., Porter, J.N. & Clegg, S. (2006). Real-time measurement of volcanic SO_2 emissions: validation of a new UV correlation spectrometer (FLYSPEC). *Bulletin of Volcanology*, 68(4), 323-327. DOI: 10.1007/s00445-005-0014-9

Huppert, H. E., & Sparks, R. S. J. (1988). The generation of granitic magmas by intrusion of basalt into continental crust. *Journal of Petrology*, 29(3), 599-624. doi: 10.1093/petrology/29.3.599

Jaupart, C., & Tait, S. (1995). Dynamics of differentiation in magma reservoirs. *Journal of Geophysical Research: Solid Earth*, 100(B9), 17615-17636. DOI: 10.1029/95JB01239

Johnson, J. B., Aster, R. C., & Kyle, P. R. (2004). Volcanic eruptions observed with infrasound. *Geophysical Research Letters*, 31(14). DOI: 10.1029/2004GL020020

Kazahaya, K., Shinohara, H., & Saito, G. (2002). Degassing process of Satsuma-Iwojima volcano, Japan: Supply of volatile components from a deep magma chamber. *Earth, planets and space*, 54(3), 327-335. DOI: 10.1186/BF03353031

Kazahaya, K., Shinohara, H., Uto, K., Odai, M., Nakahori, Y., Mori, H., Iino, H., Miyashita, M., & Hirabayashi, J. (2004). Gigantic SO_2 emission from Miyakejima volcano, Japan, caused by caldera collapse. *Geology*, 32(5), 425-428. doi: 10.1130/G20399.1

Kern, C., Sutton, J., Elias, T., Lee, L., Kamibayashi, K., Antolik, L., & Werner, C. (2015). An automated SO_2 camera system for continuous, real-time monitoring of gas emissions from Kīlauea Volcano's summit Overlook Crater. *Journal of Volcanology and Geothermal Research*, 300, 81-94. DOI: 10.1016/j.jvolgeores.2014.12.004

Lahr, J. C., Chouet, B. A., Stephens, C. D., Power, J. A., & Page, R. A. (1994). Earthquake classification, location, and error analysis in a volcanic environment: Implications for the magmatic system of the 1989–1990 eruptions at Redoubt Volcano, Alaska. *Journal of Volcanology and Geothermal Research*, 62(1), 137-151. doi:10.1016/0377-0273(94)90031-0

Langmuir, C.H., Foresyth, D.W. (2007). Mantle melting beneath Mid-Ocean Ridges. *Oceanography*, Volume 20, Number 1, pp.78-89.

Lee, C.A. & Grand, S.P. (2012). Earth science: Intraplate volcanism. *Nature*, Volume 482, Issue 7385, pp. 314-315 (2012). doi:10.1038/482314a

Lee, C., Y. J. Kim, H. Tanimoto, N. Bobrowski, U. Platt, T. Mori, K. Yamamoto, and C. S. Hong (2005), High ClO and ozone depletion observed in the plume of Sakurajima volcano, Japan, *Geophys. Res. Lett.*, 32, L21809, doi:10.1029/2005GL023785.

Linde, A. T., Agustsson, K., Sacks, I. S., & Stefansson, R. (1993). Mechanism of the 1991 eruption of Hekla from continuous borehole strain monitoring. *Nature*, 365(6448), 737-740. doi:10.1038/365737a0

Lübcke, P., Bobrowski, N., Arellano, S., Galle, B., Garzón, G., Vogel, L., & Platt, U. (2013). BrO/SO_2 molar ratios from scanning DOAS measurements in the NOVAC network. *Solid Earth Discussions*, 5(2). doi:10.5194/sed-5-1845-2013

Lundgren, P., P. Berardino, M. Coltelli, G. Fornaro, R. Lanari, G. Puglisi, E. Sansosti, and M. Tesauro (2003). Coupled magma chamber inflation and sector collapse slip observed with synthetic aperture radar interferometry on Mt. Etna volcano. *J. Geophys. Res.*, 108(B5), 2247. doi:10.1029/2001JB000657

McNutt, R. H., Crocket, J. H., Clark, A. H., Caelles, J. C., Farrar, E., Haynes, S. J., & Zentilli, M. (1975). Initial ^{87}Sr/^{86}Sr ratios of plutonic and volcanic rocks of the Central Andes between latitudes 26 and 29 south. *Earth and Planetary Science Letters*, 27(2), 305-313. doi:10.1016/0012-821X(75)90042-4

McNutt, S. R. (2005). Volcanic seismology. *Annu. Rev. Earth Planet. Sci.*, 32, 461-491. DOI: 10.1146/annurev.earth.33.092203.122459

McNutt, S. R., & Nishimura, T. (2008). Volcanic tremor during eruptions: Temporal characteristics, scaling and constraints on conduit size and processes. *Journal of Volcanology and Geothermal Research*, 178(1), 10-18. DOI:10.1016/j.jvolgeores.2008.03.010

Mogi, K. (1958). Relations between the eruptions of various volcanoes and the deformations of the ground surfaces around them. http://hdl.handle.net/2261/11909

Mora-Stock, C., M. Thorwart, T. Wunderlich, **S. Bredemeyer**, T. H. Hansteen, W. Rabbel (2012). Comparison of seismic activity for Llaima and Villarrica volcanoes prior to and after the Maule 2010 earthquake. *Int J Earth Sci (Geol Rundsch)*, Volume 103, Issue 7, pp. 2015-2028. DOI: 10.1007/s00531-012-0840-x

Mori, T., and M. Burton (2006), The SO_2 camera: A simple, fast and cheap method for ground-based imaging of SO_2 in volcanic plumes. *Geophys. Res. Lett.*, 33, L24804, doi:10.1029/2006GL027916.

Mori, T., & Notsu, K. (1997). Remote CO, COS, CO_2, SO_2, HCl detection and temperature estimation of volcanic gas. *Geophysical Research Letters*, 24(16), 2047-2050. DOI: 10.1029/97GL52058

Nadeau, P. A., Werner, C. A., Waite, G. P., Carn, S. A., Brewer, I. D., Elias, T., Sutton, A.J. & Kern, C. (2015). Using SO_2 camera imagery and seismicity to examine degassing and gas accumulation at Kīlauea Volcano, May 2010. *Journal of Volcanology and Geothermal Research*, 300, 70-80. DOI:10.1016/j.jvolgeores.2014.12.005

Nicholson, E. J., Mather, T. A., Pyle, D. M., Odbert, H. M., & Christopher, T. (2013). Cyclical patterns in volcanic degassing revealed by SO_2 flux timeseries analysis: an application to Soufrière Hills Volcano, Montserrat. *Earth and Planetary Science Letters*, 375, 209-221. DOI:10.1016/j.epsl.2013.05.032

Nordlie, B. E. (1971). The composition of the magmatic gas of Kilauea and its behavior in the near surface environment. *American Journal of Science*, 271(5), 417-463. doi: 10.2475/ajs.271.5.417

Notsu, K., Mori, T., Igarashi, G., Tohjima, Y., & Wakita, H. (1993). Infrared spectral radiometer: A new tool for remote measurement of SO_2 of volcanic gas. *Geochemical Journal*, 27(4/5), 361-366. DOI:10.2343/geochemj.27.361

Okada, J. (2006). Dacìtic magma doming associated with shallow inflation and deep deflation sources – An application to Mt. Usu, Japan. *Geophysical Bulletin of Hokkaido University*, Sapporo, Japan No. 69, March 2006, pp. 191-206. DOI: 10.14943/gbhu.69.191

Omori, F. (1911). The Usu-san eruption and earthquake and elevation phenomena. *Bull. Imper. Earthq. Invest. Com* 5, 138.

Omori, F. (1912). The eruptions and earthquakes of the Asama-yama. *Bull. Imper. Earthq. Invest. Com* 6, 1147.

Oppenheimer, C., Francis, P., Burton, M., Maciejewski, A. J. H., & Boardman, L. (1998). Remote measurement of volcanic gases by Fourier transform infrared spectroscopy. *Applied Physics B: Lasers and Optics*, 67(4), 505-515. DOI: 10.1007/s003400050536

Oppenheimer, C., Lomakina, A. S., Kyle, P. R., Kingsbury, N. G., & Boichu, M. (2009). Pulsatory magma supply to a phonolite lava lake. *Earth and Planetary Science Letters*, 284(3), 392-398. DOI: 10.1016/j.epsl.2009.04.043

Oppenheimer, C., Fischer, T. P., & Scaillet, B. (2014). Volcanic degassing: process and impact. In: *Treatise on Geochemistry (Second Edition)*, 111-179. DOI:10.1016/B978-0-08-095975-7.00304-1

Peacock, S. M. (1996) Thermal and Petrologic Structure of Subduction Zones. In: Subduction Top to Bottom (eds G. E. Bebout, D. W. Scholl, S. H. Kirby and J. P. Platt), American Geophysical Union, Washington, D. C.. DOI: 10.1029/GM096p0119

Pinel, V., & Jaupart, C. (2004). Magma storage and horizontal dyke injection beneath a volcanic edifice. *Earth and Planetary Science Letters*, 221(1), 245-262. DOI:10.1016/S0012-821X(04)00076-7

Pino, N. A., R. Moretti, P. Allard, and E. Boschi (2011), Seismic precursors of a basaltic paroxysmal explosion track deep gas accumulation and slug upraise. *J. Geophys. Res.*, 116, B02312, doi:10.1029/2009JB000826.

Proussevitch, A. A., & Sahagian, D. L. (1996). Dynamics of coupled diffusive and decompressive bubble growth in magmatic systems. *Journal of Geophysical Research: Solid Earth*, 101(B8), 17447-17455. DOI: 10.1029/96JB01342

Roman, D. C., & Cashman, K. V. (2006). The origin of volcano-tectonic earthquake swarms. *Geology*, 34(6), 457-460. doi: 10.1130/G22269.1

Rubey, William W. (1951). Geologic history of sea water. *Bull. Geol. Soc. Am.* v.62 No. 9, pp. 1111-1147. doi: 10.1130/0016-7606(1951)62[1111:GHOSW]2.0.CO;2

Rubin, A. M. (1993). Dikes vs. diapirs in viscoelastic rock. *Earth and Planetary Science Letters*, 119(4), 641-659. doi:10.1016/0012-821X(93)90069-L

Samsonov, S.V., K.F. Tiampo, A.G. Camacho, J. Fernández, and P.J. González (2014), Spatiotemporal analysis and interpretation of 1993–2013 ground deformation at Campi Flegrei, Italy, observed by advanced DInSAR, *Geophys. Res. Lett.*, 41, 6101–6108, doi:10.1002/2014GL060595.

Segall, P. (2013). Volcano deformation and eruption forecasting. *Geological Society, London, Special Publications*, 380(1), 85-106. doi:10.1144/SP380.4

Shinohara H. (2005) A new technique to estimate volcanic gas composition: plume measurements with a portable multi-sensor system. *J Volcanol Geotherm Res* 143(4):319–333. doi:10.1016/j.jvolgeores.2004.12.004

Smith, A. D. (2003). Intraplate volcanism: concepts, problems and proofs. *Astronomy & Geophysics*, 44(2), 2-8. doi: 10.1046/j.1468-4004.2003.44208.x

Sparks, R. S. J. (1978). The dynamics of bubble formation and growth in magmas: a review and analysis. *Journal of Volcanology and Geothermal Research*, 3(1-2), 1-37. doi:10.1016/0377-0273(78)90002-1

Stoiber, R. E., & Jepsen, A. (1973). Sulfur dioxide contributions to the atmosphere by volcanoes. *Science*, 182(4112), 577-578. DOI: 10.1126/science.182.4112.577

Sutton, A. J., & Elias, T. (2014). One hundred volatile years of volcanic gas studies at the Hawaiian Volcano Observatory: Chapter 7 in Characteristics of Hawaiian volcanoes (No. 1801-7, pp. 295-320). US Geological Survey.DOI: 10.3133/pp18017

Symonds, R. B., Reed, M. H., & Rose, W. I. (1992). Origin, speciation, and fluxes of trace-element gases at Augustine volcano, Alaska: Insights into magma degassing and fumarolic processes. *Geochimica et Cosmochimica Acta*, 56(2), 633-657. doi:10.1016/0016-7037(92)90087-Y

Symonds, R.B., W. I. Rose, G. J. S. Bluth and T. M. Gerlach, (1994). Volcanic gas studies: methods, results and applications, in Volatiles in Magmas , ed by., M R. Carroll and J. R. Hollaway, *Mineralogical Society of America Reviews in Mineralogy* 30: 1-66. Print ISSN: 1529-6466

Symonds, R. B., Gerlach, T. M., & Reed, M. H. (2001). Magmatic gas scrubbing: implications for volcano monitoring. *Journal of Volcanology and Geothermal Research*, 108(1), 303-341. DOI: 10.1016/S0377-0273(00)00292-4

Tamburello, G., A. Aiuppa, A. J. S. McGonigle, P. Allard, A. Cannata, G. Giudice, E. P. Kantzas, and T. D. Pering (2013). Periodic volcanic degassing behavior: The Mount Etna example, *Geophys. Res. Lett.*, 40, 4818–4822, doi:10.1002/grl.50924.

Tamburello, G., T. H. Hansteen, **S. Bredemeyer**, A. Aiuppa, F. Tassi (2014). Gas emissions from five volcanoes in northern Chile and implications for the volatiles budget of the Central Volcanic Zone. *Geophys Res Lett*, Volume 41, Issue 14, 28 July 2014, pp. 4961–4969. DOI: 10.1002/2014GL060653

Tassi, F., Aguilera, F., Vaselli, O., Darrah, T., & Medina, E. (2011). Gas discharges from four remote volcanoes in northern Chile (Putana, Olca, Irruputuncu and Alitar): a geochemical survey. *Annals of Geophysics*, 54(2). DOI: 10.4401/ag-5173

Tazieff, H. (1970). New investigations on eruptive gases. *Bulletin Volcanologique*, 34(2), 421-438.DOI: 10.1007/BF02596766

Thybo, H., & Nielsen, C. A. (2009). Magma-compensated crustal thinning in continental rift zones. *Nature*, 457(7231), 873-876. doi:10.1038/nature07688

Tryggvason, E. (1994). Surface deformation at the Krafla volcano, North Iceland, 1982–1992. *Bulletin of volcanology*, 56(2), 98-107. DOI: 10.1007/BF00304105

Tuffen, H., Dingwell, D. B., & Pinkerton, H. (2003). Repeated fracture and healing of silicic magma generate flow banding and earthquakes?. *Geology*, 31(12), 1089-1092. doi: 10.1130/G19777.1

Voight, B., Komorowski, J. C., Norton, G. E., Belousov, A. B., Belousova, M., Boudon, G., Francis, P.W., Franz, W., Heinrich, P., Sparks, R.S.J. & Young, S. R. (2002). The 26 December (Boxing Day) 1997 sector collapse and debris avalanche at Soufriere Hills volcano, Montserrat. In: DRUITT. T. H. & KOKELAAR, B. P. (eds) 2002. The Eruption of Soufriere Hills Volcano, Montserrat, from 1995 to 1999. *Geological Society. London. Memoirs*, 21, 363-407.

Wallace, P. J. (2005). Volatiles in subduction zone magmas: concentrations and fluxes based on melt inclusion and volcanic gas data. *Journal of Volcanology and Geothermal Research*, 140(1), 217-240. DOI:10.1016/j.jvolgeores.2004.07.023

Wilson, L. (1980). Relationships between pressure, volatile content and ejecta velocity in three types of volcanic explosion. *Journal of Volcanology and Geothermal Research*, 8(2-4), 297-313. doi:10.1016/0377-0273(80)90110-9

Wilson, L., & Head III, J. W. (1981). Ascent and eruption of basaltic magma on the Earth and Moon. *Journal of Geophysical Research: Solid Earth*, 86(B4), 2971-3001. DOI: 10.1029/JB086iB04p02971

CHAPTER II

Synchronous degassing patterns of the neighbouring volcanoes Llaima and Villarrica in south-central Chile: the influence of tidal forces

Synchronous degassing patterns of the neighbouring volcanoes Llaima and Villarrica in south-central Chile: the influence of tidal forces

Stefan Bredemeyer · Thor H. Hansteen

Abstract The neighbouring volcanoes Villarrica and Llaima are two of the most active volcanoes in Chile and both currently degas continuously. We present a semi-continuous time series of SO_2 fluxes for Villarrica and Llaima volcanoes. The time series was obtained using five scanning Mini-Differential Optical Absorption Spectrometers (Mini-DOAS, UV spectrometers) over 6 months (13 February to 31 July 2010) and is based on 6,829 scans for Villarrica and 7,165 scans for Llaima. Statistical analyses of the SO_2 flux time series reveal a periodicity of degassing maxima about every 7 days, and further a conspicuous synchronicity of the degassing maxima and minima between the two volcanoes. Intra-day variations in SO_2 fluxes also show a striking correlation between Villarrica and Llaima. All these patterns correlate well with the trend of the modelled solid Earth tide curves, where the 7-day degassing maxima correspond with both the fortnightly tidal maxima and minima. The intra-day degassing peaks mostly correlate well with the periods of maximum deformation rates during the diurnal tidal cycle, and further with semidiurnal minima in atmospheric pressure, a phenomenon we refer to as "the tidal pump". As there is little time lag between the tidal action and the changes in degassing rates, we infer that degassing at both volcanoes is controlled by conduit convection, involving physical separation between gas and magma at comparatively shallow levels. Variations in daily degassing rates were up to a factor of ca. 12 and 10 for Villarrica and Llaima, respectively, without any noticeable changes in the periodicity. We thus suggest that the described cyclic variations must be taken into account for all comparable volcanoes when using gas monitoring as a tool for volcanic hazard mitigation.

S. Bredemeyer (✉) SFB 574, GEOMAR Helmholtz Centre for Ocean Research Kiel, Wischhofstr. 1-3, 24148 Kiel, Germany
e-mail: sbredemeyer@geomar.de

S. Bredemeyer · T. H. Hansteen GEOMAR Helmholtz Centre for Ocean Research Kiel, Wischhofstr. 1-3, 24148 Kiel, Germany

1. Introduction

In most cases, volcanic unrest is preceded by movement of magma into the upper crust, which produces characteristic changes in seismic activity and is typically accompanied by magmatic degassing well before an eruption (e.g. Malinconico 1979 ; Casadevall et al. 1981 ; Olmos et al. 2007 ; Conde et al. 2013). Eruptions may be caused by the movement of deep-seated magma, tectonic activity and unloading of the magmatic system due to mass wasting (e.g. Sigurdsson et al. 2000). However, volcanic activity may also be influenced by external forces, which either induce periodically recurrent activity changes or discrete volcanic events (Schmincke 2004). Cyclic variations of volcanic activity at different timescales have been attributed to short-period oscillatory stress changes caused by the solid Earth tides (Johnston and Mauk 1972 ; Dzurizin 1980 ; McNutt and Beavan 1987 ; Patane et al. 1994 ; Sottili et al. 2007), regional sea-level

Fig. 1 Topographic map of the volcanic arc around Villarrica and Llaima volcanoes. Faults were adopted from Melnick et al. (2006) and include major structures comprising the dextral LOF (Liquiñe-Ofqui Fault Zone), sinistral MVF (Mocha-Villarrica Fault Zone), LF (Lanalhue Fault Zone) and GF (Gastre Fault Zone). Locations of the scanning Mini-DOAS stations are designated by small *red stars*
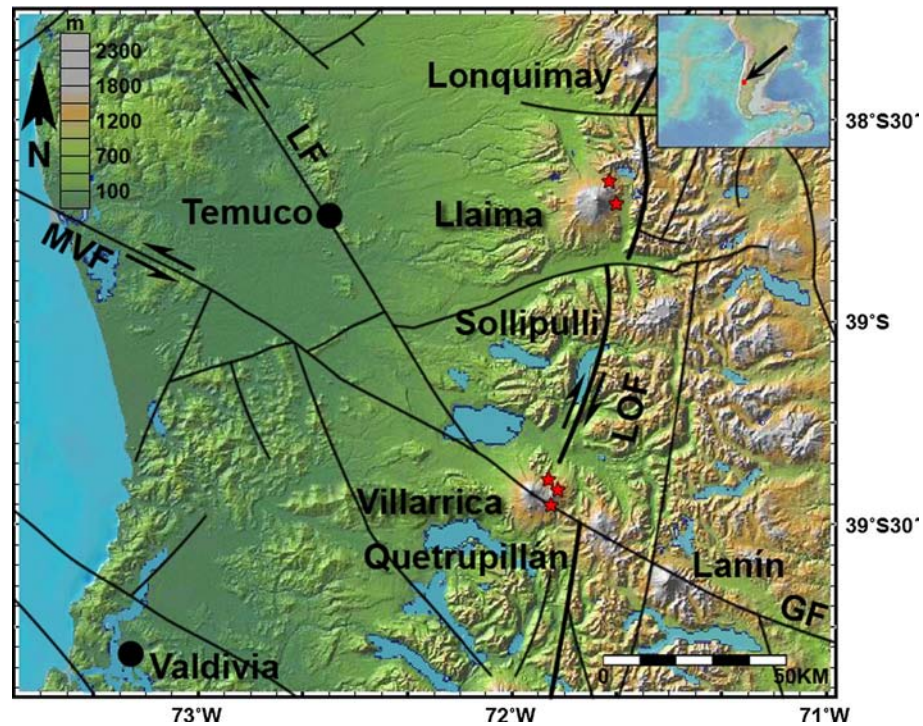
changes or ocean tides (Kasahara and Sato 2001), barometric pressure and temperature changes, as well as variations of precipitation and soil moisture (Neuberg 2000; Mason et al. 2004), all of which may potentially modulate changes within the magmatic system of a volcano. Triggering of volcanic eruptions due to external forcing has been attributed to storms and heavy rainfalls (Mastin 1994 ; Matthews et al. 2002) or to distant regional tectonic earthquakes which cause static and/or dynamic pressure changes inside the affected volcano (Yokoyama 1971 ; Linde and Sacks 1998 ; Barrientos 1994 ; Hill et al. 2002 ; Manga and Brodsky 2006 ; Walter 2007 ; Scalera 2008 ; Watt et al. 2009 ; Bonali et al. 2013).

This study is based on about 6 months of semi-continuous measurements of degassing patterns of SO_2 from Villarrica and Llaima volcanoes, using scanning Mini-DOAS UV spectrometers of the NOVAC type (Galle et al. 2002). We derive a baseline activity signal for each volcano and are also able to determine cyclic variations in degassing activity. The variations in degassing rates of the two volcanoes are compared to tidal vertical displacement variations of the solid Earth. As both volcanoes are prone to erupt, we focus on constraining processes controlling the observed repeated variations in their activity, in order to better understand the triggering of volcanic unrest.

2. Geological setting

Chile comprises about 100 volcanoes which have been active during the Holocene and display several types of volcanic activity, including large and small eruptions, passive degassing and fumarolic degassing. Volcanism in this area is related to the oblique subduction of the Nazca plate below the South American plate (Stern 2004). Llaima (39°36′S) and Villarrica (39°24′S) volcanoes are situated about 83 km apart in the northern part of the Southern Volcanic Zone (SVZ) of south-central Chile (López-Escóbar et al. 1977 ; Thorpe and Francis 1979 ; Stern 1989) (Fig. 1). They are located close to the same large fault system, the NNE-SSW-trending Liquiñe–Ofqui Fault Zone (LOF).

Villarrica volcano is the westernmost of three volcanoes forming the Villarrica–Lanín volcanic chain and is situated on the triple junction between the SE-trending Mocha–Villarrica Fault Zone (MVF) and a main fracture of the LOF. Llaima volcano in contrast is located about 10 km off-axis shifted immediately to the west of the LOF. The glacier-capped Pleistocene–Holocene stratovolcanoes are two of the most active volcanoes in South America, characterized by a postglacial period (<14,000 years) of violent explosive activity (Naranjo and Moreno 1991 ; Moreno et al. 1994), and have produced 60 and 50 mainly effusive historical eruptions, respectively (e.g. Petit-Breuihl 1994 ; Simkin and Siebert 1994). General volcanic hazards at Villarrica and Llaima volcanoes include sector collapses, pyroclastic flows, debris avalanches

and lahars (Naranjo and Moreno 1991 ; Castruccio et al. 2010). Postglacial activity at Villarrica comprises pyroclastic flows, thick lava flow sequences and fallout deposits, all of dominantly basaltic to basaltic andesite composition, while postglacial Llaima comprises lavas, ignimbrites and fallout deposits covering basaltic to dacitic compositions (Hickey-Vargas et al. 1989; Naranjo and Moreno, 1991 ; Lohmar et al. 2005 ; Mahlke 2009 ; Schindlbeck 2012).

The main edifice of Llaima has two summits which both host craters. The northern one rises about 3.120 m above sea level, and the slightly smaller Pichillaima cone on Llaimas south-eastern flank forms a second, lower summit which is about 2.920 m high (Naranjo and Moreno 2005). After the 2008/2009 eruption, the visible activity of Llaima volcano has mainly been characterized by fumarolic degassing from the craters. The 2.847 m high Villarrica volcano in contrast hosts a small (30–60 m in diameter) persistently degassing lava lake in its summit crater since its last eruption in 1984/1985 (Calder et al. 2004 ; Witter et al. 2004 ; Palma et al. 2008). The level of this lava lake is known to periodically rise and fall for about some tens of metres, oscillating between roughly 180 and 50 m below the crater rim (Fuentealba et al. 2000 ; Calder et al. 2004). Comparatively high SO_2 emission rates have been measured during high stands of the lava lake (Palma et al. 2008).

3. Methods

Semi-continuous gas measurements have been conducted at Villarrica volcano since March 2009 to determine sulphur dioxide fluxes using three automated stationary scanning dual-beam Mini-DOAS (UV spectrometers). At Llaima volcano, further two instruments were installed starting the data acquisition in February 2010. These so-called NOVAC instruments were deployed within the framework of the Network for Observation of Volcanic and Atmospheric Change (NOVAC; Galle et al. 2010) as a part of a collaboration between the Collaborative Research Center "SFB 574" (Volatiles and fluids in subduction zones—Climate feedback and trigger mechanisms for natural disasters) at the University of Kiel and the Chilean volcano observatory (OVDAS), which is a subdivision of the Chilean geological survey and mining authority (SERNAGEOMIN). The stations are distributed from south-east to north-east of the volcanoes (Fig. 1) according to the prevailing westerly wind directions yielding a temporal plume coverage of more than 80 %. The instruments scan across the sky measuring a differential spectrum of the incoming scattered sunlight at various scanning angles along a vertical or conical scanning plane which is spanning from horizon to horizon. At angles where the plume intersects the scanning plane, specific wavelengths of the sunlight spectrum are absorbed by the gases within the plume. Measurements are conducted from sunset to sundown, and each scan takes between 5 and 15 min depending on the UV intensity of the sunlight. Every scan starts with the collection of two reference spectra, a "sky spectrum" at the zenith position and a "dark spectrum" at the nadir position. According to the UV intensity measured in the sky spectrum, the instrument automatically adjusts the exposure time in the range of 50–1,000 ms, which is then used during the entire scan. Scans were evaluated using the NOVAC software (Johansson et al. 2009) in order to determine the total amount of SO_2 in the atmospheric column at each scanning angle. Evaluation was performed using a wavelength range between 310 and 325 nm of the measured differential spectra, using high-resolution absorption cross sections of SO_2 (Vandaele et al. 1994) and O_3 (Voigt et al. 2001), a ring spectrum and a solar spectrum, respectively, as references. Because the intensity of scattered UV light in the atmosphere decreases strongly when the sun approaches the Earth's horizon, the errors for UV spectroscopic measurements also increase significantly in this period. A similar situation involving rapid increase in the UV intensity occurs in a time interval following the sunrise. In order to assure internal and external consistency for all measurements, we chose to neglect spectra recorded during the first hour after sunrise and the last hour before sunset (see Supplementary material).

The calculation of accurate gas fluxes using DOAS requires knowledge of the plume height, wind direction and plume velocity, the latter typically introducing the largest error into the flux calculations, i.e. if the assumed plume velocity differs too much from its true speed (e.g. Stoiber and Jepsen 1973 ; Williams-Jones et al. 2006). In favourable cases, the above parameters can be calculated from measurements made with the scanning DOAS instrument (Johansson et al. 2009). For the sake of consistency, however, fluxes presented here were calculated using wind speeds and directions at plume height from the GDAS1 model, which is provided by the National Oceanic and Atmospheric Administration (NOAA) at https://ready.arl.noaa.gov/READYamet.php. Statistical tests were performed in

order to assure that no bias had been introduced in the time series due to, for example, possible systematic intra-day wind speed variations (see Supplementary material). Time series used in this study span the period from 13 February to 31 July 2010. This time interval was chosen firstly because of the very good continuity of degassing data from both volcanoes, and secondly because the volcanoes were in very different states of activity during that time, making a direct comparison even more interesting. Llaima had just ended an activity cycle at the end of the 2008/2009 eruption, whereas Villarrica seemingly started a new cycle of enhanced activity in the same period.

Due to the limited but variable amounts of measurements performed at most volcanoes so far, SO_2 fluxes have typically been reported as daily averages in units of metric tons per day (t day^{-1}) or kilograms per second (kg s^{-1}). In order to evaluate intra-day variations, however, we chose to perform statistical evaluations for the present paper using an hourly resolved data set (i.e. using hourly averages presented in units of kg s^{-1}), which involves using discontinuous time series, as the UV spectra could only be collected during daylight. These hourly averages were used to calculate daily averages that are presented in units of t day^{-1}.

In order to evaluate the role of the tidal stresses in modulating the degassing activity at Villarrica and Llaima volcanoes, we further calculated the theoretical vertical ground displacements due to the solid Earth tides. Calculations were made according to the IERS conventions (2010) using the CalSky online calculator provided by Arnold Barmettler at www.calsky.com (2013).

4. Results

Villarrica and Llaima volcanoes presently exhibit different degassing behaviour. Following the most recent eruption of Llaima in 2008/2009, the vents were obstructed and the craters filled with collapsed scoria deposits. Permanent fumarolic activity persists at Llaima volcano, but the gas discharges are only seldom visible from greater distance. Our impression is that magmatic degassing partly occurs as fumarole activity and partly as diffuse degassing through the permeable deposits inside the craters. The resulting plume is hardly visible due to little condensation. Time-averaged SO_2 fluxes measured at Llaima during the period from February 2010 to end of July 2010 were 256 ± 202 t day^{-1} (Fig. 2), which we consider as the baseline after the 2008/2009 eruption. The average fluxes were, however, rising slightly in the selected period. The presented values are surprisingly high, considering the "invisibility" of the emissions, though they are lower than the average SO_2 fluxes of 630 ± 286 t day^{-1} measured in February 2003 by Mather et al. (2004).

Villarrica volcano, in contrast, has a visible, well-condensed plume ascending from the main crater. A degassing baseline of 444 ± 296 tons SO_2 day^{-1} was determined for Villarrica from measurements that were conducted in 2009 (see Fig. 7 in Mora-Stock et al. 2012). These values are consistent with SO_2 fluxes determined during previous studies, which were 260 ± 170 t day^{-1} (Witter et al. 2004) in 2000, 460 ± 260 t day^{-1} in 2001 (Witter et al. 2004 ; Witter and Calder 2004), 320 ± 115 t day in 2003 (Mather et al. 2004) and 260–1,300 t day^{-1} in 2004–2006 (Palma et al. 2008). However, the SO_2 emissions derived for the period between February 2010 and July 2010 averaged $1,072 \pm 880$ tons day^{-1} (Fig. 2). Thus, Villarrica exhibited enhanced degassing activity during this time interval, and on May 10, the level of the lava lake was observed to be rising to about 100 m below the crater rim [GVN report 04/ 2010 (BGVN 35:04)]. These observations are supported by the enhanced occurrence of MODVOLC hot-spot alerts (http://modis.higp.hawaii.edu/) in the period of investigation. MODVOLC is an algorithm used to detect local high-temperature thermal anomalies and is based on data from the thermal infrared sensors of the Moderate Resolution Imaging Spectroradiometers (MODIS) on-board NASA's Earth Observing System (EOS) satellites. Since the lava lake at Villarrica is only visible for MODIS at high stands, when the level is higher than roughly 100 m below the crater rim, (<90 m in the case of GOES; Calder et al. 2004), such hot-spot alerts are indicative of enhanced lava lake activity.

In particular, because Villarrica and Llaima volcanoes exhibited different states of activity in the period of investigation, Llaima showing baseline degassing activity following the eruption in 2008/2009, and Villarrica showing a gradual but strong activity increase which started in December 2009 (Fig. 7 in Mora-Stock et al.; this volume), we wanted to test whether degassing patterns would still correlate between the two.

Our comparison of SO$_2$ flux time series obtained by continuous measurements using scanning mini-DOAS at Llaima and Villarrica volcanoes reveals synchronous changes in the degassing activity of both volcanoes, but also shorter period (2–4 days) variations characteristic for the individual systems (Fig. 2). Thus, the observed concurrence is reflected by nearly identical SO$_2$ emission patterns (i.e. equal timing of occurrence and equal duration of degassing peaks and lows).

Calculation of the Pearson's correlation coefficient yields a moderately positive correlation of $r = 0.47$ which is significantly above the approximately 95 % confidence level for the given sample size of 169 days each. The covariation between the two data sets is also underlined by the sliding correlation coefficient calculated for a moving time window of 10 days (Fig. 2a), showing that many of the local degassing maxima correlate very well. These observations are further supported by a scatter plot of the degassing pairs showing a smooth positive trend (Fig. 2b), and by the moderate positive correlation at lag zero of the cross-correlation sequence derived from both SO$_2$ flux time series (Fig. 2c). The presented correlation sequence clearly shows that the degassing maxima are not randomly distributed. Further visual examination of the daily average degassing data reveals several timescales of periodic variations in degassing rates, which both volcanoes have in common. The most obvious systematic variations are represented by near-weekly cyclic fluctuations of the emissions, spanning a factor of 1.5–10 for Llaima and a factor 1.5–12 for
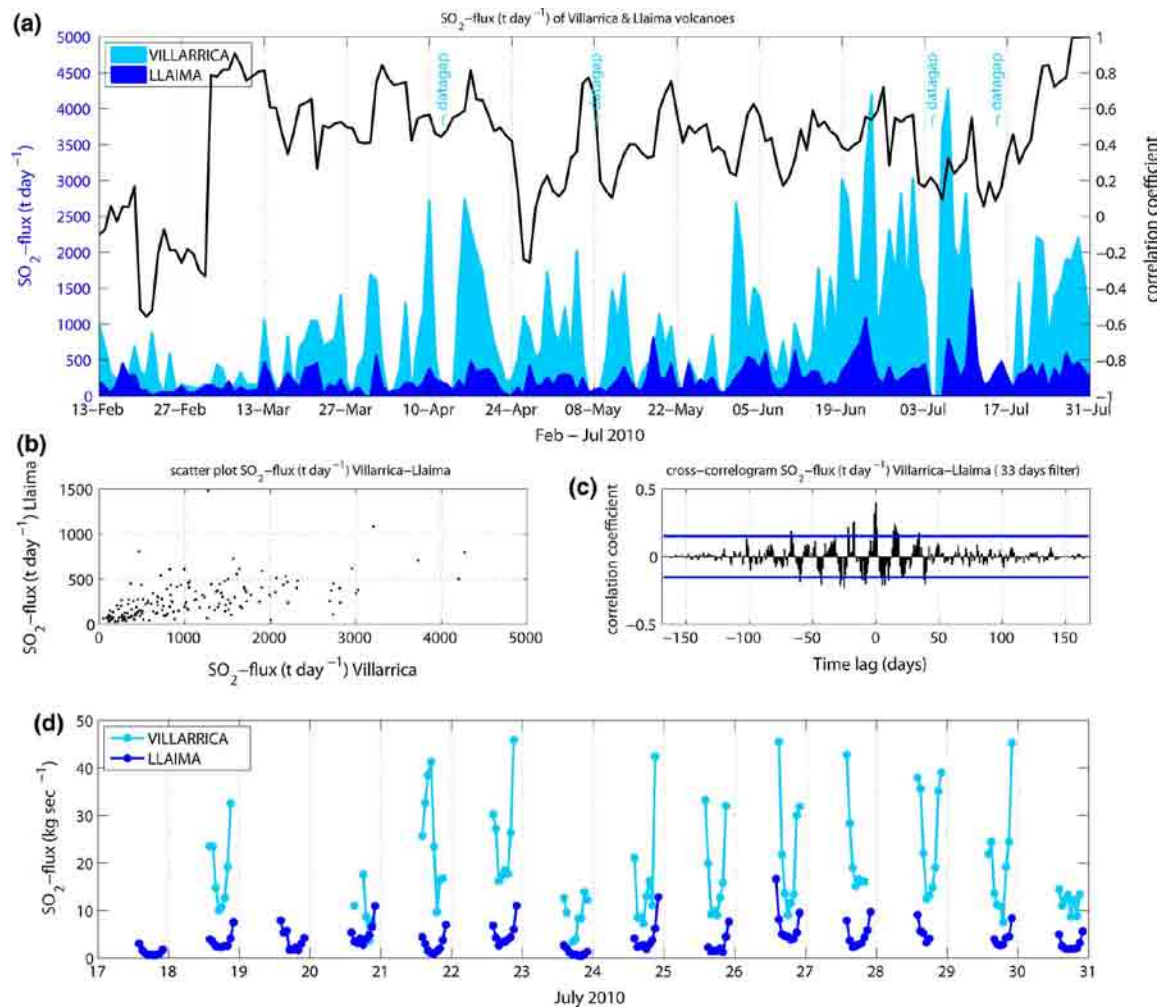

Fig.2 a Time series of SO$_2$ emissions from Villarrica and Llaima volcanoes obtained through 6,829 and 7,165 consecutive scans, respectively, of the stationary scanning Mini-DOAS arrays for the time interval between 13 February and 31 July 2010. The sliding correlation coefficient (*thin black line*) was calculated for a moving time window of 10 days. **b** Scatter plot of SO$_2$ emissions from Villarrica and Llaima showing a positive correlation between the degassing rates of both volcanoes. **c** Cross-correlogram of the Llaima and Villarrica SO$_2$ flux time series including the 95 % confidence bounds (*blue horizontal lines*). Both time series were detrended by a second-order polynomial high-pass filter (Savitzky and Golay 1964) applied to data frames of 33 days and then normalized to mean zero and a variance of 1 (*z* score) before the correlation sequence was calculated. **d** Examples of hourly resolved SO$_2$ fluxes measured during the last 2 weeks of June 2010

37

Villarrica, respectively. An additional fortnightly cycle is well-documented by the cross-correlation sequence in Fig. 2c. Such similarities of the two data sets indicate that the periodic changes in degassing activity observed at both volcanoes are controlled by common variations in certain physical phenomena, which in turn lead to synchronous variations in the outgassing of the two magmatic systems.

In order to further constrain the synchronicity of degassing from Villarrica and Llaima within a day, SO_2 time series using hourly averages were compiled for each volcano. The hourly degassing rates either show a cuspate trend with maxima in the morning and in the evening, or alternatively a maximum either in the morning or in the evening (Fig. 2d). In any case, the variations throughout the day are quite significant. Also, on such short timescales, there is a clear covariation between the data from Villarrica and Llaima, suggesting a common mechanism for the variations. The intra-day variations in SO_2 fluxes are typically the highest on days with comparatively high average degassing rates.

5. Discussion

5.1 Correlation between Earth tides and degassing

Our degassing data for the Villarrica and Llaima volcanoes show a common periodicity at the intermediate timescales observed here, i.e. at about fortnightly and weekly frequencies (Fig. 2 a–c). As such a periodicity is similar to that expected for tidal cycles, we want to test the hypothesis that the observed periodicity at both volcanoes can be explained by external forcing through tides. The vertical ground displacement Earth tide curves for Villarrica and Llaima are shown in Fig. 3 . Tides are usually classified as one of three types, namely diurnal, semidiurnal or mixed tides, according to the characteristics of the tidal pattern. The tides prevalent at latitudes of the SVZ are generally mixed-type tides consisting of both diurnal and semidiurnal waves with different amplitudes, which are interfering with each other. The tide resulting from the combination of the diurnal and the semidiurnal waves is characterized by a large inequality in diurnal and semidiurnal high tide heights, and similar low tide heights. There usually are two high tides and two low tides each day, but the semidiurnal oscillation diminishes towards the fortnightly tidal minimum, where it occasionally vanishes, becoming a diurnal tide (Fig. 3). The hourly resolved vertical tidal oscillations calculated for Villarrica and Llaima deviate in height between roughly 0.2 and 0.3 m around the conventional tide-free crust as given by the international terrestrial reference frame (ITRF). Fortnightly variations in the width of the tidal modulation envelope are more pronounced during southern hemisphere (SH) winter (Fig. 3 a), when also the highest variations in degassing rates were observed (Fig. 3 b, c).

A fast Fourier transform algorithm was applied to compare periodic variations in the hourly average SO_2 flux time series with the vertical (tidal) ground displacement time series of Villarrica and Llaima volcanoes (Fig. 4a). Spectral power estimates were calculated using Thompson's multitaper method (MTM) in which we applied a time-bandwidth product of 1.25 in order to obtain the highest possible spectral resolution, however, at the expense of a larger variance.
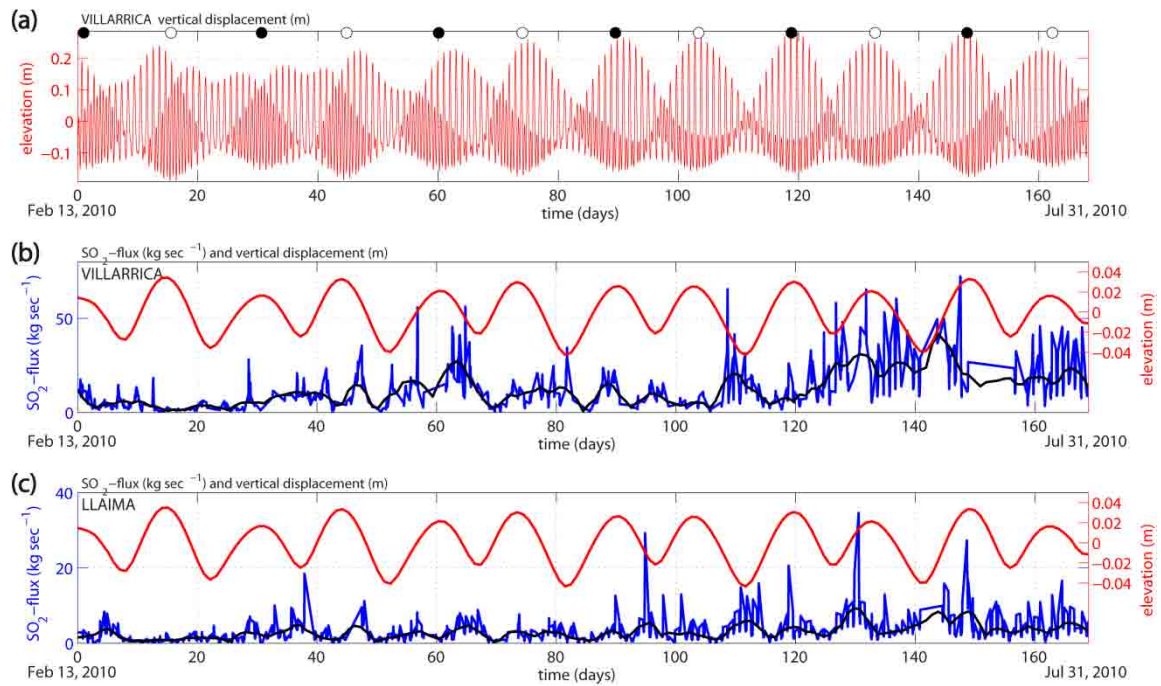
Fig.3 a Hourly resolved vertical ground displacement pattern of the solid Earth tides calculated for Villarrica volcano. The corresponding curve for Llaima is not displayed here, because it essentially looks the same, only with slightly higher amplitudes. *Empty* and *filled circles* represent the timing of full and new moon phases, respectively, which are slightly out of phase with respect to the corresponding fortnightly tidal maxima. Note the increasing amplitudes of diurnal tidal variations towards the second half of the depicted time series (SH winter), as well as increasing differences between fortnightly tidal maxima and minima. "*Darker areas*" within the tidal modulation envelope correspond to the semidiurnal oscillations. **b**, **c** Linearly interpolated hourly average SO_2 flux (*blue*) and the daily average degassing time series smoothed by a 7 days polynomial filter (*black*) and daily resolved vertical ground displacement time series (*red*) of **b** Villarrica and **c** Llaima. The daily resolved tidal curves were calculated according to Butman et al. (1983) by least-squares fitting using a combination of three semidiurnal tidal constituents (M_2 = 0.52 days—principal lunar semidiurnal, N_2 = 0.53 days—larger lunar elliptic semidiurnal and S_2 = 0.5 days—principal solar semidiurnal), which were squared and low-pass filtered in order to generate the fortnightly and monthly forcing curve. The time series in **a–c** cover the period from 13 February to 31 July 2010

The power spectra of the modelled Earth tide signal comprise a set of short-term and long-term constituents with wavelengths corresponding to solar and lunar cycles. Some of the major tidal constituents and their corresponding Darwin symbols are listed below (Table 1).

Table 1 Tidal constituents

| Darwin symbol	Tidal constituent	Period
Short term constituents		
S_3	Solar ter-diurnal	8 h
S_2	Principal solar semidiurnal	12 h
M_2	Principal lunar semidiurnal	12.42 h
S_1	Principal solar diurnal	24 h
M_1	Smaller lunar elliptic diurnal	24.85 h
O_1	Principal lunar declinational diurnal	25.81 h
Long term constituents		
M_{tm}	lunar ter-monthly	9.13 days
M_f	lunisolar fortnightly	13.66 days
MS_{sf}	lunisolar synodic fortnightly	14.77 days
M_m	lunar monthly	27.55 days
MS_m	lunisolar monthly	31.81 days

39
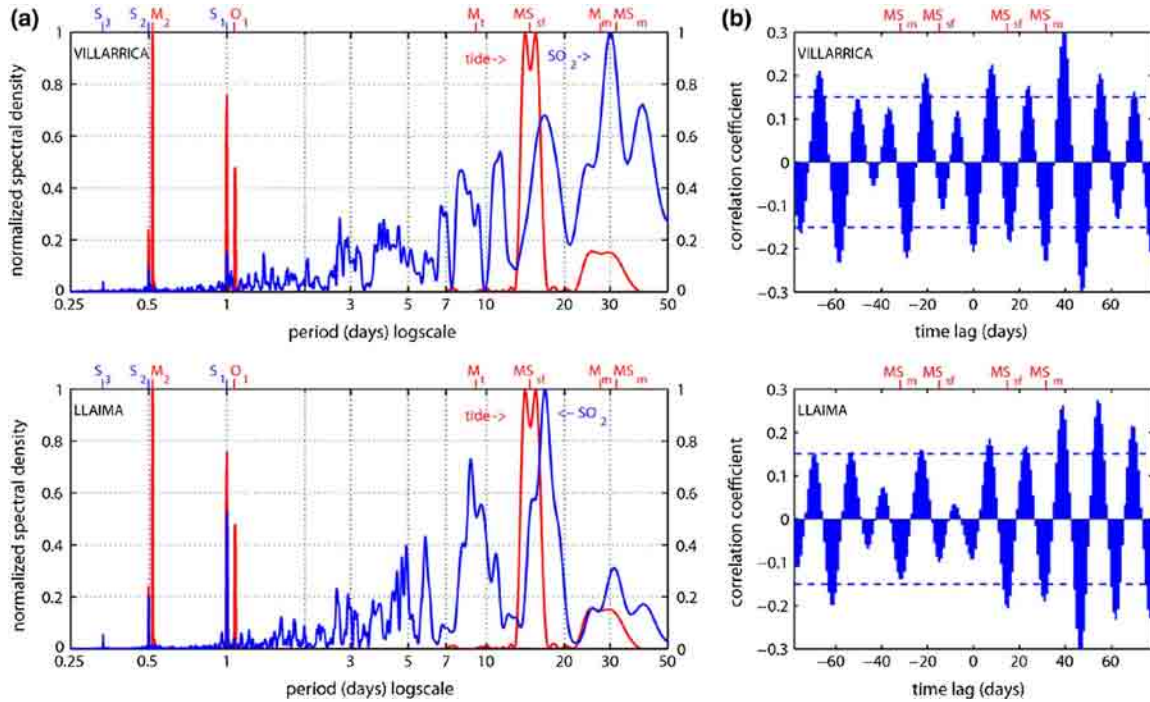
Fig.4 a Periodograms of the degassing time series (*blue*) and of the modelled Earth tide curves (*red*) for Villarrica (*top*) and Llaima (*bottom*). The *red curve* is a composite of the normalized power spectra of both the hourly (periods 0.25–50) and the daily (periods 2–50) resolved tidal model curves. Time series were detrended by a 69 days polynomial high-pass filter before Fourier transformation (as in Fig. 2 c). **b** Cross-correlograms of the detrended SO_2 flux time series and the daily resolved tidal curves of Villarrica (*top*) and Llaima (*bottom*) with the 95 % confidence intervals depicted. A high-pass filter was used to remove slow oscillations above 33 days from the SO_2 flux data, which were additionally smoothed by a 13 days low-pass filter. For orientation, some tidal constituents are indicated by their Darwin *symbols* on *top* of each diagram

5.2 Long-term variations (weekly to monthly)

Common significant cycles of the degassing time series were identified corresponding to periodicities of 28–33, 13–16, 6–9, 1 and 0.5 days, respectively. The highest amplitudes in degassing variations correspond to the approximately fortnightly oscillations and stand out against the variations of the monthly and weekly cycles. The additional higher frequency oscillations in the range between 2 and 4 days are less pronounced than the weekly (to ter-monthly; 9.13 days) cycle and correspond to rather irregular patterns of short-term variations in degassing. Cross-correlation of the degassing and the tidal time series (Fig. 4 b) shows a clear negative correlation of the signals, indicating that the stronger fortnightly degassing maxima occur preferably during the fortnightly tidal minima, whereas the remaining weekly degassing maxima are correlated with the fortnightly tidal maxima.

A possible time delay between the fortnightly tidal and degassing cycles could be inferred from the periodograms, as the degassing cycles seem to be slightly longer than the lunisolar synodic fortnightly Earth tide constituent (MS_{sf}) and have a peak at periods of 16.8 rather than 14.77 days. However, the amount of delay would add up in each consecutive fortnightly cycle, and thus, the oscillations of tide and the degassing would be completely out of phase after several fortnightly cycles, which is not the case. The quasi16-day peaks in the degassing spectra are, however, very broad, due to the gradual decrease in spectral resolution towards longer periods, and overlap with the fortnightly band of the Earth tidal spectra. A 1–2 days shift towards longer wavelengths is also apparent from the cross-correlograms (Fig. 4 b). The delay between fortnightly cycles is, however, not confirmed by the correlograms (Fig. 4 b) and probably can be assigned to spectral bias. The observed lack of phase delay between degassing maxima and the tidal minima suggests a rather shallow degassing source, or rapidly upwelling gas.
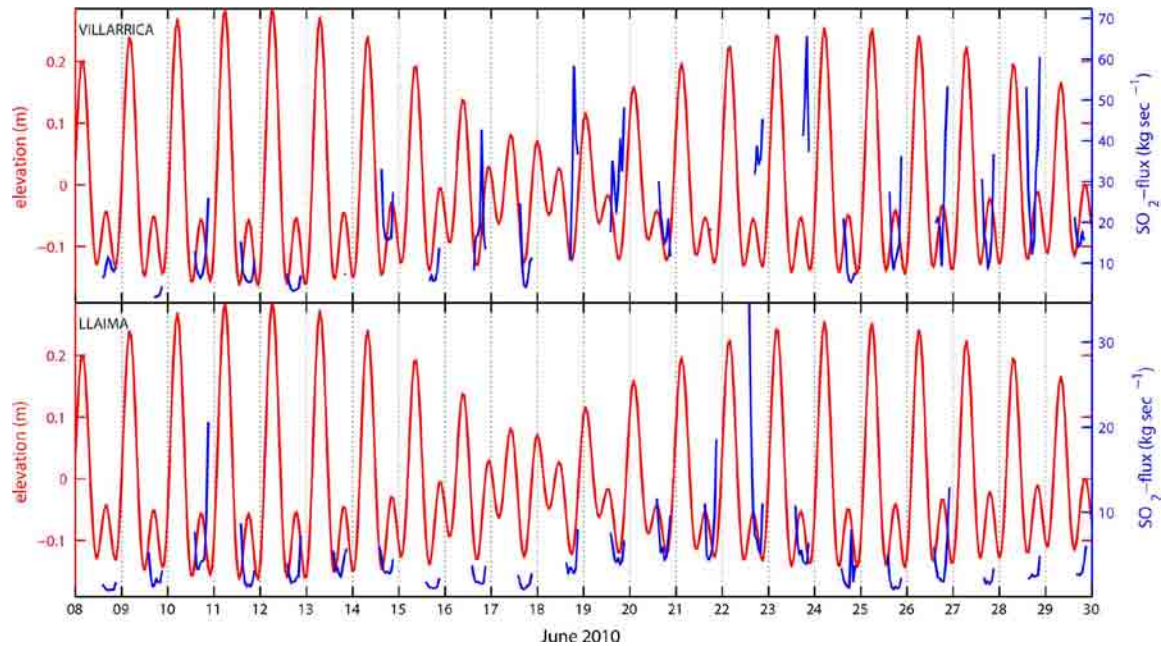
Fig. 5 SO$_2$ flux and modelled vertical tidal ground displacement at Villarrica and Llaima with an hourly resolution showing typical intraday degassing variations in June 2010. During this particular period, most of the SO$_2$ flux measurement intervals, which correspond to daylight, overlap with semidiurnal and diurnal tidal lows. Diurnal degassing minima seem to be centred on the tidal lows (and the low high tide). The strongest degassing occurs when the displacement rate is high

5.3 Short-term variations (intra-day)

The calculated hourly flux variations observed at Villarrica and Llaima were compared to the hourly variations in the local Earth tide signals (Fig. 5). For both volcanoes, there is typically a correlation between degassing minima and both the minima and maxima (i.e. both the bottom and top dead centres) of the respective vertical ground displacement curves. Further systematic patterns can be recognized when each fortnightly tidal cycle is considered separately (Fig. 5). During each fortnightly tidal minimum, the daily degassing minimum is strongly positively correlated with the minimum of the diurnal Earth tide signal. During each fortnightly tidal maximum, however, the daily degassing minimum is strongly positively correlated with the maximum of the diurnal Earth tide signal. Both situations strongly indicate that degassing rates are comparatively small during static situations when the changes in tidal forces are minimal. Accordingly, the daily maxima in degassing rates coincide with comparatively rapid dynamic changes in the tidally induced vertical ground displacement, i.e. the degassing peaks correlate with the steep flanks of the cyclic tidal signal.

In order to constrain possible causal relations, we further examine the power spectra in Fig. 4 a, which show pronounced peaks at diurnal and semidiurnal solar periods (S_1 = 24 h, S_2 = 12 h). However, the peaks in the degassing spectra at diurnal and semidiurnal lunar periods (M_2 = 12.42 h, O_1 = 25.81 h) are comparatively low, or even missing, although the M_2 constituent is the strongest one in the Earth tide signal. This observation is also corroborated by a 50-min shift day^{-1} in the cross-correlation sequence calculated for the Earth tide signal and the degassing signal (see Supplementary material Fig. S4). Such a shift suggests that the diurnal and semidiurnal oscillations of the degassing signal rather have periodicities corresponding to the 24 h length of a solar day (S_1 = 24 h) and occur at a quasi-constant local time every day. The solid Earth tide signal, in contrast, results from oscillations at wavelengths of both the solar and lunar (M_1 = 24.85 h) days, which is in turn causing the observed shift between degassing and Earth tide. An additional short-term constituent occurs in the degassing spectra at ter-diurnal periods (S_3 = 8 h), which is, however, completely missing in the Earth tide spectra, and is rather a feature typically found in atmospheric tides. We thus consider atmospheric tides as an additional forcing mechanism to explain the intra-day degassing variations.

Fig. 6 Frequency histograms for hourly degassing variations at Villarrica (*light blue*) and Llaima (*dark blue*) as a function of local time. air pressure maxima and minima are indicated (*stippled red lines*). Measurements of the whole period (13 February to 31 July 2010) were averaged, and both volcanoes show a distinct degassing minimum between 1500 and 1700 h UTC
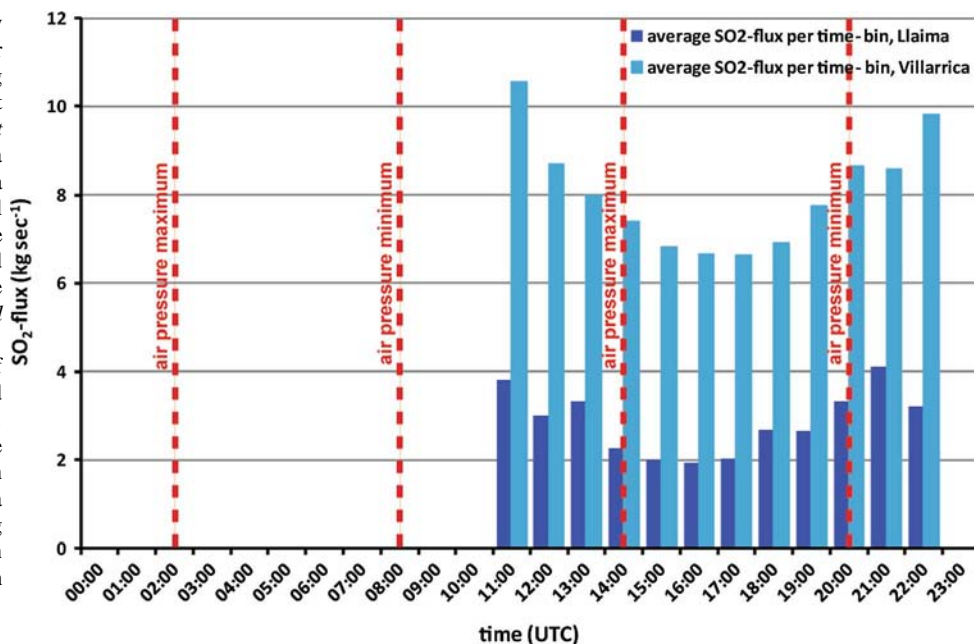
5.4 Earth tides, atmospheric tides and volcanic degassing

Atmospheric tides are periodic oscillations of the atmosphere on a global scale and thus have resemblance to Earth or ocean tides. They induce cyclic variations in barometric pressure, wind, temperature and atmospheric density. The barometric pressure variations are primarily related to periodic heating of the atmosphere by the sun, resulting in regular but small surface pressure variations, with pressure maxima every 12 and 24 h, which occur at a constant local time every day and are only to a lesser extent influenced by gravitational forces (Lindzen and Chapman 1969). In contrast, longer-period oscillations in the atmospheric tides are indirectly influenced by lunar and solar gravitational forces, as they are mainly produced by motion of the oceans and the Earth's crust, which in turn result in redistribution of atmospheric surface loads.

In order to compare the observed degassing variations with the action of atmospheric tides, we constructed a frequency histogram for hourly degassing variations as a function of local time and compared the location of time-averaged degassing maxima and minima with the theoretical pattern of surface pressure oscillations (Fig. 6). The regional theoretical air pressure maxima occur at 1400 and 0200 h UTC, and the former is followed by a degassing minimum 1–2 h later (the latter cannot be detected, as no gas data are acquired during the night). Similarly, pressure minima at 0800 and 2000 h UTC are followed by degassing maxima with a time lag between both signals of approximately 1–2 h. Taken at face value, this would imply a simple compression–decompression mechanism for the semidiurnal and diurnal degassing cycle, which can easily be integrated in the proposed model for the tidal forcing. It should be noted, however, that local pressure variations strongly depend on the weather situation and thus can only deliver part of the explanation for the observed intra-day degassing cyclicity.

In order to complete the picture, we note that both the fortnightly and weekly degassing maxima represent periods when also the intra-day degassing variations are the highest, underlining the effect of diurnal tidal variations on degassing rates. During the fortnightly degassing maxima, the action of both Earth tides and atmospheric tides is in phase. If the model presented here is correct, we would expect the effects of Earth and atmospheric tides to add up at fortnightly intervals, which is how we interpret the present data.

Summing up, covariations between degassing rates and tidal forces were observed on both diurnal and long-term (weekly/fortnightly/monthly) timescales. The diurnal maxima in degassing rates typically correlate with both the highest rates of change in the Earth tide signal and the lowest atmospheric pressure, whereas the weekly degassing maxima occur during both the fortnightly tidal minima and maxima. The slightly more pronounced fortnightly degassing maxima occur during the fortnightly tidal minima, when the

actions of Earth tides and atmospheric tides are in phase. We suggest that a combination of mechanisms acting at different timescales must be used to explain such a systematic behaviour.

5.5 The tidal pump

5.5.1 Degassing mechanisms

In order to constrain the mechanisms for tidally induced degassing, we will assume that the periodic ascent and retreat of the Villarricas lava lake can be ascribed to the gravitational forces of the Earth tides and possibly the diur-nal pressure changes through atmospheric tides. We assume that the same mechanism would work for the magma plumbing system of the partly obstructed Llaima volcano. The causal connection between Earth tides and variations in the lava lake level at Halemaumau crater (Kilauea volcano, Hawaiii) was suggested already in 1925 (Jaggar et al. 1924; Brown 1925; Shimozuru 1975). They found that the high tides of the lava lake occur when the lunisolar attraction of the solid Earth is at the minimum and vice versa, and attributed the squeezing out and draining back of the magma to a volume change in the magma reservoir due to Earth tides. Similarly, a linkage between volcanic sulphur dioxide emissions and Earth tides at Halemaumau was suggested by Connor et al. (1988), who measured gas fluxes using a correlation spectrometer (COSPEC). They were able to show a positive correlation between outgassing and the fortnightly tidal maxima. A comparison of diurnal variations of the Earth tide and gas emissions at Masaya caldera led Stoiber et al. (1986) to conclude that higher amounts of gas were more likely to be released at maximum and minimum rates of tidal strain.

   In a basaltic open-vent system, gas transport to the surface can follow both as a two-phase flow in the form of gas slugs resulting from bubble coalescence (Sparks 1978; Jaupart and Vergniolle 1988; Parfitt 2004), and also partly as bubble-bearing magma containing still-dissolved volatiles, which moves up simply by convection, even in a narrowly spaced conduit. Outgassing through convective transport of magma in a conduit is a self-sustaining mechanism, which is driven by the density differences between degassed and buoyant gas-saturated/vesiculating magma (e.g. Kazahaya et al. 1994; Stevenson and Blake 1998; Gonnermann and Manga 2007).

5.5.2 The diurnal and semidiurnal cycle

For the diurnal and semidiurnal cycle at Villarrica, we envision that the tidal compression, probably sustained by atmospheric pressure changes, causes the lava lake to rise in the conduit when approaching the low tide (Shimozuru 1975), and outgassing will be effective due to the movement of the magma column (Fig. 7a). The ascent of the lava lake stagnates and attains high stand when the tidal minimum has been reached, degassing activity diminishes and the lava lake immediately starts to crust over (Calder et al. 2004; see also Nadeau et al. 2011). Movement of the magma column picks up again when tidal expansion takes over, causing the magma to retreat, inducing accelerated down-flow, and in turn forcing the ascent of fresh magma. Thus, the degassing activity increases again until the low lava lake stand is attained. We prefer to call this mechanism "the tidal pump" and note that it can be used to explain much of the diurnal and semidiurnal variations observed in the data sets from Villarrica and Llaima, where degassing maxima typically occur during the presumed rapid changes in lava lake level, whereas the degassing minima correspond to the high and low stands.

   The observed enhanced degassing rates during rapid changes in the lava lake level can probably best be explained through conduit convection processes. If the lava stand increases, the magma column increases in length, promoting the influx of bubble-rich and thus comparatively buoyant magma to the conduit. The fresh magma releases its relatively high gas contents upon final ascent. When the lava stand in the conduit decreases, the rate of descent of degassed, comparatively dense magma is promoted by the decrease in magma column length. Further, the pressure decrease at depth promotes bubble formation. Once the return flow of denser magma arrives at deeper levels, probably at the top of a shallow reservoir that contains relatively undegassed magma, the latter is forced to rise into the conduit driven by the density contrast. Thus, both extension and reduction of the magma column height can lead to enhanced degassing.
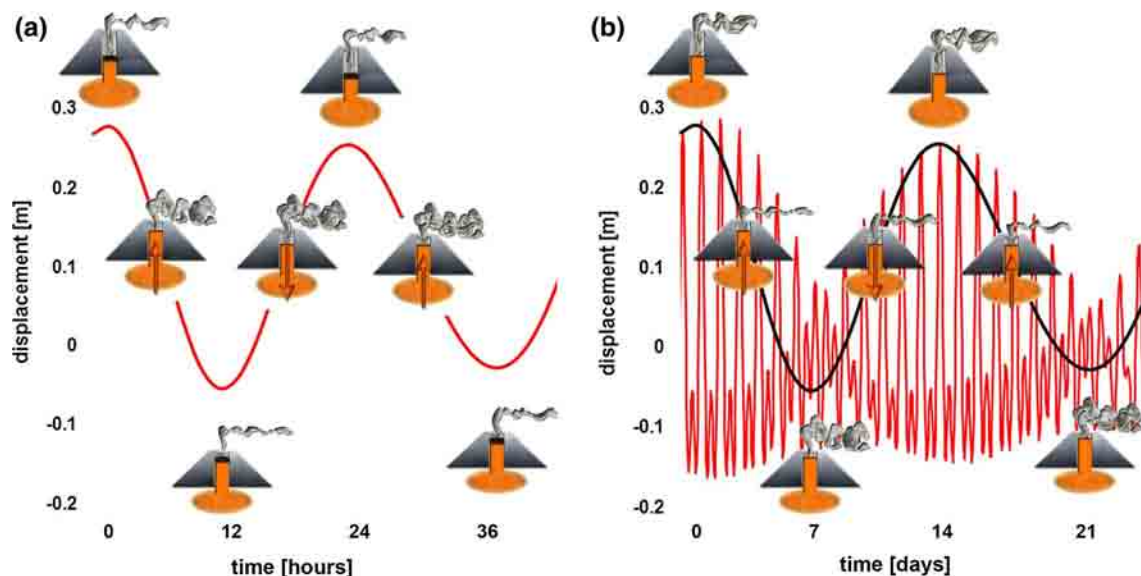
43

Fig. 7 Proposed model of the tidal outgassing cycle. **a** Diurnal tide (*red line*) and corresponding oscillation of the lava lake causing strong degassing during phases of movement and elevated tidal strain which is highest at the inflection points of the tidal wave. at the tidal turning points, i.e. during lava high stands and low stands, the surface of the lava lake encrusts and SO_2 emissions diminish. **b** Fortnightly tide (*black line*) and oscillation of the lava lake with local degassing maxima at the moment of highest compression, i.e. during fortnightly high stands, and less pronounced maxima during fortnightly low stands. Note that the black curve is amplified by a factor ~10 with respect to the given scale for graphical reasons. The diurnal/semidiurnal tidal curve (*red line*) is depicted in the background to clarify timescale differences compared to Fig. 7a

5.5.3 The fortnightly cycle

The observed fortnightly degassing cycle inherently contains the variations described for the diurnal cycle and thus includes processes occurring on various timescales. As the diurnal and semidiurnal rates of stress changes are larger than the fortnightly variations, their effect on degassing should accordingly be more pronounced, which is consistent with the high variability of the SO_2 fluxes throughout a day. Compression, however, reaches a maximum during the fortnightly tidal minimum, and accordingly, the level of the lava lake is expected to arrive at the highest high stand during the fortnightly tidal minimum, although the amplitudes of the diurnal tides are usually smaller than during the fortnightly tidal maximum (Fig. 7b). On the other hand, the concerted action of Earth and atmospheric tides in this period should compensate for the smaller diurnal variations. The degassing maxima during the fortnightly tidal minima seem to contradict the smaller amplitudes on a diurnal timescale, and accordingly little displacement of the magma column. However, the longer the magma column is, the more the forced ascent of magma is expected to promote conduit convection and thus degassing. On the other hand, during the fortnightly tidal maxima, when the lava level would be low, the stronger semidiurnal tidal oscillations may also affect deeper parts of the magma plumbing system, thus positively influencing conduit convection, like suggested above for the diurnal cycles.

In the case of Villarrica, the relative synchronicity between degassing and tidal movement suggests a domination of comparatively shallow degassing processes. This is supported by CO_2/SO_2 ratios close to unity in the Villarrica plume (Shinohara and Witter 2005), which indicate equilibrium between magma and the gas phase at low pressures, and by modelled crystallization depths of <17 MPa (Witter et al. 2004). A degassing model based on convection experiments shows that conduit convection may be an important process at Villarrica (Palma et al. 2011), perfectly in line with our results.

Summing up, both fortnightly tidal minima and maxima correspond with degassing maxima, which are best explained by a combination of magma column length and the amplitude of diurnal tidal variations, both of which promote conduit convection. Thus, the degassing patterns are modulated by tidal forces.

5.6 Seasonal variations in activity

In the case of Villarrica and Llaima volcanoes, the correlation between degassing processes and Earth tides on diurnal to monthly timescales seems unequivocal. There are, however, several factors playing a role for semi-annual cycles of crustal loading and unloading that may influence volcanic activity. Some of them are directly associated with the gravitational forces imposed by the sun and the moon, and others are related to pressure stresses due to redistribution of surface load (Blewitt et al. 2001). The seasonal snowcap of Villarrica, for example, has an estimated volume of 1.2 km^3 at the end of the winter season (Moreno et al. 1994), which is completely removed during spring and early summer, although the glacier remains. The glacier at Villarrica only retreated slightly during the recent decades (Rivera et al. 2012). Snow unloading reduces vertical pressure on the cone which may finally lead to depressurization of the magma plumbing system and enhanced magma movement (Albino et al. 2010). At the same time, the removal of the snow may cause reactivation of shallow normal faults and initiate tectonic earthquakes (Heki 2003), and further facilitate the introduction of additional water into the hydrothermal system of the volcano, which in turn could provoke phreatomagmatic activity (Tuffen 2010). Thus, seasonality is imposed on the cyclic variations described above. This is consistent with statistical analysis of eruption time series of South American volcanoes indicate a strong seasonality of eruptions with an increased occurrence rate during the period of crustal unloading which lasts from October to January and reaches a maximum in December (Mason et al. 2004). Historic eruptions of Villarrica and Llaima occurred preferably during the Chilean spring and early summer reflecting this seasonality (e.g. Ortiz et al. 2003; Simkin and Siebert 1994).

5.7 Consequences for volcano monitoring

Multi-parameter monitoring techniques used at active volcanoes are directly relevant for early warning strategies and thus for hazard mitigation (e.g. Sparks et al. 2012). Although protocols for the definition of alert levels relevant to the general public exist at all volcano observatories, the detection of processes heralding volcanic unrest remains problematic (e.g. Chouet 2011). At Villarrica and Llaima volcanoes, external forcing of activity is very characteristic and produces reproducible cyclic variations. Although volcanoes in other latitudes and climatic zones with smaller differences in seasonal precipitation and temperature may show deviations from the general pattern presented here, at least tidal forcing has to be taken into account when defining their activity state. Thus, steep increases in degassing rates at permanently degassing volcanoes, like, for example, the short-term changes up to more than one order of magnitude at Villarrica and Llaima, should be interpreted in the context of tidal cycles. In order to establish criteria for early warning purposes, each volcano should be monitored for at least several months using sensors with adequately high time resolution. Thus, the effects of the tidal signal may be filtered out. Permanent seismic measurements are still the most commonly used volcano monitoring method worldwide. As the movement of magma in the crust can be detected by both seismicity and SO_2 measurements, a combination of the two provides a very strong tool for hazard mitigation. However, such efforts are intimately connected to intelligently managed volcano observatories.

6. Conclusions

Degassing at Llaima and Villarrica volcanoes seems to be modulated by a combination of solid Earth tides and atmospheric tides, since short-term (daily, weekly, fortnightly and monthly) cycles and long-term (annual) cycles are reflected in the degassing patterns. Peak emission rates were measured during full and new moon at fortnightly time lags, but also at half moon during the fortnightly tidal minima. Also, diurnal variations typically correspond well with the tidal cycles, and degassing peaks correspond to the periods of strongest deformation rates and minima in atmospheric pressure during each cycle. Although the observed phenomena described here relate directly to two volcanoes only, the general phenomenon should be of worldwide importance. As gas monitoring of volcanoes increases steadily, such external forcing mechanisms must be taken into account in order to define activity levels for the respective volcanoes. Semi-continuous gas measurements are necessary for the evaluation of the underlying degassing mechanisms.

_____

References

Albino F, Pinel V, Sigmundsson F (2010) Influence of surface load variations on eruption likelihood—application to two Icelandic subglacial volcanoes, Grímsvötn and Katla. Geophys J Int 181:1510–1524. doi:10.1111/j.1365-246X.2010.04603.x

Barrientos SE (1994) Large thrust earthquakes and volcanic eruptions. Pure Appl Geophys 142(1):225–237. doi: 10.1007/BF00875972

Blewitt G, Lavallée D, Clarke P, Nurutdinov K (2001) A new global mode of earth deformation: seasonal cycle detected. Science 294:2342. doi:10.1126/science.1065328

Bonali FL, Tibaldi A, Corazzato C, Tormey DR, Lara L (2013) Quantifying the effect of large earthquakes in promoting eruptions due to stress changes on magma pathway: the Chile case. Tectonophysics 583:54–67. doi:10.1016/j.tecto.2012.10.025

Brown EW (1925) Tidal oscillations in Halemaumau, the Lava Pit of Kilauea. Am Jour Sci—Fifth Ser IX 2:95–112

Butman B, Noble M, Chapman DC, Beardsley RC (1983) An upper bound for the tidally rectified current at one location on the southern flank of Georges Bank. J Phys Oceanogr 13:1452–1460. DOI: 10.1175/1520-0485(1983)013<1452:AUBFTT>2.0.CO;2

Calder ES, Harris AJL, Peña P, Pilger E, Flynn LP, Fuentealba G, Moreno H (2004) Combined thermal and seismic analysis of the Villarrica volcano lava lake, Chile. Andean Geol Revista Geológica de Chile 31(2):259–272. doi: 10.4067/S0716-02082004000200005

CalSky.com (2013) Arnold Barmettler, Zürich, Switzerland, viewed 20 June 2013. http://www.calsky.com/?earthtides=&

Casadevall TJ, Johnston DA, Harris DM, Rose WI, Malinconico LL, Stoiber RE, Bornhorst TJ, Williams SN, Woodruff L, Thompson JM (1981) SO_2 emission rates at Mount St. Helens from March 29 through December, 1980. US Geol Surv Prof Pap 1250:193–200.

Castruccio A, Clavero J, Rivera A (2010) Comparative study of lahars generated by the 1961 and 1971 eruptions of Calbuco and Villarrica volcanoes, Southern Andes of Chile. J Volcanol Geotherm Res 190:297–311. doi:10.1016/j.jvolgeores.2009.12.005

Chouet BA (2011) Long-period volcano seismicity—it's source and use in eruption forecasting. Nature 380:1–8. doi: 10.1038/380309a0

Conde V, Bredemeyer S, Duarte E, Pacheco J, Miranda S, Galle B, Hansteen TH (2013) SO_2 degassing from Turrialba volcano linked to seismic signatures during the period 2008–2012 (this volume). doi: 10.1007/s00531-013-0958-5

Connor CB, Stoiber RE, Malinconico LLJR (1988) Variation in sulfur dioxide emissions related to Earth Tides, Halemaumau crater, Kilauea volcano, Hawaii. J Geophys Res 93(B12):14867–14871. doi: 10.1029/JB093iB12p14867

Dzurizin D (1980) Influence of fortnightly Earth tides at Kilauea volcano, Hawaii. Geophys Res Lett 7(11):925–928. doi: 10.1029/GL007i011p00925

Fuentealba G, Peña P, Calder ES (2000) Sustained Tremor, open system degassing and annual perturbations at the Villarrica volcano lava lake, in Chile. In: Congreso Geológico Chileno, no. 9, Actas, vol 2, pp 26–29. Puerto Varas

Galle B, Oppenheimer C, Geyer A, McGonigle AJS, Edmonds M, Horocks L (2002) A miniaturised ultraviolet spectrometer for remote sensing of SO_2 fluxes: a new tool for volcano surveillance. J Volcanol Geotherm Res 119:241–254. doi:10.1016/S0377-0273(02)00356-6

Galle B, Johansson M, Rivera C, Zhang Y, Kihlman M, Kern C, Lehmann T, Platt U, Arellano S, Hidalgo S (2010) Network for observation of volcanic and atmospheric change (NOVAC)—a global network for volcanic gas monitoring: network layout and instrument description. J Geophys Res 115:D05304. doi:10.102 9/2009JD011823

Gonnermann HM, Manga M (2007) The fluid mechanics inside a volcano. Annu Rev Fluid Mech 39:321–356. doi:10.1146/annurev. fluid.39.050905.110207

GVN, 04/2010. Villarrica. Bull Global Volcan Netw 35:04

Heki K (2003) Snow load and seasonal variation of earthquake occurrence in Japan. Earth Planet Sci Lett 207:159–164. doi: 10.1016/S0012-821X(02)01148-2

Hickey-Vargas R, Moreno-Roa H, López-Escóbar L, Frey FA (1989) Geochemical variations in Andean basaltic and silicic lavas from the Villarrica–Lanín volcanic chain (39.5 S): An evaluation of source heterogeneity, fractional crystallization and crustal assimilation. Contrib Miner Petrol 103:361–386

Hill DP, Pollitz F, Newhall C (2002) Earthquake–volcano interactions. Phys Today 55(11):41. doi:10.1063/1.1535006

Jaggar TA, Finch RH, Emerson OH (1924) The lava tide, seasonal tilt, and the volcanic cycle. Mon Weather Rev 52:142–145. doi:10.1175/1520-0493(1924)52<142:TLTSTA>2.0.CO;2

Jaupart C, Vergniolle S (1988) Laboratory models of Hawaiian and Strombolian eruptions. Nature 331:58–60

Johansson M, Galle B, Zhang Y, Rivera C, Chen D, Wyser K (2009) The dual-beam mini-DOAS technique, measurements of volcanic gas emission, plume height and plume speed with a single instrument. Bull Volcanol 71:747–751. doi:10.1007/s00445-008-0260-8

Johnston MJS, Mauk FJ (1972) Earth tides and the triggering of eruptions from Mt Stromboli, Italy. Nature 239:266

Kasahara J, Sato T (2001) Tidal effects on volcanic earthquakes and deep-sea hydrothermal activity revealed by Ocean Bottom Seismometer Measurements. J Geod Soc Jpn 47(1):424–433

Kazahaya K, Shinohara H, Saito G (1994) Excessive degassing of Izu-Oshima volcano: magma convection in a conduit. Bull Volcanol 56:207–216

Linde AT, Sacks IS (1998) Triggering of volcanic eruptions. Nature 395:888–890

Lindzen RS, Chapman S (1969) Atmospheric tides. Space Sci Rev 10: 3–188. D. Reidel Publishing Company, Dordrecht, Holland

Lohmar S, Robin C, Parada MA, Gourgaud A, López-Escobar L, Moreno H, Naranjo J (2005) The two major postglacial (13-14,000 BP) pyroclastic eruptions of Llaima and Villarrica volcanoes (Southern Andes): a comparison. In: 6th international symposium on andean geodynamics (ISAG 2005, Barcelona), extended abstracts, pp 442–445

López-Escóbar L, Frey FA, Vergara M (1977) Andesites and high-alumina basalts from the central south Chile high andes: geochemical evidence bearing on their petrogenesis. Contrib Miner Petrol 63:199–228

Mahlke J (2009) Geochemical evolution of Llaima and Villarrica Volcanoes, Central Chile. Diploma thesis, University of Kiel

Malinconico JRLL (1979) Fluctuations in SO_2 emission during recent eruptions of Etna. Nature 278:43–45

Manga M, Brodsky E (2006) Seismic triggering of eruptions in the far field: Volcanoes and Geysers. Annu Rev Earth Planet Sci 34:263– 291. doi:10.1146/annurev.earth.34.031405.125125

Mason BG, Pyle DM, Dade WB, Jupp T (2004) Seasonality of volcanic eruptions. J Geophys Res 109(B04206):1–12. doi:10.1029/2002JB002293

Mastin LG (1994) Explosive tephra emissions at Mount St Helens, 1989–1991—the violent escape of magmatic gas following storms. Geol Soc Am Bull 106:175–185

Mather TA, Tsanev VI, Pyle DM, McGonigle AJS, Oppenheimer C, Allen AG (2004) Characterization and evolution of tropospheric plumes from Lascar and Villarrica volcanoes, Chile. J Geophys Res 109:D21303. doi:10.1029/2004JD004934

Matthews AJ, Barcley J, Carn S, Thompson G, Alexander J, Herd R, Williams C (2002) Rainfall-induced volcanic activity on Monserrat. Geophys Res Lett 29(13): 22-1–22-4. doi:10.1029/2002GL014863

McNutt SR, Beavan RJ (1987) Eruptions of Pavlof volcano and their possible modulation by ocean load and tectonic stresses. J Geophys Res 92(B11):509–523

Melnick D, Rosenau M, Folguera A, Echtler H (2006) Neogene tectonic evolution of the Neuquén Andes western flank (37–39°S), in Evolution of an Andean Margin: A Tectonic and Magmatic View From the Andes to the Neuquén Basin (35°–39°S lat), edited by Kay SM, and Ramos VA. Spec Pap Geol Soc Am 407:73–95. doi:10.1130/2006.2407(04)

Mora-Stock C, Thorwart M, Wunderlich T, Bredemeyer S, Hansteen TH, Rabbel W (2012) Comparison of seismic activity for Llaima and Villarrica volcanoes prior to and after the Maule 2010 earthquake. Int J Earth Sci (Geol Rundsch), this volume. doi:10.1007/s00531-012-0840-x

Moreno H, Clavero J, Lara L (1994) Actividad explosiva postglacial del volcán Villarrica, Andes del Sur (39°25′S). en Congreso Geológico Chileno, N°7, Actas, Vol 1, pp 329–333. Concepción Nadeau PA, Werner CA, Waite GP, Brewer ID, Carn SA, Elias T, Fee D, Garcés MA, Sutton AJ (2011) High temporal SO_2 emission rate data as part of a multiparameter approach to studying summit vent activity at Kilauea volcano. Abstract V41A-2487 AGU Fall Meeting 2011

Naranjo JA, Moreno H (1991) Actividad explosiva postglacial en el volcan Llaima, Andes del Sur (38°45′S). Rev Geol Chile 18:69–80

Naranjo JA and Moreno H (2005) Geología del volcán Llaima, Región de la Araucanía. Servicio Nacional de Geología y Minería, Carta Geológica de Chile, Serie Geología Básica, 88, 1 mapa escala 1:50.000, Santiago

Neuberg J (2000) External modulation of volcanic activity. Geophys J Int 142:232–240. doi:10.1046/j.1365-246X.2000.00161.x

Olmos R, Barrancos J, Rivera C, Barahona F, López DL, Henriquez B, Hernández A, Benitez E, Hernández PA, Pérez NM, Galle B (2007) Anomalous emissions of SO_2 during the recent eruption of Santa Ana Volcano, El Salvador, Central America. Pure Appl Geophys 164:2489–2506. doi:10.1007/s00024-007-0276-6

Ortiz R, Moreno H, García A, Fuentealba G, Astiz M, Peña P, Sánchez N, Tárraga M (2003) Villarrica volcano (Chile): characteristics of the volcanic tremor and forecasting of small explosions by means of a material failure method. J Volcanol Geotherm Res 128:247– 259. doi:10.1016/S0377-0273(03)00258-0

Palma JL, Calder ES, Basualto D, Blake S, Rothery DA (2008) Correlations between SO_2 flux, seismicity, and outgassing activity at the open vent of Villarrica volcano, Chile. J Geophys Res 113:B10201. doi:10.1029/2008JB005577

Palma JL, Blake S, Calder ES (2011) Constraints on the rates of degassing and convection in basaltic open-vent volcanoes. Geochem Geophys Geosyst 12:Q11006. doi:10.1029/2011GC003715

Parfitt EA (2004) A discussion of the mechanisms of explosive basaltic eruptions. J Volcanol Geotherm Res 134:77–107. doi:10.1016/j.jvolgeores.2004.01.002

Patane G, Frasca A, Agodi A, Imposa S (1994) Earth tides and Etnean volcanic eruptions: an attempt at correlation of the two phenomena during the 1983, 1985 and 1986 eruptions. Phys Earth Planet Int 87(1–2):123–135

Petit-Breuihl M (1994) Contribución al conocimiento de la cronología eruptiva histórica del volcán Villarrica, 1958–1985. Universidad de la Frontera, Revista Frontera 13:71–99

Rivera A, Bown F, Carrión D, Zenteno P (2012) Glacier responses to recent volcanic activity in Southern Chile. Environ Res Lett 7:014036. doi:10.1088/1748-9326/7/1/014036

Savitzky A, Golay MJE (1964) Smoothing and differentiation of data by simplified least squares procedures. Anal Chem 36:1627–1639

Scalera G (2008) Great and old earthquakes against great and old paradigms—paradoxes, historical roots, alternative answers. Adv Geosci 14: 41–57. www.adv-geosci.net/14/41/2008/

Schindlbeck JC (2012) Holocene post-caldera magma evolution of Llaima volcano, Chile. Diploma thesis, University of Kiel

Schmincke HU (2004) Volcanism. Springer, Heidelberg. ISBN 3-540-43650-2

Shimozuru D (1975) Lava lake oscillations and the magma reservoir beneath a volcano. Bull Volcanol 39(4):570–580

Shinohara H, Witter JB (2005) Volcanic gases emitted during mild Strombolian activity of Villarrica volcano, Chile. Geophys Res Lett 32:L20308. doi:10.1029/2005GL024131

Sigurdsson H, Houghton B, McNutt S, Rymer H, Stix J (2000) Encyclopedia of volcanoes. Academic Press, San Diego

Simkin T, and Siebert L (1994) Volcanoes of the world, 2nd ed. Geoscience, Tuscon, Arizona

Sottili G, Martino S, Palladino DM, Paciello A, Bozzano F (2007) Effects of tidal stresses on volcanic activity at Mount Etna, Italy. Geophys Res Lett 34:L01311. doi:10.1029/2006GL028190

Sparks RSJ (1978) The dynamics of bubble formation and growth in magmas: a review and analysis. J Volcanol Geotherm Res 3:1–37

Sparks RSJ, Biggs J, Neuberg JW (2012) Monitoring volcanoes. Science 335:1310. doi:10.1126/science.1219485

Stern CR (1989) Pliocene to present migration of the volcanic front, Andean Southern Volcanic Zone. Revista Geológica de Chile 16(2):145–162

Stern CR (2004) Active andean volcanism: its geologic and tectonic setting. Revista Geológica de Chile 31(2):161–206

Stevenson DS, Blake S (1998) Modelling the dynamics and thermodynamics of volcanic degassing. Bull Volcanol 60:307–317

Stoiber RE, Jepsen A (1973) Sulfur dioxide contributions to the atmosphere by volcanoes. Science 182:577–578

Stoiber RE, Williams SN, Huebert BJ (1986) Sulfur and halogen gases at Masaya caldera complex, Nicaragua: total flux and variations with time. J Geophys Res 91:12215–12231

Thorpe and Francis (1979) Variation in Andean andesite composition and their petrogenetic significance. Tectonophysics 57:53–70

Tuffen H (2010) How will melting of ice affect volcanic hazards in the twenty-first century? Phil Trans R Soc A 368:2535–2558. doi: 10.1098/rsta.2010.0063

Vandaele AC, Simon PC, Guilmot JM, Carleer M, Colin R (1994) SO_2 absorption cross section measurement in the UV using a Fourier transform spectrometer. J Geophys Res 99(D12):25599–25605

Voigt S, Orphal J, Bogumil K, Burrows JP (2001) The temperature dependence (203–293 K) of the absorption cross sections of O3 in the 230–850 nm region measured by Fourier-transform spectroscopy. J Photochem Photobiol A 143:1–9

Walter TR (2007) How a tectonic earthquake may wake up volcanoes: stress transfer during the 1996 earthquake-eruption sequence at the Karymsky Volcanic Group, Kamchatka. Earth Planet Sci Lett 263:347–359. doi:10.1016/j.epsl.2007.09.006

Watt SFL, Pyle DM, Mather TA (2009) The influence of great earthquakes on volcanic eruption rate along the Chilean subduction zone. Earth Planet Sci Lett 277:399–407. doi:10.1016/j.epsl.2008.11.005

Williams-Jones G, Horton KA, Elias T, Garbeil H, Mouginis-Mark PJ, Sutton AJ, Harris AJL (2006) Accurately measuring volcanic plume velocity with multiple UV spectrometers. Bull Volcanol 68:328–332. doi:10.1007/s00445-005-0013-x

Witter JB, Calder ES (2004) Magma degassing at Villarrica volcano. In: Villarrica Volcano (39.5°S), Southern Andes, Chile, Bol. 61, pp 46–52, edited by Lara LE and Clavero J, Serv Nac de Geol y Miner, Santiago, Chile

Witter JB, Kress VC, Delmelle P, Stix J (2004) Volatile degassing, petrology, and magma dynamics of the Villarrica lava lake, Southern Chile. J Volcanol Geotherm Res 134:303–337. doi:10.1016/j.jvolgeores.2004.03.002

Yokoyama I (1971) Volcanic eruptions triggered by tectonic earthquakes. Bull Geophys Inst, Hokkaido Univ 25:129–139 (in Japanese with English abstract)

S1. Scan-DOAS acquisition strategy

Several external factors need to be considered for the stringent evaluation of semi-continuous scan DOAS measurements. The intensity of scattered UV light significantly changes throughout the day, and affect the signal-to-noise ratio of the recorded spectra. Low light intensity causes low signal-to-noise ratios and consequently increases the spectroscopical error of the measurements. Thus we set the limits of the daily data acquisition interval to 1 hour after sunrise and 1 hour before sunset, in order to avoid low light conditions and to assure a more constant data quality (Fig.S1).
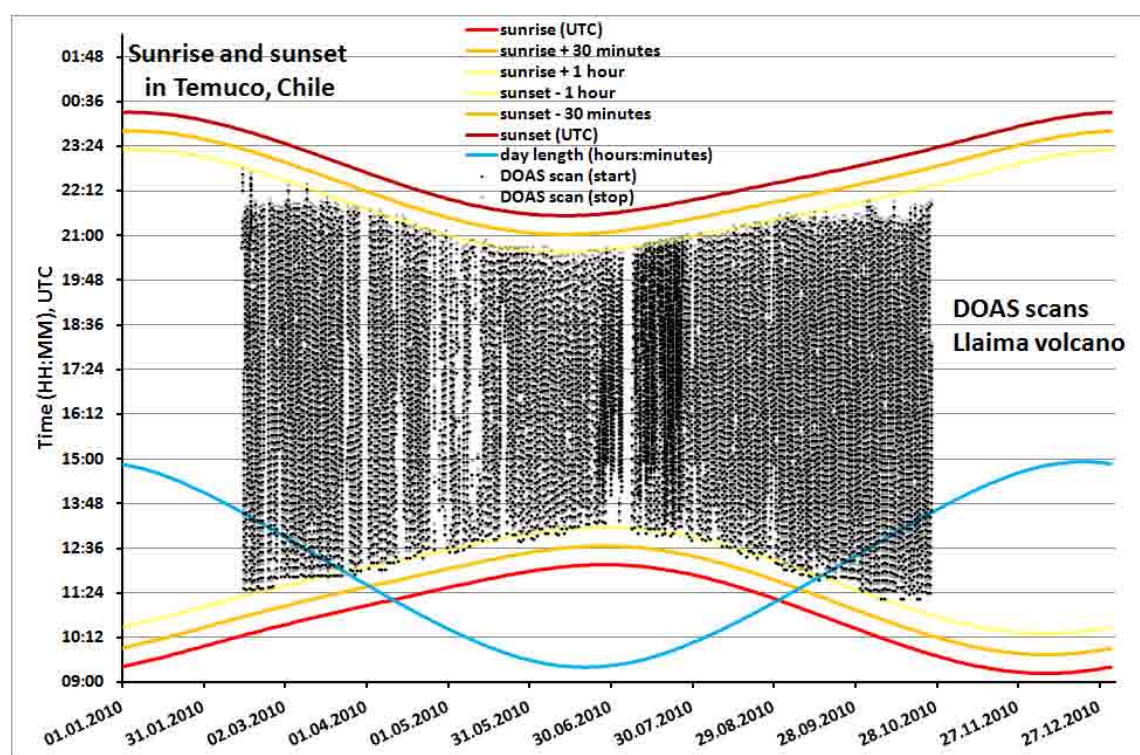

Fig. S1 Comparison between sunrise and sunset times in Temuco and the timing of Mini-DOAS scans at Llaima volcano used for the present paper.

S2. Statistical analysis of the wind field

Further external parameters that need to be considered are those used to calculate the fluxes such as wind speed and wind direction at plume height. Various statistical tests were conducted on wind speed and wind direction time series obtained from the GDAS1 model (Fig.S2). Systematic variations similar to those found in SO_2-flux time series are also observed in wind speed and wind direction time series. Especially the intra-day wind speed variations coincide with changes in strength of the gas emissions. However, even if we remove the wind speed from the calculations and use a constant wind speed of 1 meter per second to calculate fluxes, the systematic degassing variations still persist (Fig.S3). Thus the daily wind speed variations cannot alone account for the observed variations of the sulfur dioxide emissions. Of course we cannot generally rule out the influence of the wind speed on volcanic activity, as strong winds generate windward surface loads, and may trigger rockfalls and landslides. And indeed comparatively high SO_2-

fluxes were measured during stormy conditions. The influence of systematically changing wind directions on the flux measurements mainly depends on the spatial coverage of the respective scan DOAS array, because the NOVAC-software (Galle et al. 2010) automatically estimates the plume coverage of each scan. This estimate together with the wind direction from the GDAS1 model was used to distinguish between **1)** scans which missed the plume, i.e. where the plume was not within the range of the instrument and **2)** scans recorded during very low degassing activity. The DOAS stations at both Villarrica and Llaima are located east of the volcanoes, because westerly winds prevail in large parts of Southern Chile, due to the passage of frontal systems which approach from the Pacific and move eastward along the mid-latitude stormtrack (Garreaud 2009).
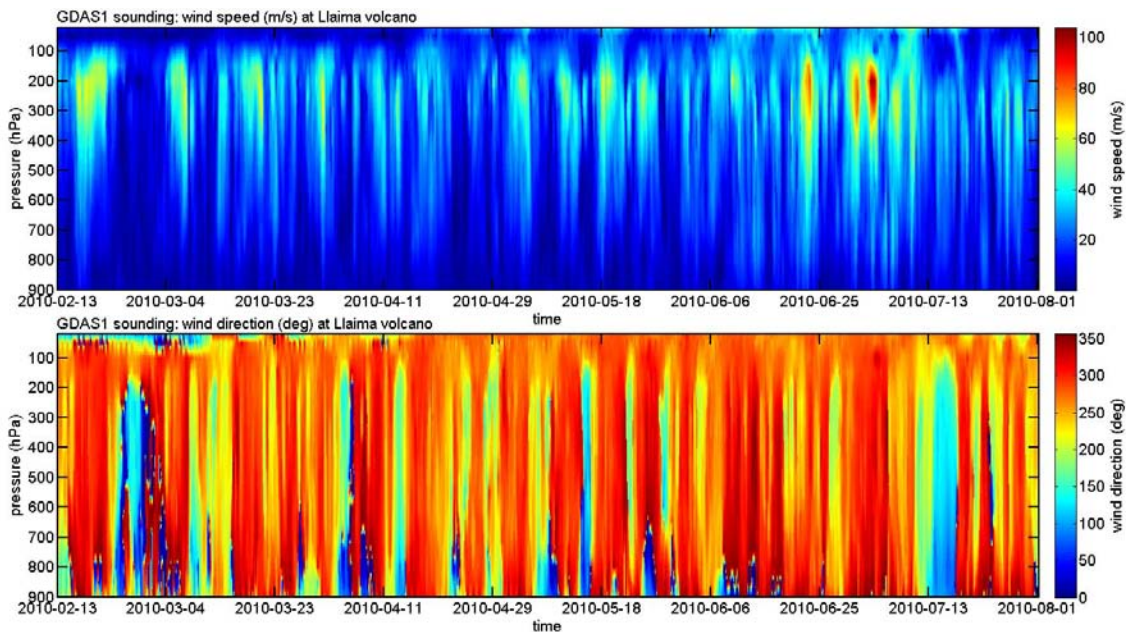

Fig. S2 Sequence of vertical atmospheric profiles (GDAS1 soundings) showing the variation of wind speed (top) and wind direction (bottom) obtained for location 38.69 S, 71.73 W (Llaima volcano). The profiles comprise 19 pressure surfaces in the range from 900 to 20 hPa, which are spaced at intervals of 50 hPa. The GDAS1 model has a temporal resolution of 1 sounding every 3 hours and a latitude-longitude grid spacing of 1 degree, i.e. it does not account for volcano-scale perturbations of the local wind field. Note that systematic daily variations of wind speed and direction appear as vertical "ripples". Wind speeds at summit height (at a pressure level of about 700 hPa) ranged from 0.3 to 37.9 m sec^{-1} during the depicted period, and were at average 12.7 m sec^{-1} . We note that wind directions are largely uniform throughout the whole atmospheric column. Strong westerly winds (orange colors) prevail particularly in the upper-levels of the atmosphere and especially during austral winter. Short phases of sustained easterly winds (light blue and cyan colors) caused some of the gaps in our SO$_2$-flux time series, since westward drifting plumes are out of range for the scan DOAS stations.
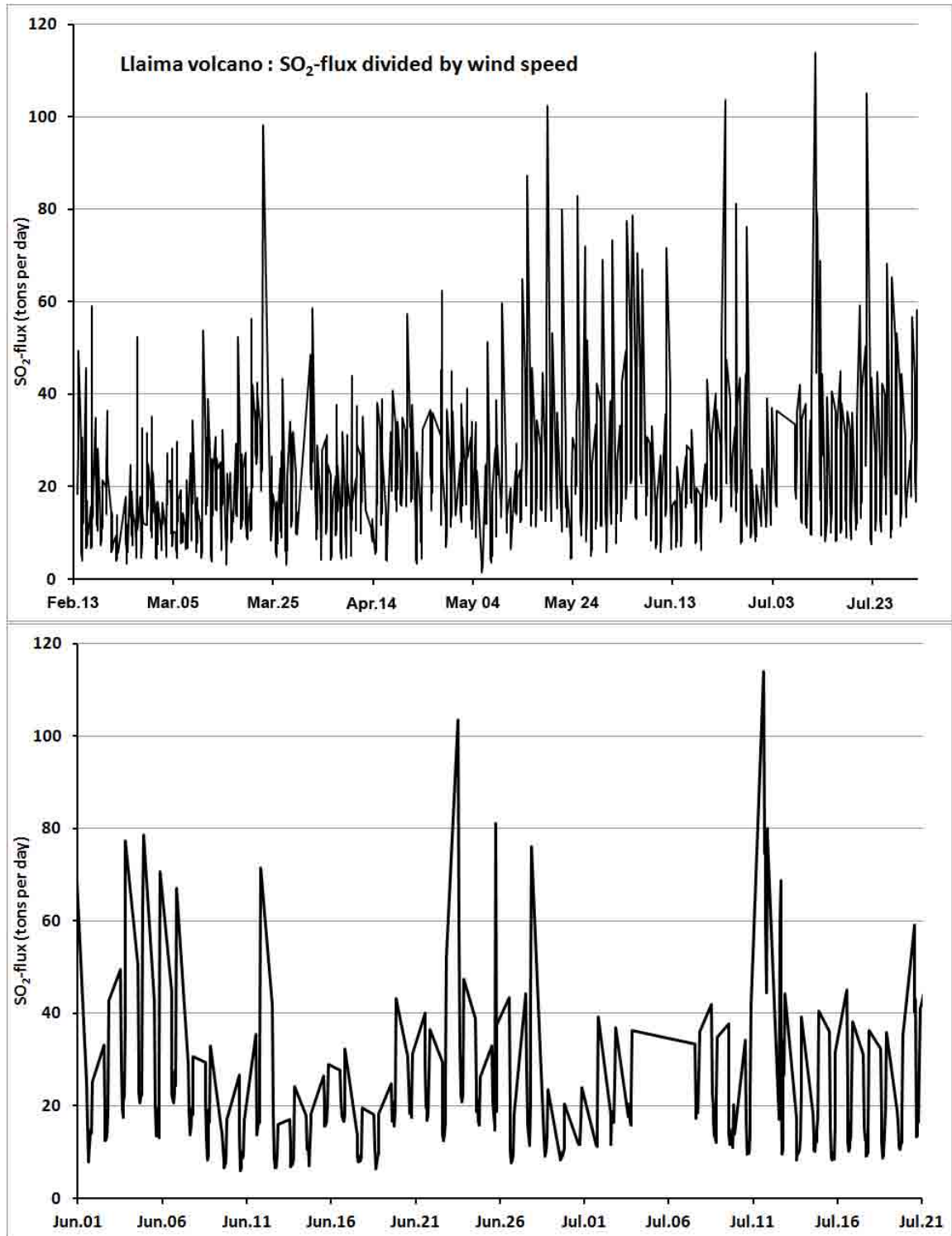
Fig. S3 Chronologic compilation of calculated SO₂ fluxes divided by wind speed data used for the flux calculations of Llaima volcano (top) and enlargement of the time series shown for the months June and July 2010 (bottom). The systematic daily variations and the scaling demonstrate that the observed patterns of variations are not controlled by the wind speeds used.
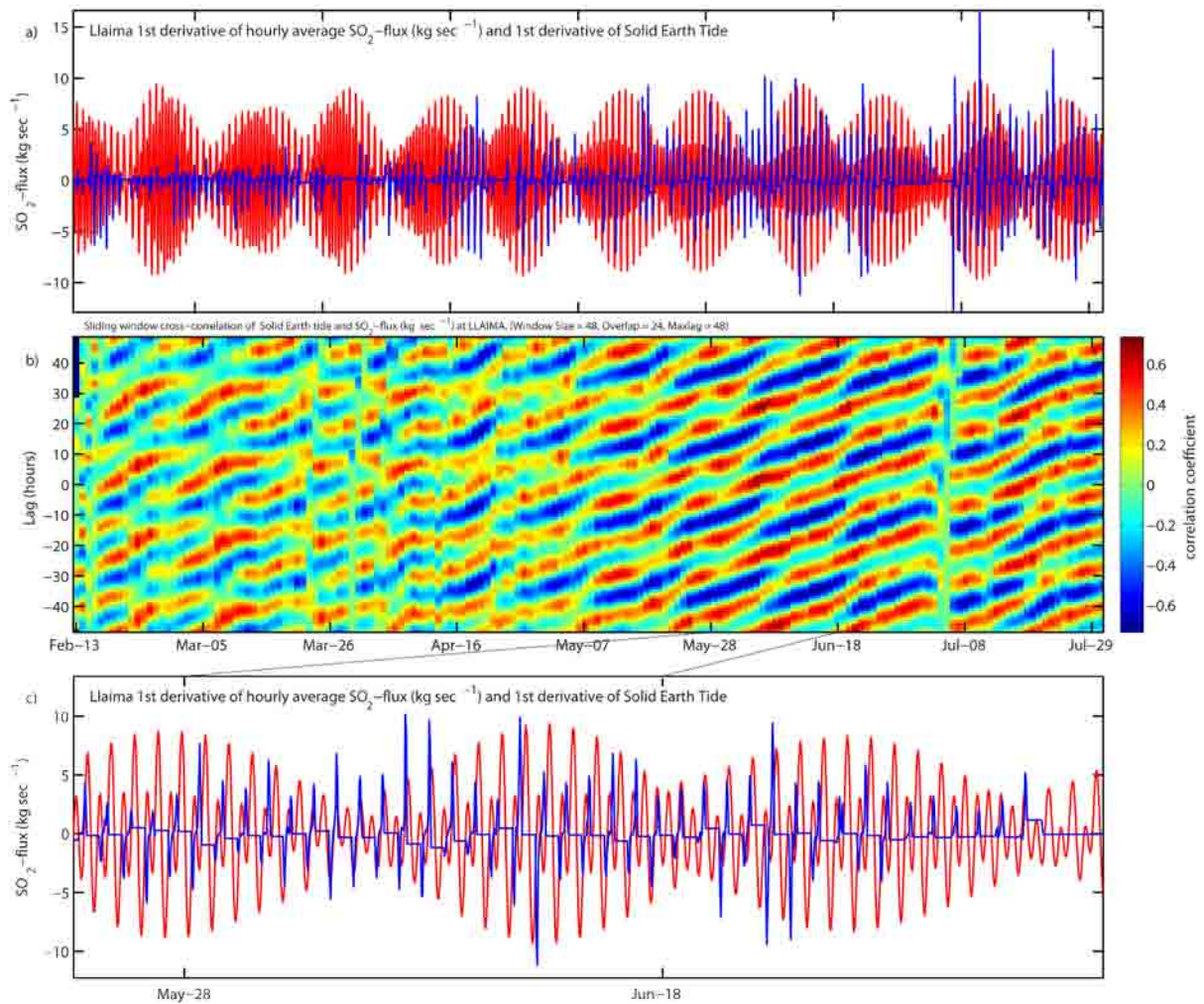
51

Fig. S4 Time series of the first derivatives of the solid Earth tidal movements and the degassing rates, respectively, for Llaima volcano. **a)** The complete time series signals and their patterns. **b)** Sliding window cross-correlation of linearly interpolated and detrended SO_2 –flux and solid Earth tidal signal. The time series reveal a shift of roughly an hour per day between the signals. c) Enlargement of the time series shown in **a)** for the month of May 2010.

References

Galle B, Johansson M, Rivera C, Zhang Y, Kihlman M, Kern C, Lehmann T, Platt U, Arellano S, Hidalgo S (2010) Network for Observation of Volcanic and Atmospheric Change (NOVAC) - A global network for volcanic gas monitoring: Network layout and instrument description. J Geophys Res 115 (D05304), doi:10.1029/2009JD011823
Garreaud, R.D. (2009). The Andes climate and weather. Adv. Geosci., 22, 3–11. doi:10.5194/adgeo-22-3-2009

CHAPTER III

SO$_2$ degassing from Turrialba Volcano linked to seismic signatures during the period 2008-2012

SO$_2$ degassing from Turrialba Volcano linked to seismic signatures during the period 2008–2012

Vladimir Conde · Stefan Bredemeyer · Eliecer Duarte · Javier F. Pacheco · Sebastian Miranda · Bo Galle · Thor H. Hansteen

Abstract In 1996, after 150 years of relative calm, Turrialba Volcano was reawakening. A visible plume and serious damage to surrounding vegetation due to acid rain are the most obvious signals. As part of the Network for Observation of Volcanic and Atmospheric Change project, four gas-monitoring stations were initially installed on the west flank of the volcano with the purpose of measuring sulphur dioxide emissions during this period of increased activity using the scanning-differential optical absorption spectroscopy technique. We present here the results of semicontinuous gas flux measurements over a period of 5 years (from 2008 to 2012), providing a novel data set that documents a relatively rapid increase in SO$_2$ fluxes from around 350 t day^{-1} to around 4,000 t day^{-1} leading up to an eruptive period, followed by a gradual return to the former baseline values. Gas flux data were also compared with seismic data for selected periods of interest, providing insights into the link between degassing and seismicity. The most important result from this comparison is the identification of an inflexion point in the gas emissions followed by a clearly increasing trend in seismic activity, distinguishable 6 months prior to a phreatic eruptive event that occurred on 5 January 2010. This signal can be interpreted as a possible indicator of future eruptive events. Monitoring of SO$_2$ thus complements seismic monitoring as a forecasting tool for eruptive events. Such monitoring is critical considering the proximity of Turrialba to the Central Valley, an area inhabited by more than 50 % of Costa Rica's population.

V. Conde (&) . B. Galle,
Department of Earth and Space Sciences, Chalmers University of Technology, Hörsalsvägen 11, 412 96 Göteborg, Sweden
e-mails: conde@chalmers.s , bo.galle@chalmers.se

S. Bredemeyer,
SFB 574 and GEOMAR Helmholtz Centre for Ocean Research Kiel, Wischhofstr. 1-3, 24118 Kiel, Germany
e-mail: sbredemeyer@geomar.de

E. Duarte . J. F. Pacheco . S. Miranda,
Observatorio Vulcanológico y Sismológico de Costa Rica (OVSICORI-UNA), Apdo 2346-3000, Heredia, Costa Rica
e-mails: eduarte@una.ac.cr , javier.pacheco.alvarado@una.cr , smiranda_brenes@hotmail.com

T. H. Hansteen,
GEOMAR Helmholtz Centre for Ocean Research Kiel, Wischhofstr. 1-3, 24118 Kiel, Germany
e-mail: thansteen@geomar.de

_____

1. Introduction

Turrialba Volcano, located about 15 km north of Turrialba city at 10.03°N 83.77°E, is the easternmost Costa Rica's Holocene volcanoes. Turrialba is part of the central volcanic range, but it is displaced about 10 km to the NE from the range axes. This 3,340-m high basaltic-to-dacitic stratovolcano covers an area of 290 km^2 and is exceeded in height only by the neighbouring Irazú volcano. The southwest end of Turrialba's broad 800 m by 2,200 m summit depression hosts three craters. The main edifice shows evidence of more than 20 eruptions and comprises pyroclastic material and lava flows occurring on Turrialba's northern, western and southern flanks (Soto 1988). The younger evolution of Turrialba comprises six explosive eruptions over the past 3,400 years, covering one plinian and five phreatic and phreatomagmatic explosive eruptions (Reagan et al. 2006). The most recent historically documented activity occurred intermittently between 1845 and 1866 when Turrialba spewed ashes that travelled as far north as Nicaragua.

1.1 The general volcanic hazards of Turrialba

Turrialba is a potentially dangerous volcano as documented by its Holocene eruptive record (e.g. Reagan et al. 2006). Natural hazards at Turrialba comprise landslides, emplacement of eruption-related pyroclastic flows, surges, lahars and ash falls, as well as reactive volcanic gases. The long-term exposure of people, buildings and crops to all these hazards makes this volcano a high-risk area (Soto 1988). Historical records from the 1864–1866 VEI 2 eruptions note ash fallout as far as 125 km from the source (Reagan et al. 2006), which suggests that fallout may have been a problem in the Central Valley, one of the most populated and important economic areas of Costa Rica.

1.2 Turrialba's period of unrest

The first signs of unrest in the current phase of activity came in the mid-1990s when several discrete seismic swarms struck the Turrialba massif and its vicinity. From May 1996 on, seismicity had increased, with reports of up to 580 long-period (LP) seismic events per month. After February 1997, an increase in the number of seismic events and their magnitude coincided with an increase in fumarolic degassing observed in the central crater, and towards the north and west walls of the west crater. Fumarolic gas samples taken during the period 1998–2001 mainly consisted of H_2O, with minor contents of CO_2 and H_2S and very low contents of typical high-temperature compounds such as HCl and HF and SO_2 (Tassi et al. 2004). From October 2000 to October 2002, four seismic swarms occurred, mainly consisting of hybrid and long-period (LP) events, reaching an average of 2,000 seismic events per month (Barboza et al. 2003). In November 2001, a sharp increase in SO_2 emissions was detected following the October 2001 seismic swarm, and the contents of HCl and HF increased as well (Tassi et al. 2004). By 2008, the amount of SO_2 had increased, reaching a SO_2/H_2S ratio of over 100. New seismic swarms occurred in 2009 accompanied by a temperature increase in the main fumaroles, from 120 °C to around 160 °C (Vaselli et al. 2010). All this indicates that the fluid system at this point had evolved from hydrothermal to a magmatic type, providing evidence of rising magma and/or progressive boiling and thus depletion of hydrothermal water (Daag et al. 1996).

After the signals indicating unrest at Turrialba and as part of the EU-funded Network for Observation of Volcanic and Atmospheric Change (NOVAC) project (http://www. novac-project.eu/), a network of optical remote sensing instruments was installed to measure SO_2 fluxes continuously. SO_2 emissions are a strong indicator of changes in volcanic activity (Symonds et al. 1994), and anomalous increments have been observed prior to eruptive events (e.g. Daag et al. 1996; Olmos et al. 2007; Casadevall et al. 1983).

Similar networks of ground-based remote sensing instruments for monitoring SO_2 emissions have been successfully applied in various locations (e.g. Burton et al. 2009; Salerno et al. 2009; Arellano et al. 2008; Grutter et al. 2008; Bredemeyer et al. 2011; Christopher et al. 2010).

During the last two decades, Turrialba Volcano has been monitored mainly by geodesy, geochemistry and seismicity. Out of these techniques, the seismic surveillance has been functioning continuously since 1990 (Martini et al. 2010). The addition of a network of instruments measuring SO_2 fluxes continuously can

provide insights into the internal processes that affect gas emissions and seismicity, thus improving the volcanic hazard assessment. Although several studies linking these two parameters have been conducted before (e.g. Arciniega-Ceballos et al. 2008; Nadeau et al. 2011; Palma et al. 2008), often they have been limited by the low time resolution of the measurements and/or the short time extent of the observations. These limitations may reduce the level of detail necessary to constrain, for instance the possible coupling of gas emissions and different seismic events, and cyclic variations in degassing rates.

This work has the aim to provide a qualitative and quantitative description of the internal processes that were operating during the active period at Turrialba Volcano from 2008 to 2012. The approach of this study consists mainly of a joint interpretation combining SO_2 fluxes and different seismic signatures through sequential stages of volcanic activity.

2. SO$_2$ flux measurements

The measurement technique primarily consists in the retrieval of SO_2 gas columns applying differential optical absorption spectroscopy (DOAS) using UV-scattered sunlight as the source of radiation (Platt and Stutz 2008). The UV-spectra acquisition was implemented in the scanning NOVAC instrument and consists of a motor-driven mirror or prism that directs the scattered light from the sky collected through a telescope defining a field of view (FOV) of 8 mrad. From the telescope, light is fed by an optical fibre to a spectrometer (Ocean Optics$^©$, S2000). By moving the mirror, the FOV of the instrument is scanned over 180° in a vertical plane from one horizon to the other, in steps of 3.6°. In addition, a 'dark' spectrum is collected in nadir position; thus, each scan contains 50 measurement spectra and one dark spectrum. If the volcanic plume is located above the scanner, its cross section will be scanned. An embedded computer implements the measurement sequence, outputting a compacted file that comprises the entire measured spectrum every time a new measurement starts. Further details of NOVAC instruments can be found in Galle et al. (2010).

The instruments run during daylight hours co-adding 15 spectra in each step, thus improving the S/N ratio. Based on the visibility conditions, the exposure time is automatically adjusted in order to avoid light saturation in the spectrometer detector. On sunny days, the typical exposure time varies between 100 and 300 ms. In view of the variability of local weather conditions, the exposure adjustment is made every time a new scan measurement starts. Under good weather conditions with better light, the exposure time tends to be lower (around 10 ms), which makes it possible to collect a scan in shorter than every 3 min.

During the spring of 2008, four NOVAC-type instruments were installed in the west flank of the volcano edifice according to the predominant easterly wind direction and security requirements. The instruments were installed at a radial distance of about 2.3 km from the crater and a mean altitude of 2,600 m.a.s.l. (Fig. 1).

2.1 Spectrum retrieval

The compressed spectra measured by the NOVAC instruments are transmitted by a local wireless network to OVSICORI-UNA, in Heredia, and automatically retrieved and evaluated by the NOVAC Software (Johansson 2009). A more careful evaluation was carried out afterwards, the results of which are reported in this paper. The outcomes of the spectrum retrieval are the SO_2 slant columns evaluated according to the DOAS method using the zenith spectrum as reference for the whole scan (Platt and Stutz 2008). The reference spectra for the DOAS fitting were obtained by convolving the high-resolution SO_2 (294 K) (Vandaele et al. 1994) and also O_3 (223 K) (Voigt et al. 2001) cross sections with the slit function of the spectrometer corresponding to the 302-nm line of a mercury lamp. After the instruments were installed, a fixed wavelength shift was constrained in each spectrometer, thus optimising the pixel wavelength calibration. Wavelength shift variations in the fitting region were tested during the measurement period by selecting random measurements on different days and at different times. These measurement samples were analysed using the program DOASIS (Kraus 2004) that performs the same DOAS analysis routines implemented in the NOVAC software but using a more user-friendly interface. The outcome of this test showed that the wavelength shift was negligible (±0.3 nm). The wavelength shift is temperature dependent,
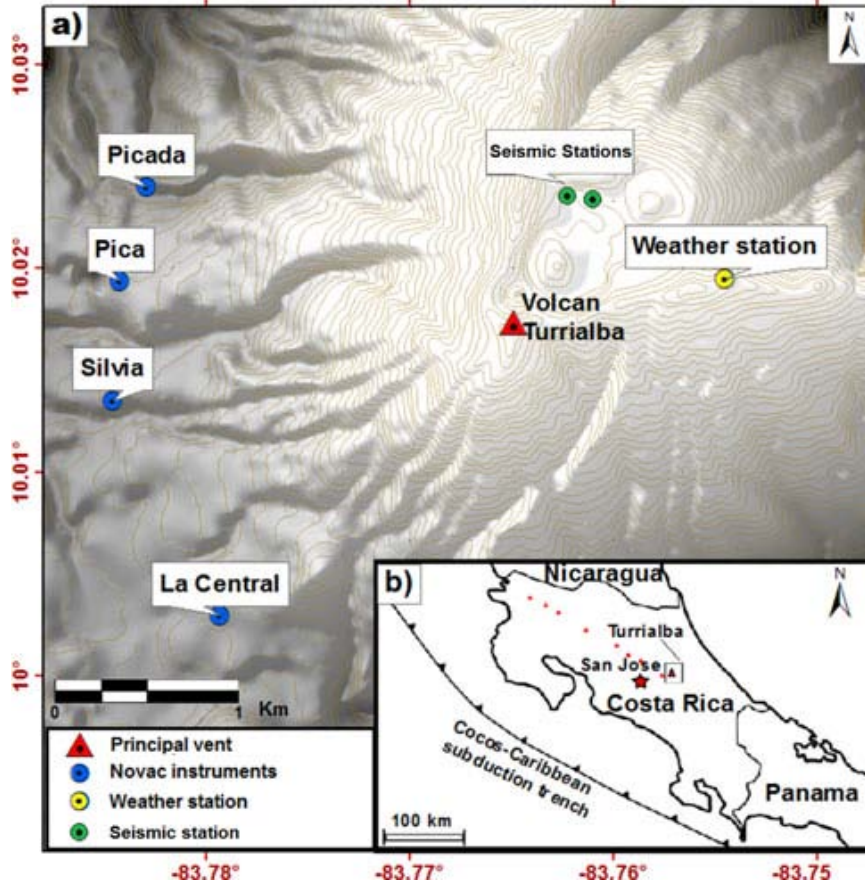
Fig. 1 a Map of Turrialba Volcano showing the location of the NOVAC instruments (*blue dots*), the weather station (*yellow dot*), seismic stations (*green dots*) and the main vent (*red triangle*). **b** Map of Costa Rica showing the location of Turrialba Volcano

and its effect varies individually in each spectrometer. An analogue temperature sensor, attached to the instrument, measured values that ranged between 17 and 20 °C. This indicates that the relatively stable wavelength shift observed in these measurements probably can be attributed to the fact that the spectrometers were not exposed to large temperature variations.

The spectrum itself cannot be used to determine the SO_2 flux directly. Plume speed, plume direction and plume height are also required in order to calculate the flux as described by Eq. 1:

$$Flux = W_s \times |\cos(W_d - compass)| \times P_H$$

$$\times \sum_{i=0}^{N-1} |\tan \alpha_{i+1} - \tan \alpha_i| \times VCD_i \qquad (1)$$

where VCD_i corresponds to the SO_2 vertical column densities estimated at the angle a_i, which corresponds to the angle between the column and the zenith. W_s and W_d are the wind speed and plume direction at the plume height, respectively, compass is the direction perpendicular to the plane of scanning, and P_H is the plume height derived from the instruments.

2.2 Plume speed

Plume speed was assumed to be equal to wind speed at the plume altitude. However, accurate wind speed at a given altitude is not straightforward to estimate and thus constitutes one of the main sources of error affecting flux measurements (e.g. Burton et al. 2009; Salerno et al. 2009; Johansson et al. 2009; Stoiber et al. 1980; Rivera et al. 2009; Hoff and Millan 1981). In 2008–2009, wind speed was retrieved using the GFS

model from the National Ocean and Atmospheric Administration (NOAA). The wind speed data used from 2010 to 2012 were obtained from a meteorological station installed by the Costa Rican National Meteorological institute (IMN) near the summit (Fig. 1). A predominant bias of +2 m/s was observed in the modelled wind speed in comparison with the wind speed data obtained from the meteorological station. Thus, a bias correction was applied to the wind speed retrieved from the GFS model in order to make it comparable to the measured wind speed, which was assumed to be a better estimate of the plume speed, than the modelled wind speed.

2.3 Plume direction and height

Plume direction and height were derived by combining the slant columns measured by two instruments simultaneously, assuming a stable wind direction (Edmonds et al. 2003).
During the first 10 months, just after the instruments were installed, all four stations were running continuously, tracking variations in plume direction within an angular range of 180°– 300° relative to North. Figure 2a shows the angular distribution of the measured plume direction during this initial period, according to which the mean angle is 247° ± 19°, indicating that the wind direction is relatively stable.

Figure 2b shows the distribution of the measured plume height during the same period, with a mean altitude of 3,366 ± 567 m.a.s.l. Compared with the wind directions, the plume height is characterised by a greater variability, with a wide range of values especially in the upper half of the distribution. This is not surprising considering that, in periods of increased activity, visual observations of a plume reaching an altitude up to 2 km above the crater have been reported (Martini et al. 2010).

2.4 Error analysis

The measurement errors in the flux measurements are a combination of factors that include spectroscopy, weather conditions and measurement geometry. The uncertainty computed for our measurements is based on the previously reported statistical methods (e.g. Rivera et al. 2009; Galle et al. 2010; Kern 2009); however, a more rigorous treatment of each of the error sources is beyond the scope of this paper.

The spectroscopic errors are associated with uncertainties in the absorption cross section, temperature effects and fitting errors, accounting for approximately 10 % of the measured flux. The scattering error accounts for 50 % of the measurement error at distances around 2.6 km and <10 % for distances around 0.6 km (Mori et al. 2006). The proximity of the NOVAC instruments surrounding Turrialba Volcano (≈400 m) allows the assumption that the scattering error is approximately 10 % of the measurement error under good weather conditions.

The size of the geometry error depends on the accuracy of the plume height and plume direction values which were used to calculate the flux. It is possible to calculate these parameters directly from the scans, when the plume is measured simultaneously by two or more NOVAC instruments (e.g. Johansson et al. 2009). Under such circumstances, the geometry error has been estimated to be no more than 10 % (Edmonds et al. 2003). However, this condition was only achieved during the first 10 months of measurements. Afterwards, it was not possible to keep all the stations working simultaneously, which means that it was no longer possible to derive the plume height and direction. Nevertheless, the geometrical measurements obtained by the instruments during the first months provided statistics about the variability of the predominant direction and height of the plume. The wind directions and plume heights in the measurement period after the initial 10 months of measurements were thus assumed to be statistically distributed as estimated in the previous sections and shown in Fig. 2a, b. Therefore, the mean values of 247° for the wind direction and 3,366 m.a.s.l. for the plume height were assumed to be valid also for the period after the initial 10 months of measurements; nevertheless, this assumption implies that the geometry error is larger for the latter period. According to Eq. 1, the angular variability of the wind direction (standard deviation of ±19°) accounts for a measurement error of approximately 5 %. Similarly, the variability of the plume height, estimated as 567 m.a.s.l., accounts for a measurement error of approximately 17 %. Using Gaussian error propagation, the original geometry error of 10 % is increased and accounts for approximately 20 %. Wind data retrieved from models provide a good representation of the regional wind
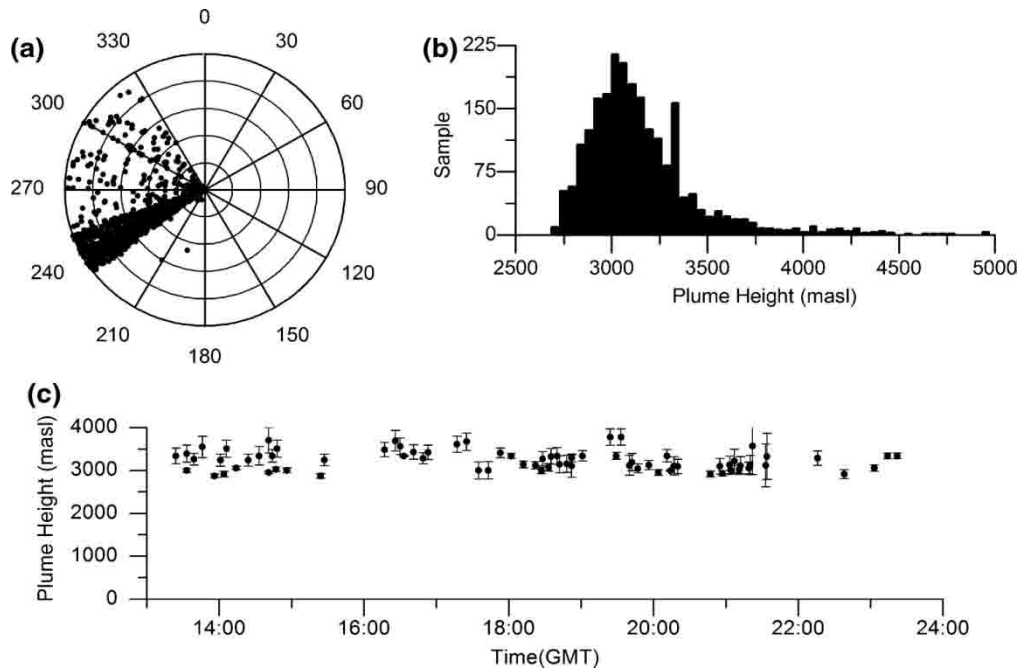
Fig. 2 Measurements of plume height and direction combining two scanning instruments.
a Angular distribution of plume direction (°) obtained from scans performed during the period May–December 2008. Notice a predominant direction between 240° and 260°.
b Distribution of plume height during the period May– December 2008.
c Example of the plume height measurements on 5 May 2008. The plume tends to be a few 100 m above the crater rim (3,340 m.a.s.l).

field. However, due to their low spatial resolution, the models are not able to resolve small-scale perturbations of the wind field resulting from the local topography, thus increasing the uncertainty of the data. Previous studies have estimated that wind speed uncertainty is 20–30 % when using wind models (e.g. Galle et al. 2010; Rivera et al. 2009). The meteorological station, which provided us with wind speed measurements, is located next to the crater rim and about 110 m below the average plume height. In view of its proximity, the wind speed uncertainty should be lower compared to the modelled wind speed; therefore, we have assumed this error to be 15 %.

Table 1 summarises the estimated measurement error sources during the different measurement periods. The estimated total error is between 27 and 33 % for optimal weather conditions. In view of the similarity of these values, a nearly constant measurement error is assumed for the whole measurement period reported in this paper.

Due to the observed high variability of the flux measurements during single days and considering that the sampling rate is not uniform, our analysis is restricted to consider the daily average of the flux emissions, and we thus applied a 'low-pass filter' in order to reduce the measurement noise.

Further studies are still required in order to better estimate the error sources. Some progress in this issue has been achieved constraining the radiative transfer error (Kern et al. 2010); however, this correction still has not been implemented in our evaluation routines.

Table 1 Estimate of the contribution from different sources to the total measurement error through two different periods

Period	Spectroscopy (%)	Atmospheric scattering (%)	Geometry (%)	Wind speed (%)	Total (%)
04/05/2008–04/03/2009	10	10	10	30	34
04/03/2009–17/07/2012	10	10	20	15	28

3. Seismic data

The flux measurements were compared with the time series of seismic events' daily count and real-time seismic amplitude measurements (RSAMs) (Endo and Murray 1991). Each individual RSAM count corresponds to the average value of the seismic amplitude during 10 min; however, the averaging time was increased up to 1 day when RSAM was compared with daily values of the SO_2 flux. The seismic measurements were made by two stations (VTUC and VTUN) that belong to the OVSICORI-UNA seismic network and are located within the summit area of the volcano (Fig. 1). VTUC was used until December 2010, and it is located 700 metres to the northeast of the vent. This station consists of a one component short-period seismometer Ranger SS-1 and a Teledyne Geotech amplifier. VTUN was installed in May 2010, and RSAM values are computed with this station since June 2010. This station is located 500 metres to the north-northeast of the vent and consists of a Trillium Compact seismometer and a 24-bit Taurus digitizer, both from Nanometrics Inc. During the overlapping period (from June to December 2010), RSAM values were compared to assure that both stations acquire the same time series, but with different amplitudes.

4. Results

As in many other locations in Central America, the weather conditions are characterised by two main seasons: a dry season (November–April) and a rainy season (May–October). However, the visibility conditions at Turrialba tend to alternate between clear sky and fog or clouds even during the dry season. The local weather conditions thus interrupted the measurements during certain periods. Continuous measurements were also hampered by technical problems due to the difficult environmental conditions in the area, the major hindrance being corrosion of the instruments due to the volcanic degassing itself, which unfortunately caused gaps in the measurement time series. Despite these difficulties, we have obtained the largest set of SO_2 emission measurements from Turrialba to date and were able to document pronounced activity changes that are discussed in this paper.

Figure 3 and Table 2 show the series of daily averaged SO_2 fluxes obtained by the DOAS instruments over the period from 29 April 2008 to 17 July 2012. There are 681 days of measurements in total, where the data from each day correspond to an average value of at least 10 complete plume scans. Typically, the measurement rate varied between 30 and 40 scans per day. Considering the whole 52-month time series, the SO_2 data set can be subdivided into three main activity periods (Fig. 3). Period 1 refers to the first 10 months of measurements from May 2008 to March 2009 and reflects comparatively steady degassing of 356 ± 246 metric tonnes per day [t day^{-1}], which is regarded as the baseline SO_2 flux (Figs. 3, 4). Period 2 from March 2009 to September 2011 is characterized by an enhanced and variable degassing activity and includes the 5 January 2010 phreatic eruption and several other phreatic events (Smithsonian-Institution 2012).
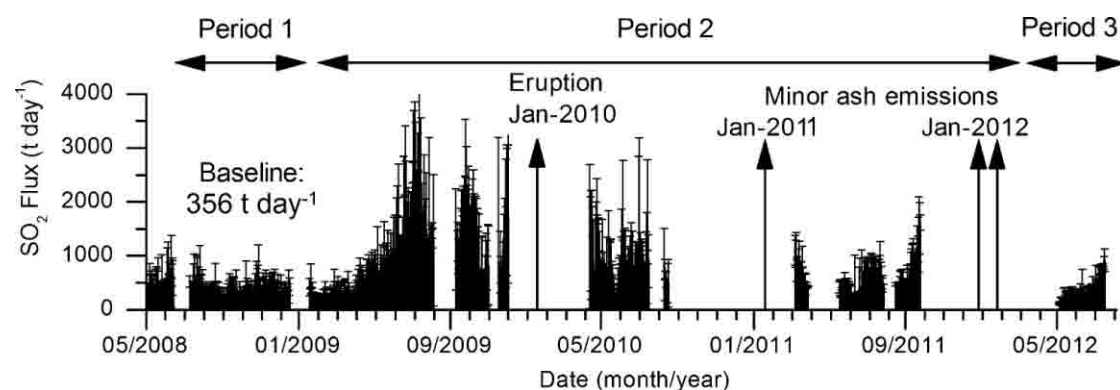

Fig. 3 Daily average SO_2 fluxes measured from April 2008 to July 2012.
Period 1 is considered to be the measurements of baseline.
Period 2 corresponds to the most active degassing phase.
Period 3 denotes the return of the emissions to the estimated baseline.

Table 2 Daily variability of SO$_2$ emissions during different measurement intervals

Initial period	Final period	Day (number)	Mean SO$_2$ flux (t day^{-1})	Maximum SO$_2$ flux (t day^{-1})	Minimum SO$_2$ flux (t day^{-1})	SD SO$_2$ flux (t day^{-1})
04/05/2008	04/03/2009	219	356	1,251	14	246
04/03/2009	03/07/2009	110	692	3,688	22	724
04/07/2009	03/12/2009	85	1,484	5,193	23	1,035
05/01/2010	17/08/2010	89	702	3,436	17	728
08/03/2011	25/09/2011	104	635	2,790	9	616
05/05/2012	17/07/2012	74	312	1,172	51	216

Number of days are days with available measurements. Flux (t day^{-1}) are the mean daily average SO$_2$ fluxes of the corresponding intervals. Standard deviation and maximum daily average fluxes reflect the large variability during these intervals and the periods shown in Fig. 3

The beginning of Period 3 at the end of April 2012 marks the return of gas fluxes to baseline values and continues until the last considered measurements are obtained in July 2012 (Fig. 3). More details about the degassing patterns corresponding to each period, including its associated seismicity, are presented below.

4.1 Gradual increase in SO$_2$ fluxes and persistent high-level degassing

Between March 2009 and July 2009, the SO$_2$ flux progressively rose from the baseline of 356 ± 246 to $2,400 \pm 850$ t day^{-1}, with some peaks in daily average fluxes ranging up to 4,000 t day^{-1}. From July 2009 until the beginning of December 2009, emissions averaged $1,484 \pm 1,034$ t day^{-1}. Approximately 1 month later, on 5 January 2010, a phreatic eruption occurred, which opened a new vent on the south-western side of the west crater. On January 6, SO$_2$ fluxes of about 5,000 t day^{-1} were obtained from satellite data (Campion et al. 2012), compatible with our data.

From May 2009, RSAM data were available as shown in Fig. 4. Unfortunately, RSAM data were not available during the baseline period, so it is not possible to evaluate variations in seismicity during the initial period and the subsequent phase of increased degassing. Nevertheless, it is interesting to note a sustained elevation in RSAM counts that proceeds until the end of September 2009. Seismic swarms that are visible in the RSAM signal from late May to the end of June 2009 coincide with the sustained upward trend in emission rates. After the SO$_2$ fluxes reached their maximum values (~4,000 t day^{-1}) in July 2009, the RSAM was characterized by low amplitudes with a slightly rising trend, whereas degassing rates showed large variations and were decreasing on average. A short gain of SO$_2$ emissions up to ~3,500 t day^{-1} at the end of September 2009 was followed by another phase of decreasing emissions in October 2009. At the same time, the RSAM signal started to show strong oscillations reflecting pronounced changes in the volcano seismic activity. On 21 December 2009, 15 days before the phreatic eruption, the volcanic tremor diminished and the RSAM dropped from 75 to approximately 10 counts, remaining low until the volcanic tremor increased again on 4 January 2010 and the day of the eruption (5 January 2010), when RSAM increased drastically to 120 counts. Chemical analysis of the material ejected during the phreatic eruption revealed the presence of about 1 % juvenile andesitic glass fragments (Reagan et al. 2011).
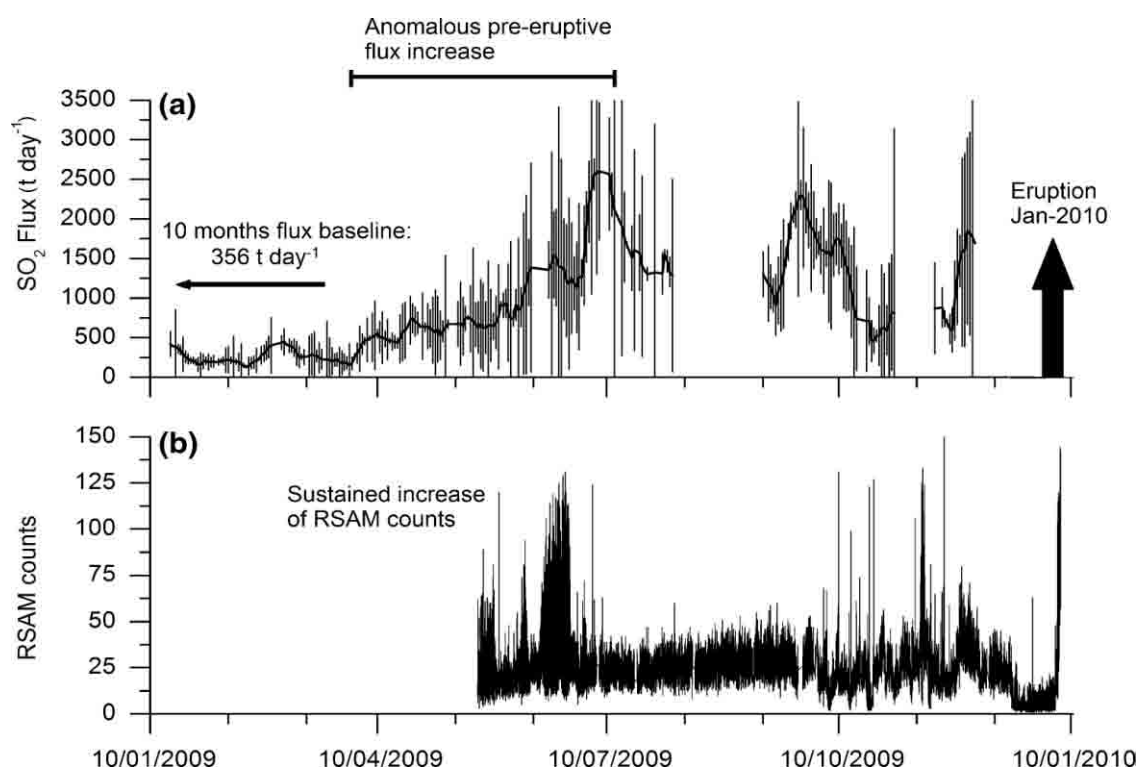
Fig. 4 a Daily average SO_2 emissions from January 2009 to December 2009. The black line corresponds to the daily flux; the grey lines correspond to the observed daily variability.
b RSAM counts, available for comparison from May 2009 to January 2010

4.2 High and variable degassing rates following the 2010 eruption

Following the January 2010 phreatic eruption, SO_2 fluxes remained high, with average fluxes of about 3,400 t day^{-1}, derived from combined SO_2 camera and satellite data (Campion et al. 2012). In 2010, DOAS measurements are only available from April to July (Fig. 5a; Table 2). During this interval, the SO_2 emission rate averaged 702 ± 721 t day^{-1}, which represents a considerable reduction compared to the period leading up to the January 2010 eruption ($1,484 \pm 1,034$ t day^{-1}). However, even though the mean emissions decreased, sustained pulses recurring cyclically with observed periods of about 10 days exhibited daily averages of 2,500–3,000 t day^{-1} without any clear upward or downward trend. In addition to RSAM (Fig. 5), the time series of various types of seismic events were available from 1 June 2010, comprising daily accumulated long-period (LP) events, very long-period (VLP) events and volcano tectonic (VT) events, and tremor duration (Fig. 6). In 2010, LP events were clearly predominant (12,309 events) compared to VLP events (1,148 events) and VT events (17 events). The 2010 degassing behaviour was accompanied by a similar pattern in the time series of RSAM (Fig. 5b), the rate of LP-VLP seismic events (Fig. 6b) and tremor duration (Fig. 6c).

4.3 Gradual decrease in SO_2 emissions to baseline values

Figure 7a shows the detailed measurements made in 2011 (March–September) and 2012 (May–July). In 2011, average SO_2 emissions declined slightly to 635 ± 621 t day^{-1}, down from 702 ± 721 t day^{-1} as estimated for the months following the January 2010 eruption. By 2012, the decreasing tendency of the SO_2 fluxes continued, reaching an average value of 312 ± 21 t day^{-1}. This amount is comparable to the baseline of 356 t day^{-1} estimated in Period 1. RSAM counts (Fig. 7b) still exhibited a pulsating pattern comparable to that observed in 2010, but nevertheless, there was also a noticeable downward trend.

Fig. 5 a SO$_2$ emissions and **b** RSAM from April to August 2010. The *dots* correspond to the individual measurements of both time series
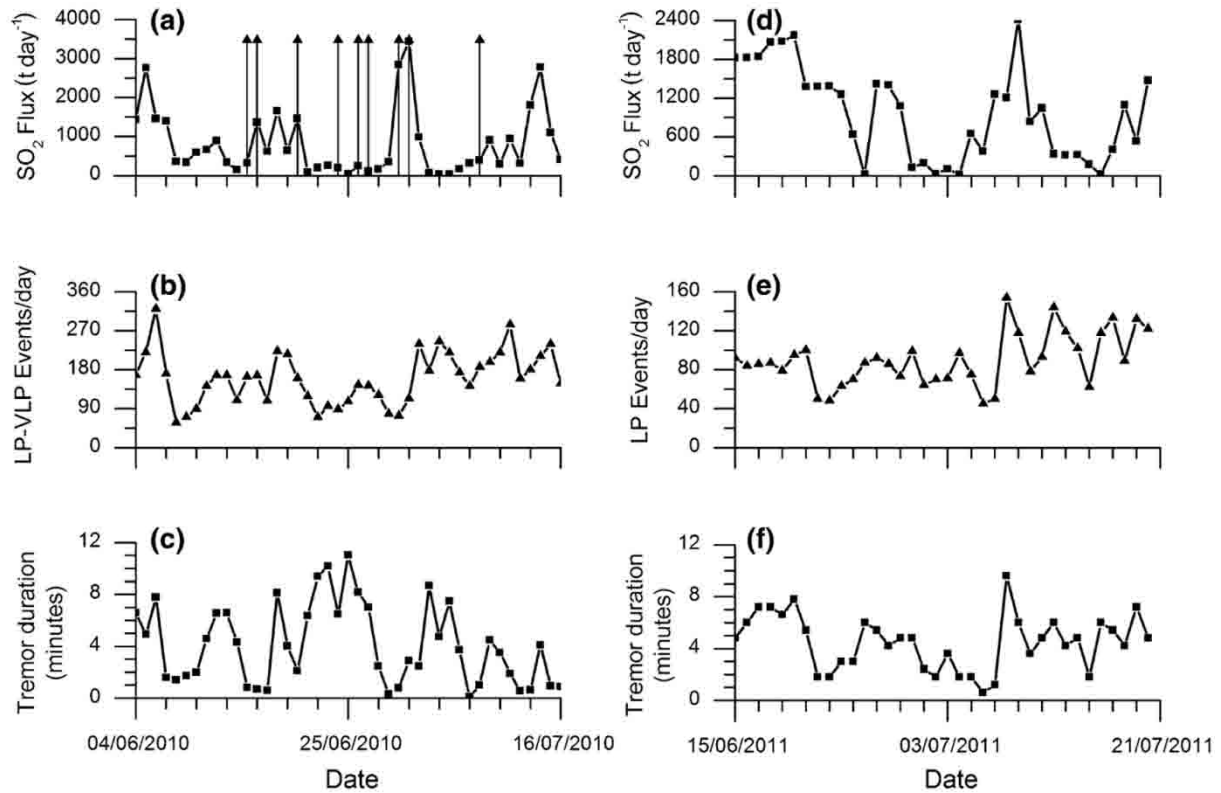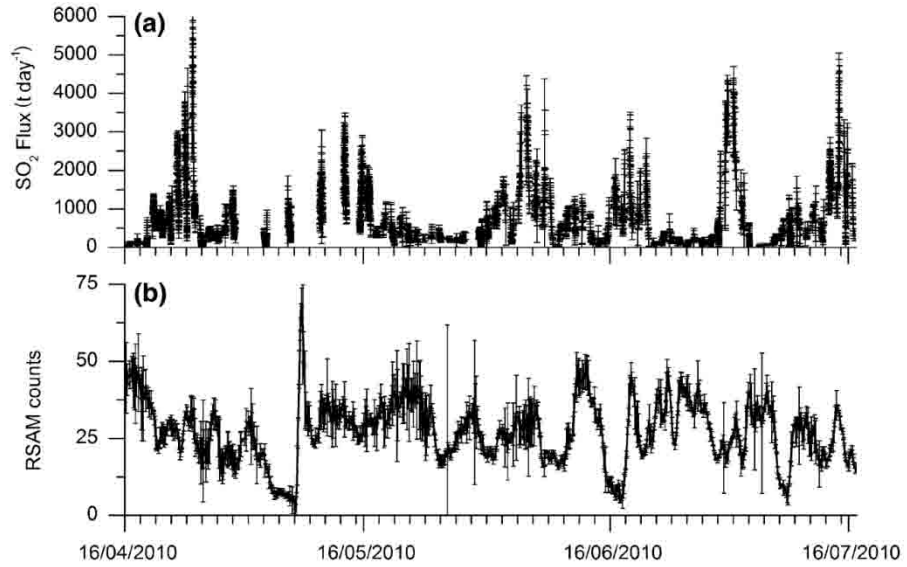

Fig. 6 SO$_2$ emissions, seismic events and tremor. June–July 2010: **a** SO$_2$ daily flux and VT events, **b** daily amount of LP–VLP events, **c** daily span of accumulated tremor June–July 2011: **d** SO$_2$ daily flux, **e** daily amount of LP events, **f** daily span of accumulated tremor

Through 2011, the average duration of tremor was within the same range (4 min), but the variability was slightly shorter than in 2010 (3 and 2 min, respectively). LP events still occurred daily, but their occurrence decreased from a background value of 150 daily events, observed in the previous year, to less than 90 daily events (Fig. 7e). VLP and VT events were scarce in 2011 and 2012. By January 2012, the seismic signals in general had reached an extremely low magnitude; thus, RSAM counts were no longer recorded in view of their minor significance under the prevailing conditions. In summary, the relatively slow reduction in the SO$_2$ flux was accompanied by a comparatively faster drop in seismic activity.
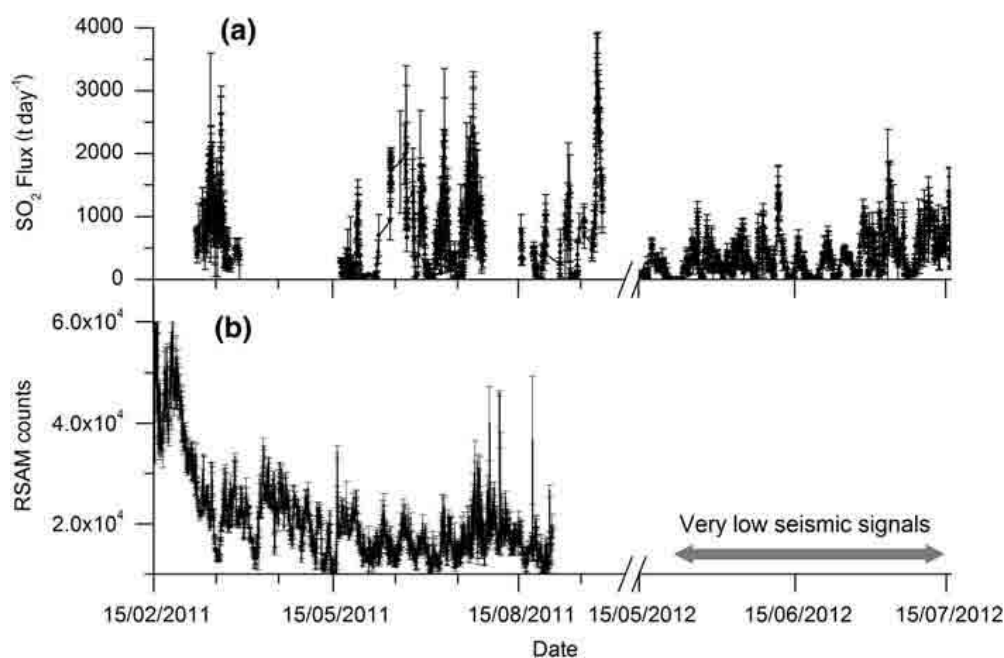
Fig. 7 a SO₂ flux (single scans) from March to September 2011 and May to July 2012. **b** RSAM (February–August 2011). Notice that the RSAM count has a larger magnitude compared to the previously reported RSAM due to a change in the sensitivity of the sensor. From January 2012, the RSAM count was no longer recorded due to the extremely low amplitude of the observed seismic signals at that time

4.4 Transient data analysis of SO₂ fluxes and seismicity

On a long term, i.e. during the 4 years investigated here, the seismic signatures observed (RSAM and various types of seismic events) broadly follow the same overall trend as the SO₂ emissions. Despite this similarity, however, comparisons at shorter timescales between weeks and months show that there is not always a clear correspondence observed between the SO₂ flux and the seismic time series. For this reason, a further analysis is required in order to investigate the link between SO₂ fluxes and seismicity. The first approach is based on the observed pulsating patterns in 2010 and 2011. Two measurement periods were chosen for the comparative analysis, due to a good continuity of the data sets, namely June to July 2010 and June to July 2011. For the first measurement period, June–July 2010, two main cycles were identified by applying a fast Fourier transform (FFT) both to the SO₂ flux and to the RSAM time series (Fig. 8a). These cycles range between ~0.07 and 0.10 day^{-1} (equivalent to 10–14 days) and ~0.13 and 0.16 day^{-1} (equivalent to 6–7 days), respectively, as shown by the grey insets in Fig. 8a. In order to further constrain the periodicity, FFT was also applied to the tremor and LP time series. The power spectral density (PSD) of each time series shows predominant cycles in agreement with each of the two main cycles previously observed in the SO₂ and RSAM time series. The longer-period (i.e. 10–14 days) cycle seems to be most pronounced in both the SO₂ flux and the tremor time series. The LP time series, in contrast, is dominated by the shorter-period (i.e. 6–7 days) cycle, while in the RSAM time series, both cycles are present to a similar extent. These results in the frequency domain show that there is an apparent systematic covariation in the time series. Other higher-frequency components depicted in Fig. 8a are considered to correspond to weak interday variations superimposed on the stronger low-frequency oscillations. However, due to their weakness and their proximity to the nyquist frequency, these higher-frequency components are considered to be of minor importance.

Similarly, the covariation between SO₂ flux and seismicity during the second selected measurement period (June–July 2011) was studied, again using the same FFT approach. The PSDs of the SO₂, RSAM, tremor and LP time series are shown in Fig. 8b. In general, these results are similar to the results for 2010. Two distinct cycles were identified and shown as grey insets in Fig. 8b. The frequency band of the longer-period cycle of the PSDs remains almost unchanged between 10 and 14 days. Nevertheless, the shorter-
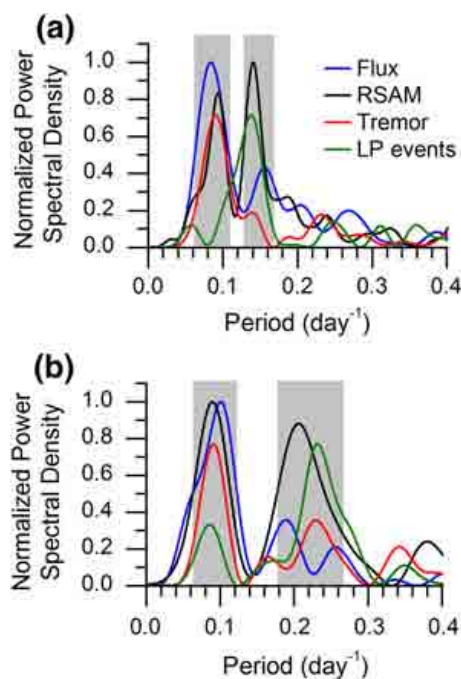
65

Fig. 8 a Periodicity of SO_2 flux, RSAM, LP events per day and tremor in June–July 2010. **b** Periodicity of SO_2 flux, RSAM, LP events per day and tremor in June–July 2011. The power spectral density in both figures is computed by fast Fourier transform using a sampling frequency of 1 day for all the time series and a Bartlett–Hanning window in order to minimise the spectral leakage. The grey insets show the periods where a common periodicity is identified amongst all the signal

period cycle is shifted from 0.13 to 0.23 day^{-1} (equivalent to a period shift from 7 to 4 days). As in 2010, the main peak in the PSD of the LP time series corresponds to the shorter-period cycle. The shift to higher frequencies indicates that even though the number of daily LP events has decreased in 2011, the LP time series is oscillating at a higher frequency. This is consistent with the shorter-period cycle of the SO_2, tremor and RSAM PSDs as shown in Fig. 8b, which also shifted to higher frequencies and broadened while the amplitudes decreased.

The spectral coupling of the RSAM with LP and tremor time series, found by frequency analyses, was expected to a certain extent, since the RSAM signal typically contains contributions of both tremor and LP earthquakes amongst other seismic signals. The link between SO_2 flux and tremor/LP time series seems to be plausible, too, as tremor and LP events are thought to originate from degassing processes and magma movement. For further analysis, we will use RSAM as a 'measure of the volcanic activity', rather than using the statistical time series that are available in the form of tremor duration and number of LP events per day, as the RSAM provides information about the amplitudes of the respective signals. Thus, in order to investigate the temporal dependence between the SO_2 flux with tremor and LP respectively, our approach consists of decomposition of the degassing and the RSAM time series by isolating the frequency bands of the respective determined cycles. For simplicity, we will refer to the longer-period cycle as the tremor cycle and to the shorter-period cycle as the LP cycle in the following text, since the longer-period cycle constitutes the main frequency band of the tremor time series and the shorter-period cycle constitutes the main frequency band of the LP time series. The individual contribution of tremor and LP cycles was decoupled by applying two subsetting filters (Brooks 2011) both to the SO_2 and to the RSAM time series. The cut-off frequencies of each filter correspond to the tremor and LP cycles as indicated by the grey insets, shown in Fig. 8a and b. The outcome of this procedure is four time series denoted as: tremor–SO_2, tremor–RSAM, LP–SO_2 and LP–RSAM (shown in the supplementary material).

After subsetting the time series, their time lag was investigated by means of a correlation analysis as described by Eq. 2. and shown in Fig. 9:

$$c(m) = \frac{1}{N} \sum_{t=0}^{N} \frac{[(S(t+m) - \mu_S)(F(t) - \mu_F)]}{\sigma_S \sigma_F}$$

$$m = -N, \dots -1, 0, 1, \dots N \qquad\qquad\qquad (2)$$

where N is the number of samples and c is the correlation coefficient at the time lag m. S(t) and F(t) are the seismic and flux time series, and ls and lF are their corresponding average values. rS and rF are the seismic and flux standard deviation, respectively.
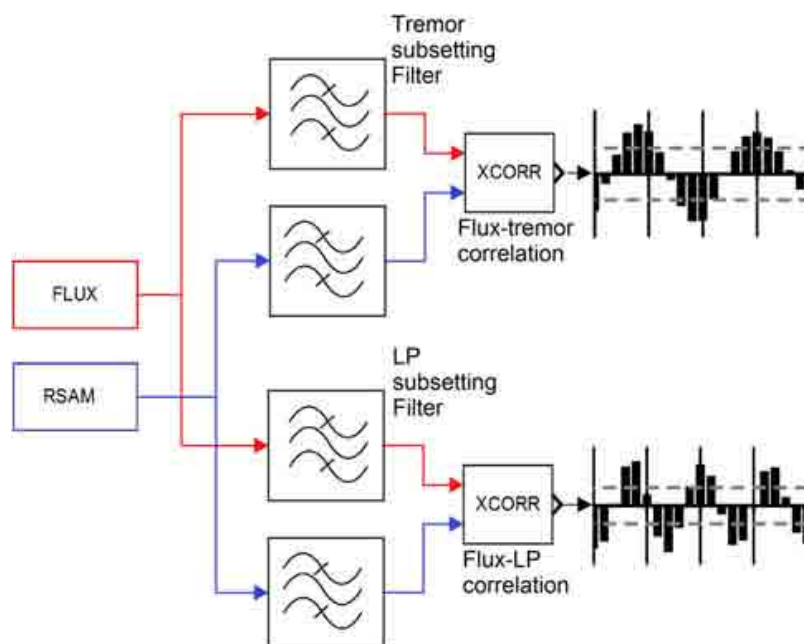
Fig. 9 Block diagram describing the process for constraining the temporal dependence between flux and seismic time series. Two different filters corresponding to tremor and LP cycles are applied to the flux and RSAM time series in order to isolate their individual contribution. A correlation analysis retrieves the time lags between the filtered time series

The correlograms corresponding to the measurements in 2010 (Fig. 10a) and 2011 (Fig. 10b) show a strong correlation at lag 0, indicating no detectable phase shift between SO_2 fluxes and LP seismicity. Similarly, the correlograms between flux and tremor corresponding to 2010 and 2011 are shown in Fig. 10c and d, respectively. In 2010, the tremor–flux correlogram shows a lag of 6–4 days, and a strong anticorrelation at lag 0 (Fig. 10c), thus indicating a delay of the SO_2 emissions after the occurrence of tremor. In 2011, the tremor–flux correlogram shows a strong correlation at lag 0, indicating no detectable time shift between the occurrence of tremor and SO_2 emissions (Fig. 10d).
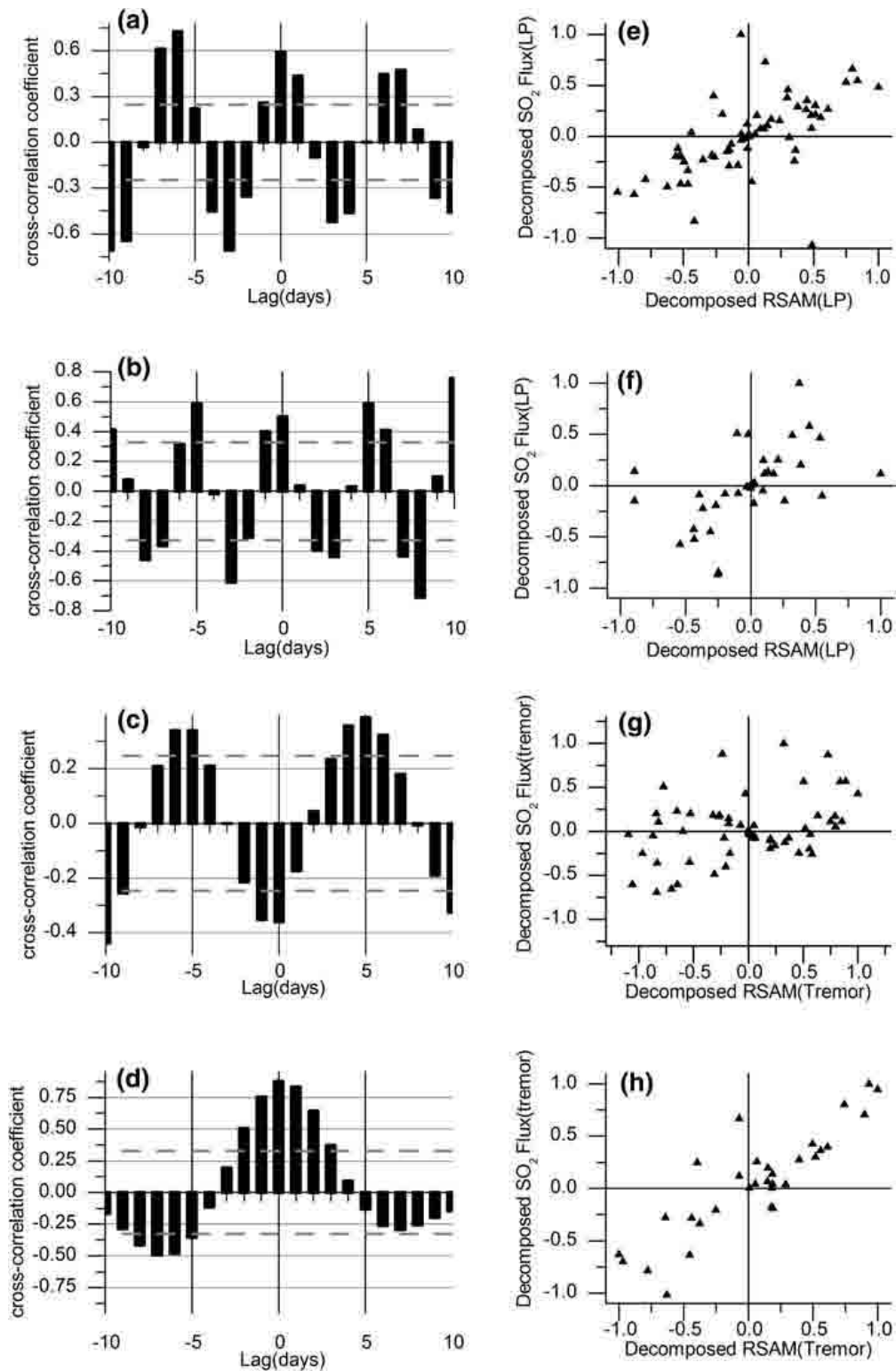
Fig. 10 Correlation between SO_2 flux and seismicity. Correlograms between LP-SO_2 and LP-RSAM: **a** June–July 2010. **b** June–July 2011. Correlogram between tremor– SO_2 and tremor–RSAM: **c** June–July 2010. **d** June–July 2011. Scattered plots: **e** Correlogram shown in **a** at lag 0. **f** Correlogram shown in **b** at lag 0. **g** Correlogram shown in **c** at the maximum lag of -6 days. **h** Correlogram shown in **d** at lag 0. The analysis corresponds to a continuous period using a sampling frequency of 1 day for both time series. The dashed horizontal lines shown in the correlograms (**a**–**d**) represent the 95 % CI threshold that indicates whether the correlation is statistically significant ($\pm 2/\sqrt{N}$, where N is the number of observed points)
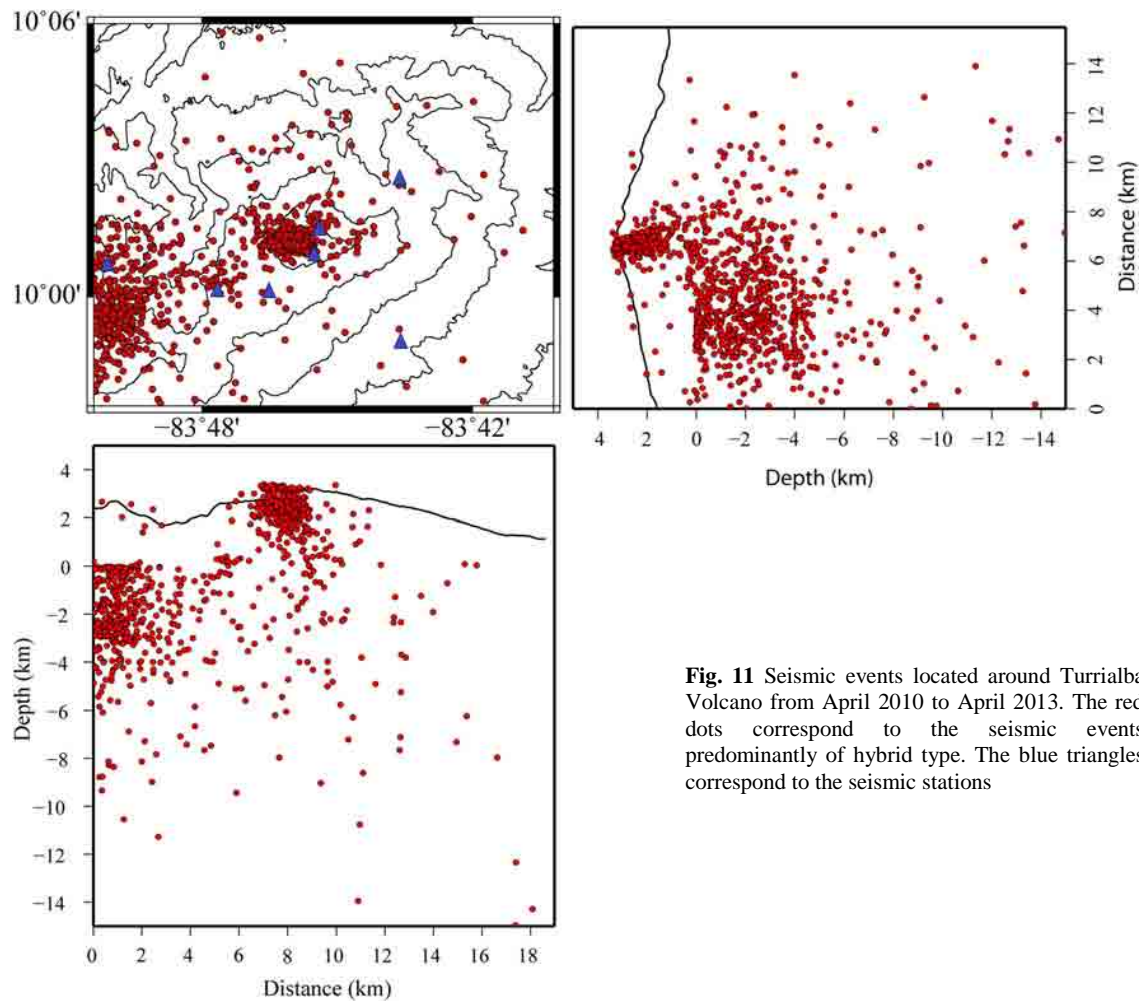
Fig. 11 Seismic events located around Turrialba Volcano from April 2010 to April 2013. The red dots correspond to the seismic events predominantly of hybrid type. The blue triangles correspond to the seismic stations

5. Discussion

5.1 Constraints on the Turrialba magma plumbing system

Based on seismic data, it is possible to constrain the upper part of the Turrialba magma plumbing system. Various seismic signals have in general been traced back to certain processes occurring within or adjacent to volcanic systems. LP, VLP and tremor events have been attributed to pressure transients within fluid-filled cracks and conduits and thus to the movement of low-viscosity magmas and their interaction with gas slugs (Chouet 2003; Rowe et al. 1998; James et al. 2006). VT events are higher-frequency signals caused by brittle failure of the wallrocks surrounding the plumbing system in response to stresses associated with magma movement (Shaw 1980). Hybrid events are composite signals intermediate between LP and VT (Lahr et al. 1994). From the clustering of localised seismic events (Fig. 11), we deduce two levels of magma storage, one probably at 4–6 km depth and the shallow one at roughly 1 km below the summit. This is also consistent with the estimates of Barboza et al. (2003) based on the localization of VT and hybrid events, and with the calculated source locations of LP events recorded in 2009 and 2011 (Eyre et al. 2013), which occurred at shallow depth (<500 m) between the western and central craters of Turrialba. This conceptual model of the magma plumbing system will be referred to in the remaining text. Further evidence for a complex magma plumbing system below Turrialba Volcano is provided by trace element analysis of pyroclastic rocks (Soto 1988; Reagan et al. 2006), though they state that the magma chambers are located at midcrustal and lower crustal levels, respectively.

69

_____

5.2 Cyclic variations in degassing rates, periodic replenishment and seismic origin

The cyclic variations in degassing rates and seismicity observed at Turrialba Volcano in 2010 and 2011 suggest that the two magma chamber levels that were identified from seismic data are periodically being replenished with relatively undegassed magma rising from greater depths. The lack of phase shift between SO_2 fluxes and LP seismicity observed by the correlation analysis is consistent with the assumption that the source location of LP events is at shallow depth. The coincidence between long-period seismicity and degassing has also been observed in other volcanoes. At Popocatépetl volcano, LP and VLP events accompanied explosions with rising ash plumes (Arciniega-Ceballos et al. 2008). At Shishaldin volcano (Aleutian Islands), an increase in the rate of occurrence of LP events was accompanied by a higher rate of observed puffs (Petersen et al. 2006). In contrast to the results obtained for LP events, the changes of the time shift between SO_2 emissions and tremor observed by the correlation analysis in 2010–2011 may indicate that the source location of tremor has been migrating. These results suggest that in June–July 2011, the source of tremor had reached a shallower level compared with the location in June–July 2010. Although tremor location is difficult to estimate, migration of tremor locations has been observed at Meakandake volcano during an active period (Ogiso and Yomogida 2012). However, further studies are required to estimate the dynamics behind these observations. Degassing from magma chambers can be achieved by conduit convection, a self-sustaining mechanism driven by density differences between degassed and undegassed magma (e.g. Kazahaya et al. 1994). However, degassing from a reservoir by buoyancy of gas slugs has been proposed as a supplementary mechanism for basaltic volcanoes (e.g. Gonnermann and Manga 2007). In any case, if we assume that SO_2 fluxes at Turrialba Volcano were solely supplied by degassing of non-erupted magma and that space in the upper part of the plumbing system is restricted, it is necessary that degassed magma drains from the upper reservoir to make space for buoyant undegassed magma entering from the deeper holding chamber. The longer period corresponds well with the fortnightly oscillations of the solid earth tides. Thus, the cyclic modulation of the degassing rates may potentially be assigned to pressure changes induced by earth tides, which thus influence magma replenishment to the Turrialba holding chamber (Fig. 12).

5.3 Chronology of degassing and seismic events

A comparison of the patterns of SO_2 emissions from 2008 to 2012 with the available seismic data has permitted us to distinguish sequential stages in volcanic activity at Turrialba right up to the last measurement reported in this paper (July 2012). As a starting point, the analysis of gas chemistry by Vaselli et al. (2010) indicates that the composition of fumarolic fluids by 2008—just after the NOVAC instruments were installed—had evolved from the hydrothermal to the magmatic type, providing evidence of rising
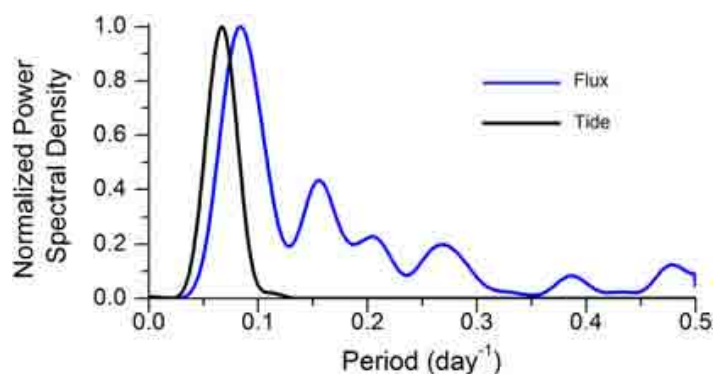

Fig. 12 Periodicity of SO_2 flux and the fortnightly solid earth tides. The power spectral density in both figures is computed by fast Fourier transform using a sampling frequency of 1 day for both time series and a Bartlett–Hanning window in order to minimise the spectral leakage

magma and/or progressive boiling and thus depletion of the hydrothermal water (Daag et al. 1996). This assumption is also supported by the opening of fissures in the summit region, formation of new fumaroles along these fissures and numerous rockslides.

During the emission baseline period, polarisation analyses of characteristic seismic low-frequency events indicate a comparatively deep source for a majority of these earthquakes (Martini et al. 2010). Although no continuous seismic time series data were available during the baseline period, it is very likely in the view of the rather stable emission rates that replenishment of fresh undegassed magma at depth was only sporadic.

From May to July 2009, the observed increase in SO_2 fluxes in parallel with the increase in RSAM counts and the subsequent detection of specks of juvenile materials may indicate sustained magma replenishment, and thus probably ascent of magma to the shallow storage level. The gradual increase in emissions was followed by a phase of sustained high and variable SO_2 fluxes (which is also visible in the low time-resolution flux data of Campion et al. 2012) preceding the phreatic eruptive event and several intermittent minor ash emissions during the following 2 years. The pulsating variations in gas discharge rates are most likely related to magma cycling by conduit convection and periodic injections of undegassed magma into the upper magma storage, in combination with an opening–sealing dynamic of the conduit by solidified magma and mineral precipitation on degassing pathways (Casadevall 1981).

When the continuous flux measurements were initiated again in April 2010, the SO_2 emissions had decreased in comparison with the values measured during the preeruptive period. The decrease in the SO_2 emissions following the eruptive event of January 2010 indicates that the magma located at the shallow level had partially degassed its SO_2 content. On the other hand, the high rate of LP and VLP seismic events observed during this period suggests that despite of diminishing gas content, the shallow magma was still in a low-viscosity state (Wassermann 2012).

The downward trend observed in the flux emissions through 2011 and 2012 was accompanied by a decrease in the amount of LP events and scarce VLP and VT events. This change in the seismic and degassing regime might indicate that the accumulated magma had exsolved enough gas to reach a phase of enhanced crystallisation and a higher viscosity. The solidification and/or increase in magma viscosity probably played a major role in order to avoid magma reaching the surface (e.g. Moran et al. 2011; Hammer et al. 2000). This assumption is reinforced by two ash explosions that took place in January 2012, which may have originated due to overpressure of the volatiles confined in the shallow magma chamber surrounded by viscous and/or cooled material (Tait et al. 1989). This explosive event did not change the decreasing tendency of SO_2 emissions, and seismicity still remained extremely low afterwards. Thus, intrusion of fresh magma from greater depth is unlikely to be the cause of this brief explosive period, though emanating incandescence from all three vents suggests that magma had indeed ascended closer to the surface. Accordingly, the magma supply rates from depth must have diminished at that stage.

5.4 Magma supply rate

The perpetuation of the gas flux at a constant level over such a long period of time can only be achieved by a sustained supply of fresh magma into the volcanic feeding system. The magma supply rate required to produce such gas fluxes can be deduced by combining the measured SO_2 emission rates with an estimate of the original magma sulphur content. Sulphur contents of glasses and melt inclusions in phenocrysts from Turrialba basaltic-andesite tephras were measured by electron microprobe analysis (Wehrmann, unpublished data). The earliest melt inclusions in olivine phenocrysts of Turrialba contain ~2,500 ppm S, whereas degassed melt inclusions and matrix glasses contain \300 ppm S. Similar sulphur contents were measured in melt inclusions of basaltic-andesitic tephras from Irazú volcano (e.g. Wehrmann et al. 2011; Benjamin et al. 2007).

With an estimate of 2,000 ppm S lost from the melt during decompression and a basalt density of 2.7 t m^{-3}, we calculate a magma supply rate of 0.38 ± 0.26 m^3 s^{-1}, which equates to the complete degassing of $33,000 \pm 23,000$ m^3 day^{-1} magma for a time-averaged SO_2 flux of 356 ± 246 t day^{-1} during the baseline phase of quiescent degassing. All along the period from April 2008 until April 2009 (before fluxes started to increase), this yields a cumulative amount of 0.01 ± 0.008 km^3 year^{-1} magma, which intruded into the system to account for the measured gas fluxes. During the following 3 years of enhanced activity (starting in May 2009 proceeding until May 2012) with a daily average of $1,111 \pm 936$ t day^{-1} SO_2 degassing from the

vent, the magma supply rate increased by a factor 3 if compared with the baseline period to 1.19 ± 1.00 $m^3 s^{-1}$, which translates to a total of 0.037 ± 0.031 $km^3 year^{-1}$.

6. Conclusions

Different stages of activity at Turrialba Volcano have been identified in this study combining SO_2 flux measurements and seismic data from a period of approximately 5 years. A relatively stable degassing period of approximately 1 year was followed by a conspicuously increasing trend preceding the phreatic eruptive event that occurred on 5 January 2010. In 2010, frequency and correlation analysis between SO_2 emissions and seismicity indicated the constant presence and repeated replenishment of magma at shallow depths. Further observations in 2011 and 2012 show a progressive decrease in the SO_2 emissions and seismicity, suggesting that magmas at shallow depth were largely degassed and/or the supply rate of fresh magma had diminished.

The last SO_2 flux measurements reported in this paper (July 2012) show values comparable to the baseline measured during the first period of measurements in 2008. Thus, this study indicates a cycle of more than 5 years with major activity changes. The evidence of a magma reaching shallow depths suggests that the observed activity changes at Turrialba Volcano could have led to a magmatic eruption during the last 3 years. However, despite all these signs, magma never reached the surface. Until our last measurements in July 2012, we can conclude that there is no evidence of a renewed degassing increase comparable to the one preceding the 2010 phreatic eruption. Nevertheless, degassing at Turrialba Volcano is still persistent, and its surveillance is highly recommended in what remains a period of potential volcanic crisis. This paper demonstrates the potential for permanent DOAS instruments to monitor degassing activity at Turrialba and similarly active volcanoes, complementing traditional methods of seismic surveillance with the purpose of volcanic hazard mitigation.

References

Arciniega-Ceballos A, Chouet B, Dawson P, Asch G (2008) Broadband seismic measurements of degassing activity associated with lava effusion at Popocatépetl Volcano, Mexico. J Volcanol Geoth Res 170(1–2):12–23

Arellano SR, Hall M, Samaniego P, Le Pennec JL, Ruiz A, Molina I, Yepes H (2008) Degassing patterns of Tungurahua volcano (Ecuador) during the 1999–2006 eruptive period, inferred from remote spectroscopic measurements of SO_2 emissions. J Volcanol Geoth Res 176(1):151–162

Barboza V, Fernandez E, Duarte E, Sa´enz W, Martı´nez M, Moreno N, Marino T, Van der Laat R, Herna´ndez E, Malavassi E, Valde´s J (2003) Changes in the activity of Turrialba Volcano: seismicity, geochemistry and deformation. 8th IAVCEI Gas Workshop, Nicaragua and Costa Rica

Benjamin ER, Plank T, Wade JA, Kelley KA, Hauri EH, Alvarado GE (2007) High water contents in basaltic magmas from Irazú Volcano, Costa Rica. J Volcanol Geoth Res 168(1–4):68–92. doi:10.1016/j.jvolgeores.2007.08.008

Bredemeyer S, Hansteen TH, Garofalo K, Mora Stock C, Rabbel W, Gil Cruz F (2011) Remote sensing of thermal emission and degassing at Villarrica Volcano, Chile. Paper presented at the AGU Fall Meeting 2011, Abstract ID: V44C-02, San Francisco, California, USA

Brooks B-G (2011) Earth Scientist's guide to discrete-time power spectrum analysis. inTech (Fourier transforms—new analytical approaches and FTIR strategies). doi:10.5772/16113

Burton MR, Caltabiano T, Mure` F, Salerno G, Randazzo D (2009) SO_2 flux from Stromboli during the 2007 eruption: results from the FLAME network and traverse measurements. J Volcanol Geoth Res 182(3–4):214–220. doi:10.1016/j.jvolgeores.2008.11. 025

Campion R, Martinez-Cruz M, Lecocq T, Caudron C, Pacheco J, Pinardi G, Hermans C, Carn S, Bernard A (2012) Space- and ground-based measurements of sulphur dioxide emissions from Turrialba Volcano (Costa Rica). Bull Volcanol 74(7):1757–1770. doi:10.1007/s00445-012-0631-z

Casadevall TJ (1981) The 1980 eruptions of Mount St. Helens, Washington. SO_2 emission rates at Mount St. Helens from March 29 through December 1980. US Geol Surv Prof Pap 1250:193–200

Casadevall T, Rose W, Gerlach T, Greenland LP, Ewert J, Wunderman R, Symonds R (1983) Gas emissions and the eruptions of Mount St. Helens through 1982. Science 221(4618):1383–1385. DOI:10.1126/science.221.4618.1383

Chouet B (2003) Volcano seismology. Pure Appl Geophys 160(3–4):739–788. DOI: 10.1007/PL00012556

Christopher T, Edmonds M, Humphreys MCS, Herd RA (2010) Volcanic gas emissions from Soufrie`re Hills Volcano, Montserrat 1995–2009, with implications for mafic magma supply and degassing. Geophys Res Lett 37(19):L00E04. doi:10.1029/2009GL041325

Daag A, Tubianosa B, Newhall C, Tun˜gol N, Javier D, Dolar M, De los Reyes P, Arboleda R, Martinez M, Regalado M (1996) Monitoring sulfur dioxide emission at Mount Pinatubo. Fire and mud: eruptions and Lahars of Mount Pinatubo Philippines Institute of Volcanology and Seismology, and University of Washington press, pp 409–414

Edmonds M, Herd RA, Galle B, Oppenheimer CM (2003) Automated, high time resolution measurements of SO_2 flux at Soufrière Hills Volcano, Montserrat. Bull Volcanol 65(8):578–586

Endo ET, Murray T (1991) Real-time seismic amplitude measurement (RSAM): a volcano monitoring and prediction tool. Bull Volcanol 53(7):533–545

Eyre TS, Bean CJ, De Barros L, O'Brien GS, Martini F, Lokmer I, Mora MM, Pacheco JF, Soto GJ (2013) Moment tensor inversion for the source location and mechanism of long period (LP) seismic events from 2009 at Turrialba volcano, Costa Rica. J Volcanol Geoth Res 258:215–223. doi:10.1016/j.jvolgeores. 2013.04.016

Galle B, Johansson M, Rivera C, Zhang Y, Kihlman M, Kern C, Lehmann T, Platt U, Arellano SR, Hidalgo S (2010) Network for observation of volcanic and atmospheric change (NOVAC)—a global network for volcanic gas monitoring: network layout and instrument description. J Geophys Res 115(D5):D05304. doi:10.1029/2009jd011823

Gonnermann HM, Manga M (2007) The fluid mechanics inside a volcano. Annu Rev Fluid Mech 39(1):321–356. doi:10.1146/annurev.fluid.39.050905.110207

Grutter M, Basaldud R, Rivera C, Harig R, Junkerman W, Caetano E, Delgado-Granados H (2008) SO_2 emissions from Popocatèpetl volcano: emission rates and plume imaging using optical remote sensing techniques. Atmos Chem Phys 8(22):6655–6663

Hammer JE, Cashman KV, Voight B (2000) Magmatic processes revealed by textural and compositional trends in Merapi dome lavas. J Volcanol Geoth Res 100(1–4):165–192. doi:10.1016/S0377-0273(00)00136-0

Hoff RM, Millan MM (1981) Remote SO_2 mass flux measurements using COSPEC. J Air Pollut Control Assoc 31(4):381–384

James MR, Lane SJ, Chouet BA (2006) Gas slug ascent through changes in conduit diameter: laboratory insights into a volcano seismic source process in low-viscosity magmas. Journal of Geophysical Research B: Solid Earth 111(5). doi:10.1029/2005jb003718

Johansson M (2009) Application of passive DOAS for studies of megacity air pollution and volcanic gas emissions. PhD thesis Chalmers University of Technology

Johansson M, Galle B, Zhang Y, Rivera C, Chen D, Wyser K (2009) The dual-beam mini-DOAS technique—measurements of volcanic gas emission, plume height and plume speed with a single instrument. Bull Volcanol 71(7):747–751. doi:10.1007/s00445-008-0260-8

Kazahaya K, Shinohara H, Saito G (1994) Excessive degassing of Izu-Oshima volcano: magma convection in a conduit. Bull Volcanol 56(3):207–216. doi:10.1007/bf00279605

Kern C (2009) Spectroscopic measurements of volcanic gas emissions in the ultra-violet wavelength region. PhD thesis, Univ. Of Heidelberg, Heidelberg, Germany

Kern C, Deutschmann T, Vogel L, Wo¨hrbach M, Wagner T, Platt U (2010) Radiative transfer corrections for accurate spectroscopic measurements of volcanic gas emissions. Bull Volcanol 72(2):233–247

Kraus N (2004) DOASIS: DOAS intelligent system. Available from http://doasis.iup.uni-heidelberg.de

Lahr JC, Chouet BA, Stephens CD, Power JA, Page RA (1994) Earthquake classification, location, and error analysis in a volcanic environment: implications for the magmatic system of the 1989–1990 eruptions at redoubt volcano, Alaska. J Volcanol Geoth Res 62(1–4):137–151

Martini F, Tassi F, Vaselli O, Del Potro R, Martinez M, del Laat RV, Fernandez E (2010) Geophysical, geochemical and geodetical signals of reawakening at Turrialba volcano (Costa Rica) after almost 150 years of quiescence. J Volcanol Geoth Res 198(3–4):416–432

Moran S, Newhall C, Roman D (2011) Failed magmatic eruptions: late-stage cessation of magma ascent. Bull Volcanol 73(2):115–122. doi:10.1007/s00445-010-0444-x

Mori T, Mori T, Kazahaya K, Ohwada M, Hirabayashi J, Yoshikawa S (2006) Effect of UV scattering on SO_2 emission rate measurements. Geophys Res Lett 33(L17315). doi:10.1029/2006GL026285

Nadeau PA, Palma JL, Waite GP (2011) Linking volcanic tremor, degassing, and eruption dynamics via SO_2 imaging. Geophys Res Lett 38(L01304). doi:10.1029/2010GL045820

Ogiso M, Yomogida K (2012) Migration of tremor locations before the 2008 eruption of Meakandake Volcano, Hokkaido, Japan. J Volcanol Geoth Res 217–218:8–20

Olmos R, Barrancos J, Ivera CR, Barahona F, Lo´pez DL, Henriquez B, Herna´ndez A, Benitez E, Herna´ndez PA, Pe´rez NM, Galle BO (2007) Anomalous emissions of SO_2 during the recent eruption of Santa Ana volcano, El Salvador, Central America. Pure Appl Geophys 164(12):2489–2506

Palma JL, Calder ES, Basualto D, Blake S, Rothery DA (2008) Correlations between SO_2 flux, seismicity, and outgassing activity at the open vent of Villarrica volcano, Chile. J Geophys Res Solid Earth 113(B10):B10201. doi:10.1029/2008JB005577

Petersen T, Caplan-Auerbach J, McNutt SR (2006) Sustained longperiod seismicity at Shishaldin Volcano, Alaska. J Volcanol Geoth Res 151(4):365–381

Platt U, Stutz J (2008) Differential optical absorption spectroscopy (DOAS), principle and applications. Springer, Heidelberg. doi:10.1007/978-3-540-75776-4

Reagan M, Duarte E, Soto GJ, Fernández E (2006) The eruptive history of Turrialba volcano, Costa Rica, and potential hazards from future eruptions. Volcan Hazards Central America 412:235

Reagan M, Rowe M, Duarte E, Hernandez E (2011) Juvenile glass fragments in phreatic explosion debris from Turrialba Volcano, Costa Rica. Paper presented at the Goldschmidt Conference, Mineralogical Magazine, 75(3), Prague, 2011

Rivera C, Garcia JA, Galle B, Alonso L, Yan Z, Johansson M, Matabuena M, Gangoiti G (2009) Validation of optical remote sensing measurement strategies applied to industrial gas emissions. Int J Remote Sens 30(12):3191–3204. doi:10.1080/01431160802558808

Rowe CA, Aster RC, Kyle PR, Schlue JW, Dibble RR (1998) Broadband recording of Strombolian explosions and associated very-long-period seismic signals on Mount Erebus volcano, Ross Island, Antarctica. Geophys Res Lett 25(13):2297–2300

Salerno GG, Burton MR, Oppenheimer C, Caltabiano T, Randazzo D, Bruno N, Longo V (2009) Three-years of SO_2 flux measurements of Mt. Etna using an automated UV scanner array: comparison with conventional traverses and uncertainties in flux retrieval. J Volcanol Geoth Res 183(1–2):76–83. doi:10.1016/j. jvolgeores.2009.02.013

Shaw H (1980) Fracture mechanism of magma transport from the mantle to the surface. In: Hargraves RB (ed) Physics of magmatic processes. Princeton University Press, Princeton, pp 201–264

Smithsonian-Institution (2012) http://www.volcano.si.edu/volcano. cfm?vn=345070

Soto G (1988) Estructuras volcano-tectónicas del Volcán Turrialba, Costa Rica, America Central. Actas Quinto Congreso Geológico Chileno- Santiago, 8–12 de Agosto de 1988 Tomo III:163–175

Stoiber RE, Williams SN, Malinconico LL (1980) Mount St. Helens, Washington, 1980 volcanic eruption: magmatic gas component during the first 16 days. Science 208(4449):1258–1259

Symonds R, Rose WI, Bluth GJS, Gerlach TM (1994) Volcanic-gas studies; methods, results, and applications. Rev Mineral Geochem 30(1):1–66

Tait S, Jaupart C, Vergniolle S (1989) Pressure, gas content and eruption periodicity of a shallow, crystallising magma chamber. Earth Planet Sci Lett 92(1):107–123

Tassi F, Vaselli O, Barboza V, Fernandez E, Duarte E (2004) Fluid geochemistry and seismic activity in the period of 1998–2002 at Turrialba Volcano (Costa Rica). Ann Geophys 47(4):1501–1511

Vandaele AC, Simon PC, Guilmot JM, Carleer M, Colin R (1994) SO_2 absorption cross section measurement in the UV using a Fourier transform spectrometer. J Geophys Res 99(D12):25,599–525605

Vaselli O, Tassi F, Duarte E, Fernandez E, Poreda RJ, Huertas AD (2010) Evolution of fluid geochemistry at the Turrialba volcano (Costa Rica) from 1998 to 2008. Bull Volcanol 72(4):397–410

Voigt S, Orphal J, Bogumil K, Burrows JP (2001) The temperature dependence (203–293 K) of the absorption cross sections of O_3 in the 230–850 nm region measured by Fourier-transform spectroscopy. J Photochem Photobiol, A 143(1):1–9

Wassermann J (2012) Volcano Seismology. In: Bormann P (ed) New manual of seismological observatory practice 2 (NMSOP-2), vol 2. Deutsches GeoForschungsZentrum GFZ, Potsdam, pp 1–77. doi:10.2312/GFZ.NMSOP-2_ch13

Wehrmann H, Hoernle K, Portnyagin M, Wiedenbeck M, Heydolph K (2011) Volcanic CO2 output at the Central American subduction zone inferred from melt inclusions in olivine crystals from mafic tephras. Geochem Geophys Geosyst 12(Q06003). doi:10.1029/2010GC003412
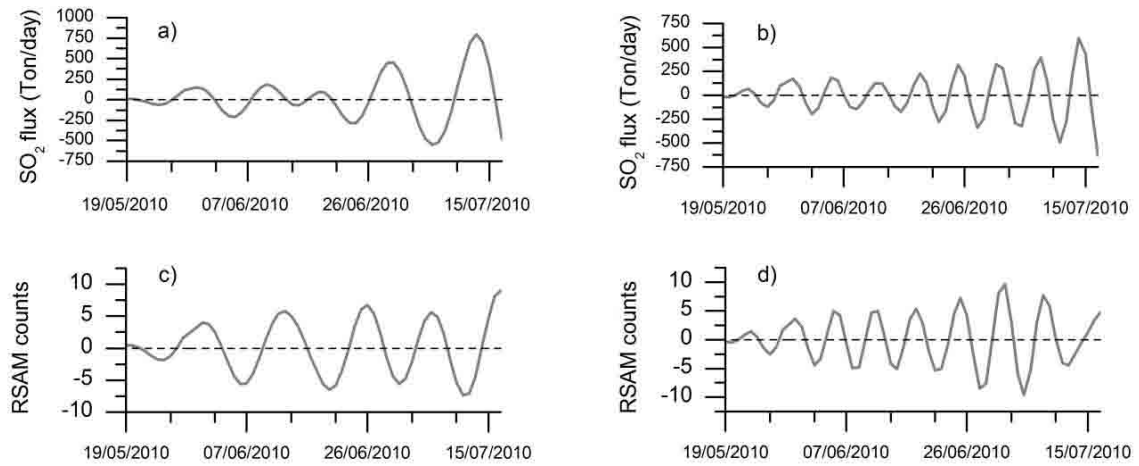
Fig.S1 Separated contribution of tremor and LP to the SO$_2$ and RSAM time series during June to July 2010. (a) tremor-SO$_2$, (b) LP- SO$_2$, (c) tremor-RSAM, (d) LP-RSAM. See text for details and discussion
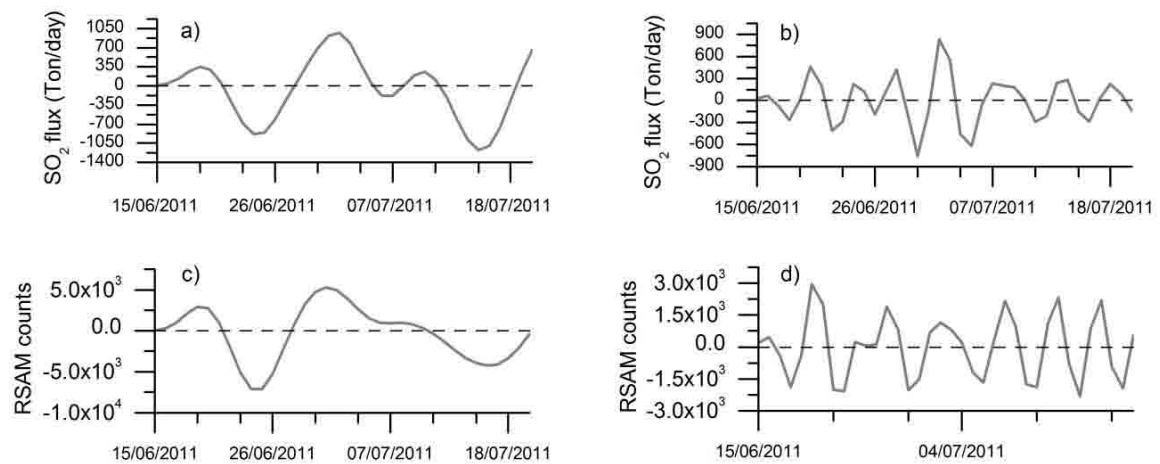

Fig.S2 Separated contribution of tremor and LP to the SO$_2$ and RSAM time series during June to July 2011. (a) tremor-SO$_2$, (b) LP- SO$_2$, (c) tremor-RSAM, (d) LP-RSAM. See text for details and discussion

CHAPTER IV

Linking SO₂ emission rates and seismicity by continuous wavelet transform: implications for volcano surveillance at San Cristóbal Volcano, Nicaragua

Linking SO₂ emission rates and seismicity by continuous wavelet transform: implications for volcanic surveillance at San Cristóbal volcano, Nicaragua

Vladimir Conde[1] · Stefan Bredemeyer[2] · J. Armando Saballos[3] · Bo Galle[1] · Thor H. Hansteen[4]

Abstract San Cristóbal volcano is the highest and one of the most active volcanoes in Nicaragua. Its persistently high activity during the past decade is characterized by strong degassing and almost annual VEI 1–2 explosions, which present a threat to the local communities. Following an eruption on 8 September 2012, the intervals between eruptions decreased significantly, which we interpret as the start of a new eruptive phase. We present here the results of semi-continuous SO_2 flux measurements covering a period of 18 months, obtained by two scanning UV-DOAS instruments installed as a part of the network for observation of volcanic and atmospheric change project, and the results of real-time seismic amplitude measurements (RSAM) data. Our data comprise a series of small to moderately explosive events in December 2012, June 2013 and February 2014, which were accompanied by increased gas emissions and seismicity. In order to approach an early warning strategy, we present a statistical method for the joint analysis of gas flux and seismic data, by using continuous wavelet transform and cross-wavelet transform (XWT) methods. This analysis shows that the XWT coefficients of SO_2 flux and RSAM are in good agreement with the occurrence of eruptive events and thus may be used to indicate magma ascent into the volcano edifice. Such multi-parameter surveillance efforts can be useful for the interpretation and surveillance of possible eruptive events and could thus be used by local institutions for the prediction of upcoming volcanic unrest.

Vladimir Conde conde@chalmers.se
Stefan Bredemeyer sbredemeyer@geomar.de
J. Armando Saballos armando.saballos@gf.ineter.gob.ni
Bo Galle bo.galle@chalmers.se
Thor H. Hansteen thansteen@geomar.de

[1] Department of Earth and Space Sciences, Chalmers University of Technology, Hörsalsvägen 11, 412 96 Gothenburg, Sweden
[2] SFB 574 and GEOMAR Helmholtz Centre for Ocean Research Kiel, Wischhofstr. 1‑3, 24118 Kiel, Germany
[3] Instituto Nicaragüense de Estudios Territoriales (INETER), Apdo., 2110 Managua, Nicaragua
[4] GEOMAR Helmholtz Centre for Ocean Research Kiel, Wischhofstr. 1‑3, 24118 Kiel, Germany

1. Introduction

Surveillance of volcanoes is fundamental for hazard assessment and mitigation prior to and during periods of volcanic crisis. During the last decades, significant progress has been achieved on this issue through the deployment of a diversity of multi-parameter surveillance methods. Seismicity is still considered one of the most reliable parameters for monitoring volcanic activity; hence, it is probably the most popular monitoring tool used by volcanologists (e.g. Tilling 2008; D'Alessandro et al. 2013). Volcanic gas emissions also play an important role in volcanic surveillance (e.g. Casadevall et al. 1983; Symonds et al. 1994; Burton et al.

2007) since eruptions are often heralded by increases in volcanic SO_2 emissions, which originate from the ascent of fresh magma to shallower crustal levels (e.g. Daag et al. 1996).

Measuring sulphur dioxide (SO_2) emissions has been successfully achieved using ground-based remote sensing techniques such as the correlation spectrometer (COSPEC; Hoff and Millan 1981), differential optical absorption spectroscopy (DOAS; Platt and Stutz 2008) and more recently SO_2 cameras (Mori and Burton 2006; Bluth et al. 2007). Mobile and scanning DOAS are among the most commonly used approaches for volcanic gas measurements (Galle et al. 2002; Edmonds et al. 2003; Platt and Stutz 2008; Burton et al. 2009; Boichu et al. 2010; Galle et al. 2010). The network for observation of volcanic and atmospheric changes (NOVAC) project is monitoring SO_2 emissions of about 20 volcanoes around the world using scanning DOAS instruments (NOVAC instruments; Galle et al. 2010). This instrumental set-up has produced a wealth of semi-continuous SO_2 flux measurements and thus allows for near-real-time side-to side evaluation of SO_2 emissions with other data set, e.g. with seismic signals. The potential of combining seismic and SO_2 measurements as a surveillance tool has been demonstrated for different scenarios (e.g. Petersen et al. 2006; Olmos et al. 2007; Nadeau et al. 2011; Conde et al. 2013; Waite et al. 2013; Hidalgo et al. 2015). The recently enhanced activity at San Cristóbal provides a suitable case study for conducting a joint analysis of seismic and gas measurements by using cross-wavelet transform (XWT), which is a technique aimed to locate the temporal occurrence of significant spikes and oscillations that may help to ascertain the underlying processes leading to eruptive events.

2. Background

San Cristóbal volcano is a 1745 m high basaltic-to-andesitic stratovolcano located in north western Nicaragua approximately 15 km north-east of the city of Chinandega (12.70°N 87.0°W; Fig. 1). Volcanic activity at San Cristóbal is characterized by a persistently strong open-vent and fumarolic degassing, as stated by previous studies summarized in Table 1 (Mather et al. 2006; Barrancos et al. 2008; Rivera et al. 2009; Fischer von Mollard 2013). San Cristóbal volcano exhibits cyclical transitions between periods of quiescent degassing and substantial increases in gas emissions during the onset of eruptive events that are mostly characterized by minor-to-moderate explosions accompanied by ash fallout. These transitions have occurred at a higher rate during the last 2 years with VEI 1–VEI 2 eruptive events occurring approximately twice a year (Smithsonian-Institution 2014).

3. Methodology

3.1 SO_2 flux measurements

SO_2 flux measurements were made by two NOVAC instruments installed on the west flank of San Cristóbal volcano (Fig. 1). The instrument acquires UV-scattered sunlight spectra by scanning along a vertical plane spanning 180° from one horizon to the other in angular steps of 3.6°. The principal component is a spectrometer (Ocean Optics®, S2000), which operates in the wavelength range 280–425 nm divided into 2048 channels yielding a spectral resolution of approximately 0.6 nm. The instrument runs during daylight hours, and the signal-to-noise ratio is improved by adding 15 spectra and adjusting automatically the exposure time in order to avoid light saturation in the spectrometer detector.

The SO_2 column amount was retrieved from the spectra for each angular step, applying DOAS in the wavelength region of 310–322 nm (Platt and Stutz 2008), where the SO_2 absorption cross section still has a pronounced signature and low sensitivity to scattering and stray light (Johansson 2009; Galle et al. 2010). More advanced details about the NOVAC instruments and column retrievals are described in Galle et al. (2010) and Edmonds et al. (2003).
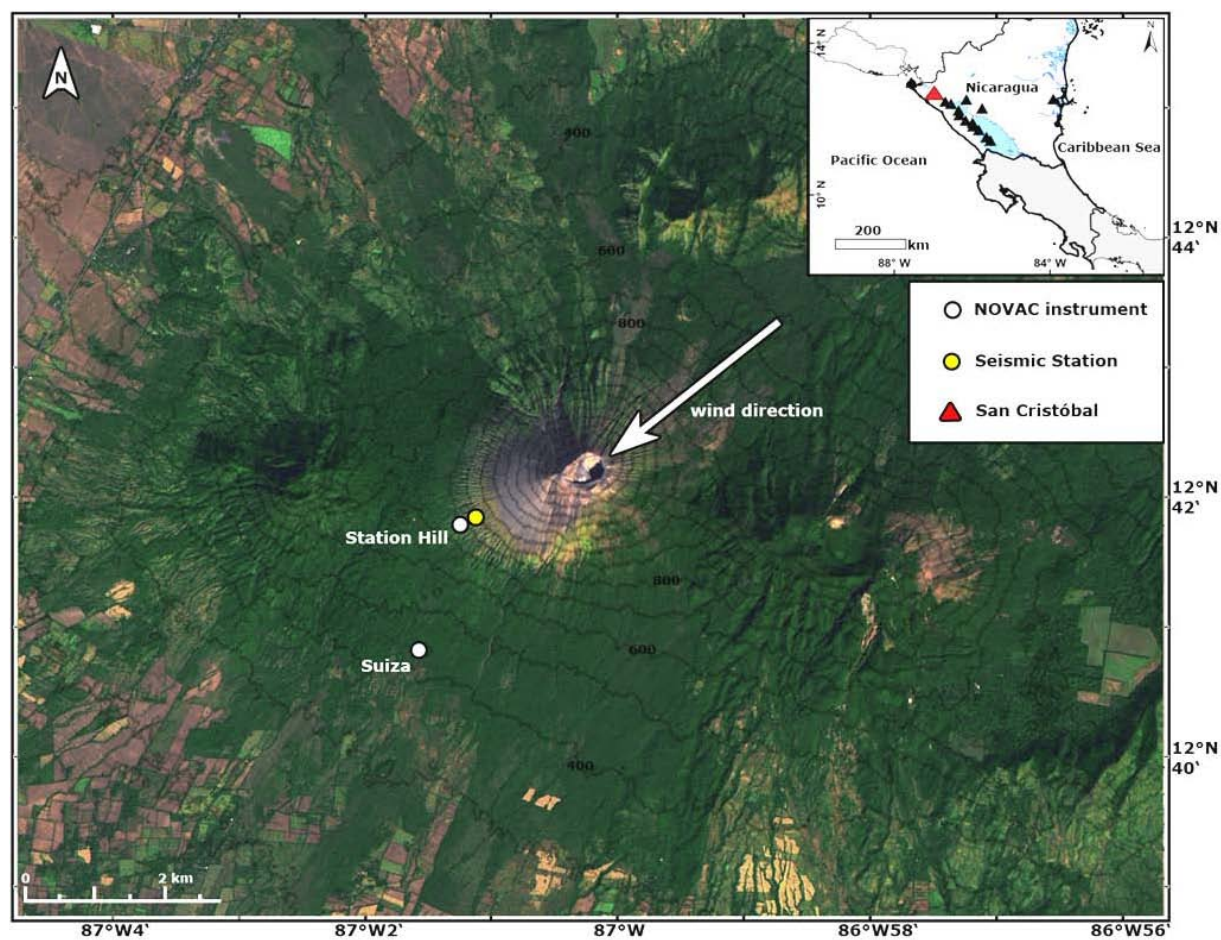
Fig. 1 Map showing the location of the NOVAC instruments and the seismic station on the south-western flank of San Cristóbal volcano. The map is based on a composite of spectral bands from Landsat 8 scene LC80170512014016LGN00 (16 January 2014) available from the US Geological Survey (https://lta.cr.usgs.gov/L8). *Inset* map of the volcanic arc in Nicaragua (*black triangles*)

Table 1 Compilation of previous SO$_2$ emission measurements at San Cristóbal volcano

Date	SO$_2$ flux (t day^{-1})	References
November 2003	800 ± 190	Mather et al. (2006)
March 2006	317 ± 274	Barrancos et al. (2008)
November 2006	1406 ± 805	Rivera (2009)
2007	515 ± 517	Fischer von Mollard (2013)
2008	244 ± 203	Fischer von Mollard (2013)
2009	1515 ± 891	Fischer von Mollard (2013)
2010	893 ± 727	Fischer von Mollard (2013)
2011	627 ± 235	Fischer von Mollard (2013)
2012	1489 ± 671	Fischer von Mollard (2013)

In order to determine the SO$_2$ flux, geometric information of the plume is required in addition to the gas columns as shown in Eq. (1) from Hoff and Millan (1981).

$$Flux = W_s \times |\cos (W_d - compass)| \times P_H \times \sum_{i=0}^{N-1} |\tan \alpha_{i+1} - \tan \alpha_i| \times VCD_i \qquad (1)$$

_____

where VCD_i is the SO_2 vertical columns density estimated at the angular step α_i, which corresponds to the angle between the column and the zenith. W_s and W_d are the wind speed and plume direction at the plume height (P_H), and *compass* is the direction perpendicular to the plane of scanning.

The plume at San Cristóbal volcano usually bends over shortly after leaving the crater; thus, P_H was assumed to be the same as the crater height (1745 m.a.s.l.), while the plume direction was geometrically calculated by combining plume height and the scanning angles α which show the strongest absorption. The plume (wind) speed was obtained from the weather forecast model GFS provided by the National Oceanic and Atmospheric Administration (NOAA), which has a grid length of 1° and a time resolution of 3 h.

The uncertainty of the flux measurements using DOAS results from a combination of various error sources including spectroscopy, local weather conditions and inaccuracies in the estimation of the plume geometry. Previous studies have provided a statistical approach in order to quantify the measurement error, whereas the modelled wind speed has been identified as the predominant error source accounting for an uncertainty of 20–30 % (e.g. Mather et al. 2006; Rivera et al. 2009; Galle et al. 2010).

Considering the proximity of the instruments to the emission source and the very well-defined plume signatures in most of the scans, the estimated total measurement error at San Cristóbal volcano is assumed to be 35 % under optimal weather conditions. The sampling period is not uniform since the exposure time is automatically adjusted depending on the visibility conditions; thus, under clear sky conditions it is possible to acquire up to 60 measurements per day. However, having an uneven sampling rate prevents the application of the data analysis methods which will be further discussed in the following sections. Due to the limitations imposed by the uneven sampling rate and the impossibility of perform measurements during nighttime, our SO_2 flux time series is portrayed as the daily average of the gas emissions and its respective daily standard deviation.

3.2 SO_2 flux pre‑processing

The daily average of the SO_2 flux can be a good approximation of the flux evolution through time, while the variability of the standard deviation is caused by a combination of several parameters including transient eruptive events, the random nature of the degassing processes and atmospheric perturbations. In order to obtain a better estimation of the underlying long-term SO_2 emissions, a common mathematical approach is to smooth the time series using the Kalman filter (Kalman 1960), which has been successfully applied for data estimation of geophysical measurements (e.g. Anderson 2001; Evensen 2003; Nagarajan et al. 2012; Yan et al. 2014). In contrast to traditional filtering techniques, which are based on the removal of "undesired components", the Kalman filter assumes a state-space (time) model estimator and explicitly accounts for measurement and modelling error as described by the following equations:

$$X_n = X_{n-1} + W_n \qquad (2a)$$

$$W_n \sim N(0, Q_n) \qquad (2b)$$

$$Y_n = X_n + V_n \qquad (3a)$$

$$V_n \sim N(0, R_n) \qquad (3b)$$

Equation (2) corresponds to the current estimate of the time-dependent process X_n, which in this case corresponds to the daily flux. The estimate of X_n is based on the previous estimate X_{n-1} and the expected variability W_n with a variance of Q_n. This estimator is termed the random walk model (RWM), which despite its simplicity has been demonstrated to be a good estimator in other atmospheric measurements scenarios (Mulquiney et al. 1995). Similarly, Eq. (3) models the estimate of X_n and its respective measurement error V_n with a variance of R_n.

The Kalman filter is implemented by means of a recursive sequence of two steps: estimation and correction. In accordance with the RWM, the estimation step is described by Eq. (4) as follows:

$$\hat{X}_n^- = \hat{X}_{n-1} \qquad (4a)$$

$$\hat{P}_n^- = \hat{P}_{n-1} + Q_{n-1} \qquad\qquad (4b)$$

where $\hat{X}_n^-$ and $\hat{P}_n^-$ correspond to model-estimated flux and variance, respectively. The most difficult aspect of assuming a RWM is a realistic estimate of the expected variability W_n. However, we have considered a statistical approach, as illustrated in Myers and Tapley (1976), where the flux variance Q_n during a period of 1 day can be assumed to be a suitable approximation of the expected variability. The correction step, described by Eq. (5), links the previously estimated parameters with the actual flux measurements Y_n based on the measurement model previously described in Eq. (3).

$$K_n = \frac{\hat{P}_n^-}{\hat{P}_n^- + R_n} \qquad\qquad (5a)$$

$$\hat{X}_n = \hat{X}_n^- + K_n\,(Y_n - \hat{X}_n^-) \qquad\qquad (5b)$$

$$\hat{P}_n = (1 - K_n)\hat{P}_n^- \qquad\qquad (5c)$$

where K_n corresponds to the so-called Kalman gain (Welch and Bishop 1995) and the error variance R_n is akin to the previously estimated flux measurement error of 35 %. $\hat{X}_n$ and $\hat{P}_n$ are the updated–estimated flux and variance, respectively, which correspond to the Kalman "filtered" values and the initial parameters for the next iteration (Eq. 4). For simplicity, the initial conditions of the algorithm are $\hat{X}_0 = Y_0$ and $\hat{P}_0 = 0$. A comparison of the Kalman estimated SO_2 flux versus the individual daily SO_2 flux measurement during a selected period of 4 months at San Cristóbal volcano is displayed in Fig. 2 where it is shown that smoothing the time series by means of a Kalman filter provides a balanced trade-off between the signal trend and its natural variability. A more general description of the recursive estimator–corrector Kalman Filter algorithm can be found elsewhere (e.g. Myers and Tapley 1976; Mulquiney et al. 1995; Welch and Bishop 1995).

3.3 Seismic data

Real-time seismic amplitude measurements (RSAM; Endo and Murray 1991) were calculated from measurements of the three-component broadband station CRIN that belongs to the seismic network of Instituto Nicaragüense de Estudios Territoriales (INETER) and is located on the southwestern flank of the volcano (Fig. 1). Each individual RSAM measurement corresponds to the average value of the seismic amplitude during 10 min; however, the averaging time was increased up to 1 day in order to make it coherent with the daily sampling rate of the SO_2 flux. The RSAM time series was pre-processed using a Kalman filter algorithm with the same approach as the one described in the previous section.
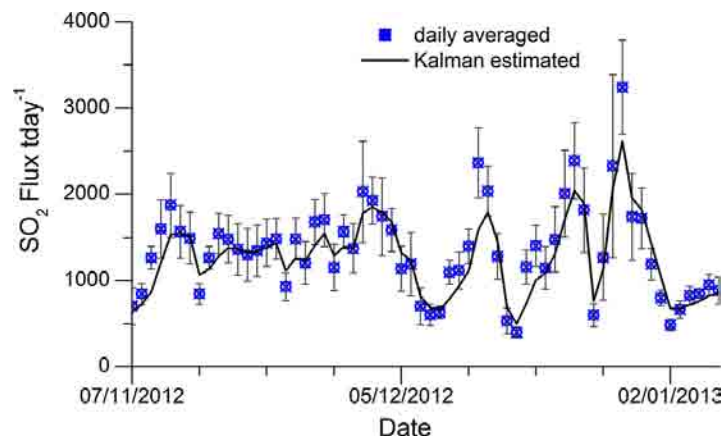

Fig. 2 Comparison between daily average SO_2 fluxes and the Kalman estimated fluxes from November 2012 to January 2013

3.4 Wavelet analysis

Several methods can be applied in order to perform a joint analysis of volcanic SO_2 fluxes and RSAM. Some classical approaches such as cross-correlations and Fourier transform may produce acceptable results when considering time series with short-time windows and some degree of stationarity. However, through extended periods of analysis, the underlying volcanic processes exhibit transient changes, which are associated with variations in the eruptive regime and are reflected in discontinuities of the spectral characteristics of the both SO_2 fluxes and RSAM time series. Continuous wavelet transform (CWT) is a mathematical tool that achieves to resolve both stationary and transient changes in a signal. It decomposes a time series into time–frequency components allowing time localization of spectral characteristics that are statistically significant during a particular period. Due to the non-stationary nature of many geophysical and atmospheric systems, several studies have applied this time-series analysis technique, e.g. in climatology and astrophysics (e.g. Kestin et al. 1998; Torrence and Webster 1999; De Moortel et al. 2000; Mwale and Gan 2005; Wang and Gao 2013).

In simplified words, a wavelet $\psi(n/s)$ is a finite energy function that resembles a short oscillation, which can be time translated and scale compressed or expanded. The mathematical basis and details concerning the choice and design of wavelet functions are out of the scope of this article and can be found elsewhere (e.g. Daubechies 1990; Weng and Lau 1994; Lau and Weng 1995); however, out of several possible wavelet functions, this article examines the performance of four popular wavelets: the complex wavelets Morlet and Paul and the real wavelets derivative of Gaussian (DOG) of m-th order DOG ($m = 2$) and DOG ($m = 6$) as shown in Fig. 3.

The CWT $W_n(s)$ can be defined as the convolution of the time series X_n with a scaled wavelet function $\psi(n/s)$.

$$W_n(s) = \sum_{n=0}^{N-1} X_t \psi \left[\frac{n'-n}{s} \delta_t \right] \qquad (6)$$

where δ_t is the sampling period and s is the CWT scale (period). The spectral decomposition is achieved by discretely compressing and/or expanding the scale s prior to performing the convolution. One of the most important criteria concerning the choice of wavelet is the trade-off between time and frequency resolution. In this regard, the Morlet wavelet is highly popular in geophysical applications due to its well-balanced proportion between these two parameters (Torrence and Compo 1998). However, for applications that aim at an enhanced period–frequency resolution the Paul wavelet may be a better choice. The outcome of $W_n(s)$ is an array of coefficients distributed according to their corresponding timescale, normally displayed as a contour or temperature map where the amplitudes of the wavelet coefficients (W_n) are plotted at their respective period (or frequency) and time. Figure 4 shows a comparison between the CWT for SO_2 flux measurements at San Cristóbal volcano during a period of 4 month using Morlet and Paul wavelets.

The statistical significance of the coefficient amplitudes was calculated, assuming that their spectral properties depict increased amplitude at lower frequencies. This spectral feature that is commonly observed in geophysical time series is normally referred as red noise and can be modelled by a stochastic first-order autoregressive (AR1) process (Allen and Smith 1996). A typical assumption is to consider that the statistical significance of wavelets coefficients is 5 % (95 % confidence level) against red noise (Grinsted et al. 2004).

The XWT is just an extension of the CWT for performing a joint analysis of two time series by the conjugate product ($*$) of their CWT, as shown in Eq. (7).

$$W_n (s)^{xy} = W_n (s)^x W_n (s)^{y*} \qquad (7)$$

Unlike traditional correlation methods, XWT allows to correlate common spectral–amplitude signatures of a pair of signals at localized periods, and thus, it can be used to detect transient association between both signals. Further details of the implementation of the CWT, XWT and the 5 % statistical significance can be found in Torrence and Compo (1998) and Grinsted et al. (2004), respectively.
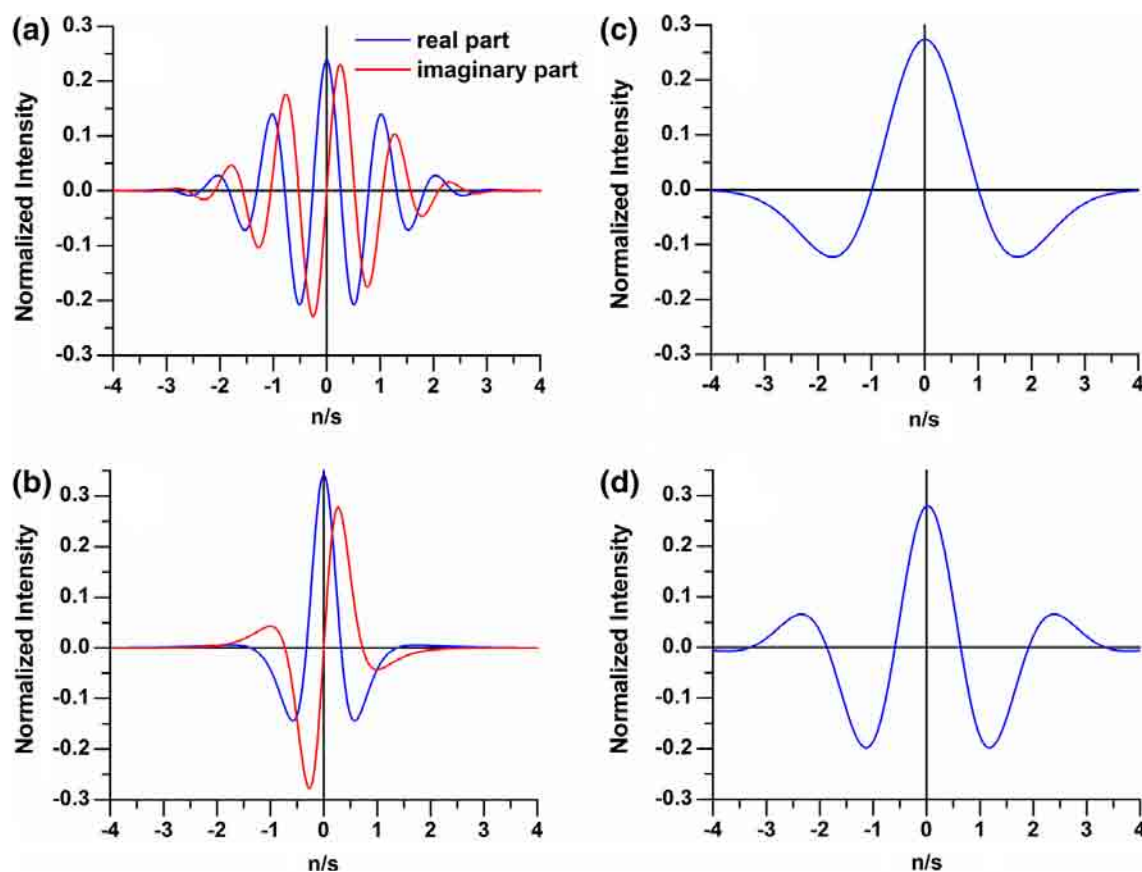
Fig. 3 Normalised mother wavelets $\psi(n/s)$ used in this paper. The *plots* on the *left side* of the picture correspond to complex wavelets, while the *plots* on the *right side* correspond to real wavelets. **a** Morlet, **b** Paul. DOG of mth order: **c** DOG ($m = 2$), **d** DOG ($m = 6$)

4. Results

4.1 Chronology of SO$_2$ degassing and seismicity

Figure 5 shows a comparison between SO$_2$ fluxes and RSAM, outlining three periods of enhanced volcanic activity characterized by small-to-moderate explosions, ash emissions and strong degassing. The first period started during the first week of November 2012, when seismicity sharply increased by a factor of 2 and SO$_2$ emissions even quadrupled from a background of 250 t day^{-1} measured during the second half of October, to approximately 1000 t day^{-1} in mid-November. Gas emissions featured pulsating patterns which continually increased through mid-December and culminated in a peak value of approximately 2500 t day^{-1} on December 26, only 1 day after the eruption started. About 3 weeks before the onset of the eruption (December 25), the co-variation between RSAM and degassing trends started to increase, gaining correlation towards the explosive events. Approximately 1 week after the crisis started, there were no more reports of explosive activity and SO$_2$ emissions gradually decreased, which was additionally reflected by a decrease in the pulsating patterns and a decrease in correlation between the two signals. By the middle of February through mid-April 2013, the SO$_2$ emissions remained relatively stable, reaching an average flux of $\approx$250 t day^{-1}. Unfortunately RSAM could not be calculated for the period 28 December 2012 to 01 March 2013, since the seismic station did not work properly as a result of ash depositions from the eruptions. Seismograms provided by INETER, however, clearly show that post-eruptive seismicity gradually dec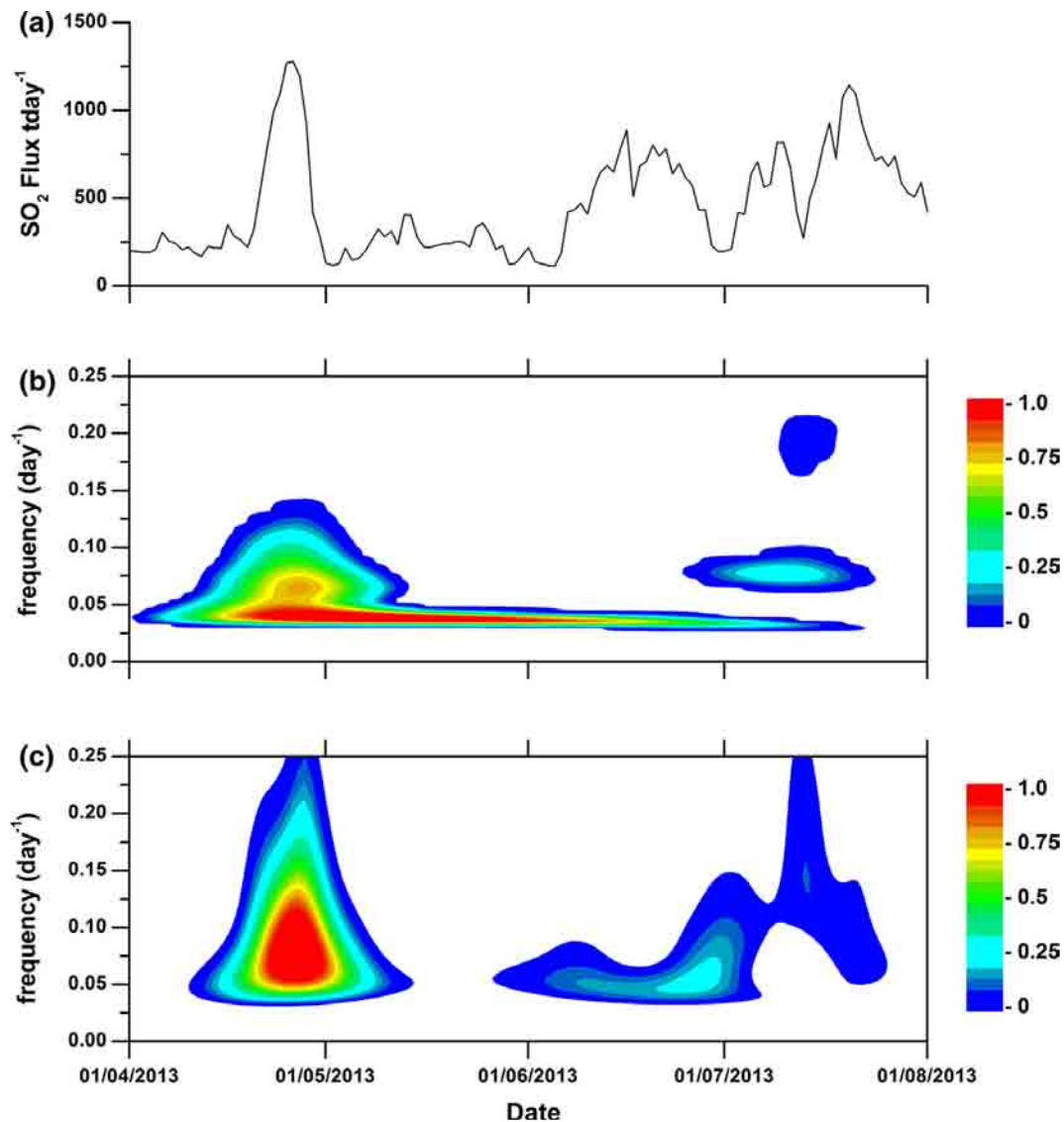reased with some recurrent short episodes of banded tremor (http://www.vol-canodiscovery. com/san-cristobal/news/2013/all.html).

85

Fig. 4 Comparison between the wavelets Morlet and Paul for SO_2 fluxes at San Cristóbal during the period April–August 2013. **a** SO_2 fluxes. **b** Contour map of SO_2 CWT power spectrum coefficients using a Morlet Wavelet. **c** Contour map of SO_2 CWT power spectrum coefficients using a Paul Wavelet. The *coloured* contours correspond to the wavelet coefficients with greater than 95 % significant difference from *red* noise

Volcanic activity increased during the second half of April 2013 and climaxed in a relatively abrupt gas exhalation event end of April 2013 (April 21–29), which was clearly correlated with an increase in RSAM counts by a factor 3, and the SO_2 flux raised from 250 to approximately 800 t day^{-1} through a period of about 10 days before returning to its initial value. Following this precursory event, gas emissions diminished to about 100 t day^{-1} and were well below background shortly before a series of VEI 1 explosive events occurred during the period 7–11 June 2013, accompanied by ash emissions. Seismicity and gas emissions gradually increased after the explosions.

Despite the intensity of the explosions, SO_2 emissions, however, increased only slightly to values around 500 t day^{-1}, while in contrast, RSAM increased significantly by a factor 4. Afterwards, SO_2 emissions and RSAM gradually returned to their pre-eruptive background values.

Following approximately 6 months of relative calm, volcanic activity resumed again during the period 17 January to 4 February 2014. A threefold increase in RSAM correlated well with a series of 12 gas exhalation events on January 17 followed by VEI 1–2 explosive events on 4 February 2014 and a sustained increase in the SO_2 emissions which reached a peak value of approximately 3000 t day^{-1} during the explosive events.
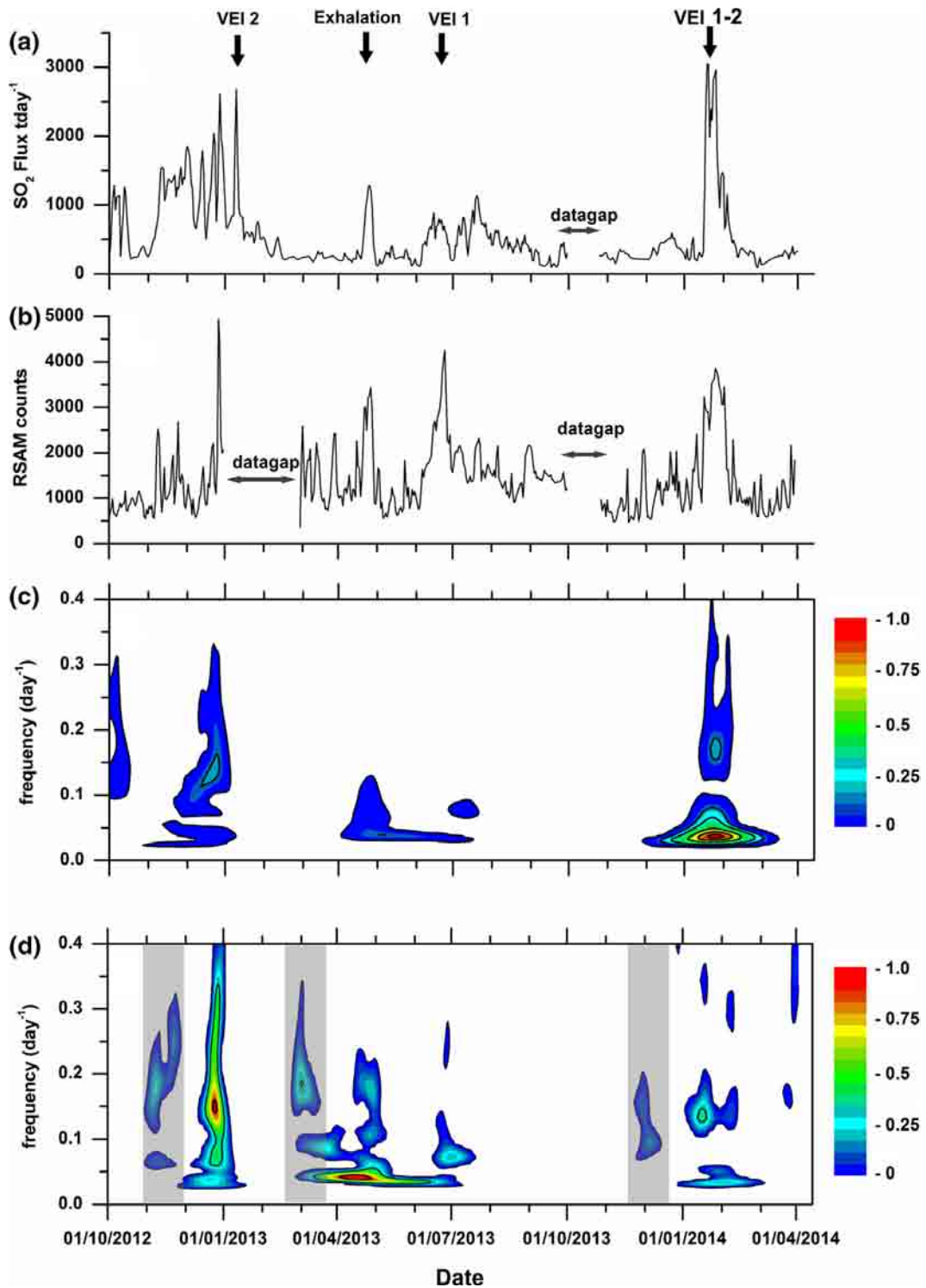
Fig. 5 Estimated fluxes and RSAM with their respective wavelet transform at San Cristóbal during the period: October 2012–April 2014. **a** SO$_2$ fluxes. **b** RSAM counts. **c** Contour map of SO$_2$ CWT power spectrum coefficients. **d** Contour map of RSAM CWT power spectrum coefficients with precursory periods highlighted by the *grey insets*. The CWT power spectrum coefficients were obtained by using the Morlet wavelet. The *coloured* contours correspond to the wavelet coefficients with greater than 95 % significant difference from *red* noise. The *arrows mark* periods of enhanced eruptive activity and amplitude estimates of explosions are indicated by the volcanic explosivity index (VEI)

87
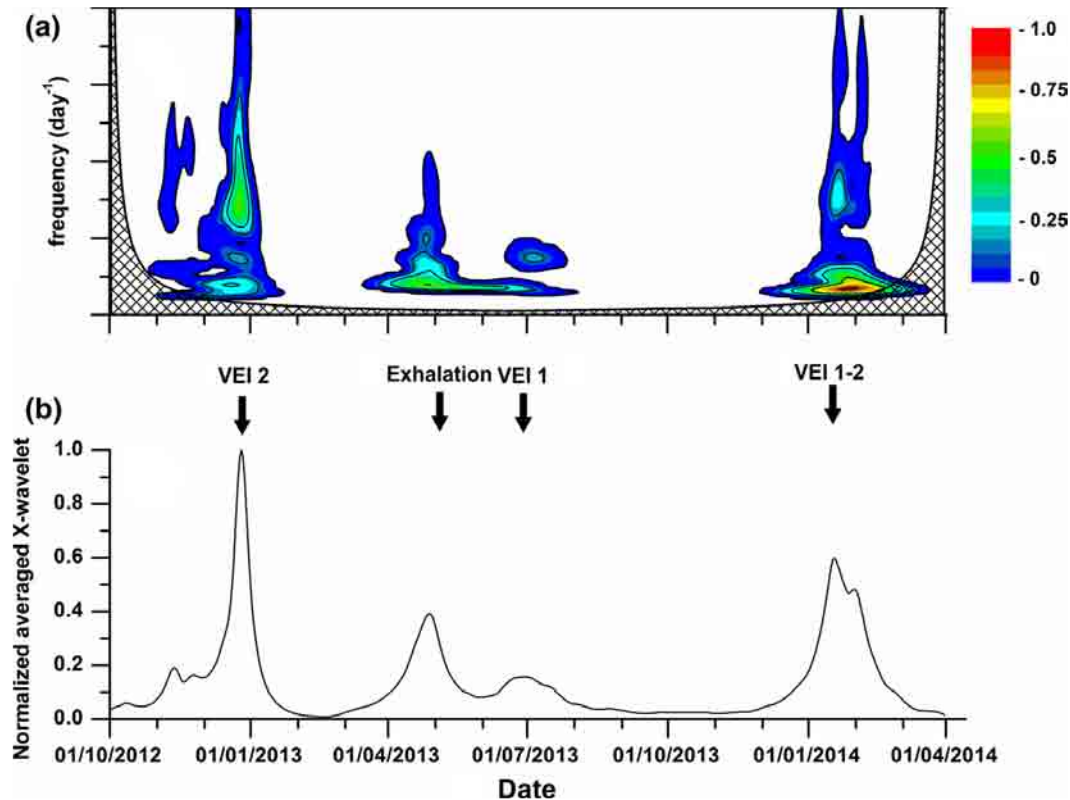
Fig. 6 a Contour map of XWT power spectrum coefficients between the SO_2 fluxes and RSAM (Fig. 5a, b). The *coloured contours* correspond to the cross-wavelet coefficients with greater than 95 % significant difference from *red* noise. The *area filled* with *black crosses* and *outlined* in *black* indicates the COI, where edge effects become important, **b** XWT scale-averaged coefficients. The *arrows mark* the *onset* of periods of enhanced eruptive activity which are shown in Fig. 5. The discontinuities correspond to measurement gaps

4.2 XWT joint analysis

During time windows close to and including the main eruptive events, the Morlet CWTs of both time series show clear patterns of statistically significant coefficients and frequency shifts from a background periodicity of 0.1–0.35 day^{-1} (10–2.8 days) (Fig. 5c, d). Hence, the correlation between both times series was investigated in view of their common spectral–amplitude signatures by applying XWT, and the resultant coefficients are shown in Fig. 6a. In comparison with the individual CWT of both SO_2 fluxes and RSAM, the patterns of the statistically significant coefficients of the XWT exclusively show the features, which both time series have in common and reveal a pronounced signature. These are explicitly restricted to periods with immediate temporal proximity to evident eruptive activity. A better representation of the temporal variation is obtained by averaging the statistically significant XWT coefficients amidst their predominant periodical range (0.03–0.4 day^{-1} or 33.3–2.5 days). Figure 6b shows the result of the averaged XWT coefficients, and the main eruptive events are in good agreement with the averaged coefficient peaks.

5. Discussion

The SO_2 time series indicate that persistent degassing of San Cristóbal averaged approximately 1000 t day^{-1} during the period reported in this study, while in the immediate temporal proximity of eruptive events, significant increases in the SO_2 emissions and seismicity are observed in their time series and the patterns of the corresponding CWT coefficients. A closer look at the grey insets of Fig. 5d indicates that periods of high RSAM CWT coefficients precede the eruptive events in comparison with the periods of high emissions rate CWT coefficients. This feature can be interpreted as a precursory increment of seismic

energy which may be attributed to intrusion of fresh magma batches at shallower crustal levels (Chouet 2003; Battaglia et al. 2005). This assumption is consistent with the enhanced occurrence of tremor and long-period seismicity as reported by INETER for the same periods, and in turn reflected within the RSAM itself time series. Tremor and other low-frequency seismic signatures have been typically associated with displacements of magma and fluids through the conduit (Julian 1994; Chouet 1996; Yamamoto et al. 2002; Langer et al. 2011; Matsumoto et al. 2013). Accordingly, progressive gas exsolution accompanied by transitions between sealing and opening of the upper conduit may precede the explosive events (Casadevall 1981).

Table 2 Illustration of different padding methods for the example time series: $X_0, X_1, X_2 \ldots X_{n-2}, X_{n-1}$

Padding method	Illustration
Zero padding	… 0, 0, 0, $X_0, X_1, X_2 \ldots X_{n-2}, X_{n-1}, X_n$, 0, 0, 0 …
Symmetric padding (SYM)	…$X_2, X_1, X_0, X_0, X_1, X_2 \ldots X_{n-2}, X_{n-1}, X_n, X_n, X_{n-1}, X_{n-2}$ …
Antisymmetric padding (ASYM)	…$-X_2, -X_1, -X_0, X_0, X_1, X_2 \ldots X_{n-2}, X_{n-1}, X_n, -X_n, -X_{n-1}, -X_{n-2}$ …

The activity period comprising the gas exhalation event in April 2013 and the following eruption in June 2013 was slightly distinct in comparison with the eruptive events of December 2012 and February 2014. During the exhalation event, a significant pulse of SO_2 was freely released, suggesting that gas accumulated below the obstructed conduit was discharged without any explosive activity after the gas pressure in the conduit grew enough to remove the material that obstructed the vent. In view of the increasing seismicity that accompanied the exhalation event, it is plausible to consider that this exhalation was the result of incoming magma releasing gas at elevated pressures, combined with minor physical obstruction. A significant decrease in gas emissions below the normal background level prior to the explosions in June 2013 suggests that the obstruction of the conduit had intensified before the eruption, and the subsequent gradual increase in the emissions indicates that the obstructed vent was at least partially cleared by the eruptions.

   The relatively low increase in the SO_2 flux measured during and following the explosive events suggests either that the intruded magma was already essentially degassed, or alternatively, that the clearing of the conduit was not very efficient. Although the heavy rain season during July–September may have contributed to partially seal the upper part of the conduit and a subsequent overpressure, the former option is likely more plausible since the sustained decreasing of both, SO_2 emissions and RSAM, indicates that a shallow gas accumulation is doubtful. This is further supported by the fact that the eruptions in February 2014 were again preceded by gradually increasing gas emissions, without any indication of a sustained obstruction. Further studies involving petrological evidence are required in order to better estimate the mechanisms behind the eruptive events described in this study.

   Following approximately 6 months of relative calm, volcanic activity resumed again during the period 17 January to 4 February 2014. A threefold increase in RSAM correlated well with a series of 12 gas exhalation events on January 17 followed by VEI 1–2 explosive events on 4 February 2014 and a sustained increase in the SO_2 emissions which reached a peak value of approximately 3000 t day^{-1} during the explosive events.

5.1 Implications for volcanic surveillance

The CWT coefficient signals produced by each eruptive have similar features: at the eruption onset and during eruptive periods both time series show significant CWT coefficients with increased magnitudes shifted to higher frequencies. From previous studies where continuous SO_2 flux and RSAM measurements were made, it has correspondingly been demonstrated that by analysing the spectral signatures of their time series it is to some extent possible to identify the separate contributions of geophysical parameters such as deformation, tremor, long-period seismicity and tidal cycles (Conde et al. 2013; Bredemeyer and Hansteen

2014; Saballos et al. 2014). Moreover, the spectral contents of these time series are typically not stationary. Hence, major variations of their spectral signatures can be associated with anomalies, which in the case of San Cristóbal volcano are in good agreement with eruptive events. Thus, the ability of the XWT for detecting common spectral anomalies of SO_2 and RSAM makes this tool suitable for surveillance of volcanoes with a similar eruptive behaviour as San Cristóbal. In addition, as described in Eqs. (2)–(7), these algorithms are relatively easy to implement in a near-real-time graphical data presentation of qualitative changes in eruptive activity.

Despite the potential of this method as a volcanic activity forecasting tool, CWT and XWT have one main limitation, since the time series are finite and CWT assumes a cyclic time series, the resulting coefficients at both ends of the times series have some degree of distortion. The area where edge distortion occurs on a CWT or XWT contour map is typically termed as the cone of influence (COI), shown in Fig. 6a. This limitation may be of minor importance for studies intended to perform a post-analysis of the eruptive records. However, when considering the XWT of SO_2 emissions and RSAM as a potential tool for near-real-time volcanic monitoring, it is necessary to note that the most recent measurements are going to lie within the COI. Many different approaches have been suggested in order to reduce the distortion caused by the border effects in the COI. However, the simplest solution consists of extending the borders of the original time series by appending values (padding) before applying either the CWT or XWT, while the output of the analysis is shortened to the originals borders. The padding methods investigated in this study and illustrated in Table 2 include zero padding, extended padding, periodical padding and antisymmetric padding (Su et al. 2011; Pacola et al. 2013). In addition, it is important to underline that the area of the COI depends on the selected wavelet, because narrower wavelets result in less distorted coefficients since the area of the COI is smaller (Torrence and Compo 1998).

We examine the distortion of the COI by combining different padding methods and different wavelets. To do this, we simulated a time series of XWT averaged coefficients derived from the SO_2-RSAM measurements, by sequentially calculating their XWT for every daily measurement within a time window containing the previous 100 measurements. The simulated time series comprises the scale-averaged XWT coefficients at the end of the current time window, which are distorted due to the border effect and represent a real-time scenario when a new measurement of SO_2 and RSAM is added to the time series. The Morlet wavelet is well suited for analysing time series over extended periods, due to its time–frequency properties. Hence, the Morlet scale-averaged XWT shown in Fig. 6b provides a good reference for comparing the performance of the simulated time series. The results of this comparison of different wavelets on the simulated time series are shown in Fig. 7a–d. After several evaluations, it was found that the antisymmetric padding produced lower errors except in the case of the wavelet DOG ($m = 6$) where zero padding was used instead. Although at first glance the distortion is obvious, the curve progression of the averaged coefficients inside the COI still resembles the qualitative variations of the averaged coefficients that are not affected by distortion.

The qualitative comparisons for different wavelets are completed with the cross-correlation analysis shown in Fig. 7e–h. By observing the full width at half maximum (FWHM), we can state that out of the considered wavelets, Paul (Fig. 7e) and DOG (2) (Fig. 7f) have a lower distortion due to the COI effect, which is not surprising considering that these two wavelets are narrower. Although the Morlet wavelet coefficients are optimal for analysing time series over extended periods, the symmetry and smoothness of the correlogram shown in Fig. 7e suggest that the Paul wavelet, at least in this case, is the best option for applying averaged XWT coefficients as a qualitative forecasting tool for a joint analysis of SO_2 emissions and RSAM in near real time.

6. Conclusions

The continuous activity at San Cristóbal volcano, notable by its persistent degassing and seismicity, has allowed us to propose a novel approach for a joint analysis of SO_2 fluxes and RSAM. Initially we have described a SO_2 flux pre-processing approach implemented by using the Kalman filter which takes into account measurement errors and the estimated variability. Several studies with the aim of better constraining flux measurement errors are in progress, and this simplified statistical approach for SO_2 flux time series can be easily adapted to further improve error analysis and thus provide more accurate statistics. Furthermore, it has been shown that analysing SO_2 fluxes and RSAM by observing their CWT coefficients
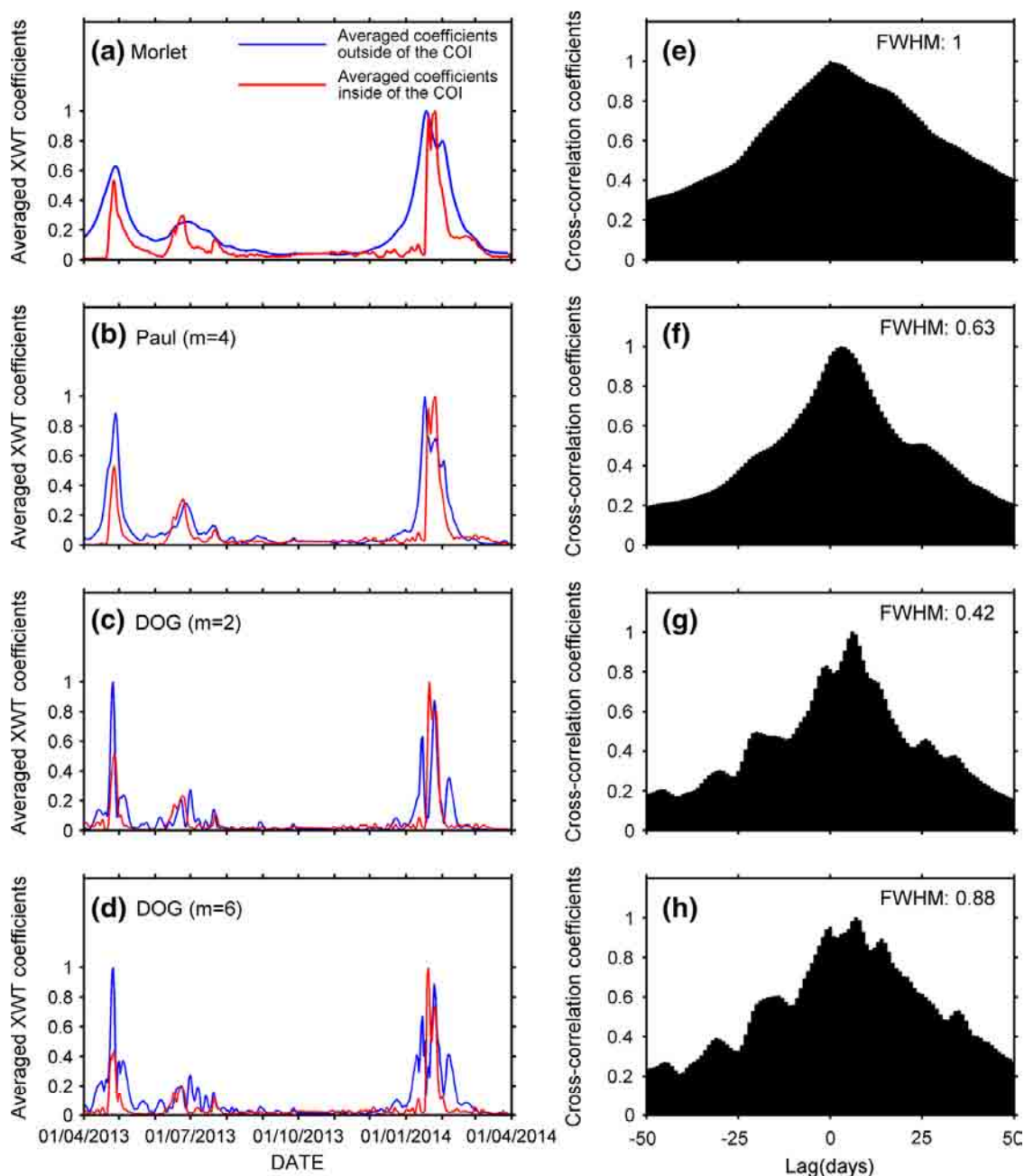
Fig. 7 Comparison of the XWT and border effects. In the *left column*, the *blue lines* correspond to the XWT scale-averaged coefficients unperturbed by the COI. The *red lines* correspond to the averaged coefficients lying in the *left* boundary of the COI. The pairs of time series in **a**–**c** were padded using antisymmetric padding (ASYM), whereas in **d** zero padding was used instead. In the *right column*, the cross-correlations between each pair of time series on the *left side* are depicted. The FWHM of the different wavelets is relative to the FWHM of the Morlet wavelet. The lower FWHMs suggest that the wavelets Paul (**f**) and DOG ($m = 2$) (**g**) are less affected by the border effect

provides additional insights that are not so obvious at first glance. As a result, it was graphically easy to identify the increasing seismic energy preceding major eruptive events, which may be associated with magma emplacement to shallower crustal levels.

Although joint analysis of seismicity and emissions has been applied in several scenarios, the analysis presented here demonstrates the use of CWT and XWT for interpretation and surveillance of eruptive events. In the case of San Cristóbal volcano, the contours of the XWT coefficients and the peaks of the averaged coefficients correlate well with the reported eruptive events. We have also demonstrated the possibility of implementing a routine for near real-time observations by analysing the errors and distortion

_____

due to the border effect. In this case, by using narrower wavelets such as Paul, it is possible to reduce this artefact. Although such techniques can be applied to other volcanoes with continuous degassing, an extensive analysis of previous degassing and seismic reports is necessary in order to define a suitable threshold that allows to identify significant changes in the ongoing volcanic activity.

In summary, this paper demonstrates another application of using permanent DOAS instruments for continuous measurements of SO_2 in complement to the widely used seismic monitoring techniques.

References

Allen M, Smith LA (1996) Monte Carlo SSA: detecting irregular oscillations in the presence of colored noise. J Clim 9(12):3373–3404. doi:10.1175/1520-0442(1996)009<3373:MCSDIO>2.0 .CO;2

Anderson JL (2001) An ensemble adjustment Kalman filter for data assimilation. Mon Weather Rev 129(12):2884–2903. doi:10.1175/1520-0493(2001)129<2884:AEAKFF>2.0.CO;2

Barrancos J, Roselló JI, Calvo D, Padrón E, Melián G, Hernández PA, Pérez NM, Millán MM, Galle B (2008) SO_2 emission from active volcanoes measured simultaneously by COSPEC and mini-DOAS. Pure appl Geophys 165(1):115–133

Battaglia J, Ferrazzini V, Staudacher T, Aki K, Cheminée J-L (2005) Pre-eruptive migration of earthquakes at the Piton de la Fournaise volcano (Réunion Island). Geophys J Int 161(2):549–558. doi:10.1111/j.1365-246X.2005.02606.x

Bluth G, Shannon J, Watson I, Prata A, Realmuto V (2007) Development of an ultra-violet digital camera for volcanic SO_2 imaging. J Volcanol Geoth Res 161(1):47–56. DOI:10.1016/j.jvolgeores.2006.11.004

Boichu M, Oppenheimer C, Tsanev V, Kyle PR (2010) High temporal resolution SO_2 flux measurements at Erebus volcano, Antarctica. J Volcanol Geoth Res 190(3):325–336. DOI:10.1016/j.jvolgeores.2009.11.020

Bredemeyer S, Hansteen T (2014) Synchronous degassing patterns of the neighbouring volcanoes Llaima and Villarrica in southcentral Chile: the influence of tidal forces. Int J Earth Sci (Geol Rundsch) 103(7):1999–2012. doi:10.1007/s00531-014-1029-2

Burton M, Allard P, Mure F, La Spina A (2007) Magmatic gas composition reveals the source depth of slug-driven Strombolian explosive activity. Science 317(5835):227–230. doi:10.1126/science.1141900

Burton MR, Caltabiano T, Murè F, Salerno G, Randazzo D (2009) SO_2 flux from Stromboli during the 2007 eruption: results from the FLAME network and traverse measurements. J Volcanol Geoth Res 182(3–4):214–220. doi:10.1016/j.jvolgeores.2008.11.025

Casadevall TJ (1981) The 1980 eruptions of Mount St. Helens, Washington. SO_2 emission rates at Mount St. Helens from March 29 through December 1980. US Geol Surv Prof Pap 1250:193–200

Casadevall T, Rose W, Gerlach T, Greenland LP, Ewert J, Wunderman R, Symonds R (1983) Gas emissions and the eruptions of Mount St. Helens through 1982. Science 221(4618):1383–1385. DOI:10.1126/science.221.4618.1383

Chouet BA (1996) Long-period volcano seismicity: its source and use in eruption forecasting. Nature 380(6572):309–316. DOI:10.1038/380309a0

Chouet B (2003) Volcano seismology. Pure appl Geophys 160(3–4):739–788. DOI:10.1007/PL00012556

Conde V, Bredemeyer S, Duarte E, Pacheco J, Miranda S, Galle B, Hansteen T (2013) SO_2 degassing from Turrialba Volcano linked to seismic signatures during the period 2008–2012. Int J Earth Sci (Geol Rundsch). doi:10.1007/s00531-013-0958-5

Daag AS, Tubianosa BS, Newhall CG, Tungol NM, Javier D, Dolan MT, Delos Reyes PJ, Arboleda RA, Martinez MML, Regalado TM (1996) Monitoring sulfur dioxide emission at Mount Pinatubo. In: Newhall C, Punongbayan R (eds) Fire and mud: eruptions and lahars of Mount Pinatubo, Philippines, Philippine Institute of Volcanology and Seismology, Quezon city, and University of Washington Press, Seattle, pp 409–414

D'Alessandro A, Scarfi L, Scaltrito A, Di Prima S, Rapisarda S (2013) Planning the improvement of a seismic network for monitoring active volcanic areas: the experience on Mt. Etna. Adv Geosci 36:39–47. doi:10.5194/adgeo-36-39-2013

Daubechies I (1990) The wavelet transform, time-frequency localization and signal analysis. IEEE Trans Inf Theory 36(5):961–1005. doi:10.1109/18.57199

De Moortel I, Ireland J, Walsh R (2000) Observation of oscillations in coronal loops. Astron Astrophys 355:L23–L26

Edmonds M, Herd RA, Galle B, Oppenheimer CM (2003) Automated, high time resolution measurements of SO_2 flux at Soufrière Hills Volcano, Montserrat. Bull Volcanol 65(8):578–586. DOI:10.1007/s00445-003-0286-x

Endo ET, Murray T (1991) Real-time seismic amplitude measurement (RSAM): a volcano monitoring and prediction tool. Bull Volcanol 53(7):533–545. DOI:10.1007/BF00298154

Evensen G (2003) The ensemble Kalman filter: theoretical formulation and practical implementation. Ocean Dyn 53(4):343–367. DOI:10.1007/s10236-003-0036-9

Fischer von Mollard K (2013) Variationen in den SO_2-Ausstößen des San Cristóbal Vulkans zwischen 2006 und 2012 ermittelt anhand von bodenbasierter UV-Spektrometrie (Mini-DOAS). University of Kiel, Kiel

Galle B, Oppenheimer C, Geyer A, McGonigle AJS, Edmonds M, Horrocks L (2002) A miniaturised ultraviolet spectrometer for remote sensing of SO_2 fluxes: a new tool for volcano surveillance. J Volcanol Geoth Res 119(1–4):241–254. DOI:10.1016/S0377-0273(02)00356-6

Galle B, Johansson M, Rivera C, Zhang Y, Kihlman M, Kern C, Lehmann T, Platt U, Arellano SR, Hidalgo S (2010) Network for observation of volcanic and atmospheric change (NOVAC)—a global network for volcanic gas monitoring: network layout and instrument description. J Geophys Res 115(D5):D05304. doi:10.1029/2009jd011823

Grinsted A, Moore JC, Jevrejeva S (2004) Application of the cross wavelet transform and wavelet coherence to geophysical times series. Nonlinear Process Geophys 11(5–6):561–566

Hidalgo S, Battaglia J, Arellano S, Steele A, Bernard B, Bourquin J, Galle B, Arrais S, Vásconez F (2015) SO_2 degassing at Tungurahua volcano (Ecuador) between 2007 and 2013: transition from continuous to episodic activity. J Volcanol Geoth Res 298:1–14. DOI:10.1016/j.jvolgeores.2015.03.022

Hoff RM, Millan MM (1981) Remote SO_2 mass flux measurements using COSPEC. J Air Pollut Control Assoc 31(4):381–384. doi:10.1080/00022470.1981.10465233

Johansson M (2009) Application of passive DOAS for studies of megacity air pollution and volcanic gas emissions. Ph.D. thesis Chalmers University of Technology

Julian BR (1994) Volcanic tremor: nonlinear excitation by fluid flow. J Geophys Res Solid Earth 99(B6):11859–11877. doi:10.1029/93JB03129

Kalman RE (1960) A new approach to linear filtering and prediction problems. Trans ASME J Basic Eng 82(Series D):35–45. doi:10.1115/1.3662552

Kestin TS, Karoly DJ, Yano JI, Rayner NA (1998) Time-frequency variability of ENSO and stochastic simulations. J Clim 11(9):2258–2272. doi:10.1175/1520-0442(1998)011<2258:TFVOEA>2.0.CO;2

Langer H, Falsaperla S, Messina A, Spampinato S, Behncke B (2011) Detecting imminent eruptive activity at Mt Etna, Italy, in 2007–2008 through pattern classification of volcanic tremor data. J Volcanol Geoth Res 200(1–2):1–17. doi:10.1016/j.jvolgeores.2010.11.019

Lau K, Weng H (1995) Climate signal detection using wavelet transform: how to make a time series sing. Bull Am Meteorol Soc 76(12):2391–2402. doi:10.1175/1520-0477(1995)076<2391:CSDUWT>2.0.CO;2

Mather TA, Pyle DM, Tsanev VI, McGonigle AJS, Oppenheimer C, Allen AG (2006) A reassessment of current volcanic emissions from the Central American arc with specific examples from Nicaragua. J Volcanol Geoth Res 149(3–4):297–311. doi:10.1016/j.jvolgeores.2005.07.021

Matsumoto S, Shimizu H, Matsushima T, Uehira K, Yamashita Y, Nakamoto M, Miyazaki M, Chikura H (2013) Short-term spatial change in a volcanic tremor source during the 2011 Kirishima eruption. Earth Planets Space 65(4):323–329. DOI:10.5047/eps.2012.09.002

Mori T, Burton M (2006) The SO_2 camera: a simple, fast and cheap method for ground-based imaging of SO_2 in volcanic plumes. Geophys Res Lett 33(24):L24804. doi:10.1029/2006GL027916

Mulquiney JE, Norton JP, Jakeman AJ, Taylor JA (1995) Random walks in the Kalman filter: implications for greenhouse gas flux deductions. Environmetrics 6(5):473–478. doi:10.1002/env.3170060509

Mwale D, Gan TY (2005) Wavelet analysis of variability, teleconnectivity, and predictability of the September–November East African rainfall. J Appl Meteorol 44(2):256–269. doi:10.1175/JAM2195.1

Myers K, Tapley BD (1976) Adaptive sequential estimation with unknown noise statistics. IEEE Trans Autom Control 21(4):520–523. doi:10.1109/TAC.1976.1101260

Nadeau PA, Palma JL, Waite GP (2011) Linking volcanic tremor, degassing, and eruption dynamics via SO_2 imaging. Geophys Res Lett 38(1):L01304. doi:10.1029/2010GL045820

Nagarajan K, Judge J, Monsivais-Huertero A, Graham WD (2012) Impact of assimilating passive microwave observations on rootzone soil moisture under dynamic vegetation conditions. IEEE Trans Geosci Remote Sens 50(11 PART1):4279–4291

Olmos R, Barrancos J, Ivera CR, Barahona F, López DL, Henriquez B, Hernández A, Benitez E, Hernández PA, Pérez NM, Galle BO (2007) Anomalous emissions of SO_2 during the recent eruption of Santa Ana volcano, El Salvador, Central America. Pure Appl Geophys 164(12):2489–2506. DOI:10.1007/s00024-007-0276-6

Pacola ER, Quandt VI, Schneider FK, Sovierzoski MA (2013) The wavelet transform border effect in EEG spike signals. In: Long M (ed) IFMBE proceedings of the world congress on medical physics and biomedical engineering, May 26–31, 2012, Beijing, China, vol 39. Springer, Berlin, pp 593–596. doi:10.1007/978-3-642-29305-4_155

Petersen T, Caplan-Auerbach J, McNutt SR (2006) Sustained long-period seismicity at Shishaldin Volcano, Alaska. J Volcanol Geoth Res 151(4):365–381. DOI:10.1016/j.jvolgeores.2005.09.003

Platt U, Stutz J (2008) Differential optical absorption spectroscopy (DOAS), principle and applications. Springer, Heidelberg. doi:10.1007/978-3-540-75776-4

Rivera C (2009) Application of passive DOAS using scattered sunlight for quantification of gas emissions from anthropogenic and volcanic sources. Chalmers tekniska högskola, Gothenburg

Rivera C, Garcia JA, Galle B, Alonso L, Yan Z, Johansson M, Matabuena M, Gangoiti G (2009) Validation of optical remote sensing measurement strategies applied to industrial gas emissions. Int J Remote Sens 30(12):3191–3204. doi:10.1080/01431160802558808

Saballos J, Conde V, Malservisi R, Connor C, Álvarez J, Muñoz A (2014) Relatively short-term correlation among deformation, degassing, and seismicity: a case study from Concepción volcano, Nicaragua. Bull Volcanol 76(8):1–11. doi:10.1007/s00445-014-0843-5

Smithsonian-Institution (2014) http://www.volcano.si.edu/volcano.cfm?vn=344020

Su H, Liu Q, Li J (2011) Alleviating border effects in wavelet transforms for nonlinear time-varying signal analysis. Adv Electr Comput Eng 11(3):55–60. DOI:10.4316/AECE.2011.03009

Symonds R, Rose WI, Bluth GJS, Gerlach TM (1994) Volcanic-gas studies; methods, results, and applications. Rev Mineral Geochem 30(1):1–66.

Tilling RI (2008) The critical role of volcano monitoring in risk reduction. Adv Geosci 14:3–11. DOI:10.5194/adgeo-14-3-2008

Torrence C, Compo GP (1998) A practical guide to wavelet analysis. Bull Am Meteorol Soc 79(1):61–78. doi:10.1175/15200477(1998)079<0061:APGTWA>2.0.CO;2

Torrence C, Webster PJ (1999) Interdecadal changes in the ENSO—monsoon system. J Clim 12(8):2679–2690. doi:10.1175/1520-0442(1999)012<2679:ICITEM>2.0.CO;2

Waite GP, Nadeau PA, Lyons JJ (2013) Variability in eruption style and associated very long period events at Fuego volcano, Guatemala. J Geophys Res Solid Earth 118(4):1526–1533. DOI: 10.1002/jgrb.50075

Wang P, Gao J (2013) Extraction of instantaneous frequency from seismic data via the generalized Morse wavelets. J Appl Geophys 93:83–92. DOI:10.1016/j.jappgeo.2013.04.003

Welch G, Bishop G (1995) An introduction to the Kalman filter. University of North Carolina, Chapel Hill

Weng H, Lau K (1994) Wavelets, period doubling, and time-frequency localization with application to organization of convection over the tropical western Pacific. J Atmos Sci 51(17):2523–2541. DOI: 10.1175/1520-0469(1994)051<2523:WPDATL>2.0.CO;2

Yamamoto M, Kawakatsu H, Yomogida K, Koyama J (2002) Long-period (12 sec) volcanic tremor observed at Usu 2000 eruption: seismological detection of a deep magma plumbing system. Geophys Res Lett 29(9):43-1–43-4. DOI:10.1029/2001GL013996

Yan Y, Barth A, Beckers JM (2014) Comparison of different assimilation schemes in a sequential Kalman filter assimilation system. Ocean Model 73:123–137. DOI:10.1016/j.ocemod.2013.11.002

CHAPTER V

Gas emissions from five volcanoes in Northern Chile and implications for the volatile budget of the Central Volcanic Zone

Gas emissions from five volcanoes in northern Chile and implications for the volatiles budget of the Central Volcanic Zone

G. Tamburello[1] · T. H. Hansteen[2] · S. Bredemeyer[2] · A. Aiuppa[1,3] · F. Tassi[4]

Abstract This study performed the first assessment of the volcanic gas output from the Central Volcanic Zone (CVZ) of northern Chile. We present the fluxes and compositions of volcanic gases (H_2O, CO_2, H_2, HCl, HF, and HBr) from five of the most actively degassing volcanoes in this region—Láscar, Lastarria, Putana, Ollagüe, and San Pedro—obtained during field campaigns in 2012 and 2013. The inferred gas plume compositions for Láscar and Lastarria (CO_2/S_{tot} = 0.9–2.2; S_{tot}/HCl = 1.4–3.4) are similar to those obtained in the Southern Volcanic Zone of Chile, suggesting a uniform magmatic gas fingerprint throughout the Chilean arc. Combining these compositions with our own UV spectroscopy measurements of the SO_2 output (summing to ~1800 t d^{-1} for the CVZ), we calculate a cumulative CO_2 output of 1743–1988 t d^{-1} and a total volatiles output of >20,200 t d^{-1}.

Key Points:
• Gas output from the Central Volcanic Zone of northern Chile
• Identification of a common magmatic end-member of Chilean volcanism
• Comparison between measured and petrologically estimated carbon/sulfur fluxes

Supporting Information:
• Readme
• Table S1
• Table S2
• Table S3

Correspondence to:
G. Tamburello, e-mail: giancarlo.tamburello@unipa.it

[1]DiSTeM, Università di Palermo, Palermo, Italy,   [2]GEOMAR, Helmholtz Centre for Ocean Research, Kiel, Germany,
[3]INGV, Sezione di Palermo, Palermo, Italy,   [4]Dipartimento di Scienze della Terra, Università di Firenze, Florence, Italy

1. Introduction

The Chilean Andes is a 4500 km long segment of the Andean Cordillera, extending from the Arica and Parinacota regions to Cape Horn (16°S to 56°S), with more than 200 active (Quaternary) volcanoes distributed into four distinct zones [Stern, 2004; Thorpe and Francis, 1979; Thorpe, 1984].

   The Chilean segment of the Central Volcanic Zone (CVZ; 17°S to 26°S, Figure 1) comprises a ~600 km long volcanic district and contains ~34 active volcanoes [Stern, 2004]. Farther to the south, the Southern Volcanic Zone (SVZ; 34°S to 46°30′S) includes at least 60 historically active volcanoes [Stern, 2004] which volcanism is associated with a 70 km thick crust and high degrees of magma differentiation [Hildreth and Moorbath, 1988; Davidson et al., 1990].
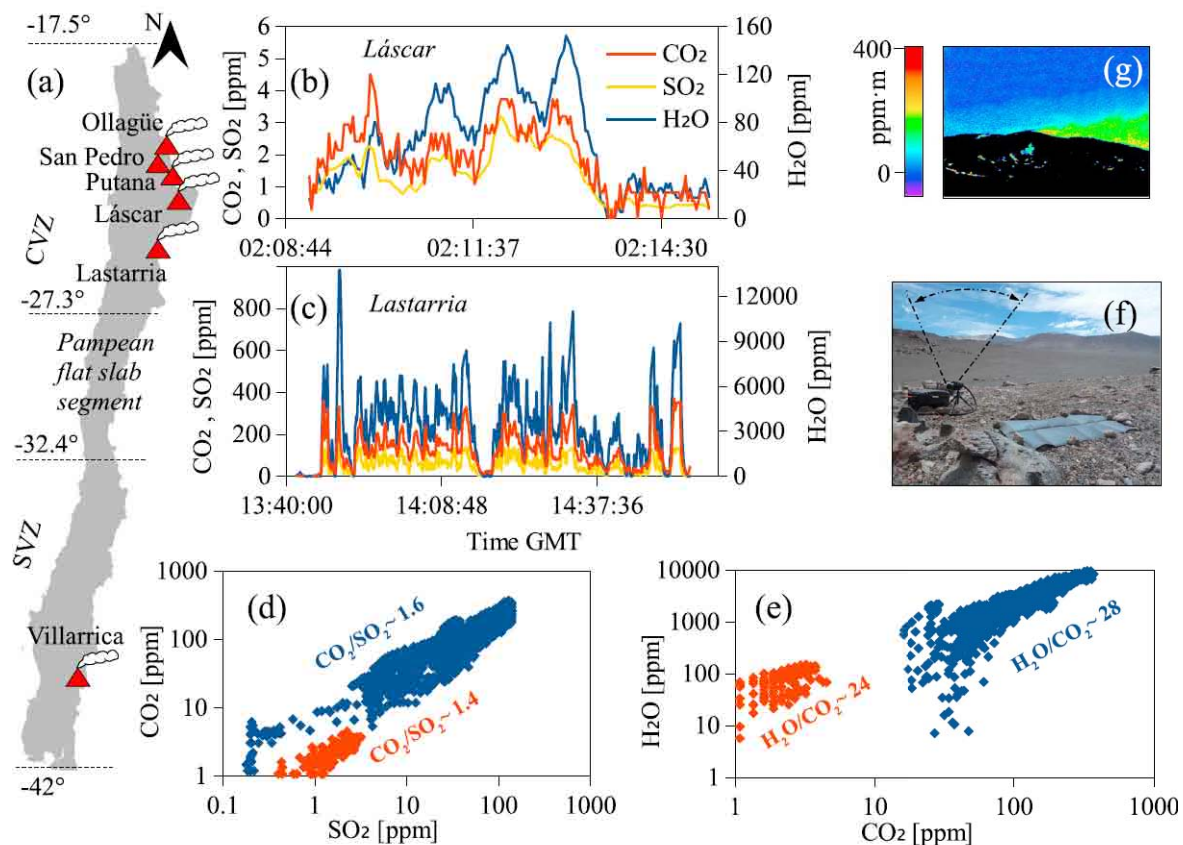
Figure 1. (a) Map of Chile showing the volcanoes of the CVZ and the SVZ targeted in this study. **(b, c)** Time series of CO_2, SO_2, and H_2O background-subtracted concentrations measured with the Multicomponent Gas Analyzer System (MultiGAS) at Láscar (Figure 1b) and Lastarria (Figure 1c). **(d, e)** Despite the significant temporal and spatial variabilities of concentrations, remarkably constant molar ratios were obtained at both Láscar (red) and Lastarria (blue). **(f)** Mobile scanning Mini-differential optical absorption spectroscopy (DOAS) instrument deployed at Lastarria. **(g)** SO_2 column densities measured at Putana volcano with an SO_2 camera on 5 December 2012.

Despite the presence of several persistently degassing volcanoes, the present-day volcanic gas output of the CVZ remains poorly known. Gas composition data have been reported for several volcanoes [Tassi et al., 2009, 2011; Capaccioni et al., 2011; Aguilera et al., 2012], but fluxes of major volcanic gas species (H_2O and CO_2) have not been reported. Compared to other, better-characterized arc segments (e.g., Central American Volcanic Arc (CAVA) [Mather et al., 2006; Freundt et al., 2014] and SVZ [Völker et al., 2014]), the paucity of gas flux measurements and poor knowledge of subducted sediment composition [Plank and Langmuir, 1998] result into an inadequate understanding of the recycling of volatiles along this sector of the Chilean volcanic front.

Here we report on the first combined assessment of volatiles emissions from five of the most active volcanoes of the CVZ in northern Chile. Using rapid deployment scanning Mini-DOAS (differential optical absorption spectroscopy) instruments [Galle et al., 2010] and a dual UV camera system [Kantzas et al., 2010], we obtained new data of the SO_2 output from the Putana, Láscar, Lastarria, Ollagüe, and San Pedro volcanoes (Figure 1 and Table S1 in the supporting information). These results were integrated with plume compositional data obtained using the INGV-type (Istituto Nazionale di Geofisica e Vulcanologia, Palermo, Italy) Multicomponent Gas Analyzer System (MultiGAS), filter packs, and direct fumarolic gas sampling (Tables S2 and S3 in the supporting information) to indirectly calculate—for the first time—the fluxes of the following other volcanic species: H_2O, CO_2, H_2, HCl, HF, and HBr. Comparison of our results with gas composition data from other Chilean volcanoes (e.g., Villarrica [Shinohara and Witter, 2005; Sawyer et al., 2011]) suggests the presence of a common magmatic gas fingerprint across several thousands of kilometers of the arc. We further propose the first estimate of the total volcanic gas output from the CVZ in northern Chile.

2. Volcanic Activity

Láscar is a calc-alkaline stratovolcano located east of Salar de Atacama (23.37°S, 67.73°W) and is the most active volcano of the Chilean segment of the central Andes [Oppenheimer et al., 1993]. Several small-to-moderate vulcanian eruptions have been recorded from Láscar since the midnineteenth century (some recently registered eruptions occurred in 2013, 2006–2007, 2005, 2002, 2000, 1994–1995, 1994, 1993–1994, 1993, and 1991–1992), most of which created ash columns with heights of up to a few kilometers above the summit. The activity of Láscar has been cyclic since 1984 [Matthews et al., 1997]; in each cycle a lava dome is extruded into the active crater, accompanied by vigorous degassing through high-temperature fumaroles distributed on and around the dome. The Quaternary Lastarria volcano is located on the Chile-Argentina border at 25.17°S, 68.50°W and rises to 5706 m above sea level (asl). The north-northwest-trending edifice contains five nested summit craters. The youngest (<0.3 Myr) volcanic feature is a lava dome on the northern crater rim [Naranjo, 1986]. Although no historic eruption has been recorded, the youthful morphology of deposits and the ongoing uplift (~2.5 cm yr^{-1}) that began in 1996 [Pritchard and Simons, 2002; Froger et al., 2007] support the active nature of Lastarria. Putana volcano is a 600 km^2 cone of andesitic-basaltic to dacitic lavas with a summit crater that is ~0.5 km in diameter at 5890 masl. It has been characterized since the nineteenth century by persistent active degassing from four main summit fumarole fields, which feed a sustained steam plume [Casertano, 1963]. San Pedro (21.88°S, 68.14°W) is a composite basaltic andesite-to-dacitic volcano with several recorded historic eruptions, most recently in 1960 [e.g., O'Callaghan and Francis, 1986]. Steady fumarole activity on the upper western volcano flank has been documented from at least 2012 (Observatorio volcanológico de los Andes del Sur Monthly Reports). Ollagüe (21.30°S, 68.18°W) is also a composite volcano, consisting of high-K calc-alkaline rocks of dominantly andesitic to dacitic composition, but also comprises basaltic andesites [Feeley et al., 1993]. The last eruption occurred in 1903, and the present-day persistent fumarole activity is associated with a summit lava dome.

3. Results

3.1 Láscar

At the time of our field survey of Láscar in 2012 (during 4–7 December), a sustained steam plume was produced by the persistent fumarole field, which is located ~200m below the rim of its active central crater. The MultiGAS was deployed on the crater's rim in order to measure the bulk plume composition. We detected a dilute plume with strongly correlated volcanic H_2O, CO_2, and SO_2 mixing ratios (Figure 1b). The CO_2/SO_2 and H_2O/CO_2 molar ratios ranged from ~1 to ~1.7 and from ~12 to ~34, respectively, during our monitoring period (Figure 1d). Sets of base-treated filter packs were simultaneously collected to derive the in-plume halogen/SO_2 ratios. Our 2012 results (HCl/SO_2 ~ 0.7, HF/SO_2 ~ 0.06, and HBr/SO_2 = 2.2×10^{-4}) indicate a more F-poor gas than in 2003 (HCl/SO_2 ~ 0.6 and HF/SO_2 ~ 0.5 [Mather et al., 2004]). The Láscar plume was measured for several hours on 3–7 December 2012 and on 2–4 and 8 December 2013 by placing one or two scanning Mini-DOAS stations at various distances from 2.5 to 11 km downwind of the summit. The overall SO_2 output over the two measurement periods was 554 ± 217 t d^{-1} (mean ± standard deviation). Although SO_2 emissions from Láscar occasionally peak at ~2300 t d^{-1} [Andres et al., 1991; Mather et al., 2004], our results agree well with previous results obtained during periods of low degassing [Andres et al., 1991; Matthews et al., 1997; Henney et al., 2012].

3.2 Lastarria

There has been continuous fumarole activity at the summit (upper fields) and northwest flank (bottom field) of Lastarria since the earliest available records. The bottom field is located at ~5000 masl and is the largest (~0.023 km^2) emission area on the volcano. On 27 November 2012, we used the MultiGAS to characterize the chemical structure and heterogeneity of the bottom field. Our analysis reveals that the Lastarria bottom field has a homogeneous composition (see Figure 1c). The mean CO_2/SO_2 molar ratio was 1.6 (Figure 1d;

Table 1 Summary Table of Derived Volatiles Output

Volcano	H_2O	CO_2	SO_2	H_2S	HCl	HF	HBr	Total (t d^{-1})
Putana (t d^{-1})			68.5					68.5
Lastarria (t d^{-1})	11,059	973	884	174	385	5.8	0.6	13,480
Láscar (t d^{-1})	5,195	534	554	30	199	9.4	0.15	6,517
Ollagüe (t d^{-1})			150					76
San Pedro (t d^{-1})			161					81
Total^a (t d^{-1})	16,521	1,506	1,818	204	604	15.2	0.76	>20,220
(t yr^{-1})	6×10^6	5.5×10^5	6.7×10^5					
Total CVZ^b (t d^{-1})	$2.2\text{-}3.3 \times 10^4$	1,743-1,988	1,818					
(t yr^{-1})	$8\text{-}12 \times 10^6$	$6.4\text{-}7.3 \times 10^5$	6.7×10^5					
Extrusive+Inrusive^c (t yr^{-1})		$3.3\text{-}8.1 \times 10^5$	5.3×10^5					

^{a}Calculated from measured gas compositions and fluxes.
^{b}H_2O and CO_2 fluxes calculated using molar H_2O/CO_2=30–40 and CO_2/SO_2=0.9–2.2 for Putana, Ollagüe, and San Pedro volcanoes.
^{c}Calculated petrological volatiles output.

range, 1.1–2.3), and the characteristic H_2O/CO_2 and H_2/H_2O ratios were 27.8 ± 2.8 and $6\pm2\times10^{-5}$, respectively. Our filter pack-based halogen/SO_2 molar ratios were HCl/SO_2~0.8, HF/SO_2~0.022, and HBr/SO_2=5×10^{-4}. The plume was measured downwind of Lastarria for several hours on 27–29 November 2012 with the scanning Mini-DOAS stations placed about 8 km from the plume source. The wind speed at the plume height obtained using the Global Data Assimilation System model fitted well with our own anemometer data. The daily fluxes on these 3 days were 1917 ± 607, 473 ± 188, and 433 ± 314 t d^{-1}, respectively, with an overall value for the 3 days of 884 ± 779 t d^{-1}.

3.3 Putana, San Pedro, and Ollagüe

On 5 December 2012, we performed UV camera measurements at ~4.7 km from Putana crater (Figure 1g), which yielded an SO_2 output from this volcano of 40 ± 11 t d^{-1} (Table 1). The plume was again measured for several hours on 5, 6, and 9 December 2013 using two scanning Mini-DOAS stations. The daily fluxes on these 3 days were 55 ± 14, 133 ± 104, and 77 ± 24 t d^{-1}, respectively, with an overall value of 97 ± 78 t d^{-1}. Similarly, the plumes of San Pedro and Ollagüe were measured for several hours using scanning Mini-DOAS instruments on 10 and 12 December 2013 and on 11 and 12 December 2013, respectively; the daily fluxes were 182 ± 188 and 150 ± 140 t d^{-1} at San Pedro (overall, 161 ± 150 t d^{-1}), and 47 ± 18 and 220 ± 181 t d^{-1} at Ollagüe (overall, 150 ± 162 t d^{-1}) (Table 1). Unfortunately no MultiGAS or filter pack data are available for these volcanoes.

4. Discussion

4.1. Magmatic Gas End-Member Composition of Chilean Volcanism

Figures 2, 3 compare our Láscar and Lastarria data set with the results of previous observations at Chilean volcanoes, from Tacora in the north (17°43.2′S) to Villarrica in the south (39°25.2′S). To identify the nature (magmatic versus hydrothermal) of the measured gases, we report in Figure 2a two distinct gas end-members: Villarrica gas and Tacora gas. Gas samples from Villarrica, which originate from a persistent lava lake, represent the best available compositional proxy for the magmatic gas end-member in Chile. In contrast, the CO_2-rich (CO_2/SO_2 ~ 27.9) signature of Tacora gas [Capaccioni et al., 2011] is typical of residual fluids formed after prolonged gas-water-rock interactions [Symonds et al., 2001] and is therefore taken as representative of the hydrothermal compositional end-member.
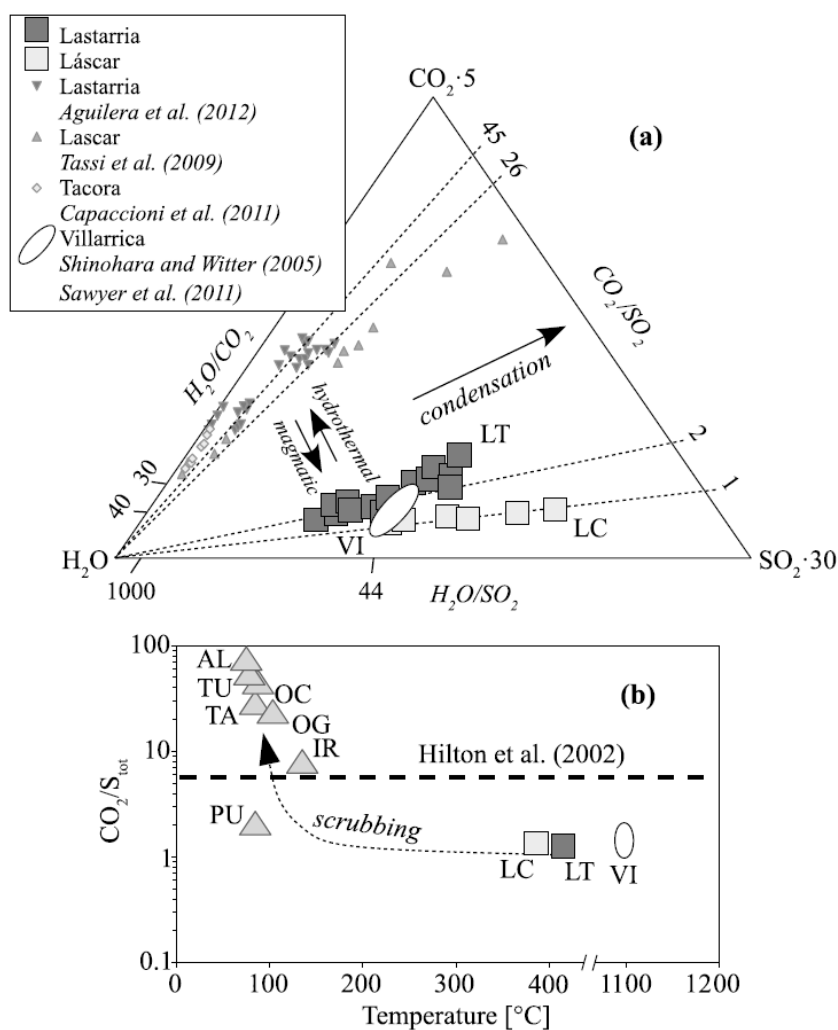
Figure 2. (a) Triangular H_2O-CO_2-SO_2 plot showing the water variability in Lastarria (LT) and Láscar (LC). Compositional data obtained in previous studies (Lastarria, Láscar, and Tacora) show a more hydrothermal nature of the sampled fumarolic gases. Gas compositions converge toward the composition of Villarrica high-temperature gas, which is less affected by water condensation. **(b)** Temperature dependence of CO_2/S_{tot} molar ratios in gas samples from Alitar (AL), Tupungatito (TU), Olca (OC), Ollagüe (OG), Tacora (TA), Irruputuncu (IR), Putana (PU), Láscar (LC), and Lastarria (LT) in the CVZ within northern Chile, and from Villarrica (VI) in the SVZ. Additional data are from Aguilera et al. [2012], Capaccioni et al. [2011], Benavente et al. [2013], Tassi et al. [2011], and Shinohara and Witter [2005].

    Our Láscar and Lastarria results demonstrate considerable fluctuations of water contents (at nearly constant CO_2/S molar ratios) at both volcanoes during the measurement periods (Figure 2a). We ascribe this effect to variable extents of water loss—due to condensation—from the plume prior to the sampling associated with MultiGAS measurements. However, we notice that the more-hydrous and thus possibly less-fractionated compositions of the Lastarria and Láscar gas samples converge in Figure 2a toward the composition of Villarrica gas [Shinohara and Witter, 2005], and cluster at CO_2/SO_2 and H_2O/CO_2 molar ratios of 1–2 and 30–40, respectively. We conclude from Figure 2a that both the Lastarria and Láscar gas samples have a clear magmatic signature. This is in stark contrast with the more S-depleted (Figure 2a) and Cl-depleted (Figure 3) compositions seen in previous direct-sampling studies performed at Láscar (2002–2006 [Tassi et al., 2009]) and Lastarria (2006–2009 [Aguilera et al., 2012]), which supported the presence of gases with a more hydrothermal nature. This difference may merely reflect dissimilar sampling conditions: while the 2012 MultiGAS observations concentrated on the "bulk" plume, the earlier direct sampling studies (2002–2009) concentrated on a small number of easily accessible, low-flux fumaroles. These fumaroles are potentially more affected by secondary processes (e.g., scrubbing), making their composition potentially unrepresentative of bulk gas emissions. Alternatively, the more magmatic signature of the 2012 gases, relative to pre-2009 geochemical studies show that the SVZ slab component is also uniform across the arc [Jacques et al., 2013]. Thus, we interpret the similarly low Ba/La ratios (15–25) in SVZ and CVZ magmas to imply a uniform, more modest (relative to CAVA) contribution from slab-derived fluids, fitting well the low-carbon signature of Chilean volcanic gases seen in this study. We admit, however, that since only three volcanoes with high-T gases were measured, more observations are needed to corroborate our hypothesis.
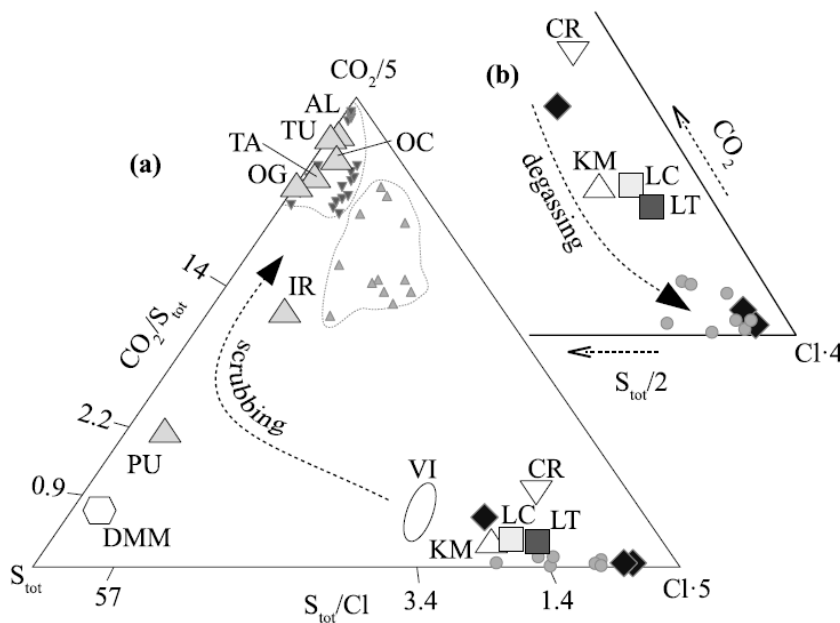
Figure 3. (a) Triangular CO_2-S_{tot}-HCl plot of the molar gas compositions of northern Chile volcanoes and Villarrica. The compositions of the melt inclusions from Villarrica (dark gray diamonds) and residual glasses from Llaima (small gray circles) are shown. Previous data of Láscar [Tassi et al., 2009] and Lastarria [Aguilera et al., 2012] fumaroles are displayed within the dotted gray lines. For comparison, the Costa Rica magmatic gas (CR, white triangle) from A. Aiuppa et al. (The Costa Rica-Nicaragua volcanic segment: along-arc variations in volcanic gas chemistry and an improved CO_2 budget, submitted to Earth and Planetary Science Letters, 2014) is also shown. Compositional data of depleted mid-ocean ridge basalt mantle (DMM, white hexagon) are from Saal et al. [2002]. (b) Magnification of the lower right part of the triangular plot highlighting a degassing trend from a CO2-rich end-member to a Cl-rich end-member.

4.2. Volatiles Output from the CVZ

Given the magmatic nature of the gas samples discussed above, we now attempt to constrain the total output of volatiles from the CVZ. The scanning Mini-DOAS and UV camera measurements made at Lastarria, Láscar, Putana, San Pedro, and Ollagüe lead to a cumulative SO_2 output from the five volcanoes of ~1800 t d^{-1} (or 6.6×10^5 t yr^{-1}) in 2012–2013 (Table 1). Three additional volcanoes (Irruputuncu, Olca, and Tacora) in this arc segment are reported to comprise high-temperature fumaroles [Capaccioni et al., 2011; Tassi et al., 2011]. The strongest S emitter of the three volcanoes is probably Irruputuncu, a volcano that typically vents S-rich gas [Tassi et al., 2011]. However, even Irruputuncu has regularly failed to produce any statistically significant signal in OMI (Ozone Monitoring Instrument) satellite data sets [Carn et al., 2013], implying an SO_2 flux of ≤190 t d^{-1} (considering the OMI detection limit quoted by Fioletov et al. [2011]). Assuming that each of the three volcanoes emits ~100 t d^{-1} on average, the cumulative SO_2 output would only rise to a maximum of ~2100 t d^{-1}. We therefore consider the cumulative SO_2 output from Lastarria, Láscar, Putana, San Pedro, and Ollagüe as a good proxy for the total SO_2 output from the CVZ (Table 1). We avoid using extrapolation techniques to quantify unmeasured emissions [e.g., Hilton et al., 2002] because the validity of the power law assumption of Brantley and Koepenick [1995] has recently been questioned [Mori et al., 2013]. However, we argue that if the recently recorded peak (2300 t d^{-1}) SO_2 emissions from Láscar were to be taken into account [Andres et al., 1991; Mather et al., 2004], the cumulative CVZ SO_2 output would increase to ~3500 t d^{-1} (1.3×10^6 t yr^{-1}). With our assumptions, the total CVZ SO_2 output of 6.6×10^5 to 1.3×10^6 t yr^{-1} would therefore correspond to 19–40% of the extrapolated annual flux from the Andes (~3×10^6 t yr^{-1} [Andres and Kasgnoc, 1998; Hilton et al., 2002]), and to 3.3–5.1% of the estimated global SO_2 fluxes from subduction zone volcanoes [Andres and Kasgnoc, 1998; Hilton et al., 2002; Shinohara, 2013]. For comparison, this inferred CVZ SO_2 output is of the same order as the combined SO_2 output from Villarrica and Llaima (~3.5×10^5 t yr^{-1} [Mather et al., 2004; Sawyer et al., 2011]), which are the two most actively degassing volcanoes in the SVZ (a similar rate of quiescent SO_2 degassing (~7.66×10^5 t yr^{-1}) was recently proposed by Völker et al. [2014] for the SVZ). Considering the unknown but potentially additional large contributions from recently erupting volcanoes (e.g., Puyehue-Cordón Caulle and Copahue), SVZ is probably the strongest degassing source in Chile.

The measured SO_2 fluxes combined with the volcanic gas compositions of Láscar and Lastarria provide the basis for quantifying the outputs of other major volatiles. Despite its apparent long inactivity, Lastarria currently represents the most important gas source in the CVZ, with a total volatiles output (~13,500 t d^{-1}) that is twice that of Láscar (~6517 t d^{-1}) (Table 1). These two volcanoes have a combined CO_2 output of ~1500 t d^{-1}. We additionally estimate, based on a total SO_2 output of ~1800 t d^{-1} and a magmatic CO_2/S_{tot} ratio of 0.9–2.2, that the total CO_2 output from the CVZ is 1743–1988 t d^{-1}. Based on these calculations, northern Chile contributes only a minor fraction (~1%) of the total CO_2 output from subaerial volcanoes worldwide [Burton et al., 2013]. We stress that this CO_2 budget does not take into account the contribution of diffuse soil degassing, which is poorly constrained for Chilean volcanoes, except for Villarrica. At this volcano, CO_2 soil degassing was found to be negligible compared to summit crater degassing [Witter et al., 2004].

In an attempt to evaluate how representative our 2012–2013 measurements are of the long-term degassing behavior of the CVZ, we compared the present-day gas fluxes of Table 1 with petrological volatiles output inventories. In the last 12 Myr, the rate of magma extrusion along the ~330 km long Central Andean trench (from 12°30′S to 22°30′S) has been ~2.2 × 10^{-6} km^3 km^{-1} yr^{-1} [Crisp, 1984]. A comparable rate (10–13 × 10^{-6} km^3 km^{-1} yr^{-1}) was estimated by Völker et al. [2011] for the SVZ. If we tentatively extend the Central Andean magma extrusion rate to northern Chile and scale it to the total trench length of 1500 km, we then obtain an order of magnitude estimate for the CVZ magma eruption rate of ~3.3 × 10^{-3} km^3 yr^{-1}. For a magma density of 2800 kg m^{-3} (andesite) and for preeruptive and posteruptive magmatic S contents of ~4100 and ~300 mg kg^{-1}, respectively (as for S in primitive undegassed melt inclusions and residual glasses of Láscar [Andres et al., 1991]), this would correspond to a time-averaged SO_2 output of ~7.6 × 10^4 t yr^{-1} from CVZ volcanism. The proposed (mass) ratio between intrusive and extrusive volcanism for the Andes is ~6/1 [Crisp, 1984], which leads to a total (intrusive + extrusive) SO_2 output of ~5.3 × 10^5 t yr^{-1} (Table 1). Finally, the magmatic gas CO_2/S_{tot} ratio of ~0.9–2.2 (molar) converts the SO_2 output into a total CO_2 output of 3.3–8.1 × 10^5 t yr^{-1} (Table 1). The resulting annual SO_2 and CO_2 petrological outputs are in close agreement with our present-day (2012–2013) outputs of ~6.4–7.3 × 10^5 and 6.3 × 10^5 t yr^{-1}, respectively (Table 1). While our calculations here should be taken as order of magnitude estimates (given the overall uncertainties in the input parameters), the similarity of these values suggests (i) that the present-day fluxes are representative of the long-term CVZ degassing behavior and (ii) that Láscar and Lastarria contribute most of the CVZ gas output. The absence of Deep Sea Drilling Project/Ocean Drilling Program reference sites offshore of northern Chile, and the lack of knowledge about the compositions of subducted materials [Plank and Langmuir, 1998], precludes quantitative comparison between our measured CO_2 output and the CO_2 input flux at the trench (as recently obtained for other arc segments [Freundt et al., 2014; Völker et al., 2014]).

5. Conclusions

The Láscar and Lastarria volcanoes in northern Chile emitted in 2012–2013 a typically magmatic gas phase whose compositions of major species (H_2O/CO_2=30–40, CO_2/S_{tot}=0.9–2.2; S_{tot}/HCl = 1.4–3.4) resembled those of high-temperature open-vent emissions from Villarrica in the SVZ. This similarity suggests stable magmatic volatiles contents and origin along several thousands of kilometers of the southern Andean trench. We calculate that the CVZ presently emits more than 10^7 t yr^{-1} H_2O-rich volcanic gases into the atmosphere, essentially in a quiescent (noneruptive) form. Our measured CO_2 (~1500 t d^{-1}) and SO_2 (~1800 t d^{-1}) outputs in 2012–2013 correspond, respectively, to ~1.3% and ~3.3–5.1% of the corresponding global gas outputs from arc volcanoes. These present-day fluxes closely match the petrologically estimated long-term outputs obtained from intrusive + extrusive magma fluxes and preeruptive S contents.

_____

References

Aguilera, F., F. Tassi, T. Darrah, S. Moune, and O. Vaselli (2012), Geochemical model of a magmatic-hydrothermal system at the Lastarria volcano, northern Chile, Bull. Volcanol., 74, 119–134.

Aiuppa, A. (2009), Degassing of halogens from basaltic volcanism: Insights from volcanic gas observations, Chem. Geol., 263, 99–109, doi:10.1016/j.chemgeo.2008.08.022.

Aiuppa, A., G. Giudice, M. Liuzzo, G. Tamburello, P. Allard, S. Calabrese, L. Chaplygin, A. J. S. McGonigle, and Y. Taran (2012), First volatile inventory for Gorely volcano, Kamchatka, Geophys. Res. Lett., 39, L06307, doi:10.1029/2012GL051177.

Andres, R. J., and A. D. Kasgnoc (1998), A time-averaged inventory of subaerial volcanic sulfur emissions, J. Geophys. Res., 103, 25,251–25,262, doi:10.1029/98JD02091.

Andres, R. J., W. I. Rose, P. R. Kyle, S. de Silva, P. Francis, M. Gardeweg, and H. M. Roa (1991), Excessive sulfur dioxide emissions from Chilean volcanoes, J. Volcanol. Geotherm. Res., 46, 323–329. DOI:10.1016/0377-0273(91)90091-D

Benavente, O., F. Tassi, F. Gutiérrez, O. Vaselli, F. Aguilera, and M. Reich (2013), Origin of fumarolic fluids from Tupungatito Volcano (Central Chile): Interplay between magmatic, hydrothermal, and shallow meteoric sources, Bull. Volcanol., 75, 746, doi:10.1007/s00445-013-0746-x.

Brantley, S. L., and K. W. Koepenick (1995), Measured carbon emissions from Oldoinyo Lengai and the skewed distribution of passive volcanic fluxes, Geology, 23, 933–936. doi: 10.1130/0091-7613(1995)023<0933:MCDEFO>2.3.CO;2

Burton, M. R., G. M. Sawyer, and D. Granieri (2013), Deep carbon emissions from volcanoes, Rev. Mineral. Geochem., 75, 323–354, doi:10.2138/rmg.2013.75.11.

Capaccioni, B., F. Aguilera, F. Tassi, T. Darrah, R. J. Poreda, and O. Vaselli (2011), Geochemical and isotopic evidences of magmatic inputs in the hydrothermal reservoir feeding the fumarolic discharges of Tacora volcano (northern Chile), J. Volcanol. Geotherm. Res., 208, 77–85, doi:10.1016/j.jvolgeores.2011.09.015.

Carn, S., N. A. Krotkov, K. Yang, and A. J. Krueger (2013), Measuring global volcanic degassing with the Ozone Monitoring Instrument (OMI), in Remote Sensing of Volcanoes and Volcanic Processes: Integrating Observation and Modelling, Spec. Publ., vol. 380, edited by D. M. Pyle, T. A. Mather, and J. Biggs, pp. 229–257, Geological Society, London, U. K.

Casertano, L. (1963), General characteristics of active Andean volcanoes and a summary of their activities during recent centuries, Bull. Seismol. Soc. Am., 53, 1415–1433. doi:10.1016/0040-1951(79)90101-X

Crisp, J. A. (1984), Rates of magma emplacement and volcanic output, J. Volcanol. Geotherm. Res., 20, 177–211. doi:10.1016/0377-0273(84)90039-8

Davidson, J. P., N. J. McMillan, S. Moorbath, G. Woerner, R. S. Harmon, and L. Lopez-Escobar (1990), The Nevados de Payachata volcanic region (18°S/69°W. N. Chile). II. Evidence for widespread crustal involvement in Andean magmatism, Contrib. Mineral. Petrol., 105, 412–432. DOI:10.1007/BF00286829

de Maisonneuve, C., M. A. Bouvet, O. B. Dungan, and A. Burgisser (2012), Insights into shallow magma storage and crystallization at Volcán Llaima (Andean Southern Volcanic Zone, Chile), J. Volcanol. Geotherm. Res., 211–212, 76–91. doi:10.1016/j.jvolgeores.2011.09.010

Feeley, T. C., J. P. Davidson, and A. Armendia (1993), The volcanic and magmatic evolution of Volcan Ollagüe, a high-K, late Quaternary stratovolcano in the Andean Central Volcanic Zone, J. Volcanol. Geotherm. Res., 54, 221–245. doi:10.1016/0377-0273(93)90065-Y

Fioletov, V. E., C. A. McLinden, N. Krotkov, M. D. Moran, and K. Yang (2011), Estimation of SO2 emissions using OMI retrievals, Geophys. Res. Lett., 38, L21811, doi:10.1029/2011GL049402.

Fischer, T. P. (2008), Fluxes of volatiles (H_2O, CO_2, N_2, Cl, F) from arc volcanoes, Geochem. J., 42, 21–38. DOI: 10.2343/geochemj.42.21

Freundt, A., I. Grevemeyer, W. Rabbel, T. H. Hansteen, C. Hensen, H. Wehrmann, S. Kutterolf, R. Halama, and M. Frische (2014), Volatile (H_2O, CO_2, Cl, S) budget of the Central American subduction zone, Int. J. Earth Sci. (Geol Rundsch), doi:10.1007/s00531-014-1001-1.

Froger, J. L., D. Remy, S. Bonvalot, and D. Legrand (2007), Two scales of inflation at Lastarria-Cordon del Azufre volcanic complex, central Andes, revealed from ASAR-ENVISAT interferometric data, Earth Planet. Sci. Lett., 255(1–2), 148–163. doi:10.1016/j.epsl.2006.12.012

Galle, B., M. Johansson, C. Rivera, Y. Zhang, M. Kihlman, C. Kern, T. Lehmann, U. Platt, S. Arellano, and S. Hidalgo (2010), Network for Observation of Volcanic and Atmospheric Change (NOVAC)—A global network for volcanic gas monitoring: Network layout and instrument description, J. Geophys. Res., 115, D05304, doi:10.1029/2009JD011823.

Global Volcanism Program (1994), Láscar, volcanic activity reports, BGVN 18:04. [Available at http://www.volcano.si.edu.]

Henney, L., L. Rodríguez, and I. Watson (2012), A comparison of SO2 retrieval techniques using mini-UV spectrometers and ASTER imagery at Láscar volcano, Chile, Bull. Volcanol., 74(2), 589–594, doi:10.1007/s00445-011-0552-2.

Hildreth, W., and S. Moorbath (1988), Crustal contributions to arc magmatism in the Andes of Central Chile, Contrib. Mineral. Petrol., 98, 455–489.

Hilton, D. R., T. P. Fischer, and B. Marty (2002), Noble gases and volatile recycling at subduction zones, Rev. Mineral. Geochem., 47, 319–370.

Jacques, G., K. Hoernle, J. Gill, F. Hauff, H. Wehrmann, D. Garbe-Schönberg, P. van den Bogaard, I. Bindeman, and L. E. Lara (2013), Across-arc geochemical variations in the Southern Volcanic Zone, Chile (34.5–38.0°S): Constraints on mantle wedge and slab input compositions, Chem. Geol., 371, 27–45, doi:10.1016/j.gca.2013.05.016.

Jacques, G., K. Hoernle, J. Gill, H. Wehrmann, I. Binderman, and L. E. Lara (2014), Geochemical variations in the Central Southern Volcanic Zone, Chile (38–43°S): The role of fluids in generating arc magmas, Chem. Geol., 371, 27–45, doi:10.1016/j.chemgeo.2014.01.015.

Kantzas, E. P., A. J. S. McGonigle, G. Tamburello, A. Aiuppa, and R. G. Bryant (2010), Protocols for UV camera volcanic SO2 measurements, J. Volcanol. Geotherm. Res., 194, 55–60, doi:10.1016/j.jvolgeores.2010.05.003.

Mather, T. A., V. I. Tsanev, D.M. Pyle, A. J. S. McGonigle, C. Oppenheimer, and A. G. Allen (2004), Characterization and evolution of tropospheric plumes from Láscar and Villarrica volcanoes, Chile, J. Geophys. Res., 109, D21303, doi:10.1029/2004JD004934.

Mather, T. A., D. M. Pyle, V. I. Tsanev, A. J. S. McGonigle, C. Oppenheimer, and A. G. Allen (2006), A reassessment of current volcanic emissions from the Central American arc with specific examples from Nicaragua, J. Volcanol. Geotherm. Res., 149, 97–311, doi:10.1016/j.jvolgeores.2005.07.021.

Matthews, S. J., A. P. Jones, and M. C. Gardeweg (1994), Láscar volcano, northern Chile: Evidence for steady-state disequilibrium, J. Petrol., 59, 72–82.

Matthews, S. J., M. C. Gardeweg, and R. S. J. Sparks (1997), The 1984 to 1996 cyclic activity of Láscar volcano, northern Chile: Cycles of dome growth, dome subsidence, degassing and explosive eruptions, Bull. Volcanol., 59, 72–82.

Matthews, S. J., R. S. J. Sparks, and M. C. Gardeweg (1999), The Piedras Grandes–Soncor eruptions, Láscar Volcano, Chile; Evolution of a zoned magma chamber in the Central Andean upper crust, J. Petrol., 40(12), 1891–1919, doi:10.1093/petroj/40.12.1891.

Mori, T., H. Shinohara, K. Kazahaya, J. Hirabayashi, T. Matsushima, T. Mori, M. Ohwada, M. Odai, H. Iino, and M. Miyashita (2013), Time-averaged SO_2 fluxes of subduction-zone volcanoes: Example of a 32 years exhaustive survey for Japanese volcanoes, J. Geophys. Res. Atmos., 118, 8662–8674, doi:10.1002/jgrd.50591.

Naranjo, J. A. (1986), Geology and evolution of the Lastarria volcanic complex, north Chilean Andes, MSc thesis, The Open Univ., Milton Keynes, Bucks., U. K.

O'Callaghan, L. J., and P. W. Francis (1986), Volcanological and petrological evolution of San Pedro volcano, Provincia El Loa, north Chile, J. Geol. Soc. London., 143, 275–286.

Oppenheimer, C., P. W. Francis, D. A. Rothery, and R. W. T. Carlton (1993), Infrared image analysis of volcanic thermal features: Láscar volcano, Chile 1984–1992, J. Geophys. Res., 98, 4269–4286, doi:10.1029/92JB02134.

Plank, T., and T. P. Langmuir (1998), The chemical composition of subducting sediment and its consequences for the crust and mantle, Chem. Geol., 145, 325–394.

Pritchard, M. E., and M. Simons (2002), A satellite geodetic survey of large-scale deformation of volcanic centres in the central Andes, Nature, 418, 167–171.

Richards, J. P., F. Jourdan, R. A. Creaser, G. Maldonado, and S. A. DuFrane (2013), Geology, geochemistry, geochronology, and economic potential of Neogene volcanic rocks in the Laguna Pedernal and Salar de Aguas Calientes segments of the Archibarca lineament, northwest Argentina, J. Volcanol. Geotherm. Res., 268, 47–73, doi:10.1016/j.jvolgeores.2013.04.004.

Saal, A. E., E. H. Hauri, C. H. Langmuir, and M. R. Perfit (2002), Vapour undersaturation in primitive mid-ocean-ridge basalt and the volatile content of the Earth's upper mantle, Nature, 419, 451–455, doi:10.1038/nature01073.

Sadofsky, S. J., M. V. Portnyagin, K. Hoernle, and P. van den Bogaard (2008), Subduction cycling of volatile and trace elements through the Central American volcanic arc: Evidence from melt inclusions, Contrib. Mineral. Petrol., 155(4), 433–456, doi:10.1007/s00410-007-0251-3.

Sawyer, G. M., G. G. Salerno, J. S. Le Blond, R. S. Martin, L. Spampinato, T. J. Roberts, T. A. Mather, M. L. I. Witt, V. I. Tsanev, and C. Oppenheimer (2011), Gas and aerosol emissions from Villarrica volcano, Chile, J. Volcanol. Geotherm. Res., 203, 62–75.

Shinohara, H. (2013), Volatile flux from subduction zone volcanoes: Insights from a detailed evaluation of the fluxes from volcanoes in Japan, J. Volcanol. Geotherm. Res., doi:10.1016/j.jvolgeores.2013.10.007.

Shinohara, H., and J. Witter (2005), Volcanic gases emitted during mild Strombolian activity of Villarrica volcano, Chile, Geophys. Res. Lett., 32, L20308, doi:10.1029/2005GL024131.

Stern, C. R. (2004), Active Andean volcanism: Its geologic and tectonic setting, Rev. Geol. Chile, 31(2), 161–206.

Symonds, R. B., T. M. Gerlach, and M. H. Reed (2001), Magmatic gas scrubbing: Implications for volcano monitoring, J. Volcanol. Geotherm. Res., 108, 303–341.

Tassi, F., F. Aguilera, O. Vaselli, E. Medina, D. Tedesco, A. Delgado Huertas, R. Poreda, and S. Kojima (2009), The magmatic- and hydrothermal dominated fumarolic system at the Active Crater of Láscar volcano, northern Chile, Bull. Volcanol., 71, 171–183.

Tassi, F., F. Aguilera, O. Vaselli, T. Darrah, and E. Medina (2011), Gas discharges from four remote volcanoes in northern Chile (Putana, Olca, Irruputuncu and Alitar): A geochemical survey, Ann. Geophys., 54(2), doi:10.4401/ag-5173.

Thorpe, R. S. (1984), The tectonic setting of active Andean volcanism, in Andean Magmatism: Chemical and Isotopic Constraints, Shiva Geological Series, edited by R. S. Harmon and B. A. Barreiro, pp. 5–8, Shiva Publications, Nantwich, U. K.

Thorpe, R. S., and P. W. Francis (1979), Variations in Andean andesite compositions and their petrogenetic significance, Tectonophysics, 57, 53–80.

Völker, D., S. Kutterolf, and H. Wehrmann (2011), Comparative mass balance of volcanic edifices at the southern volcanic zone of the Andes between 33°S and 46°S, J. Volcanol. Geotherm. Res., 205, 114–129, doi:10.1016/j.jvolgeores.2011.03.011.

Völker, D., H. Wehrmann, S. Kutterolf, K. Iyer, W. Rabbel, J. Geersen, and K. Hoernle (2014), Constraining input and output fluxes of the southern Central Chile Subduction Zone: Water, chlorine, sulfur, Int. J. Earth Sci., doi:10.1007/s00531-014-1002-0.

Watt, S. F. L., D. M. Pyle, T. A. Mather, and J. A. Naranjo (2013), Arc magma compositions controlled by linked thermal and chemical gradients above the subducting slab, Geophys. Res. Lett., 40, 2550–2556, doi:10.1002/grl.50513.

Wehrmann, H., K. Hoernle, G. Jacques, D. Garbe-Schönberg, K. Schumann, J. Mahlke, and L. E. Lara (2014a), Volatile (sulphur and chlorine), major, and trace element geochemistry of mafic to intermediate tephras from the Chilean Southern Volcanic Zone (33–43°S), Int. J. Earth Sci., doi:10.1007/s00531-014-1006-9.

Wehrmann, H., K. Hoernle, D. Garbe-Schönberg, G. Jacques, J. Mahlke, and K. Schumann (2014b), Insights from trace element geochemistry as to the roles of subduction zone geometry and subduction input on the chemistry of arc magmas, Int. J. Earth Sci., doi:10.1007/s00531-013-0917-1.

_____

Witter, J. B., C. Victor, P. Kress, J. Delmelle, and J. Stix (2004), Volatile degassing, petrology, and magma dynamics of the Villarrica Lava Lake, Southern Chile, J. Volcanol. Geotherm. Res., 134, 303–337.)

Supplementary Material to Tamburello et al (2014) Gas emissions from five volcanoes in northern Chile, and implications for the volatiles budget of the Central Volcanic Zone. Geophys Res Lett

S1. Sulphur dioxide emission rates

S1.1 Mini-DOAS data

SO_2 fluxes were measured using two transportable scanning Mini-DOAS systems. These instruments contain a scanning UV spectrometer similar to the Version I system of the Network for Observation of Volcanic and Atmospheric Change (NOVAC) project (Galle et al., 2010), but are integrated into a transportable, ready-to-deploy unit. Data acquisition and analysis were performed according to the procedures adopted in the NOVAC project. The instruments were located as close as possible to directly beneath the plume, and scans were performed perpendicular to the plume direction. Plume heights were determined by triangulation between simultaneous scans performed using two instruments, and the wind speed at the plume height was estimated with the GDAS (Global Data Assimilation System) model of NOAA (National Oceanic and Atmospheric Administration), and scaled according to the results of independent wind-speed measurements.

   Such wind-speed measurements were made at least once per volcano and field campaign, and included direct measurements using an SO_2 camera or an upward-looking dual-channel Mini-DOAS system, or via time-lapse photography of the visible plume.

Table S1. Statistical summary of SO_2 flux data used in this study. The table contains the SO_2 flux data for 5 volcanoes in northern Chile during the period November 2012 – December 2013, measured using two transportable scanning Mini-DOAS systems described in further detail in the paper.

Volcano	Date	Scans/day	Average [t d⁻¹]	Min [t d⁻¹]	Max [t d⁻¹]	St.Dev. [t d⁻¹]	Wind speed [m s⁻¹]
Lastarria	2012-11-27	27	1916.68	1352.84	2868.98	607.24	16.4
	2012-11-28	65	472.85	268.73	782.23	187.72	13.2
	2012-11-29	54	433.49	205.41	1054.50	314.19	13.5
Total		**146**	**883.62**	**205.41**	**2868.98**	**778.98**	**14.2**
Láscar	2012-12-03	58	363	117	1193	352	7.2
	2012-12-05	21	972	524	1317	407	6.8
	2012-12-06	46	277	138	643	200	10.3
	2012-12-07	25	730	252	1178	464	10.0
	2013-12-02	32	604	157	1964	680	6.8
	2013-12-03	23	711	155	1492	620	5.6
	2013-12-04	31	127	67	230	67	3.4
	2013-12-08	19	645	447	749	172	4.7
Total		**255**	**554**	**67**	**1964**	**217**	**6.8**
Putana	2013-12-05	79	55.21	35.03	65.73	13.83	4.9
	2013-12-06	108	131.50	31.97	335.91	104.34	7.4
	2013-12-09	44	77.18	42.50	96.95	24.47	6.7
Total		**231**	**96.67**	**31.97**	**335.91**	**77.72**	**6.5**
San Pedro	2013-12-10	54	182.20	55.72	461.83	188.22	4.6
	2013-12-12	54	149.84	56.83	465.97	140.13	9.7
Total		**108**	**160.63**	**55.72**	**465.97**	**149.70**	**8.0**
Ollagüe	2013-12-11	32	46.92	33.50	71.98	17.75	1.8
	2013-12-12	33	219.56	89.18	552.26	181.05	11.5
Total		**65**	**150.50**	**33.50**	**552.26**	**162.06**	**7.6**

Header description:
1.1 Column "Volcano", Name of the volcano which SO_2 flux has been measured.
1.2 Column "Scans/day", Number of DOAS scans performed on the specified date.
1.3 Column "Average", t·d⁻¹, Average SO_2 flux on the specified date.
1.4 Column "Min", t·d⁻¹, Minimum SO_2 flux measured on the specified date.
1.5 Column "Max", t·d⁻¹, Maximum SO_2 flux measured on the specified date.
1.6 Column "St.Dev.", t·d⁻¹, Standard deviation of the daily SO_2 flux dataset.
1.7 Column "Wind speed", m·s⁻¹, Wind speed used for the calculation of the SO_2 flux for each day.

S2. Chemical composition of volcanic gas emissions

S2.1 Multi-GAS data

The concentrations of major volcanogenic constituents in the volcanic plume were monitored using a portable version of the MultiGAS (Aiuppa et al., 2007). This device employs an LI-840 NDIR closed-path spectrometer for measuring CO_2 (measurement range, 0–3000 ppm; accuracy, ±1.5%) and H_2O (measurement range, 0–80 ppt; accuracy, ±1.5%), a suite of electrochemical sensors for measuring SO_2 (calibration range, 0–200 ppmv; accuracy, ±2%; resolution, 0.5 ppmv; sensor type 3ST/F, City Technology), H_2S (calibration range, 0–50 ppmv; accuracy, ±5%; resolution, 0.7 ppmv; sensor type 2E, SensoriC), and H_2 (0–200 ppm; EZT3HYT "Easy Cal" electrochemical sensor, City Technology), and sensors for measuring temperature (measurement range, from 30°C to 70°C; resolution, 0.01°C) and relative humidity (measurement range, 0–100% Rh; accuracy, ±2%; Galltec). For the present field campaigns the sensors were housed in a waterproof box mounted on a backpack frame, and were calibrated both before and after performing the fieldwork using standard calibration gases. Signals from all sensors were simultaneously captured at 0.5 Hz with a data-logger board, on which the signals could also be stored. In-plume measurements were run for several hours during each field survey, resulting in the acquisition of a large number of measurements; the raw data were processed according to Shinohara et al. (2008) and Aiuppa et al. (2010) to derive the characteristic molar ratios of volcanic gas species.

S2.2 Filter pack data

Acidic gases (SO_2, HF, HCl, and HBr) in the plumes were collected using the filter-pack technique (Finnegan et al., 1989). Plume air was pumped at a constant flow rate (4 $l \cdot m^{-1}$; sampling time, 80–280 min) through a sampler consisting of three filter holders in series, with each containing one filter impregnated with 1 N $NaHCO_3$. In the laboratory, filters were leached in bidistilled water (+H_2O_2) and the leachates were analyzed for F (using an ion-selective electrode), Cl and SO_4^{2-} [using ion chromatography (IC)], and Br (inductively coupled plasma mass spectrometry) (Aiuppa et al., 2005).

Table S2. Gas molar ratios of Lastarria and Láscar volcanoes. The table contains the gas molar ratios obtained using the INGV-type Multicomponent Gas Analyzer System (MultiGAS) and sets of base-treated filter packs. *Multi-GAS derived molar ratios and # Filter pack derived molar ratios.

Method:	Multi-GAS				Filter packs			
Volcano	CO_2/SO_2*	SO_2/H_2S*	CO_2/S_{tot}*	H_2O/CO_2*	S_{tot}/Cl#	Cl/F#	S_{tot}/Br#	Br/I#
Lastarria	1.6	2.7	1.17	27.8	1.31	36.15	2000	586
Láscar	1.4	9.9	1.27	23.8	1.59	11.57	4718	NA

Header description:
2.1 Column "Volcano", Name of the volcano which gas composition has been measured.
2.2 Column "CO_2/SO_2", molar ratio, MultiGAS derived CO_2/SO_2 molar ratios.
2.2 Column "SO_2/H_2S", molar ratio, MultiGAS derived SO_2/H_2S molar ratios.
2.4 Column "CO_2/S_{tot}", molar ratio, MultiGAS derived CO_2/S_{tot} molar ratios.
2.5 Column "H_2O/CO_2", molar ratio, MultiGAS derived H_2O/CO_2 molar ratios.
2.6 Column "S_{tot}/Cl", molar ratio, filter-pack derived S_{tot}/Cl molar ratios.
2.7 Column "Cl/F", $m \cdot s^{-1}$, filter-pack derived Cl/F molar ratios.
2.8 Column "S_{tot}/Br", filter-pack derived S_{tot}/Br molar ratios.
2.9 Column "Br/I", filter-pack derived Br/I molar ratios.

S2.3 Direct gas sampling data

Gas samples from the Ollagüe fumaroles were collected according to the method outlined for Cd-soda bottles by Montegrossi et al. (2001). Gases were analyzed using a Shimadzu 15A gas chromatograph equipped with a thermal conductivity detector and a packed molecular sieve 5A column. #Liquid and solid phases representing the adsorbed gases were analyzed using wet chemistry and IC (Montegrossi et al., 2001). *Water vapor was quantified based on the sample mass difference after subtracting the absorbed gas masses; the analytical uncertainty was <5%.

Table S3. Chemical composition of two fumaroles sampled on Ollagüe volcano. The table contains the first chemical composition of two fumaroles of Ollagüe fumarolic system collected on June 5, 2005.

Sample	Latitude	Longitude	Altitude	T°C	CO$_2$#	HCl#	HF#	SO$_2$#	H$_2$S#	H$_2$O*	N$_2$	CH$_4$	Ar	O$_2$	H$_2$	He	CO	δ^{13}C
OL1	21°18'45" S	68°10'23" O	5570	107	66	0.01	0.002	1.6	1.5	929	1.8	0.059	0.0034	0.0021	0.071	0.00026	0.0038	-6.78
OL2	21°18'45" S	68°10'23" O	5570	111	72	0.02	0.002	1.8	1.2	923	1.6	0.063	0.0031	0.0015	0.089	0.00034	0.0044	-6.27

Header description:
3.1 Column "Latitude", degrees, latitude of the sampled fumarole.
3.2 Column "Longitude", degrees, longitude of the sampled fumarole.
3.3 Column "Altitude", m, altitude of the sampled fumarole.
3.4 Column "Temperature", °C, temperature of the gas at the sampling site.
3.5-3.7 Columns, mmol·mol^{-1}, concentration of the specified gas.
3.8 Column "δ^{13}C", ‰, measure of the ratio of stable isotopes ^{13}C.

References

Aiuppa, A., R. Moretti, C. Federico, G. Giudice, S. Gurrieri, M. Liuzzo, P. Papale, H. Shinohara, and M. Valenza (2007), Forecasting Etna eruptions by real-time observation of volcanic gas composition, *Geology*, 35, 1115–1118, doi:10.1130/G24149A.1.

Aiuppa, A., A. Bertagnini, N. Métrich, R. Moretti, A. Di Muro, M. Liuzzo and G. Tamburello (2010), A model of degassing for Stromboli volcano, *Earth Planet. Sci. Lett.,* 295, 195–204, doi:10.1016/j.epsl.2010.03.040.

Finnegan, D., J. Kotra, D. Hermann and W. Zoller (1989), The use of ^{7}LiOH-impregnated filters for the collection of acidic gases and analysis by instrumental neutron activation analysis, *Bulletin of Volcanology*, 51, 83–87. DOI: 10.1007/BF01081977

Galle, B., M. Johansson, C. Rivera, Y. Zhang, M. Kihlman, C. Kern, T. Lehmann, U. Platt, S. Arellano and S. Hidalgo (2010), Network for Observation of Volcanic and Atmospheric Change (NOVAC); A global network for volcanic gas monitoring: Network layout and instrument description, *J. Geophys. Res.* 115, D05304, doi:10.1029/2009JD011823.

Montegrossi, G., F. Tassi, O. Vaselli, A. Buccianti, K. Garofalo (2001). Sulfur species in volcanic gases, *Anal. Chem.*, 73, 3709-3715. DOI: 10.1021/ac001429b

Shinohara, H., A. Aiuppa, G. Giudice, S. Gurrieri and M. Liuzzo, (2008), Variation of H$_2$O/CO$_2$ and CO$_2$/SO$_2$ ratios of volcanic gases discharged by continuous degassing of Mount Etna volcano, Italy, *J. Geophys. Res.*, 113, B09203, doi:10.1029/2007JB005185.

CHAPTER VI

Radar path delay effects in volcanic gas plumes: The case of Láscar volcano, Northern Chile

Radar path delay effects in volcanic gas plumes: The case of Láscar volcano, Northern Chile

Stefan Bredemeyer[1,2] · **Franz-Georg Ulmer**[3] · **Thor H.Hansteen**[2] · **Nicole Richter**[4] · **Elske De Zeeuw van Dalfsen**[4] · **Thomas Walter**[4]

Abstract Interferometric Synthetic Aperture Radar (InSAR) is largely affected by changes in atmospheric refractivity, in particular by changes which can be attributed to the distribution of water vapour in the atmospheric column. Gas emissions from continuously degassing volcanoes contain abundant water vapour and thus produce variations in the atmospheric water vapour content above and downwind of the volcano. These variations may in turn cause differential phase errors due to excess radar path delay effects within the volcanic gas plume. Mitigation of such phase signatures demands estimation of the precipitable water vapour (PWV) content in the plume at the time of SAR acquisitions. In this work we investigate the radar path delays that were generated by water vapour contained in the volcanic gas plume of the persistently degassing Láscar volcano, which is located in the dry Atacama Desert of Northern Chile, aiming to quantify the effect and to propose a method that enables mitigation of such disturbances. Estimates of water vapour contents were based on measurements from a ground-based scanning Mini-DOAS (Differential Optical Absorption Spectroscopy; UV spectrometer) station permanently installed at Láscar volcano, and a multi-GAS (multi-component Gas Analyzer System; IR spectrometer and electrochemical gas sensors) survey conducted during a measurement campaign in 2012. Sulphur dioxide emission measurements obtained from the Mini-DOAS, were scaled by H_2O/SO_2 molar mixing ratio, derived from in-situ gas concentration measurements of the multi-GAS instrument deployed on the crater rim of the volcano. In order to calculate the water vapour content in the downwind portion of the plume, where an increase of water vapour is expected, we further applied a correction involving estimation of potential evaporation rates of water droplets governed by turbulent mixing of the condensed volcanic plume with the dry atmosphere. This yielded daily average PWV contents inside the volcanic gas plume of 0.2-2.5 mm equivalent water column, which translate to a slant wet delay of 1.6-20 mm. These estimates were used in combination with TerraSAR-X observations, in order to investigate the spatial distribution of repeating atmospheric delay patterns generated by volcanic gas emissions, by means of the Cinderella algorithm. The observed effect is significant, and should be investigated in more detail, as gas plume related interferometric signals of volcanoes may be interpreted as deformation signals.

Keywords InSAR · scan-DOAS · multi-GAS · volcanic gases · PWV estimates · radar path delay · Cinderella algorithm · Láscar volcano

S. Bredemeyer (✉) [1]SFB 574, [2]GEOMAR Helmholtz Centre for Ocean Research Kiel, Wischhofstr. 1-3, 24148 Kiel, Germany
e-mail: sbredemeyer@geomar.de

T. H. Hansteen [2]GEOMAR Helmholtz Centre for Ocean Research Kiel, Wischhofstr. 1-3, 24148 Kiel, Germany

F.-G. Ulmer [3]Deutsches Zentrum für Luft- und Raumfahrt (DLR), Institut für Methodik der Fernerkundung, Oberpfaffenhofen, 82234 Weßling, Germany

N. Richter, E. De Zeeuw van Dalfsen, T. Walter [4]GFZ German Research Centre for Geosciences, Telegrafenberg, 14473 Potsdam, Germany

_____

1. Introduction

Time series measurements of volcanic degassing rates and deformation allow for the evaluation of deep-seated processes influencing the volcano behaviour. Dynamics of degassing are critical for understanding pressure fluctuations in a magmatic and hydrothermal system, which may be related to deformation of the volcanic edifice (Tait et al., 1989; Watson et al., 2000; Sparks et al., 2003; Green & Neuberg, 2006). Differential interferometric synthetic aperture radar (DInSAR) measurements allow for the detection of mm-scale line of sight displacements of the observed surface (Massonnet et al., 1995; Rosen et al., 2000; Lu 2007). The accuracy of satellite radar ground deformation measurements is, however, largely affected by changes in atmospheric refractivity, in particular by changes which can be attributed to the highly variable distribution of water vapour in the observed atmospheric column (Goldstein, 1995; Zebker et al., 1997; Emardson et al., 2003; Remy et al., 2003). Atmospheric contributions to D-InSAR data may have similar magnitudes and wavelengths as the actual ground deformation signal, and thus they need to be removed from interferograms, when deformation measurements are the purpose of monitoring. Interfering contributions from a moist atmosphere can coarsely be predicted and compensated by means of high-resolution numerical weather models like e.g. the Mesoscale Meteorology Model 5 (MM5), or the Weather Research and Forecasting Model (WRF), which provide the information required to predict the atmospheric delay in the line of sight of an interferometric measurement (Foster et al., 2006; Pichelli et al., 2010; Jung et al., 2014; Ulmer & Adam, 2015).

Degassing volcanoes, however, produce their own atmospheric disturbances, and volcanic gas emissions are typically not considered in weather models. Volcanic gas plumes contain abundant water vapour and thus produce variations in the atmospheric water vapour content above and downwind of the volcano. These variations may in turn cause differential phase errors in interferometric measurements due to excess radar path delay effects within the volcanic gas plume (Rosen et al. 1996; Bonforte et al., 2001; Wadge et al., 2002; Wadge et al., 2006; González et al., 2015). Volcanic plumes are emitted from spatially localized emission sources, and transported by advection, i.e. the horizontal movement of air. Such plumes commonly have a more or less well defined lateral direction during each SAR acquisition, which can result in repeating patterns, when the plume direction is similar at the time of several subsequent SAR observations. Prevailing trade wind directions, typically lead to a preferred direction of plume transport and thus each volcano features one sector downwind of its emission source, which is more often covered by the plume than the rest of its surroundings. The respective sector is prone to be affected by pronounced differential phase signatures, which can be misinterpreted as a deforming surface, and may thus obscure the real deformation information of an interferogram. Rosen et al. (1996) described in detail the consequences that such propagation delays would have on interferometric deformation measurements using the examples of phase signatures that occurred on the SW-flank of Kilauea volcano and south of the Pu'u o'o lava vent in Hawaii, which they obtained from repeat-pass interferometric measurements of the shuttle imaging radar C (SIR-C) mission conducted in April and October 1994. The tip of the wedge-shaped signature at Kilauea originated from the Halema'uma'u summit crater, and fanned out in direction of the local trade winds. Rosen et al. however found several reasons that contradicted the hypothesis of a gas emission induced propagation delay, which lead them to conclude that these signatures were not related to volcanic gas emissions. Similarly Wadge et al. (2006) observed enhanced tropospheric delays in GPS measurements on the leeward side of Soufrière Hills Volcano on Montserrat, and estimated a gas plume related radar delay of about 0.05 m from ground based sulphur dioxide flux and gas compositional measurements, which would be negligible with respect to InSAR accuracy. Such putatively gas plume related disturbances are however often observed in interferograms of degassing volcanoes (e.g. at Pico do Fogo in González et al., 2015), and thus deserve closer attention.

Mitigation of phase signatures that have been generated by delay effects in volcanic gas plumes demands estimation of the precipitable water vapour (PWV) content in the plume at the time of SAR acquisitions. Precipitable water vapour is the amount of water vapour vertically integrated in an atmospheric column, and can be expressed as kilograms per square meter, or as the height of an equivalent column of liquid water in meters. Spaceborne radar interferometric delay measurements can in principle be used to map the spatial distribution of water vapour in the atmosphere (Saastamoinen, 1972; Hanssen et al., 1999; Mateus et al., 2013), if the contributions from topographic phase and ground deformation are known, or when independent PWV estimates are used as a reference. Accordingly, those measurements also enable to map the spatial extent of a volcanic gas plume when the strength of the degassing source is known, and

independent PWV estimates are integrated into analysis.

In this work, SO_2 was measured at Láscar volcano using a ground-based scanning Mini-DOAS UV spectrometer to obtain SO_2 column densities. Multi-GAS (multi-component Gas Analyzer System) measurements of H_2O / SO_2 ratios were used in combination with the Mini-DOAS data to obtain the apparent PWV contents in the gas plume above the crater rim. Due to the strongly condensed nature of the Láscar plume at the crater rim, the PWV contents were upscaled using an evaporation model to account for the evident increase in water vapour contents in the plume downwind of the volcano. These estimates were combined with TerraSAR-X observations in order to investigate the propagation delay that was generated by volcanic gas emissions in interferometric SAR measurements. For this purpose the estimated PWV contents were integrated into the Cinderella algorithm (Ulmer 2015), in order to estimate the repeated contribution of the volcanic gas plume to the radar delay in the interferometric measurement and thus determine the plume-induced delay variations which can be falsely interpreted as a deformation signal.

2. Geological and atmospheric setting

Láscar volcano is one of the most active volcanoes of the central Andes (Glaze et al., 1989a; Gardeweg & Medina 1994; Déruelle et al., 1996; Matthews et al., 1999) and currently the second largest emission source of volcanic gases in Northern Chile (Tamburello et al., 2014). Volcanism in this area is caused by the oblique subduction and dehydration of the oceanic Nazca plate, which is subducted beneath the continental South American plate (Stern 2004). The calc-alkaline stratovolcano (Figueroa et al., 1994) is located east of the Salar de Atacama basin (23.37°S, 67.73°W), on the western margin of the hyper-arid Puna plateau (Fig.1a), which is one of the driest areas on Earth. Much of the plateau around the 5,592 m high Láscar volcano has an altitude of more than 4 km above sea-level. Background atmospheric precipitable water vapour (PWV) over the region is very low most of the year, generally less than 1mm total water column (Marín et al., 2013). Cloudless skies, an extremely low atmospheric water content, and the high altitude lead to an exceptionally high atmospheric transparency (Otarola et al., 2005; Giovanelli et al., 2001), which in general is conducive for remote sensing applications.

The volcanic edifice of Láscar comprises two truncated intersecting composite cones, termed Western and Eastern edifice hereafter, and hosts 5 nested craters, which are aligned along an ENE-WSW trending lineament (Matthews et al., 1994; Gardeweg et al., 1998). Recent activity is characterized by persistently strong fumarolic degassing from the remnants of a dacitic dome, which is located in the westernmost crater of the Eastern edifice (Fig.1b & c). The dome covers an area of about 40,000 m^2 (about 230 meters in diameter) in the center of the crater. During the past two decades Láscar exhibited several periods of cyclic dome growth and collapses, which were punctuated by occasional explosive vulcanian to plinian eruptions (Matthews et al., 1997, Bluth et al., 1997). Eruptions were typically preceded by subsidence of the crater floor (e.g. Pavez et al., 2006) and a decrease in gas emissions (Matthews et al., 1997). Numerous high temperature fumaroles (about 300°C) are distributed on top of the dome and the surrounding inner crater walls (Tassi et al., 2009; Menard et al., 2014, Gonzales et al., 2015). Several low temperature fumaroles and diffuse vent sites are located in the eastern craters of the Eastern edifice and on the southern crater rim, but the high temperature gases ascending from the dome and the fumaroles in the active crater are the main emission source. Their presence is confirmed by a persistent thermal anomaly in the middle of the crater, which already occurred during previous phases of dome growth (Glaze et al., 1989b; Oppenheimer et al., 1993; Wooster & Rothery 1997; Wooster 2001). Gas emissions from Láscar volcano are very moist in contrast to the dry atmospheric background. Water vapour emissions from Láscar account for more than 90% of its total gas emissions, as for most degassing arc volcanoes, and water vapour emission rates are on the order of several metric kilotons per day (Tamburello et al., 2014). The persistently degassing, and largely unvegetated stratovolcano (Fig.1d) thus provides ideal conditions to examine radar path delays caused by refraction in volcanic gas.
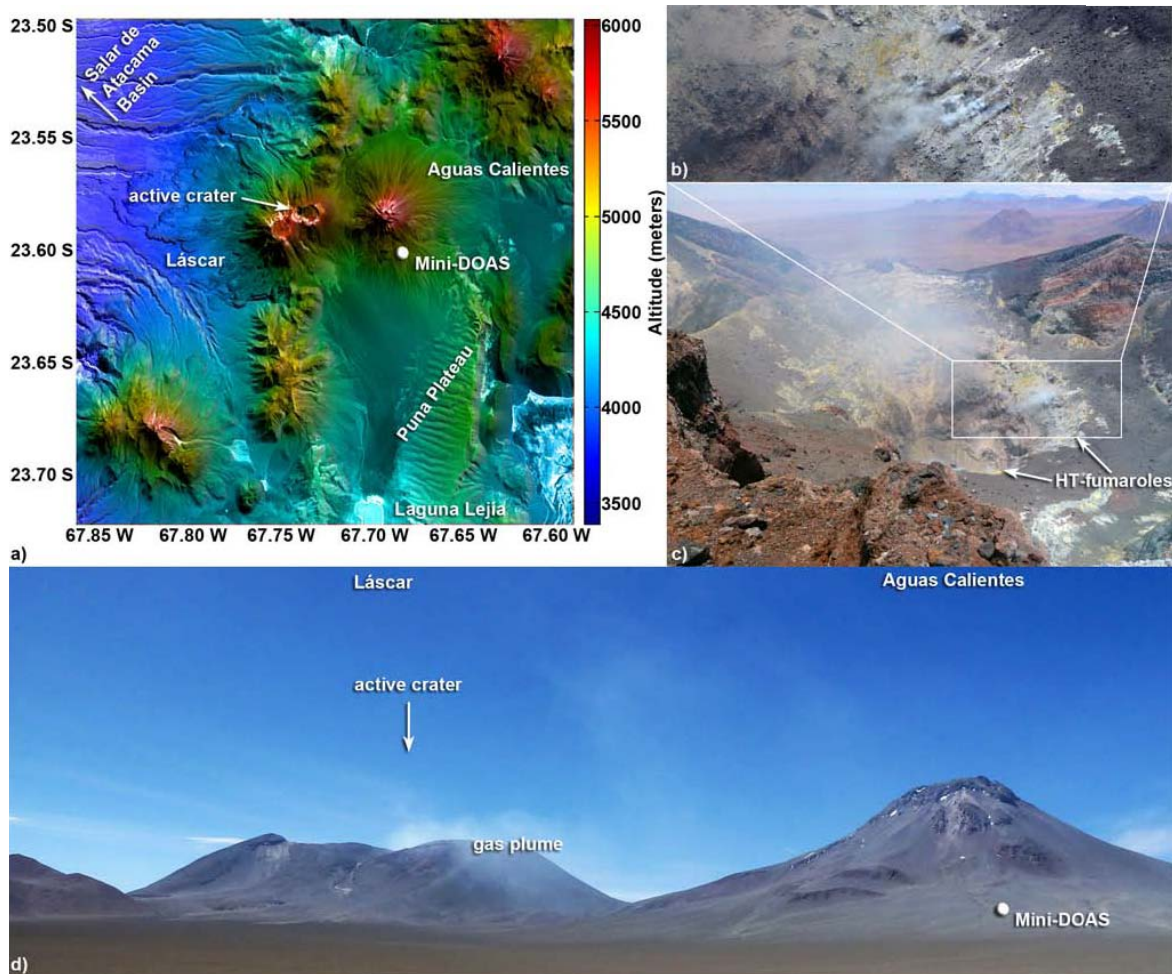
Fig 1. Láscar and adjacent Aguas Calientes volcanoes. The location of the Mini-DOAS station is indicated by the white dot on the southern flank of Aguas Calientes volcano. **a)** Aster visual composite of April 29, 2013 draped onto SRTM-1 grid. **b)** Close-up of high temperature fumaroles in the active crater **c)** View from the southern crater rim into the active crater of Láscar showing fumarolic activity during the multi-GAS survey on the Southern crater rim on December 02, 2012 **d)** Panoramic view from South showing a dispersed gas plume emanating from Láscars' active crater and drifting towards SE, which corresponds to the main transport direction during daylight time.

3. Data and Methods

3.1 SO₂ column density retrieval and estimation of PWV contents

Sulphur dioxide path-length concentrations in the plume of Láscar volcano were measured using a NOVAC-type stationary scanning mini-DOAS instrument (Fig.1; Galle et al., 2010; NOVAC: **N**etwork for the **O**bservation of **V**olcanic and **A**tmospheric **C**hange) that was permanently installed in April 2013 by the Chilean volcano observatory **O**bservatorio **V**olcanológico **D**e los **A**ndes del **S**ur (OVDAS). The DOAS station (Lejía DOAS) was deployed on the southern slope of the neighbouring Aguas Calientes volcano, immediately east of Láscar, according to prevailing westerly wind directions. The instrument scans across the sky from horizon to horizon along a semi-conical surface (Fig.2a) and measures the spectra of the incoming scattered sunlight at 51 angular steps of 3.6 degrees. Each complete scan takes about 5-10 minutes and yields a crosswind sulphur dioxide total column profile, i.e. perpendicular to the transport direction of the volcanic gas plume. Measurements are conducted during daylight, i.e. when UV intensities are sufficient to achieve an acceptable signal-to-noise ratio. At these latitudes the required conditions are met during a time interval approximately ranging from about 11:00 AM to 10:00 PM (UTC) in austral summer, and 12:00 AM to 09:00 PM (UTC) in austral winter. Times of SAR observations thus deviate up

to two hours from the daytime interval used for the DOAS measurements (Fig.2b). Due to this deviation in acquisition times and in the view of strong diurnal degassing variations, which are characterized by pronounced emission maxima around sunrise and sunset (Bredemeyer & Hansteen, 2014), we thus used daily average PWV contents, in order to obtain representative values for the time of the SAR observation. Determination of daily average PWV contents was also necessary, because the SAR delay estimation by means of the Cinderella algorithm requires only one representative PWV value for each SAR image. Such time averaged values however inevitably lead to systematic underestimation of the water content in the volcanic plume around sunrise and sunset.

SO_2 differential slant column densities (SCDs) were retrieved from the sunlight spectra by means of the DOAS method (Platt & Stutz, 2008), using the fully automated DOAS evaluation routine of the dedicated NOVAC-software (Galle et al., 2010). Evaluation was performed in the wavelength range 310-325 nm using absorption reference spectra of SO_2 (Vandaele et al., 1994), and O_3 (Voigt et al., 2003), which were convolved to the spectral resolution of the instrument. In addition, a ring spectrum and a solar spectrum were included in the DOAS-fit, in order to correct for scattering effects due to the so-called ring effect (Grainger & Ring, 1962), and SO_2-contaminated background sky reference spectra that were recorded by the instrument before each scan.

Simultaneous measurements of Multi-GAS and DOAS instruments were unfortunately not available for the period considered for DInSAR analysis. Moreover, volcanic gas plumes contain variable amounts of condensed liquid water, in addition to gaseous water. Multi-GAS instruments, however, exclusively measure gaseous water vapour and do not take into account the liquid water content (LWC) in the volcanic cloud. Similarly, liquid water has a negligible effect on radar propagation in comparison to water vapour, and accounts for only a few millimeters delay, even in cumulus clouds (Hanssen et al., 1999). Thus it is necessary to consider condensation and evaporation processes, which change the liquid to vapour ratio during transport of the volcanic plume. Liquid water concentrations are typically elevated close to the emission source and decrease with increasing downwind distance, due to further entrainment of dry ambient air, causing evaporation of cloud droplets. This in turn results in an increase of water vapour in the downwind proportion of the volcanic cloud, which is expected to be reflected as an enhancement of the radar delay in interferometric measurements. Due to the obvious condensed nature of the plume at the crater rim, resulting in an underestimation of the water vapour contents downwind, PWV contents were thus estimated on the basis of the maximum molar H_2O/SO_2 ratio of 34 derived from gas composition measurements conducted at the southern rim of the active crater on December 02, 2012 (Fig.2a; Tamburello et al. 2014), which was used to scale the SO_2 SCDs (see section **a)** in Results and Discussion for more details).

3.2 SAR data and InSAR methods

TerraSAR-X was tasked to acquire high resolution spot light SAR scenes covering Láscar volcano on both ascending and descending passes of the orbit. TerraSAR-X flies along the day-night boundary of the Earth in a near-polar sun-synchronous dusk-dawn orbit with an 11-day repeat cycle. SAR observations are thus conducted at day times of about 10:00 AM (UTC) on descending nodes and 11:00 PM (UTC) on ascending nodes of the orbit, i.e. around sunrise and sunset. Diurnal atmospheric transparency variations typically provide much better observing conditions during night, yielding the best observing conditions around sunrise. The DInSAR time series considered here covers a 5 months period during austral spring and summer ranging from October 18, 2013 to February 16, 2014 (Fig.2b). DInSAR preparation and analysis was done using the dedicated modular InSAR software system GENESIS from DLR. A set of SAR images from descending track 111 was chosen according to availability of complementary scan-DOAS data (Fig.2b), and these images were used to create two temporally overlapping interferogram subsets. SAR images were combined to form interferograms with very small spatial baselines, which accordingly resulted in different temporal baselines for each interferogram as depicted in Figure 2c and Table 1. The very small spatial baselines chosen here prevent from unwrapping failures due to a coarse digital elevation model (see section **b)** in Results and Discussion for more details).

Fig.2: Spatio-temporal relationships between the methods used for the gas plume estimate. **a)** Sketch showing the measurement geometry and location of the Multi-GAS and Mini-DOAS instruments at Láscar volcano during an overpass of TerraSAR-X. Refractive delay of the radar occurs inside the volcanic plume, which is heading towards East, due to predominantly westerly winds. See text for discussion. **b)** Date versus time plot depicting acquisition times of scan-DOAS measurements and SAR images. Measurement times are indicated using Coordinated Universal Time (UTC), which is offset by +3 hours with respect to Chile Summer Time (CLST). *Red arrows* indicate the temporal offset between SAR images and scan-DOAS data chosen for analysis. **c)** Spatial and temporal baselines of SAR images used in subsets 01 (*blue*) and 02 (*red*). Master scenes of subset 1 and subset 2 are from 2013-10-18 and 2013-12-12, respectively, and each computed interferogram is represented by a line between two images.
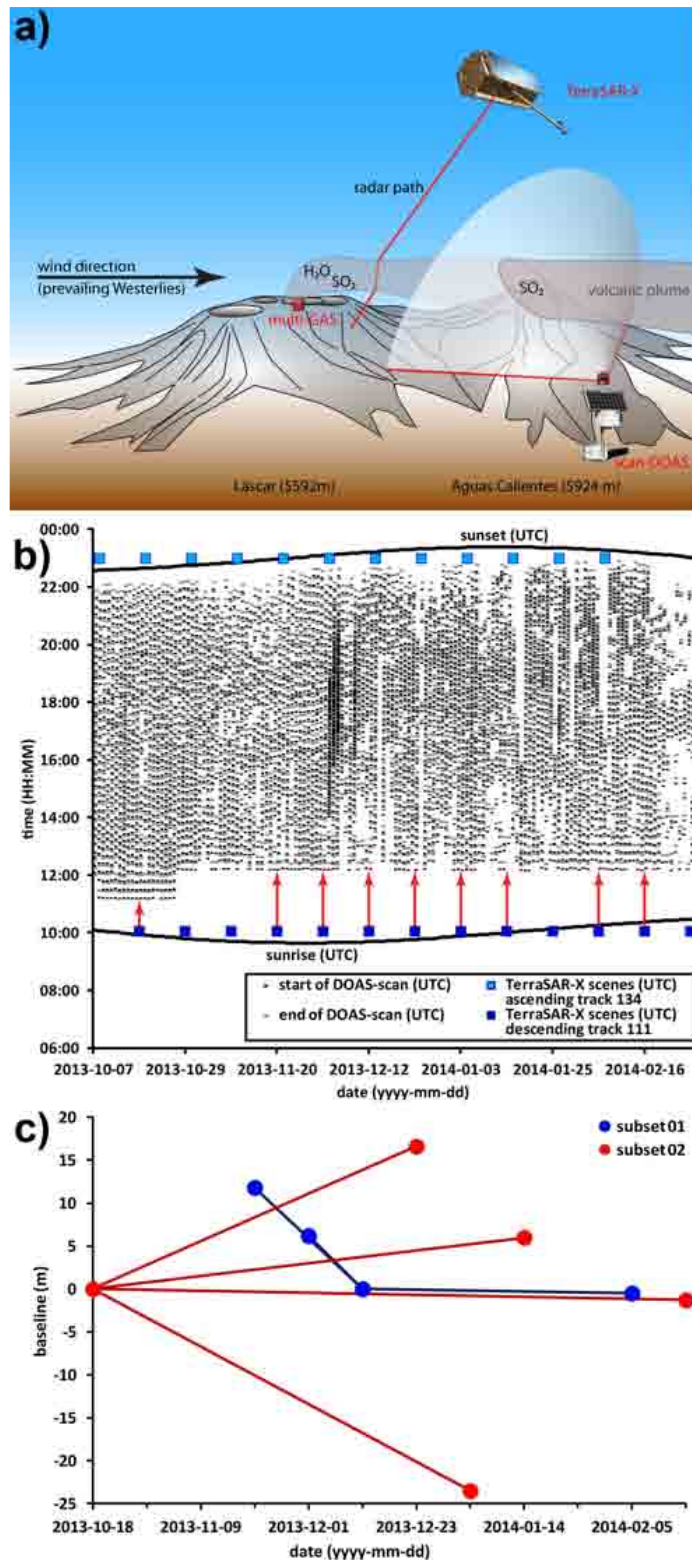
Table 1: Combinations of SAR acquisitions used in subsets 01 & 02, and their respective spatial and temporal baselines.

Slave scene Date (y-m-d)	Spatial baseline (m)	Temporal baseline (days)
Subset 01 (master scene: 2013-12-12)		
2013-11-20	11.8	-22
2013-12-01	6.2	-11
2014-02-05	-0.5	55
Subset 02 (master scene: 2013-10-18)		
2013-12-23	16.6	66
2014-01-03	-23.5	77
2014-01-14	6	88
2014-02-16	-1.3	121

118

3.3 Cinderella algorithm

Commonly, the persistent scatterer interferometry (Ferretti et al., 2001; Hooper et al. 2004; Hooper et al., 2007), or the Small Baseline Subset algorithm (Berardino et al., 2002; Jung et al., 2008) is used to compensate atmospheric disturbances in SAR data, if large stack sizes are available. The Cinderella technique (Ulmer 2015) was developed to deal with temporally unconnected subsets, small stack sizes, and does not use the isotropy assumption to mitigate the atmospheric effect. The algorithm is based on Dual-tree complex wavelet transform (DT ℂWT), which is being used in a wide range of applications in the field of signal and image processing, where it commonly serves as a tool for signal/ image fusion, decomposition, and de-noising (Selesnik et al. 2005). The DT ℂWT calculates the complex transform of a signal using two separate discrete wavelet transform (DWT) decompositions (tree a and tree b), which may be regarded as equivalent to filtering the input signal with two separate banks of band pass filters, that separately produce the real and imaginary coefficients of the complex wavelet. The conventional DWT allows to capture both frequency and location information of a multidimensional signal, i.e. the times and locations at which these frequencies occur. Due to the redundancy of the two separate DWT decompositions the DT ℂWT thus combines the benefits of DWT with important additional properties, comprising near shift invariance, directional selectivity, and enabling near perfect reconstruction of the input signal (Kingsbury 1998).

The Cinderella technique works as follows (Fig.3). First, the DT ℂWT representations of all interferograms are derived. Second, each complex wavelet is analyzed using priors containing information on the temporal evolution of processes that contributed to the total phase of the interferograms. Prior information about signal strength relations are given by chance, e.g. including prior information on the signals related to spatial baseline, temporal baseline, and the gas emissions. Cinderella uses this prior

| DInSAR time series | DT CWT representations | signal strength time series | prior time series | DT CWT estimate of priors | delay estimates |

● differential signal   ≈ fits best

| signal strength   ≠ does not fit
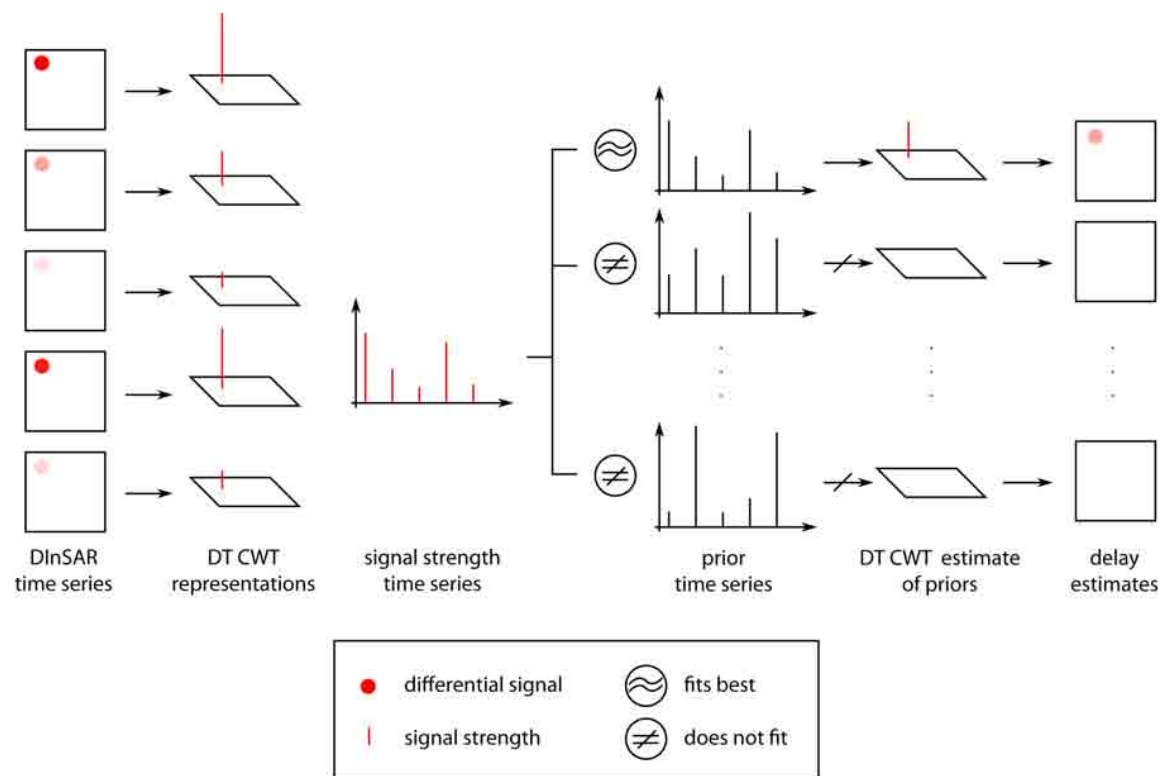
Fig.3: Technical diagram depicting the processing steps of the Cinderella algorithm. In a DInSAR time series each DInSAR pixel (respectively range azimuth position) is characterized by a certain temporal evolution of its differential signal strength. Computation of the DT ℂWT representations of each DInSAR enables to capture the temporal evolution of the signal strength of all SAR pixels of the DInSAR time series by means of a small number of complex wavelet coefficients. Similarly each process which causes changes in SAR signal strength can be described by a time series, which reflects the temporal variations of the process (e.g. variations in spatial baseline, relative humidity, ground temperature, or pressure). The algorithm uses the time series of these processes as a priori knowledge on a related possible change in SAR signal strength and assigns the SAR signals to their likely causes by comparison of the prior time series with the temporal evolution of SAR signal strength, which decomposes the interferograms into different phase screens.

_____

information to assign each complex wavelet to their likely causes, depending on their best temporal correlation with the prior knowledge. This decomposes the interferograms into signals related to the priors. The decomposition thus yields one separate estimate for each prior that was included in the Cinderella analysis. An interferometric signal that e.g. most closely correlates with the gas emission time series, is identified as a gas plume related signal. This means that the estimated signal may additionally contain phase information related to any other interferometric signal that coincidently correlates with the gas plume signal. In order to successfully isolate the plume-induced signal from total phase, it is thus necessary to include the priors of potentially interfering signals, e.g. the priors of temporal and spatial baseline. Signals that correlate more closely with the spatial or temporal baseline are then automatically identified and mitigated for the gas plume estimate. This works, because the effect of the DEM error in the displacement estimate typically evolves proportionally to the spatial baseline history of a set of SAR acquisitions (Fattahi & Amelung, 2013), and linear deformation evolves proportionally to the temporal baseline history. The signal estimate related to the spatial baseline thus contains the signals, which are caused by the error in the digital elevation model, while the signal estimate associated to the temporal baseline contains signals that are interpreted to change linearly in time, as would be indicative for a ground surface deformation.

   The Cinderella technique does not use any information about the localization of the desired interferometric signal. Also, no information about the interferometric signal strength, rather merely the shape of the prior time series is used, which is why the prior information can be scaled arbitrarily. Correspondingly, the Cinderella estimates can be validated by the position of the estimated signal and the signal strength. The algorithm consequently does not require any information on the location of the plume, in order to find the related disturbance in the interferometric signal. This is of particular advantage to the application described here, since we lack precise information on the heading of the plume at the times of SAR observations, apart from a rough approximation that can be derived from wind directions offered by the weather models. The gas plume is transported by advection, therefore has a direction, and is correspondingly anisotropic. For this reason, and since only a few interferograms were available, where the corresponding gas emissions were known, the Cinderella technique is the best choice for the gas plume pattern estimate. Additionally, the ability to use temporally unconnected subsets enables to use only those DInSARs which have a very small spatial baseline. This helps avoid unwrapping errors due to erroneous digital elevation models.

3.4 Wind field during SAR acquisitions

Wind, in particular over arid regions, plays a major role for the transport of humidity in the atmosphere, which is also true for the humidity originating from volcanoes. In order to understand humidity variations in the atmosphere above a volcano, it is thus necessary to know about local variations in wind speed and wind direction. The temporal variations of the wind field above Láscar volcano were examined using modeled wind directions and velocities of the Global Forecast System (GFS), which were derived from archived atmospheric soundings of the Global Data Assimilation System with one-degree grid spacing (GDAS1) provided by the National Oceanic and Atmospheric Administration (NOAA). The soundings were concatenated to form time series of wind speed and direction (Fig.4a and 4b). Wind speeds at plume altitude ranged from 0.1 to 18 m sec^{-1} during the period of interest, and generally decreased throughout the whole atmospheric profile during austral summer (December to February) (Fig.4a). High altitude winds over the region usually are prevailing westerly throughout the year (orange colours in the upper part of Fig.4b), and are interrupted by short periods, which are dominated by easterly wind anomalies during austral summer. Surface winds typically are oriented according to topography, as in any other mountain wind system, and exhibit pronounced diurnal variations (alternating blue and orange colours in the lower part of Fig.4b). These diurnal variations are characterized by valley winds (anabatic upslope breezes depicted by orange colours in the lower part of Fig.4b) that typically occur during daytime due to insolation of mountain flanks, and increasing wind speeds towards the evening (light blue colours in the lower part of Fig.4a), whereas rather calm mountain winds (katabatic downslope breezes and over-hill flows) prevail during the night (depicted by blue colours in the lower part of Fig.4b and dark blue colours in Fig.4a). Diurnal variations in surface wind directions are more prominent during summer, frequently resulting in a characteristic diurnal pattern of plume transport directions. In the morning hours of a summer day the plume typically drifts towards west or northwest, turning over south towards east before noon, where it

stays more or less steady until sunset. Downslope winds frequently force the plume to follow the steep morphology of the volcano.

Time series of wind directions in the range of typical plume heights, namely several 100 meters above and below the summit of Láscar volcano were extracted from the 500 and 550mbar pressure levels of the GDAS1 soundings, respectively, in order to narrow down the range of possible plume transport directions at the times of SAR acquisitions (Fig.4c & d). Wind directions at the time of SAR acquisitions of track 111, which were conducted around sunrise at about 10:00 UTC (Fig.2b), were predominantly westerly during spring 2013 and late summer 2014, whereas easterly directions prevailed during early summer 2013. Wind directions were generally very similar over the broad altitude range of both pressure levels, indicating relatively stable wind conditions. Pronounced differences in wind directions above and below summit were mainly observed during early summer, when winds tended to be less stable with respect to the direction, and were characterized by low velocities.
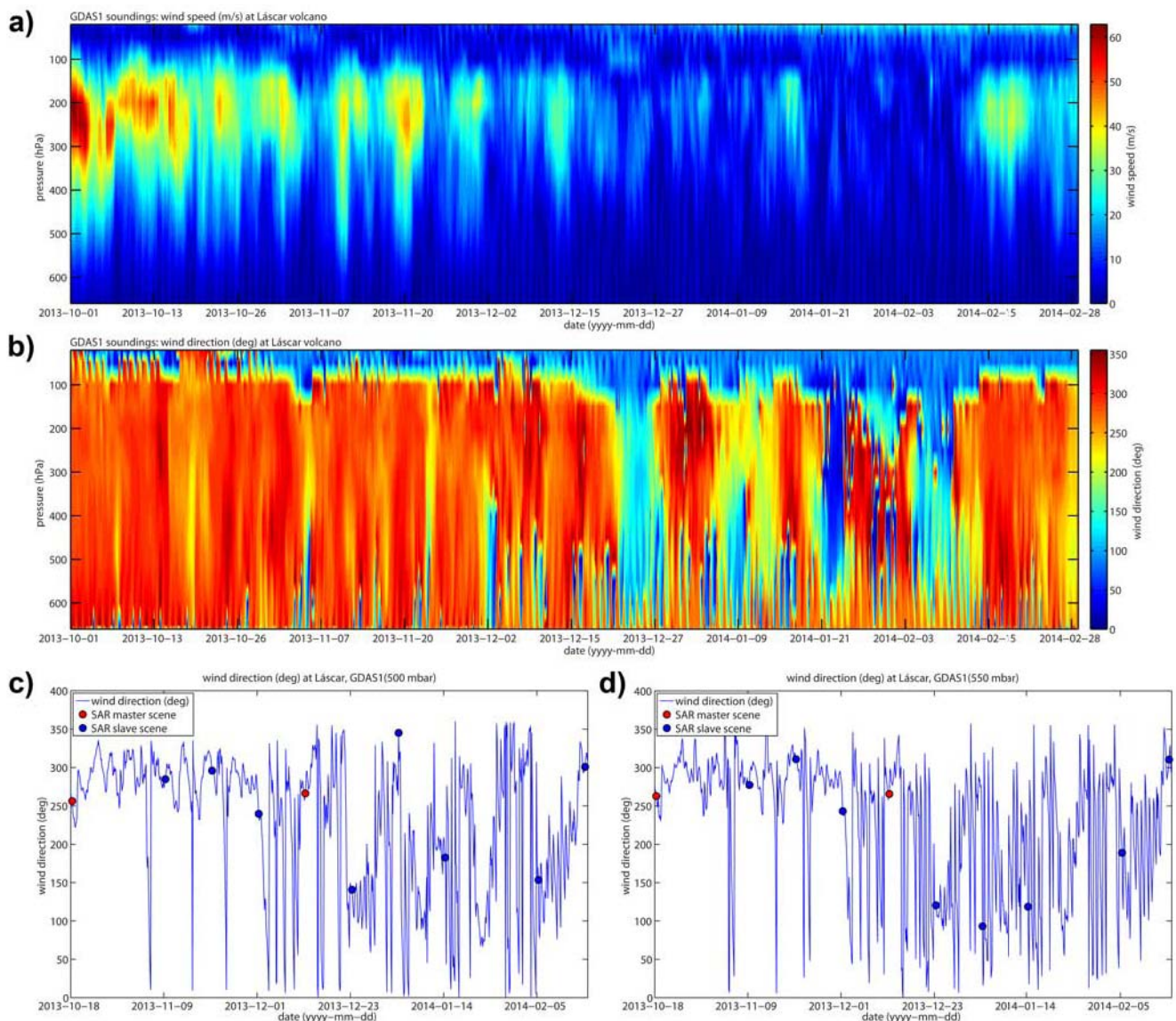
Fig.4 a&b) Time series of vertical atmospheric profiles depicting variations in **a)** wind speed and **b)** wind direction. Note the weak winds accompanied by strong variations of wind directions during austral summer (ranging from December 2013 to February 2014). **c&d)** Time series of wind directions some 100 meters **c)** above and **d)** below the summit of Láscar (500 and 550mbar pressure levels of the GDAS1 soundings, respectively). Wind directions at the time of SAR observations are indicated by red (master scene) and blue dots (slave scene). Wind directions during austral summer (ranging from December 2013 to February 2014) were predominantly easterly at the time of SAR observations.

An additional wind field analysis was conducted using 3-dimensional gridded hindcasts of the Weather Research and Forecasting model (WRF) in order to resolve how the wind field evolves from turbulent flow close to the ground surface to laminar flow at higher altitude during the times of SAR acquisitions. For this purpose the WRF simulation was run using a 900 meters horizontal grid spacing and a vertical division of 51 terrain following eta levels. Surface wind fields obtained from the lowest eta level of the WRF simulation, reveal that katabatic (downslope) winds prevailed during most SAR acquisition times (Fig.5).

Fig.5: Time series of surface wind fields obtained from the lowest eta level of WRF, determined for acquisition times of each SAR image. Katabatic (downslope) mountain winds prevail at the time of SAR acquisitions, which were recorded during the early morning hours at about 10:04 AM (UTC), respectively 07:04 AM (CLST).

The wind fields of all acquisition times were averaged, in order to match the cumulative SAR delay estimates produced by the Cinderella algorithm. This was done for the first eta level, which represents the wind conditions closest to the surface (Fig.6a). Changing conditions with increasing altitude were captured by means of gradually increasing the number of eta levels, which were included into the averaged wind field. In other words eta levels 1-5, 1-10, and 1-15 were combined to yield averaged wind fields (Figs.6b-d). Average wind direction of the terrain following winds close to the surface was predominantly towards southeast aloft the plateau, and heading downslope, which is mainly oriented towards west, over the western flank of the plateau (Fig.6a). Gradual integration of more eta levels into the average wind field nicely illustrates the turning direction of the winds with increasing altitude (Fig.6a-d), finally arriving at upper tropospheric westerly trade wind directions, which are typical for this region (Fig.6d).
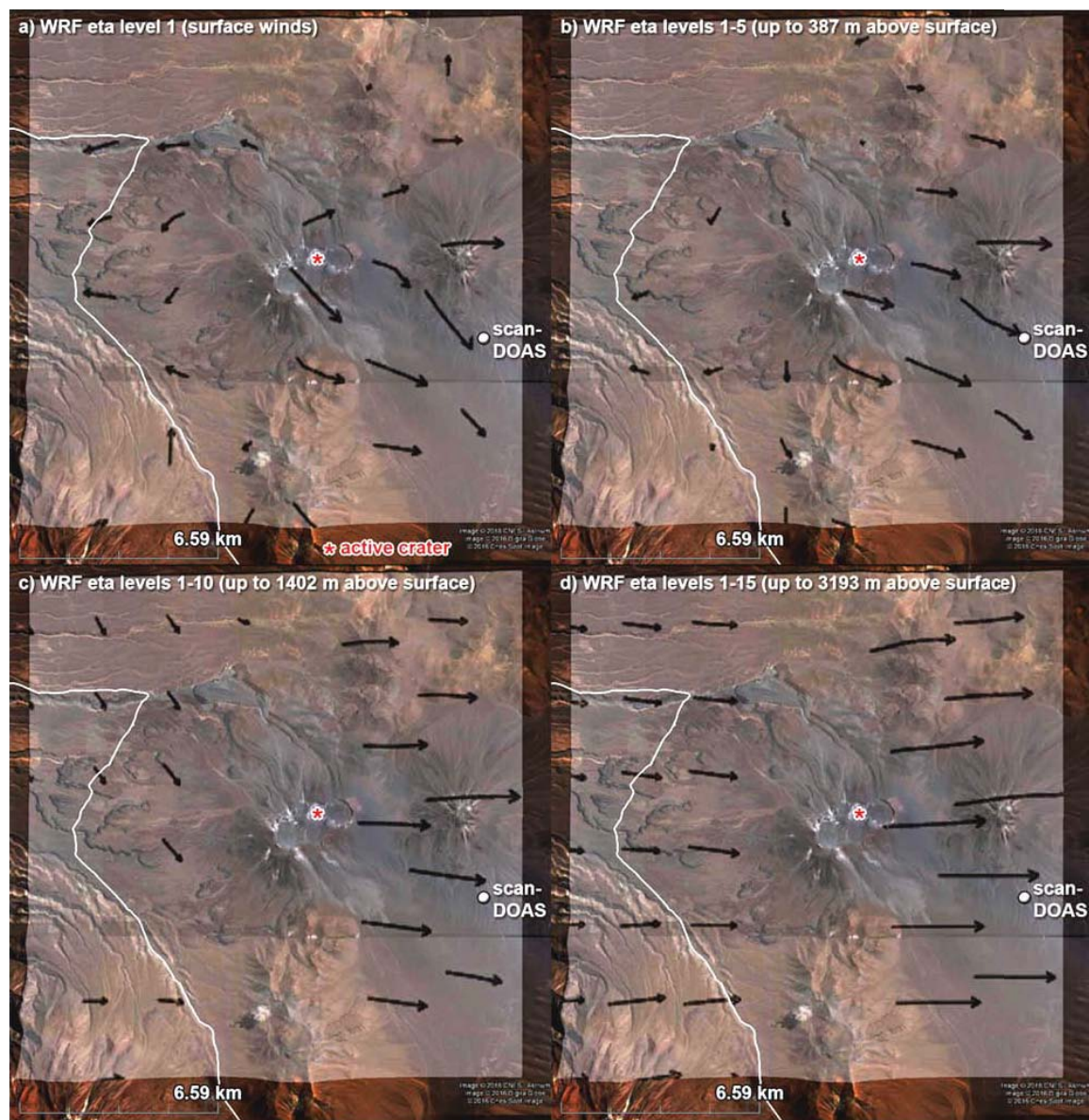
Fig.6: Averaged wind fields combining wind fields of all SAR observation times. **a)** Average surface winds from eta level 1 **b)** Average winds up to 387 m above surface **c)** Average winds up to 1402 m above surface **d)** Average winds up to 3193 m above surface.

4. Concept of data preparation

4.1 Identifying the effect of water vapour in a volcanic plume on SAR acquisitions

In order to verify the effect of PWV in the Láscar plume on SAR acquisitions, the following sequence of work was applied (Fig.7):

a1) Estimation of the total precipitable water in the plume downwind of the volcano involved several consecutive work steps. Due to the strongly condensed nature of the Láscar plume, H_2O / SO_2 ratios determined using Multi-GAS at the crater rim had to be upscaled using a selected evaporation model to account for the strong evaporation expected due to the extremely dry nature of the local atmosphere in the Atacama region.

a2) Determination of PWV contents in the local atmosphere was done to be able to approach the relative and absolute effects of the plume on the specific SAR acquisitions.

b) DInSAR data was prepared by removal of a coarsely resolved digital elevation model (SRTM-1) and removal of large scale tropospheric delays, which were determined from WRF hindcasts of vapour pressure, temperature and pressure.

c) The PWV estimates were used as input for the Cinderella algorithm, yielding SAR delay estimates, which were used to investigate the effect of PWV in the plume on the SAR data.

d) SAR delay estimates obtained from Cinderella analysis were used for mitigation of non-deformation related delays in the DInSAR data prepared in section b).
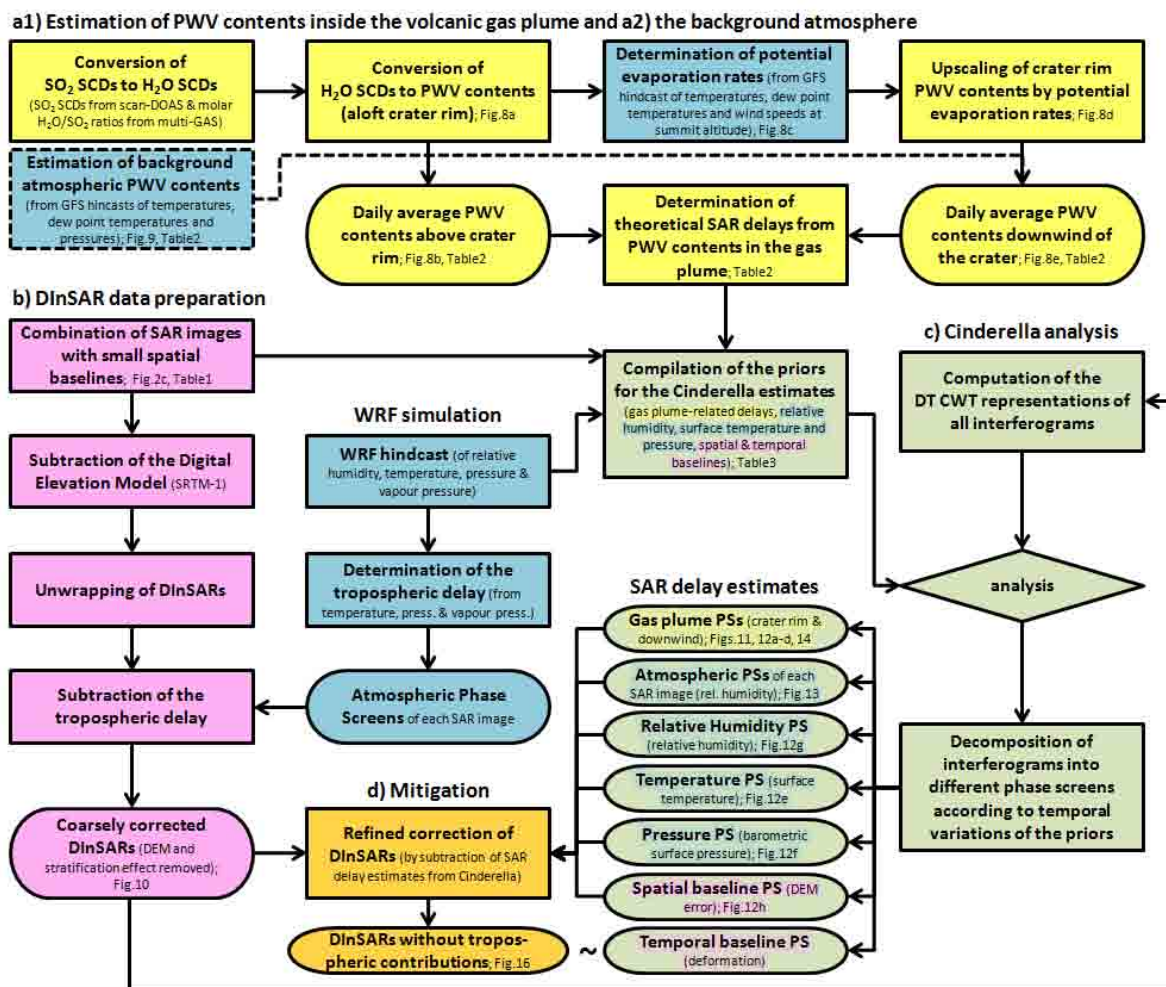
Fig.7: Flowchart of the work sequence that was applied to retrieve estimates of the gas plume related and tropospheric propagation delays, and the DEM error related delays, which can be used for mitigation of non-deformation related delays. Step a2) is indicated by stippled lines, since it is not a part of the processing chain and was only done for comparison with results from step a1).

4.2 a1) Estimation of water vapour contents in the Láscar plume

Liquid water contents in the plume above the crater rim were unknown, thus it was not possible to determine the actual evaporation rate from a defined amount of liquid water. Considering increasing water vapour concentrations, respectively increasing H_2O/SO_2 ratios in the downwind portion of the volcanic plume, we thus calculated the drying power of the ambient air, respectively potential evaporation rates at plume height, by means of an aerodynamic approach using climatic variables obtained from GDAS1 soundings, and information on surface properties regarding the average height of obstacles in the trajectory of the volcanic plume (see Appendix A2. for details). Potential evaporation rates were then used to scale our fixed H_2O/SO_2 ratio of 34 in order to compensate for downwind evaporation. Potential evaporation rates correspond to the amount of liquid water that can be transformed to vapour through evaporation, if sufficient water is available. Assuming an unlimited availability of water, evaporation can in such a situation continue until the air above the evaporating surface approaches saturation humidity, and therefore actual evaporation cannot exceed potential evaporation. In the present case, availability of liquid water does not seem to be a limiting factor inside the plume, since the plume typically is partly condensed when it arrives at the scan-DOAS. We thus assume that scaling by the potential evaporation rate yields a feasible approximation of the increase in water vapour at the expense of liquid water in the downwind portion of the volcanic cloud. We further assume that downwind dilution of water vapour due to dispersion of the plume is largely covered by the variations of the SO_2 column densities measured by the DOAS, since both water vapour and SO_2 are equally affected by diffusion and turbulent mixing processes. The amount of evaporation occurring inside the plume is largely controlled by the humidity of the entrained ambient air and the degree of turbulent mixing with air parcels of the plume, which is mainly governed by wind speed and atmospheric stability. Evaporation is thus commonly more pronounced during periods with dry atmospheric conditions and high wind velocities, which cause the transport of the plume to be more turbulent, and it is less significant, when the atmosphere is more humid and less turbulent, due to small transport velocities.

4.2.1 Daily average PWV contents above the crater rim

PWV estimates were obtained by conversion of SO_2 SCDs at each scan angle of the plume cross sections, without application of the compensation factor (Fig.8a; see Appendix A1 for details). The amount of water vapour in the centerline of the plume was determined by finding the maximum PWV contents of each scan, and these were used to determine the daily average PWV contents for days with TerraSAR-X acquisitions. Estimated daily average PWV contents obtained from the centerline of the plume ranged from 0.007 to 0.015 mm at the times of SAR observations (Fig.8b). Additionally the average amount of water vapour in each scan was determined and used to calculate the daily average PWV contents of the bulk plume, i.e. taking into account the whole cross sections at this time. Daily average bulk plume PWV contents ranged from 0.002 to 0.0035 mm (Fig.8b). PWV contents from the plume center were used for the gas plume estimate of the Cinderella algorithm. These values reflect H_2O vapour contents at the crater rim, and are thus not representative for PWV contents arriving at the scanning plane of the scan-DOAS (Fig.2a), since they do not take into account downwind evaporation.

4.2.2 Upscaling of crater rim PWV contents by potential evaporation rates

Potential evaporation rates were thus determined for the measurement periods of the scan-DOAS (Fig.8c; see Appendix A2 for details on evaporation calculation), and used to upscale the H_2O/SO_2 ratio, which was thereby adjusted to increase proportionally to evaporation rates, which strongly depend on wind speeds (Fig.8d) over arid areas. The resulting variable ratio was then used to upscale the SO_2 SCDs at each scan angle of the plume cross sections as described above (Appendix A1), at this time however taking into account the effect of downwind evaporation (Fig.8e). Upscaling of the PWV estimates by the potential evaporation rate was iteratively done in two steps involving a first approximation of the PWV contents and associated theoretical slant wet delays, which were then integrated into the Cinderella algorithm to estimate

the corresponding phase contribution (as described in the SAR delay estimates section). Information on the difference between estimated and theoretical delay was used to further amplify/attenuate the effect of evaporation on the H_2O/SO_2 ratio, which in turn was used to up-/downscale the PWV estimate. This second PWV estimate was again integrated into Cinderella resulting in a estimated delay that matched the theoretical delay at this time.

4.2.3 Daily average PWV contents downwind of the crater

Such estimates retrieved from scan-DOAS measurements in combination with multi-GAS measurements, thus now provide a more reasonable approximation of the temporal variations in precipitable water vapour on different points along the cross sections through the volcanic plume. The amount of water vapour in the centerline of the plume was determined by finding the maximum PWV contents of each scan, and these were used to determine the daily average PWV contents for days with TerraSAR-X acquisitions. Estimated daily average PWV contents obtained from the centerline of the plume ranged from 0.8 to 9.6 mm at the times of SAR observations (Fig.8f). The position of the plume center varied strongly during the measurement period, because the gas plume of Láscar commonly strongly meanders within the scan range of the scan-DOAS. Transport directions of the plume changed between north-easterly and south-easterly transport directions approximately every 10 minutes, which roughly corresponds to the duration of 1 complete DOAS scan. This resulted in different plume positions in consecutive scans, which is why the sequences of consecutive scans in Figures 8a and 8e generate surfaces with a rippled appearance. We thus assume that the resulting daily average plume center statistic may not be representative for the effect that the bulk plume has on SAR measurements, since the gas distribution along plume cross sections is highly irregular, when the plume meanders. Thus additionally the average amount of water vapour in each scan was determined and used to calculate the daily average PWV contents of the bulk plume, i.e. taking into account the whole cross sections at this time. Daily average bulk plume PWV contents ranged from 0.2 to 2.5 mm (Fig.8f), and were used for the gas plume estimate of the Cinderella algorithm.
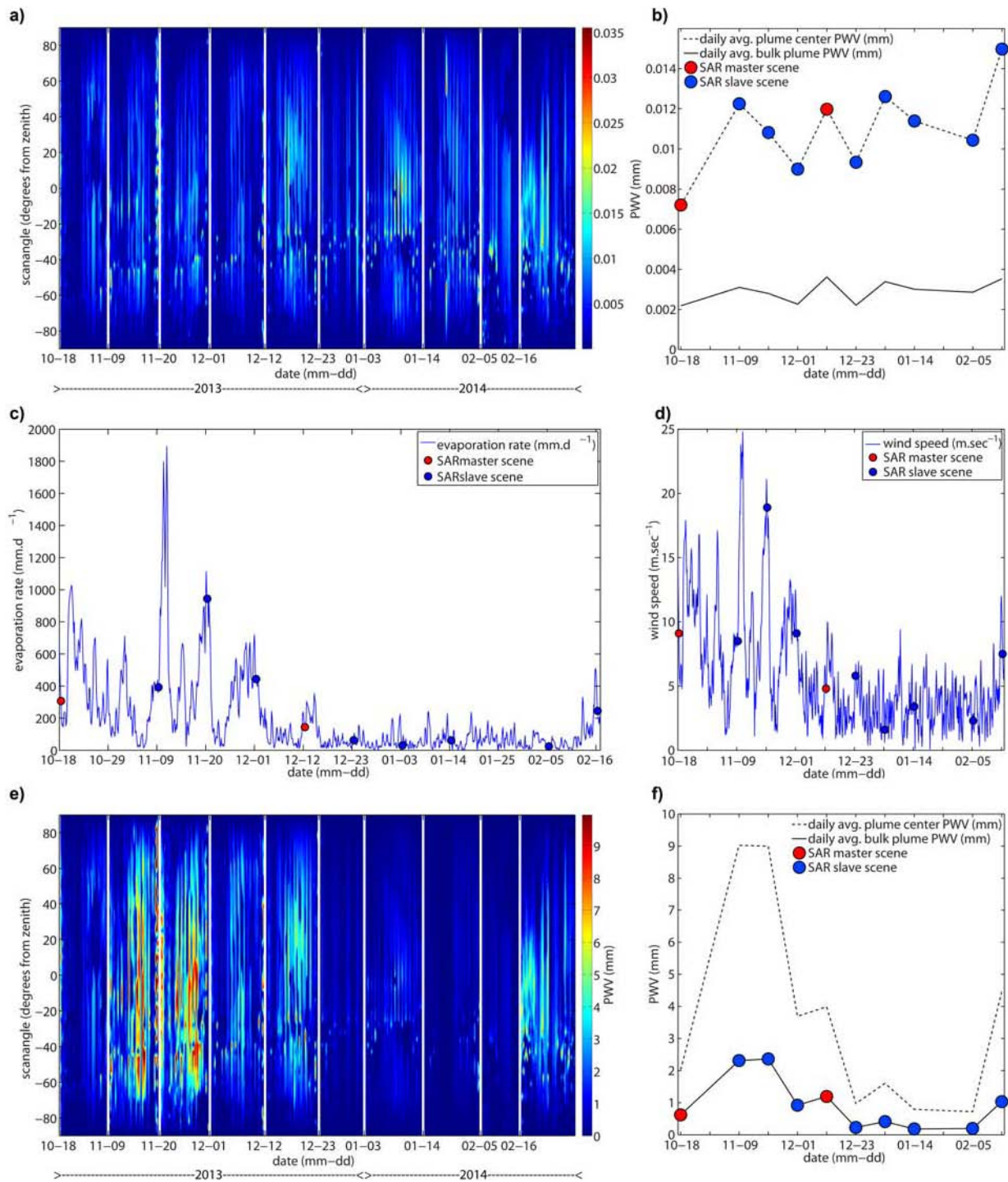
Fig.8 a) Time series of scanning Mini-DOAS plume cross-sections depicting SO$_2$ SCDs upscaled and converted to precipitable water vapour (PWV mm). **Result without compensation of evaporation. b)** Daily average PWV contents in the centreline of the plume (*stippled line*) and the bulk plume (*solid line*), which are representative for the moisture distribution **above the crater rim**, were calculated for the days with available SAR acquisitions. PWV contents in the centreline of the plume were used as a prior time series for the first gas plume estimate in the Cinderella analysis. **c)** Time series of potential evaporation rates at plume height above the summit of Láscar volcano, obtained from GDAS1 soundings. These values were used for upscaling of the uncorrected PWV estimate. Evaporation rates at the times of SAR observations are indicated by *red* (master scenes) and *blue* (slave scenes) *dots*. Note the pronounced correlation between potential evaporation rates and wind speeds depicted in Supplementary Figure S1a. **d)** Time series of wind speeds at summit altitude, which were used for calculation of potential evaporation rates. Note the pronounced correlation of wind speeds with evaporation rates reflecting the major contribution of moisture transport by wind to evaporation over arid areas. **e)** Time series of scanning Mini-DOAS plume cross-sections depicting SO$_2$ SCDs upscaled and converted to precipitable water vapour (PWV mm). **Evaporation compensated result.** Upper bound of the colour scale was reduced from 30 to 10 mm, thus depicting all values larger than 10 mm in *dark red*, in order to accentuate the less prominent low amplitude variations. The sequences in a) and e) are compilations of scans recorded on the days of TerraSAR-X acquisitions (2013.10.18 - 2014.02.16). The time scale thus is not linear. **f)** Daily average PWV content in the centreline of the plume (*stippled line*) and the bulk plume (*solid line*) **downwind of the volcano** calculated for the days with available SAR acquisitions. Bulk plume PWV contents were used for the second gas plume related excess path estimate of the Cinderella algorithm.

4.3 a2) Estimation of background atmospheric PWV contents

Atmospheric disturbances due to volcanic gas plumes are expected to be more pronounced during periods with high emission rates and low background atmospheric humidity. In the Atacama region the driest conditions are typically found during the period late March to early December, and between local midnight and 11 AM (Giovanelli 2002). Background PWV contents in the atmosphere above the volcano were retrieved from vertical atmospheric GDAS1 profiles provided by NOAA (see Appendix A3. for equations). These estimates were compared to PWV estimates obtained from radiometer measurements (Fig.9) provided by the Atacama Pathfinder EXperiment (APEX), which is also located on the western rim of the Puna plateau, but about 30 km north of Láscar, and at a very similar altitude of 5,100 meters above sea level, thus reflecting similar weather conditions.

The considered period covers parts of the "dry season", which is characterized by dry prevailing westerly synoptic winds, and is spanning most of the year (here October, November and second half of February are included), as well as the "wet season" ranging from December to February, which is characterized by less stable atmospheric conditions, resulting in more humidity being transported to the Andes by frequently recurrent easterly winds (Vuille 1999). Measured and estimated atmospheric PWV contents were at average below 1 mm during October and November 2013, sharply increased to 5 mm in December 2013, stayed enhanced through the first half of February 2014, and finally decreased again to 1 mm in the second half of February 2014. The comparatively low PWV values determined for the times of SAR observations reflect the pronounced atmospheric transparency around sunrise.

Estimated PWV contents inside the volcanic gas plume (Figs.8b and 8f) and estimated atmospheric PWV contents outside the plume (Fig.9) were compared in order to assess the humidity/refractivity contrast between background atmosphere and volcanic plume. The comparison revealed that PWV contents at the downwind plume centerline (0.8 to 9.6 mm) were generally larger than the PWV contents of the ambient air (<1 mm) during periods with dry atmospheric conditions, i.e. most of the year. During early summer the situation is different, and the downwind plume PWV content (<1 mm) is less contrasting with respect to the PWV content of the atmospheric background (2-5 mm). PWV contents of the downwind bulk volcanic plume (0.2 to 2.5 mm) were accordingly much less contrasting most of the year, if compared to background atmosphere, and were slightly higher than background atmospheric humidity only during the first three SAR observations of the time series (days 2013-10-18, 2013-11-20, and 2013-12-01). PWV contents determined for the proximal part of the plume above the crater rim were in general negligible with respect to PWV contents of the background atmosphere (0.007 to 0.015 mm on the centerline of the plume, and 0.002 to 0.0035 mm averaged over the bulk plume).
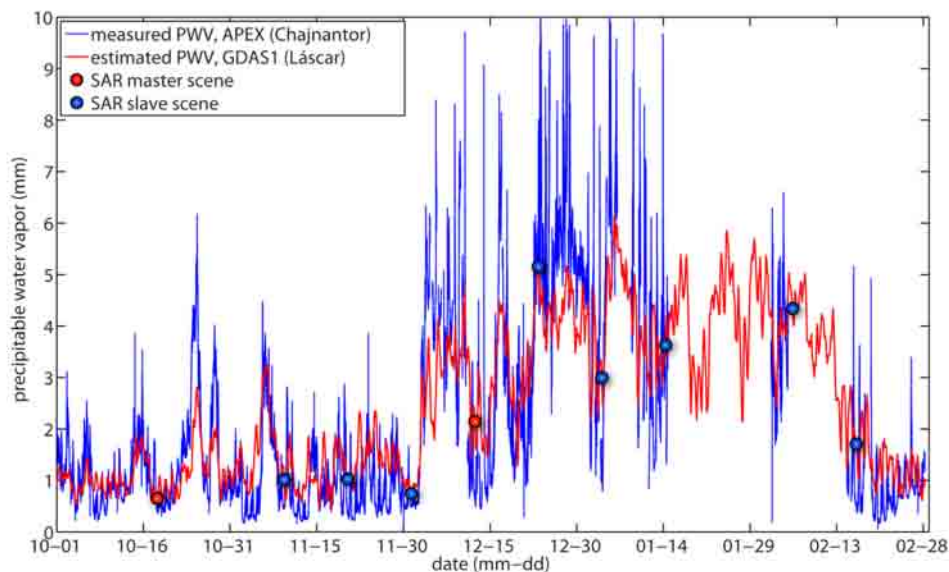
Fig.9: Background atmospheric PWV contents estimated from GDAS1 soundings above Lascar volcano (*red curve*), compared to radiometer measurements conducted at APEX (*blue curve*). Good agreement between the two curves reflects similar weather conditions caused by a similar morphologic exposition of both sites, and may additionally be attributed to the coarse spatial resolution of the GDAS1 data. PWV estimates for the times of SAR observations are indicated by *red* (master scene) and *blue* (slave scene) *dots*, respectively.

4.4 b) DInSAR data preparation

Estimation of the plume related delay by means of the Cinderella technique requires several pre-processing steps, which are now briefly outlined. SAR images were combined to form interferograms with very small spatial baselines as depicted in Fig.2c and Table 1. These interferograms were corrected using a low resolution digital elevation model (DEM) from the Shuttle Radar Topography Mission (SRTM-1 with one arc second horizontal resolution and a vertical accuracy of 6 meters) obtaining coarsely corrected differential interferograms (DInSARs), which however still contain some small-scale topographical errors. DInSARs were then unwrapped and further corrected by means of numerical weather hindcasts of the WRF, in order to remove atmospheric contributions, in particular to avoid altitude correlated distortions known as stratification effect, which is the most prominent atmospheric disturbance in the presence of strong topography (Ulmer & Adam, 2015). For this purpose the differential tropospheric delay was computed at each pixel (range azimuth position) of the interferograms from temperature, pressure and vapour pressure, using a horizontal grid spacing of 900 meters and a vertical division of 51 eta levels for the WRF simulation. The resulting DInSARs however still contain small-scale phase contributions that were caused by a turbulent atmosphere (Fig. 10).

4.5 c) Cinderella analysis

4.5.1 Determination of gas plume related phase delays

Daily average gas plume PWV contents estimated for each SAR acquisition date were used to determine the theoretical slant wet delay (SWD) that such PWV contents would produce in the line of sight (LOS) of a SAR image. Determination of the theoretical slant wet delay is straight forward, since it can be inferred from the zenith path delay (ZPD), which is linearly related to the vertically integrated water vapour (IWV) contents, where 1 mm in precipitable water vapour contents roughly results in a 6.5 mm zenith path delay (Bevis et al., 1992; Ulmer 2016). Columnar water vapour can be converted to zenith path delay using equation (1)

$$\delta^{ZP} = \Pi_{T_s} \, IWV \qquad\qquad\qquad (1)$$

where δ^{ZP} is the zenith path delay in (mm), IWV is the columnar integrated water vapour in (kg.m^{-2}), which is approximately equal to PWV contents in (mm), and Π_{T_s} ($\approx$ 6.5) is the conversion factor approximated using surface temperature T_s in (K). Calculation of the theoretical slant wet delay thus merely requires further conversion of the zenith path delay, taking into account the incidence angle of acquisitions, in order to obtain the corresponding delay along the line of sight. The conversion factor used for the calculation of the theoretical slant wet delay was calculated by equation (2).

$$\delta^{SW} = \delta^{ZP} * 1 / \cos(\theta) \qquad\qquad\qquad (2)$$

where δ^{SW} corresponds to the path delay along the line of sight, and θ to the incidence angle of SAR observations. The incidence angle of acquisitions from track 111 was inclined 37 degrees with respect to zenith path resulting in a conversion factor of $1/\cos(37) = 1.25$.

Theoretical gas plume related SWDs determined for SAR observations used in this study were in the submillimeter range and thus negligible compared to the InSAR accuracy in the proximal part of the plume above the crater rim, where SWDs ranged from 0.07 to 0.1 mm in the centreline of the plume and 0.02 to 0.03 mm in the bulk plume (Table 2). The SWDs in the more distal part of the plume downwind of the crater, however, were on the order of background atmospheric SWDs (5.3 to 41.5 mm), and ranged from 1.6 to 20 mm in the bulk volcanic plume and from 6.4 to 77.0 mm along the plume centerline (Table 2), which is large enough to produce a considerable effect on interferometric measurements.
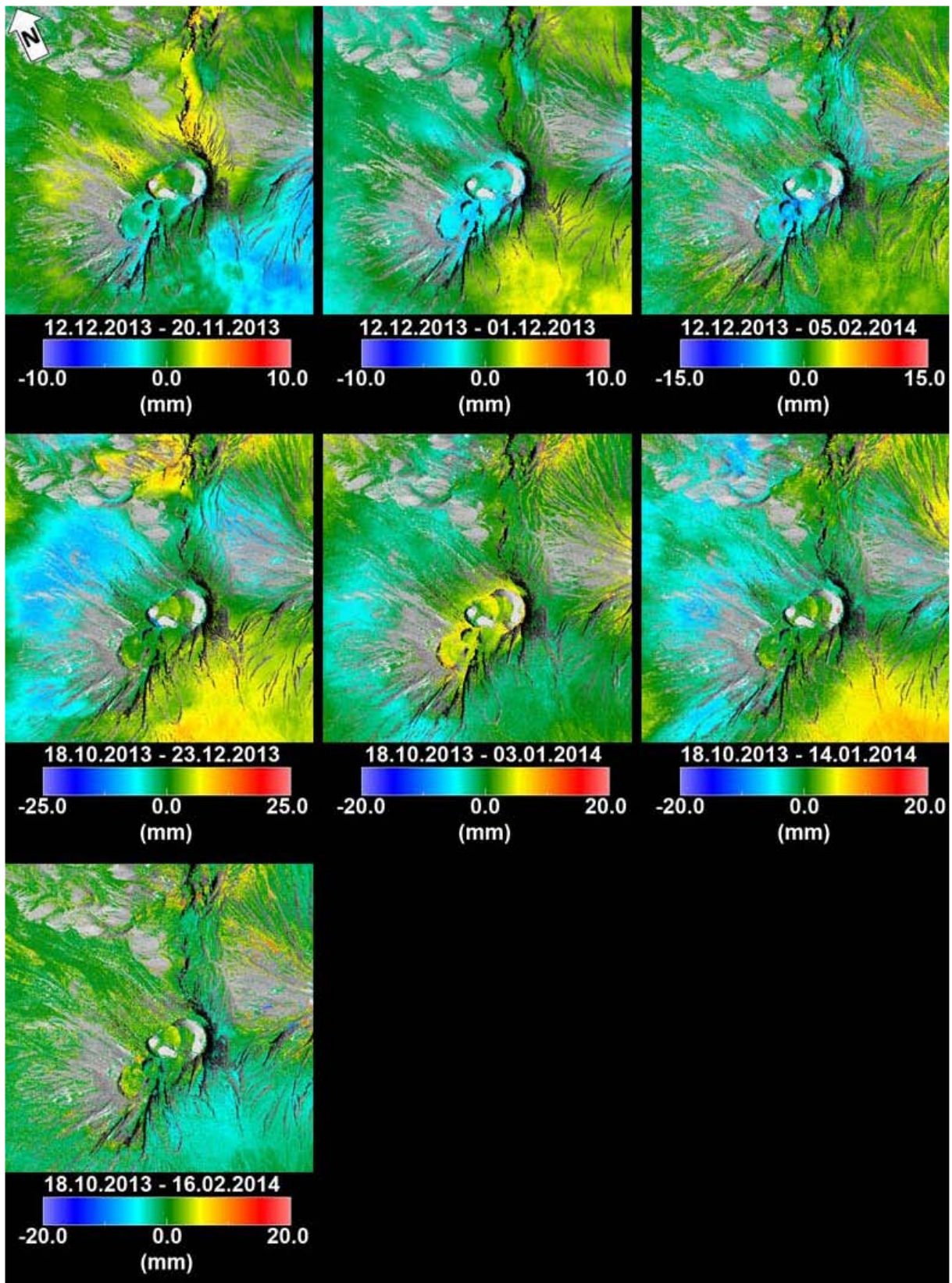
Fig.10: Coarsely corrected DInSARs showing turbulent tropospheric delay patterns comprising gas plume related delays and atmospheric delays. Scales indicate range change in millimetres.

Scene	Date (y-m-d)	PWV (mm)				Π_{T_s} (mm)	SWD (mm)			
		Crater rim Plume Center	Down-wind Plume Center	Down-wind Bulk Plume	Average Back-ground Atmos-phere		Crater rim Plume Center	Down-wind Plume Center	Down-wind Bulk Plume	Average Back-ground Atmos-phere
Subset 01										
Master	2013-12-12	0.012	4.3	1.3	2.1	6.42	0.096	34.59	10.38	17.25
Slave	2013-11-20	0.011	9.4	2.4	1.0	6.58	0.089	77.01	20.16	8.46
Slave	2013-12-01	0.009	4.3	1.1	0.7	6.39	0.072	34.44	8.61	5.97
Slave	2014-02-05	0.010	0.8	0.2	4.3	6.41	0.084	6.43	1.76	34.85
totals		**0.042**	**18.8**	**5.0**	**8.3**		**0.341**	**152.46**	**40.91**	**66.52**
Subset 02										
Master	2013-10-18	0.007	2.2	0.7	0.7	6.51	0.059	17.98	5.51	5.31
Slave	2013-12-23	0.009	1.1	0.3	5.2	6.43	0.075	8.91	2.10	41.48
Slave	2014-01-03	0.013	1.8	0.5	3.0	6.38	0.101	14.15	3.64	23.96
Slave	2014-01-14	0.011	0.9	0.2	3.6	6.39	0.091	7.27	1.67	29.06
Slave	2014-02-16	0.015	4.9	1.1	1.7	6.44	0.121	39.30	9.11	13.78
totals		**0.056**	**10.9**	**2.7**	**14.1**		**0.447**	**87.60**	**22.03**	**113.58**

Table 2: Combinations of SAR acquisitions used in subsets 01 & 02, and corresponding estimates of PWV contents inside the plume, and the background atmosphere are listed along with conversion factors Π_{T_s} used for calculation of theoretical SWDs.

4.5.2 Compilation of the priors used for Cinderella analysis

Differences between PWV contents estimated for the acquisition dates of the master image and the slave images were calculated ($PWV_{diff} = PWV_{master} - PWV_{slave}$), and used to determine the theoretical differential slant wet delay (SWD) that such differential PWV contents would produce in each interferogram (Table 3). The differential theoretical SWD time series were then used as prior information for the Cinderella algorithm, aiming to estimate exclusively those interferometric phase variations, which are characterized by a similar temporal evolution as that determined for the PWV contents in the gas plume. In order to capture the whole plume it was necessary to include both, the gas plume related delay time series determined for the proximal part of the plume above the crater rim and the delay time series determined for the downwind portion of the plume, since these are characterized by very different temporal evolutions (compare Figs.8b and 8f).

Phase corrections conducted previous to the Cinderella analysis did not completely remove topography related phase contributions (DEM error and deformation) and tropospheric delay effects, which are commonly referred to as the atmospheric phase screen (APS). Prior information on atmospheric phase screen variations, spatial baselines and temporal baselines were thus included in the Cinderella analysis, in order to mitigate the remaining corresponding phase contributions from the gas plume estimate (Table 3; APS priors are not displayed). Prior information for the APS estimation in Cinderella was derived from the tropospheric delay maps, which were already used for the removal of the stratification effect detailed in the *DInSAR data preparation* section. In addition to APS estimation the temporal variations of relative humidity, surface temperature and surface pressure derived from a single spot on the summit of the volcano were separately included as priors (Table 3). This was done for further refinement of the APS estimation, in order to remove also those small-scale tropospheric disturbances, which were not captured by the APS estimates. Moreover, this approach decomposes the refractivity related propagation delay into different contributions of the single physical processes, which contribute to the variations of the tropospheric delay, and thus enables to separately examine the delay effects of the different physical processes in the troposphere.

131

Master scene Date (y-m-d)	Slave scene Date (y-m-d)	Volcanic diff. SWD priors (mm)		Troposphere related priors			Topography related priors	
		Crater rim Plume center	Downwind Bulk plume	Relative humidity (%)	Surface temperature (K)	Surface pressure (hPa)	Spatial baseline (m)	Temporal baseline (days)
Subset 01								
2013-12-12	2013-11-20	0.007	-9.78	-0.05	4.60	0.96	11.8	-22
2013-12-12	2013-12-01	0.024	1.77	18.09	-3.32	-1.49	6.2	-11
2013-12-12	2014-02-05	0.013	8.62	-37.95	0.05	0.02	-0.5	55
Subset 02								
2013-10-18	2013-12-23	-0.016	3.40	-48.55	-4.57	-0.19	16.6	66
2013-10-18	2014-01-03	-0.042	1.87	-17.55	-3.05	1.85	-23.5	77
2013-10-18	2014-01-14	-0.032	3.84	-29.09	-4.35	-1.09	6	88
2013-10-18	2014-02-16	-0.062	-3.60	-9.42	-2.73	-0.45	-1.3	121

Table 3: Priors used in the Cinderella analysis include two gas plume related differential slant wet delay (diff. SWD) time series, differential time series of relative humidity, surface temperature and surface pressure, as well as spatial and temporal baselines. Priors for the turbulent atmospheric phase screen (single event) estimation are not displayed.

5. Results and Discussion

5.1 SAR delay estimates

Radar propagation delays in the free atmosphere aloft Láscar volcano were examined by means of the SAR delay estimates obtained from Cinderella analysis. SAR delay estimates were computed using the coarsely corrected DInSARs, which were presented in section *b) DInSAR data preparation* (Fig.10). Cinderella analysis yields one SAR delay estimate for each prior time series, that was included in the analysis, and one APS estimate for each SAR image. APS estimates are presented in the form of simple delay maps, where the scale indicates lengthening or shortening of the radar delay in units of millimetres.

The remaining SAR delay estimates are presented in the form of delay correlation maps, which depict the correlation between the input prior time series and spatial signals present in the DInSAR time series. The scales of these maps thus indicate the linear relationship between the prior and the DInSAR signal strength. The type of correlation between prior and signal strength estimate, respectively whether this relationship is positive or negative, is mainly determined by the direction of the radar delay, which can be expected of the physical process described by the prior time series that was used to obtain the delay estimate. Enhancing the water vapour content, or atmospheric pressure generally increases the refractivity and thus causes lengthening of the radar path delay, whereas an increase in temperature decreases refractivity, and causes shortening of the delay (see e.g. equation 7 in Smith & Weintraub, 1953). Priors describing the temporal evolution of water vapour contents and pressure are thus expected to be positively related to delay direction of the estimate, whereas temperature related priors are expected to be negatively related to delay direction. The presented delay estimates have to be interpreted as differences to the surrounding area, since DInSAR measures relative displacements with respect to an area, which can be considered as stable within the interferogram. If an estimated signal has a different sign than expected, then either the zero-point of the area considered as stable is wrong/offset, or the signal corresponds to another process that is negatively correlated to the delay expectation.

A volcanic gas plume e.g. contains more water vapour than the surrounding atmosphere, which results in lengthening of the radar path delay (positive delay) over the area of the plume with respect to its surroundings, and thus the gas plume related positive delay is expected to be positively related to the gas plume prior. In the delay correlation maps this is reflected by signatures indicating a positive correlation over those areas, which are affected by the higher water vapour concentrations of the gas plume.

5.1.1 Gas plume related phase delays

Gas plume estimates were computed using a limited number of three, respectively four temporally interconnected interferograms, which is close to the minimum amount of two interferograms required for analysis, which was done in order to separately examine the two interferogram subsets. Presented are the results obtained from the Cinderella run, that was conducted without including surface temperature and pressure priors, i.e. the delays associated to pressure and temperature were not removed from the gas plume estimates. Gas plume estimates of both subsets show a positively correlated cloud-shaped interferometric pattern depicted by yellow to orange colours on the south-eastern flank of Láscar volcano (Fig.11a&b), corresponding to the common direction of plume transport (Fig.4c&d, Fig.5 and 6). The negatively correlated delay patterns (depicted by cyan to blue colours), which are distributed over the western flanks of Láscar and Aguas Calientes volcanoes, indicate the contribution of another process (or other processes), which was (were) not mitigated from the gas plume estimate. Subset 02 was additionally processed without the SAR acquisition of 2014-01-03, in order to display the resulting reduction of the plume related repeating signal (Fig.11c). PWV contents inside the plume and their respective differences were larger for SAR observations of subset 01, than for observations of subset 02 (Table 2), suggesting a stronger influence on the signal of subset 01 (Fig.11a), if compared to subset 02 (Fig.11b&c). The amplitudes of the estimated delays displayed in Figures 11a-c are thus consistent with their respective input values, and are also in accordance with humidity contrast between plume and atmosphere (Table 2).
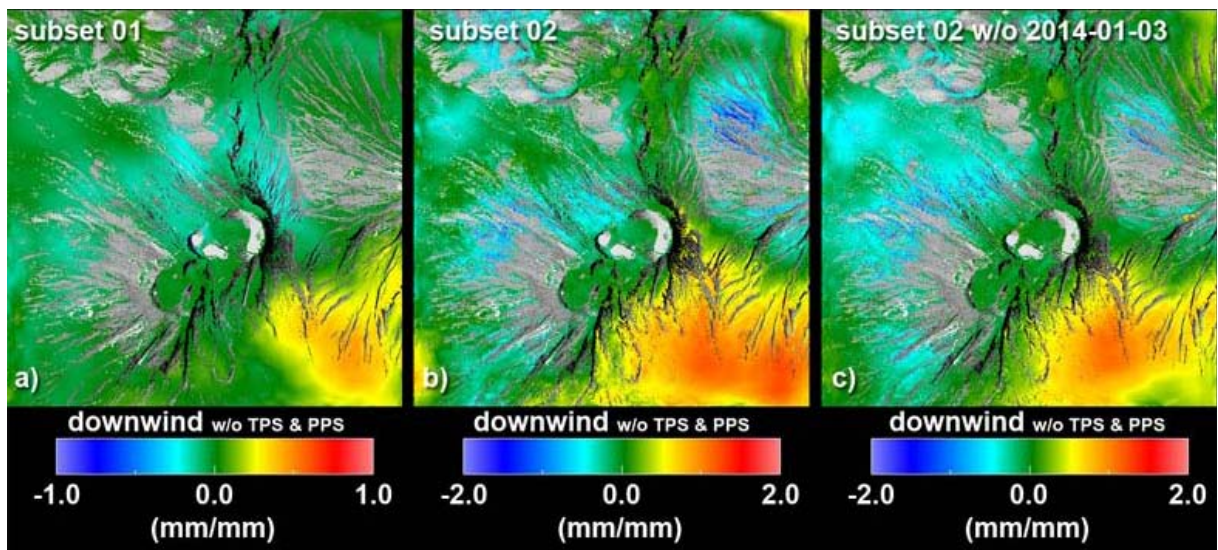
Fig.11: Delay correlation maps depicting estimated interferometric gas plume patterns from **a)** subset 01 and **b)** subset 02. **c)** Estimated interferometric pattern from subset 02, where the SAR observation of 2014-01-03 was removed. All three estimates contain phase contributions of the temperature and pressure related phase screens (TPS & PPS not removed). Scales correspond to estimated delay (mm) per theoretical delay (mm). Upper and lower bounds of the scale bar are equal to unity in subset 01, but not in subset 02, indicating that the estimated delay in subset 02 was by a factor 2 larger than the theoretical delay.

Gas plume estimates were calculated including all DInSARs of both subsets in the analysis. Each of these estimates thus contains the repeating gas plume related phase contributions, which are present in all interferograms of the DInSAR time series. Gas plume estimates were processed with (Fig.12a and 12b) and without (Fig.12c and 12d) additionally including prior information on the temporal evolution of surface temperature and pressure in order to show the effect of mitigation by the corresponding temperature and pressure phase screens (Fig.12e and f). Prior information on relative humidity variations where included in both of the above mentioned cases, yielding a relative humidity related delay estimate (Fig.12g), which was mitigated from all other delay estimates.

_____

The estimate resulting from the prior time series of the gas plume related delay above the crater rim (Fig.12a) shows a weak shortening of the delay over an area which is largely confined to the summit region of the volcano. The location of this signature is thus consistent with the assumption that the numbers, which were used as a prior for this estimate, are representative for temporal evolution of the delay that was measured above the crater. The observed shortening of the delay however contradicts the hypothesis that this signature can be attributed to enhanced moisture over the respective area, since a water vapour field would produce a lengthening of the delay. Repeating delay effects due to enhanced moisture thus seem to be negligible in the buoyant part of the gas plume directly above the emission source and the near range leeside section of the summit area where the plume is supposed to be most dense. The absence of plume-induced disturbances above the emission source may partly be attributed to the condensed nature of the plume close to the emission source, and to thermal delay effects, resulting from the temperature difference between the warm gas in the ascending part of the volcanic plume and the colder surrounding ambient air. Higher temperatures of the air inside the plume decrease the refractivity of the plume and thus cancel out the enhanced refractivity due to the larger moisture content with respect to the dry background atmosphere.

Delay estimates determined for the downwind portion of the gas plume (Fig.12b-d) show a cloud-shaped pattern that indicates lengthening of the delay due to enhanced moisture over an area that agrees well with the most common eastward plume transport directions observed during spring and late summer of that period (Fig.4c&d). Westward drifting plumes, which may have occurred during early summer (Fig.4c&d and 5), did obviously not leave any traces in the SAR signal, due to a less pronounced humidity/refractivity contrast between plume and surrounding atmosphere. This is further supported by the fact that easterly winds over the Atacama region have a lower velocity (Fig.5), and tend to be less stable with respect to their direction (Fig.4c&d), resulting in unsteady plume transport directions, which thus very likely do not produce pronounced repeating patterns. Wind speeds were generally larger during periods with eastward plume transport (spring and late summer; Fig.4a and 5), causing plume transport to be more turbulent, and thus the volcanic plume was very likely less condensed, and instead contained more vapour during that period. Furthermore, the gas plume phase screens clearly show that the repeating patterns of the gas plume signal (Fig.12c&d) can readily be reduced (Fig.12b), when a surface temperature and pressure correction (Fig.12e&f) is included in the Cinderella analysis. The gas plume related delay estimate depicted in Figure 12b thus clearly represents the result, in which separation of gas plume related delays from other phase contributions was most successful.

5.1.2 The decomposed APS: Temperature, pressure and relative humidity related phase delays

Delay patterns in the temperature dependent phase screen (Fig.12e) are asymmetrically distributed with respect to topography of the volcanic edifice, which can be attributed to the distinct exposure of mountain flanks to sunlight. All SAR observations used in this study were made around sunrise, thus the western flank commonly lies in the shadow of the volcanic edifice, resulting in cooler air masses with a higher refractivity aloft the western flank, which produces a lengthening of the delay, whereas the air masses above the flat plain southeast of the volcano, the summit region, and the eastern flanks are subjected to diabatic heating due to a more pronounced insolation, which causes refractivity to be smaller due to higher air temperature. Delay patterns of the pressure related phase screen (Fig.12f) indicate a lengthening of the delay over several confined areas, which are particularly exposed to westerly winds. The delay patterns of the temperature and pressure phase screens (Fig.12e&f) thus have the opposite direction, if compared to the delay patterns of the gas plume estimates (Fig.12c&d), resulting in a partial cancellation of the plume related delay (Fig.12b). Cancellation of the opposing phase screens hence reflect the negative dependence of volcanic gas emissions on barometric pressure and ambient temperature (Bredemeyer & Hansteen, 2014). This is further supported by the spatial distribution of relative humidity related delays (Fig.12g), which indicate enhanced relative humidity over exactly the same areas, which show a decreased temperature in the temperature phase screen (Fig.12e).

5.1.3 DEM error related phase delays

Delay patterns in the delay estimate obtained for the spatial baseline prior are intimately linked to topographic features. Lengthening of the delay occurs along the steep southeastern flank of Láscar and along the base of Aguas Calientes, while the delay is shortened in the summit region of Láscar and on the SW flank of Aguas Calientes (Fig.12h). The delay patterns in this estimate strongly resemble the patterns observed in the delay estimate obtained for the proximal part of the gas plume above the crater rim (Fig.12a), suggesting that the delays, which the algorithm attributed to the gas plume above the crater, are in fact rather related to spatial baseline. The signal obviously was assigned to both priors by the Cinderella algorithm, since this signal does not match perfectly to any of the priors.

5.1.4 Calibration curve for the correction of gas plume related delays and validation of the gas plume related estimate

The signal strength of the gas plume pattern in each DINSAR was compared to the strength of the theoretical differential delays, which served as a prior for the gas plume estimate. The signal strength of the gas plume contribution in the DInSARs was determined using the amplitude of the orange gas plume pattern in the delay estimate of the downwind portion of the plume depicted in Figure 12b by means of following equation (3).

$$S = signum(X * Y) * sqrt(abs(sum(X * Y))) , \quad (3)$$

where X corresponds to the amplitude of the gas plume estimate obtained from Cinderella and Y is the measured signal from the DInSARs, which were used in the Cinderella analysis. The comparison revealed a moderate positive linear relationship between signal strength and theoretical strength, which is fairly well represented by the regression line depicted in Figure 12i, since 61% (R^2=0.61) of the total variation in measured signal strength can be explained by the linear relationship between theoretical strength and signal strength. This regression line thus can in principle be used to determine the gas plume related delay in DInSARs for which no corresponding ground-based gas measurements were available.
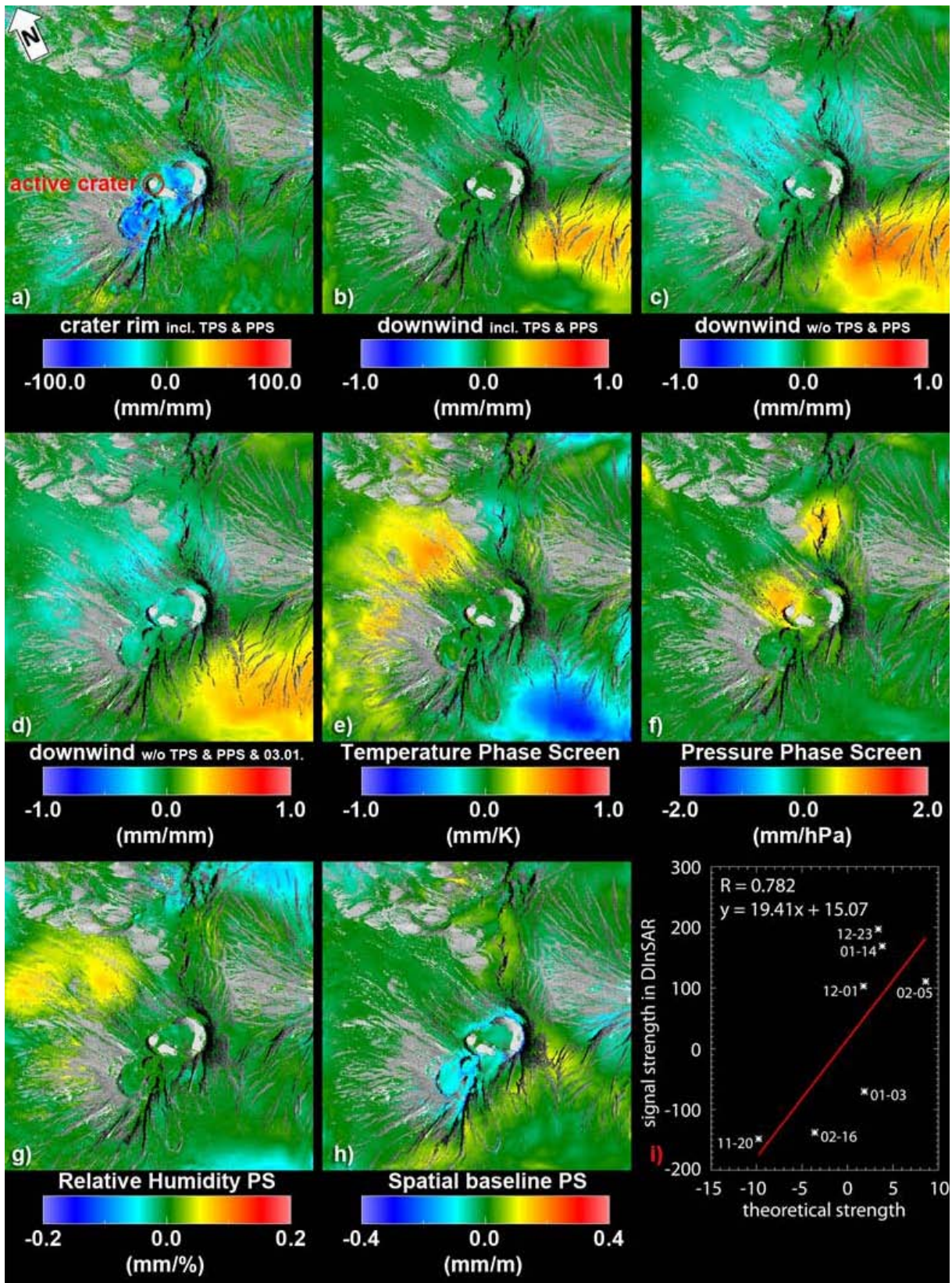
Fig.12: Delay correlation maps depicting the estimated SAR delays obtained from the priors, which were included in the Cinderella analysis. The active crater (*red circle*) currently is the main degassing source of Láscar volcano. **a)** Delay estimate for the gas plume aloft the crater **b-d)** Delay estimates for the downwind portion of the gas plume b) with and c) without additional removal of pressure and temperature dependent phase screens by including/excluding respective priors in the Cinderella analysis. **d)** Gas plume estimate as in c), however omitting the SAR observation of 2014-01-03. Scales correspond to estimated delay (mm) per theoretical delay (mm). Scalebar limits of the gas plume estimate obtained for the proximal part of the plume above the crater indicate that theoretical delays are by a factor 100 smaller than the delay estimate. **(Continued)**

136

Fig.12 (Continued): Upper and lower limits of the scale bars of the estimates obtained for the downwind portion of the gas plume are equal to unity, indicating concurrence of theoretical and estimated delay. The red to yellow coloured signature in the lower right corner of the image indicates a lengthening of the delay, where the effect of H_2O emissions is large. The affected area corresponds to the most common plume transport directions and positions (see Figure 6a - b) where the volcanic plume regularly touches the ground (fumigation). **e)** Estimates of surface temperature and **f)** surface pressure related delays. Scales indicate mm estimated delay per Kelvin, respectively hPa of the input prior. **g)** Delay estimate obtained for the relative humidity prior **h)** Delay estimate for the spatial baseline. **i)** Scatterplot of theoretical delay (mm) versus determined signal strength of the gas plume contribution in the DInSARs used for the gas plume estimate in b). Each asterisk symbol represents one of the DInSARs and corresponding slave dates (mm-dd) are indicated.

5.1.5 Atmospheric phase delays

Delay maps of the atmospheric phase screens (APS) that were generated to mitigate atmospheric disturbances from the gas plume estimate, were used to infer the meteorological conditions during each SAR observation (Fig.13). Such delay maps are snapshots of the meteorological situation, reflecting the spatial distribution of water vapour fields at the times of SAR acquisitions. Atmospheric disturbances aloft volcanoes are generally more pronounced and show more complex flow patterns on the lee side of the volcanic edifice (Wadge et al., 2002). This anisotropic distribution of turbulent atmospheric patterns can be attributed to the presence of volcanic gas plumes on the one hand, but also to orographic effects that govern the transport of moist air over mountainous terrain (Bonforte et al., 2001; Wadge et al., 2006). Orographic effects comprise diabatic heating of air masses over insolated mountain flanks and orographic lifting of air masses that are pushed by the wind, causing upslope advection of moist air that is forced to rise following the steep topography and to cool adiabatically causing an increase of the relative humidity.

APS delay patterns were compared to wind directions and atmospheric PWV contents estimated for the times of SAR acquisitions to assure that the modelled and measured wind directions and PWV estimates are consistent with the location and strength of associated delay patterns. Wind directions determined for the summit region of Láscar were prevailing westerly during the early morning hours of the "dry season", whereas wind directions of the "wet season" were predominantly easterly (Figs. 4c&d, 5, and 6). This is reflected by the spatial distribution of cloud shaped signatures, which are confined to the plateau east of the volcano during the "dry season", while pronounced cloud shaped signatures are mainly confined to the western flank of the volcano during early summer, indicating that moist air has been transported at low-altitude by easterly winds towards the edge of the plateau during the "wet season" (period comprising SAR acquisitions of 23.12.2013 to 14.01.2014). Wind directions are thus consistent with the spatial distribution of observed delay patterns and PWV estimates agree with the strength of these patterns. Enhanced humidity during SAR acquisitions of early summer can further be ascribed to the SAR acquisition strategy. Space based SARs typically repeat their observations at the same local time, causing SAR observations of early summer to be more affected by atmospheric disturbances, since they are recorded later with respect to sunrise, due to variations in the length of the day (Fig.2b). At Láscar volcano this effect is additionally enforced by more humid conditions that generally occur during that period.

5.1.6 Relative effect of the gas plume related delays

The delay estimate obtained for the downwind portion of the gas plume (Fig.12b) was used to determine the gas plume related phase contributions in each DInSAR of the time series. For this purpose the theoretical differential slant wet delays, which were used as a prior for this estimate, were multiplied by the respective delay estimate, which resulted in simple delay maps depicting the repeating gas plume related phase contribution present in each of the DInSARs (Fig.14). The delay maps use the same scale bounds as those used in Fig.10 in order to display the relative effect of the gas plume related delay on the interferometric measurements with respect to other phase contributions. As expected, the delay maps disclose that the differences in gas plume water vapour content between the two acquisitions that were used to form these interferograms, were much more contrasting with respect to other phase contributions in the DInSARs of subset 01.

The gas plume related delays depicted in Figure 14 were subtracted from the coarsely corrected DInSARs depicted in Figure 10 in order to mitigate the gas plume related phase contribution. The resulting

DInSARs (Fig.15) differ clearly from the coarsely corrected DInSARs, which still contain the gas plume signal. As expected, the removal of the gas plume signal is most obvious in the DInSARs of subset 01, where the mitigation resulted in a change to the opposite delay direction over the area which was affected by the gas plume.

5.2 d) Mitigation of non-deformation related delays from DInSARs

The delay estimates obtained from Cinderella analysis were subtracted from the coarsely corrected DInSARs that were presented in section *b) DInSAR data preparation* in order to obtain interferograms, which mainly contain topographic contributions resulting from a deforming ground surface (Fig.16). This refined correction more or less efficiently removed small scale delay patterns, which were caused by the volcanic gas plume and a turbulent atmosphere, as well as small-scale DEM errors related to acquisition geometry, respectively spatial baseline, leaving only some faint and blurry signatures with small amplitude.

In between the blurry residuals of non-deformation related phase contributions a putative small-scale ground deformation signal can be observed in the North-eastern summit craters. The signature occurs in each of the DInSARs, and indicates a progressively subsiding crater floor confined to an arcuate fault, where Pavez et al. (2006) detected co-eruptive subsidence of the crater floor during the 1995 eruption.
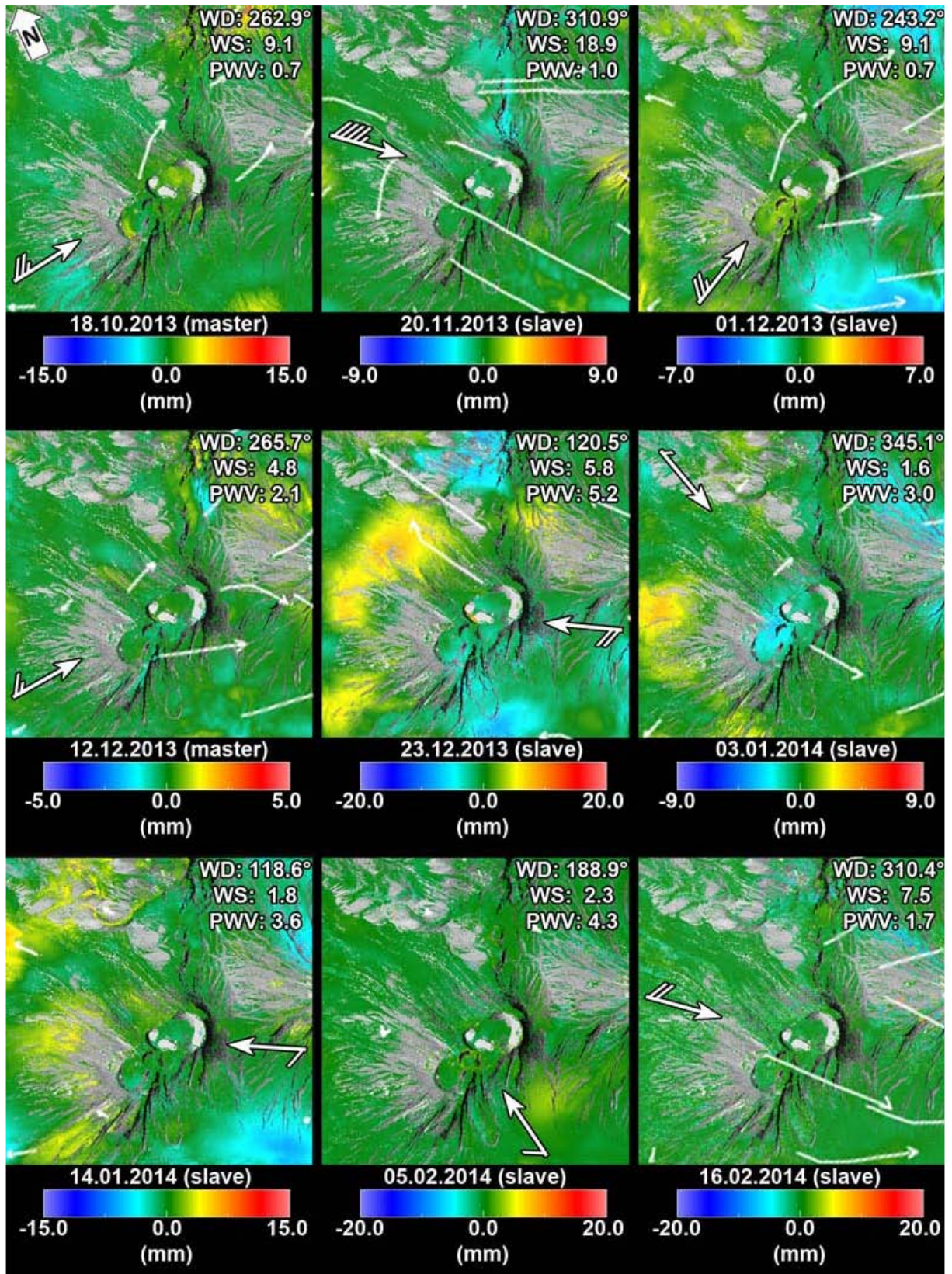
Fig.13: Estimates of atmospheric phase screens (APS) superimposed by surface wind fields obtained from the lowest eta level of WRF (*thin white arrows*). Scales indicate range change in millimetres, and are unique to each image, in order to enhance contrast by depicting the full range of each image. Katabatic (downslope) mountain winds prevail at the time of SAR acquisitions recorded during the early morning hours (10:04 GMT, local time is offset -3 hours). Wind barbs indicate wind directions and wind speeds above the summit of Láscar volcano, which were obtained from GFS hindcasts at the times of SAR acquisitions. The barbs are displaced upstream in order not to cover the delay signatures of the summit area. The individual lines of the barbs represent the wind speeds in units of knots (half strokes correspond to 5 knots and full strokes correspond to 10 knots). Wind directions (clockwise degrees from North), wind speed (m sec^{-1}) and estimated average PWV contents (mm) are additionally indicated in the upper right corner of each image.
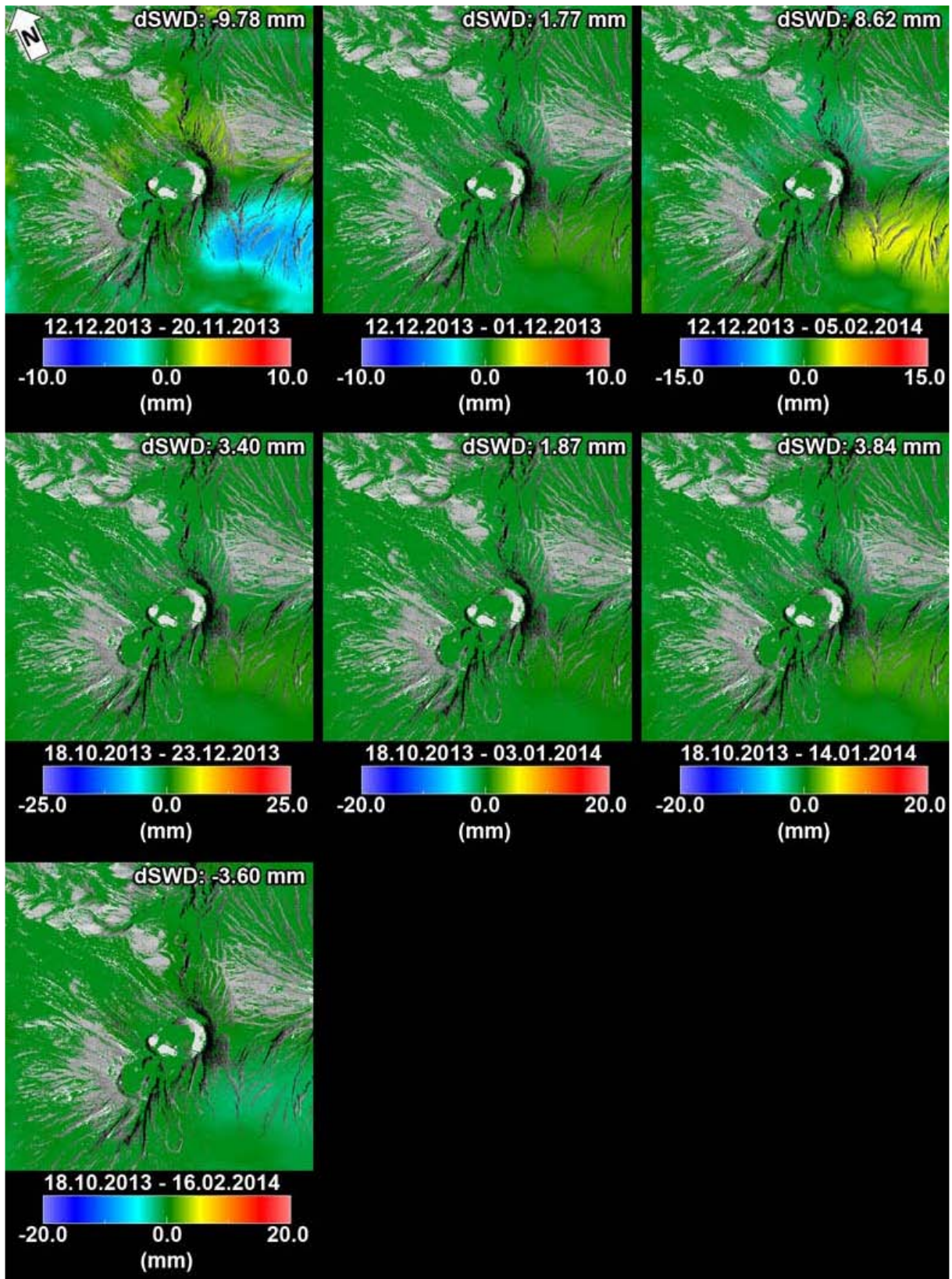
Fig.14 Delay maps of the gas plume related phase contribution. Scales indicate range change in millimetres, and are unique to each image using the same scale bounds as in Fig.10 for the sake of comparability with other phase contributions. The theoretical differential slant wet delays, which were used to obtain the corresponding delay maps, are indicated in the upper right corner of each map.
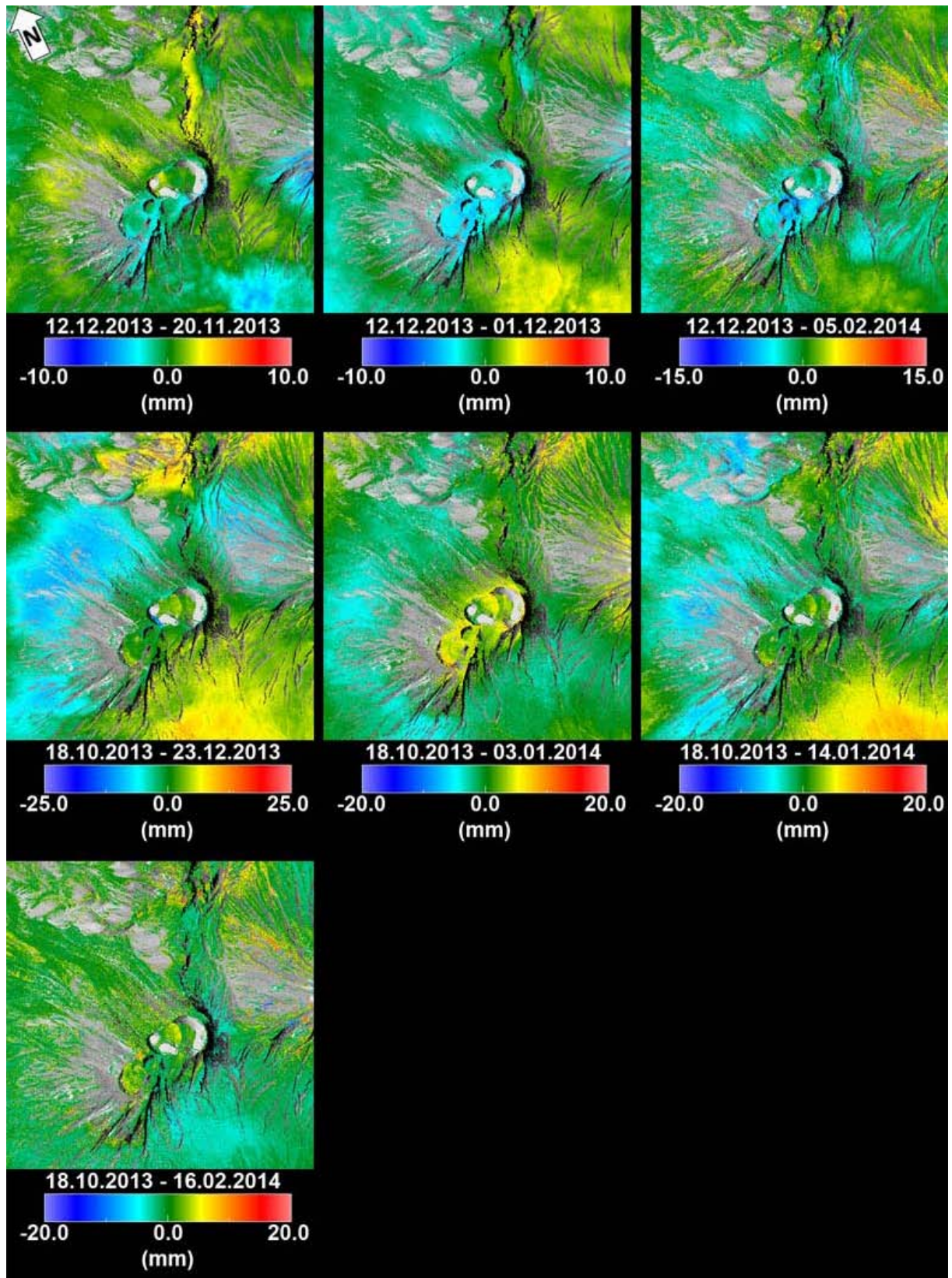
Fig.15 Coarsely corrected DInSARs, where the gas plume related delays were removed. Turbulent tropospheric delay patterns are thus restricted to non-volcano related atmospheric delays. Scales indicate range change in millimetres, and scale bounds are unique to each image using the same scale bounds as in Fig.10 and Fig.14 for the sake of comparability with other phase contributions.
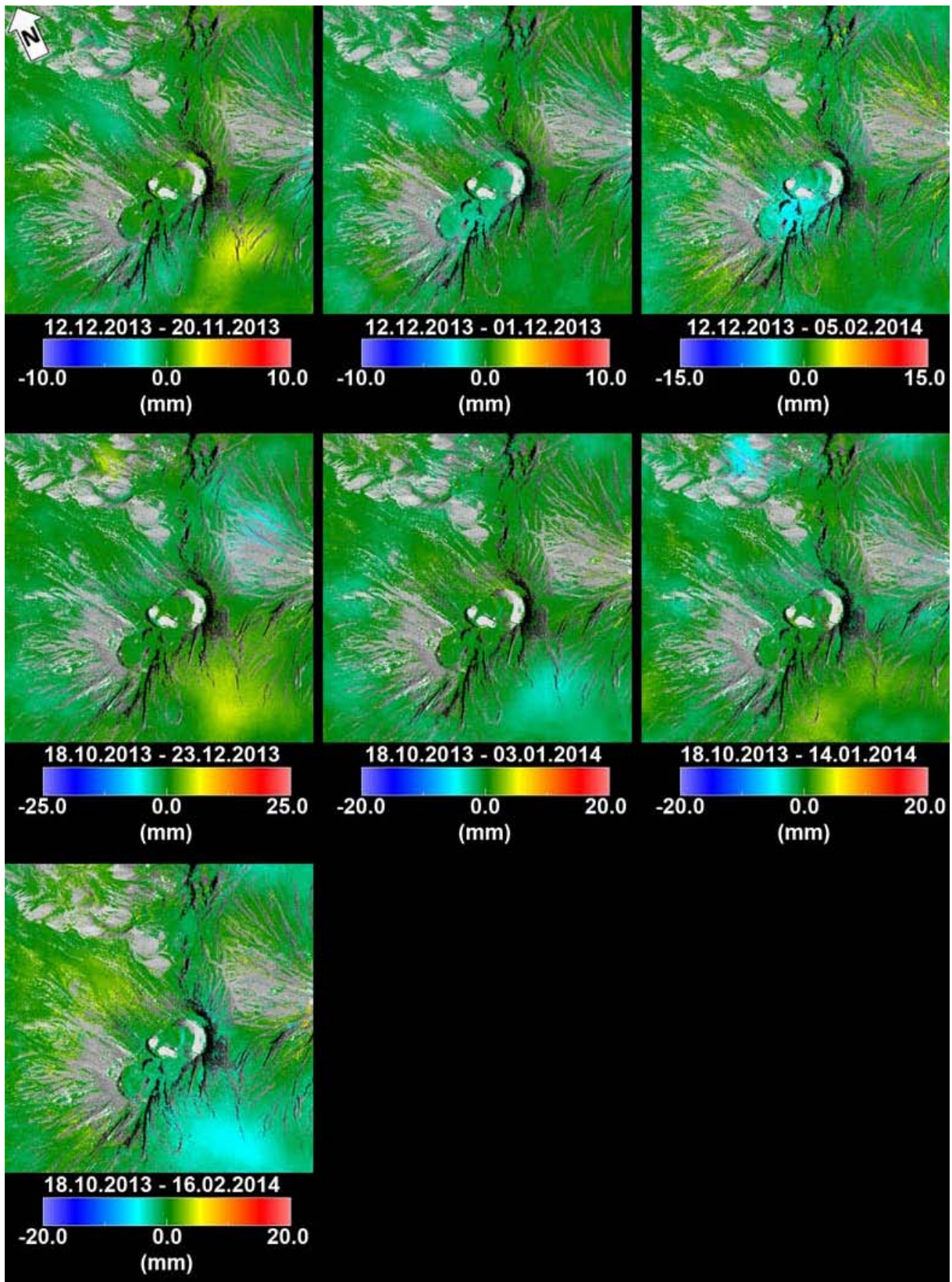
Fig.16: DInSARs obtained from the refined correction using the delay estimates obtained from Cinderella analysis. Scales indicate range change in millimetres, and are unique to each image using the same scale bounds as in Fig.10, Fig.14, and Fig.15 for the sake of comparability with other phase contributions.

6. Conclusions

Most modern SAR satellites revolve Earth on a sun-synchronous dusk-dawn orbit, and record their data along the day-night boundary, i.e. at a time, when emission rates of continuously degassing volcanoes typically are the highest (Aumento et al., 2002; Bredemeyer & Hansteen, 2014), which in turn increases the risk of having disturbances due to volcanic emissions in InSAR measurements. Deformation monitoring on volcanoes typically demands rapid response, in order to assess the volcanic hazard in a timely manner, and often relies on a limited number of available SAR acquisitions demanding a method that allows to remove atmospheric and gas plume-related disturbances from small sets of interferograms, where conventional methods as persistent scatterer interferometry and the small baseline subset algorithm would fail. The presented method using the Cinderella algorithm enables us to identify and mitigate repeating interferometric patterns caused by refractivity changes within volcanic gas plumes that were drifted in a similar direction during several subsequent SAR acquisitions. The algorithm requires only a relatively short time series of interferograms comprising at least 2 temporally interconnected interferograms, respectively 3 observations, and when more than 2 interferograms are available, these do not necessarily have to be temporally connected, in order to capture the plume related delay. The method allows iterative determination of PWV contents by matching the estimated delays with theoretical phase delays, which resulted in reasonably realistic values for the gas plume of Láscar volcano.

   Examination of PWV contents and associated delay effects in the Láscar volcanic gas plume yielded daily average bulk plume PWV contents of 0.2 to 2.5 mm water column, which would generate plume wide excess path delays in the range of 1.6 to 20 mm. Daily average PWV contents in the center of mass of the plume were even larger, spanning from 0.8 to 9.6 mm water column, which translate to theoretical slant wet delays of 6.4-77.0 mm, which are confined to spatially localized small areas of the plume, and thus less likely produce repeating patterns. Locations of the corresponding interferometric patterns in the delay estimates are consistent with determined locations of the volcanic plume, and variations in delay amplitudes are in good agreement with variations in the strength of the emission source and humidity of the background atmosphere, which seems to be proof enough, that the phase variations detected by the Cinderella algorithm are really related to refraction in the volcanic plume. Additional independent data on plume location at the time of SAR acquisitions would help to corroborate our results. Taking into account that the presented method mitigates all non-repeating gas plume related differential delay patterns, refraction in volcanic gas plumes can thus be considered to have a significant effect on DINSAR measurements, especially when only small stack sizes are available. In dual-pass interferometric measurements (where only one single interferogram, respectively two SAR observations are available), the delay effect will accordingly be even more pronounced, hence requiring extreme caution, when an alleged deformation signal is detected downwind of a volcano.

   The Cinderella algorithm thus provides the possibility to mitigate the plume-induced phase delay, where deformation measurements are the main purpose of monitoring. Combined analysis of gas emission measurements, meteorological data, and InSAR time series thus potentially improves results from volcano deformation studies.

_____

Appendix

A1. Estimation of PWV contents in the volcanic cloud

SO_2 SCDs were converted into vertical column densities (VCDs) using a geometrical air-mass factor (AMF_G) derived from equation (1).

$$AMF_G = \sqrt{\frac{(\cos(\beta)\cos(\delta) + \sin(\beta)\cos(\theta)\sin(\delta))^2 + (\sin(\beta)\sin(\theta))^2}{(\cos(\beta)\sin(\delta) + \sin(\beta)\cos(\theta)\cos(\delta))^2} + 1} \quad , \tag{1}$$

where θ is the scan angle (which corresponds to the angle between observing elevation and zenith position), $\delta=0$ is the tilt of the scanner, and $\beta=60$ is half the opening angle of the conical scanning plane.

The SO_2 VCDs correspond to the ratio of SO_2 SCDs and air mass factor expressed in equation (2).

$$SO_2 \ VCD(ppm.m) = \frac{SO_2 \ SCD}{AMF_G} \tag{2}$$

Radiative transfer corrections were not performed. Resulting SO_2 VCDs are path-length concentrations given in units of ppm*m, and approximation of PWV contents in units of mm water column requires several steps of conversion, which are combined in equation (3)

$$PWV \ (mm) = 10 * \frac{SO_2 \ VCD(ppm.m) * 2.5 \ x \ 10^{15} * H_2O/SO_2}{3.3 \ x \ 10^{22}} \tag{3}$$

Single steps of this conversion equation are derived from the following relationships. SO_2 VCDs in units of ppm.m are transformed to SO_2 VCDs in molecules.cm^{-2} using relation (4).

$$1 \ ppm.m \ SO_2 = 2.5 \ x \ 10^{15} \ SO_2 \ molecules.cm^{-2} \tag{4}$$

SO_2 VCDs in units of molecules.cm^{-2} are then scaled by the molar H_2O/SO_2 ratio of 31.5 determined from Multi-GAS measurements yielding vertically integrated water vapour concentrations in units of H_2O molecules.cm^{-2}.

H_2O VCDs in units of molecules.cm^{-2} are converted to the total amount of water vapour present in a vertical atmospheric column, also known as column integrated water vapour (IWV), which is commonly stated as the vertically integrated mass of water vapour per unit area (e.g. kg.m^{-2}) by following relation (5).

$$3.3 \ x \ 10^{22} \ H_2O \ molecules.cm^{-2} = 1 \ g.cm^{-2} = 10 \ kg.m^{-2} \approx 10 \ mm \ water \ column \tag{5}$$

Conversion of IWV in units of kg.m^{-2} to PWV in units of mm water column is obtained using equation (6)

$$PWV \ (mm) = IWV/\rho_{LW} \quad , \tag{6}$$

where ρ_{LW} is the density of liquid water, and thus a water vapour density of 1 kg.m^{-2} roughly corresponds to 1 mm height of an equivalent column of liquid water.

A2. Compensation of downwind evaporation

Potential evaporation rates were estimated, and used to scale our fixed H_2O/SO_2 ratio in order to compensate for downwind evaporation. Evaporation rates were calculated by an aerodynamic method, using temperatures, dew point temperatures, and wind speeds obtained from GDAS1 soundings provided by the National Oceanic and Atmospheric Administration (NOAA). The aerodynamic approach can be expressed by a Dalton-type equation (7) (Dalton 1803; Penman 1948),

$$E_P(cm.sec^{-1}) = f(u)(e_s - e) \quad , \tag{7}$$

in which E_P is the rate of potential evaporation (cm.sec^{-1}), f(u) is a wind speed function (cm.sec^{-1}.hPa^{-1}), respectively the vapour transfer coefficient, which is based on a logarithmic vertical wind velocity profile, and the second term (e$_s$-e) is the humidity term corresponding to the vapour pressure deficit of air (hPa). The product of both is typically referred to as the drying power of air. The wind function of the Dalton-type equation can be taken equal to (8)

$$f(u)(cm.sec^{-1}.hPa^{-1}) = 0.622k^2 \rho_{AIR} \frac{u_1}{P \rho_{LW} \log\left(\frac{z_1}{z_0}\right)^2} \quad , \tag{8}$$

where k = 0.40 is the dimensionless von Karman's constant describing the logarithmic velocity profile of a turbulent fluid flow near a boundary with a no-slip condition, i.e. it is assumed that wind speed is zero directly above the surface. ρ_{AIR} and ρ_{LW} correspond to the density of moist air and liquid water (g.cm^{-3}), respectively. u_1 refers to the wind speed (cm.s^{-1}) at measurement height z_1 (cm above ground surface), and P is barometric pressure (mbar or hPa) at measurement height z_1 . z_0 is the surface roughness height (cm above surface), which is related to the average height of obstacles in the trajectory of the wind.

The air density (g.cm^{-3}) was calculated using the ideal gas law, which requires knowledge of the temperature T (°C), pressure P (hPa) and specific humidity qv (g.g^{-1}) expressed in equation (9).

$$\rho_{AIR}(g.cm^{-3}) = \frac{0.1P}{287.04(1+0.608qv)(T+273.15)} \tag{9}$$

Specific humidity qv (g.g^{-1}) was approximated by equation (10)

$$qv \ (g.g^{-1}) = 0.622\left(\frac{e}{P}\right) \quad , \tag{10}$$

where 0.622 is the ratio of the molecular weight of water vapour to the average molecular weight of dry air, e is the partial pressure of water vapour in hPa, and P is barometric pressure in hPa.

Saturation vapour pressure e$_s$ was calculated using a Magnus-type equation (11) with coefficients determined by Sonntag (1990).

$$e_s \ (hPa) = 6.112 * exp\frac{17.62*T}{243.12+T} \quad , \tag{11}$$

where T is temperature in Celsius degree. Vapour pressure e was calculated using equation (12)

$$e(hPa) = \frac{RH}{100} * e_s \quad , \tag{12}$$

where RH is relative humidity, P is barometric pressure in hPa, T is temperature in Kelvin, and e$_s$ saturation vapour pressure at the ground level of the GDAS1 sounding. Relative humidity (%) was calculated using equation (13).

$$RH(\%) = 100 * \frac{\exp \ (T_D*17.625)/(T_D+243.04)}{\exp \ (T*17.625)/(T+243.04)} \quad , \tag{13}$$

where T and T_D are temperatures, and respectively dew point temperatures in Celsius degree.

Density of liquid water (kg.m^{-3}) was calculated from temperatures (°C) at plume height using equation (14) that was empirically determined by Jones & Harris (1992)

$$\rho_{LW}(kg.m^{-3}) = 999.85308 + 6.32693\text{x}10^{-2}T - 8.523829\text{x}10^{-3}T^2 - 6.943248\text{x}10^{-5}T^3 -$$
$$3.821216\text{x}10^{-7}T^4 . \tag{14}$$

The roughness height z_0 was approximated by equation (15), which was experimentally determined by Plate & Quraishi (1965) in wind tunnel experiments, and which yields fair results in the absence of more precise information (Hansen, 1993).

$$z_0 = 0.15h \quad , \tag{15}$$

where h is the average height of roughness elements (cm). As in this work the volcano is the main obstacle, and since the evaporating surface, respectively the volcanic plume typically is located roughly at summit altitude of the volcano, the average height of roughness elements relevant for the turbulent mixing of the plume with the atmosphere, was assumed to be equal to the height of the volcano above the surrounding plateau (about 750 m).

A3. Estimation of PWV contents in the atmosphere

Background precipitable water vapour PWV contents in the atmosphere above the volcano were estimated by means of an empirically determined approximation equation (16) (Garrison & Adler, 1990; Nann & Riordan, 1990). The calculation requires climatic variables including pressure, dew point temperature and temperature, which were obtained from vertical atmospheric GDAS1 profiles provided by NOAA.

$$PWV(mm) = \frac{RH * P * 4.1173}{(273.16 + T) * 1013} * e_s + 0.2 \quad , \tag{16}$$

where RH is relative humidity, P is barometric pressure in hPa, T is temperature in Kelvin, and e_s saturation vapour pressure at the ground level of the GDAS1 sounding. Note that we reduced the intercept of the equation from +2 to +0.2 mm, in order to adapt the formula to hyper-arid conditions, characterized by average PWV contents of less than 1 mm. Relative humidity (%) was calculated using equation (13) and saturation vapour pressure was calculated using equation (11).

References

Aumento F. (2002) Radon tides on an active volcanic island: Terceira, Azores. Geofísica Internacional, vol. 41, núm. 4, pp. 499-505, Universidad Nacional Autónoma de México, México

Berardino P., Fornaro G., Lanari R. and Sansosti E. (2002) A new algorithm for surface deformation monitoring based on small baseline differential SAR interferograms. Institute of Electrical and Electronics Engineers Transactions on Geosciences and Remote Sensing, 2002, 40(11), 2375-2383.

Bevis, M., Businger, S., Herring, T. A., Rocken, C., Anthes, R. A., & Ware, R. H. (1992). GPS meteorology: Remote sensing of atmospheric water vapour using the Global Positioning System. Journal of Geophysical Research: Atmospheres, 97(D14), 15787-15801. DOI: 10.1029/92JD01517

Bluth, G. J., Rose, W. I., Sprod, I. E., & Krueger, A. J. (1997). Stratospheric loading of sulfur from explosive volcanic eruptions. The Journal of Geology, 105(6), 671-684. DOI:10.1086/515972

Bonforte, A. and Ferretti, A. and Prati, C. and Puglisi, G. and Rocca, F. (2001). Calibration of atmospheric effects on SAR interferograms by GPS and local atmosphere models: first results. Journal of Atmospheric and Solar-Terrestrial Physics, 63, pp. 1343-1357. DOI: 10.1016/S1364-6826(00)00252-2

Dalton, J. (1802) Experimental essays on the constitution of mixed gases on the force of steam or vapor from water and other liquids in different temperatures, both in a Torricellian vacuum and in air; on evaporation and on the expansion of gases by heat. Mem. Lit. Philos. Soc. Manchester, 5(part 2), 535–602.

Déruelle B., Figueroa A.O., Medina T.E., Viramonte G.J., Maragaño C.M. (1996). Petrology of pumices of April 1993 eruption of Lascar (Atacama, Chile). Terra Nova, 8(2), 191-199

Emardson T.R., Simons M., Webb F.H. (2003) Neutral atmospheric delay in interferometric synthetic aperture radar applications: Statistical description and mitigation. Journal of Geophysical Research, Vol. 108, No. B5, 2231. doi:10.1029/2002JB001781

Fattahi, H., & Amelung, F. (2013). DEM error correction in InSAR time series. IEEE Transactions on Geoscience and Remote Sensing, 51(7), 4249-4259. DOI:10.1109/TGRS.2012.2227761

Ferretti A., C. Prati, and F. Rocca (2001) Permanent scatterers in SAR interferometry, IEEE Trans. Geosci. Remote Sens., 39, 8–20. DOI: 10.1109/36.898661

Figueroa O., Medina E., Déruelle B., and M. Maragano (1994). La erupcion del 19-20 Abril de 1993 del Volcán Láscar, II Region de Antofagasta: Correlaciones entre Petrologia y Volcanologia. 7° Congreso Geológico Chileno 1994, Actas Volumen I, pg.281-285.

Fischer T.P. (2008). Fluxes of volatiles (H_2O, CO_2, N_2, Cl, F) from arc volcanoes. Geochemical Journal, Vol. 42, pp. 21 to 38, 2008. DOI:10.2343/geochemj.42.21

Foster J., B. Brooks, T. Cherubini, C. Shacat, S. Businger, and C. Werner (2006), Mitigating atmospheric noise for InSAR using a high resolution weather model, Geophys. Res. Lett., 33, L16304, doi:10.1029/2006GL026781.

Francis, P.W. and Rothery, D.A. (1987) Using the Landsat Thematic Mapper to detect and monitor active volcanoes: an example from the Lascar volcano, northern Chile, Geology, 15, 614- 617.

Francis, P.W., Glaze L.S. and Rothery, D.A. (1989) Lascar volcano set to erupt? Nature, 339, 434.

Francis P.W. and Rothery D.A. (2000). Remote sensing of active volcanoes. Annu. Rev. Earth Planet. Sci. 2000. Vol.28:81–106. DOI: 10.1146/annurev.earth.28.1.81

Galle B, Johansson M, Rivera C, Zhang Y, Kihlman M, Kern C, Lehmann T, Platt U, Arellano S, Hidalgo S (2010) Network for Observation of Volcanic and Atmospheric Change (NOVAC) - A global network for volcanic gas monitoring: Network layout and instrument description. J Geophys Res 115 (D05304), doi:10.1029/2009JD011823

Gardeweg M. C., Medina E. (1994) La erupcion subpliniana del 19–20 de Abril de 1993 del Volcan Lascar, N de Chile. Actas 7° Congreso Geologico Chileno, Santiago 1994, 1, 299-304.

Gardeweg M.C., Sparks R.S.J., and Matthews S. J. (1998). Evolution of Lascar Volcano, northern Chile. Journal of the Geological Society of London, 155, Part 1, 89-104.

Gardeweg, M., Amigo. A. (2011) Mapa Preliminar de peligros volcánicos Volcán Láscar. Región de Antofagasta. Escala 1:50.000. Informe inédito, Subdirección Nacional de Geología. Programa de Riesgo Volcánico, Santiago.

Garrison, J. D., & Adler, G. P. (1990). Estimation of precipitable water over the United States for application to the division of solar radiation into its direct and diffuse components. Solar Energy, 44(4), 225-241. doi:10.1016/0038-092X(90)90151-2

Glaze L.S., Francis P.W., Self S., and Rothery D.A. (1989a). The Lascar September 16th eruption: satellite investigations. Bull. Volcanol. 51, 149-160.

Glaze L.S., Francis, P.W., and Rothery D.A. (1989b). Measuring thermal budgets of active volcanoes by satellite remote sensing. Nature 338, 144 - 146. doi:10.1038/338144a0

Giovanelli R., Darling J., Henderson C., Hoffman W., Barry D., Cordes J., Eikenberry S., Gull G., Keller L., Smith J.D., and G. Stacey (2001) The optical-infrared astronomical quality of high Atacama sites. II - Infrared characteristics. Publications of the Astronomical Society of the Pacific, Volume 113, Number 785 (PASP 113 785). DOI: 10.1086/322136

Giovanelli R. (2002) Optical seeing and infrared atmospheric transparency in the upper Atacama desert. Astronomical Site Evaluation in the Visible and Radio Range. ASP Conference Proceedings, Vol. 266. Edited by J. Vernin, Z. Benkhaldoun, and C. Muñoz-Tuñón. ISBN: 1-58381-106-0. San Francisco, Astronomical Society of the Pacific, 2002., p.366

Goldstein, R.M. (1995) Atmospheric Limitations to repeat-track radar interferometry. Geophysical Research Letters, Vol.22, pp.2517-2520. DOI: 10.1029/95GL02475

González C., Inostroza M., Aguilera F., González R., Viramonte J., & Menzies A. (2015). Heat and mass flux measurements using Landsat images from the 2000-2004 period, Lascar volcano, northern Chile. *Journal of Volcanology and Geothermal Research*, Volume 301, 277–292. doi:10.1016/j.jvolgeores.2015.05.009

González, P. J., M. Bagnardi, A. J. Hooper, Y. Larsen, P. Marinkovic, S. V. Samsonov, and T. J. Wright (2015), The 2014–2015 eruption of Fogo volcano: Geodetic modeling of Sentinel-1 TOPS interferometry, Geophys. Res. Lett., 42, 9239–9246, doi:10.1002/2015GL066003.

Grainger, J. F. and Ring, J. (1962). Anomalous Fraunhofer line profiles. Nature, 193, 762. doi:10.1038/193762a0

Green, D. N., & Neuberg, J. (2006). Waveform classification of volcanic low-frequency earthquake swarms and its implication at Soufrière Hills Volcano, Montserrat. Journal of Volcanology and Geothermal Research, 153(1), 51-63. doi:10.1016/j.jvolgeores.2005.08.003

Hansen, F. V. (1993). Surface roughness lengths (No. ARL-TR-61). ARMY RESEARCH LAB WHITE SANDS MISSILE RANGE NM 88002-5501.

Hanssen R.F., Weckwerth T.M., Zebker H.A., Klees R. (1999). High-resolution water vapour mapping from interferometric radar measurements. Science, 283, 1295-1297, February-26 1999. DOI: 10.1126/science.283.5406.1297

Hooper, A., H. Zebker, P. Segall, and B. Kampes (2004). A new method for measuring deformation on volcanoes and other natural terrains using InSAR persistent scatterers, Geophys. Res. Lett., 31, L23611, doi:10.1029/2004GL021737.

Hooper A., P. Segall, and H. Zebker (2007). Persistent scatterer interferometric synthetic aperture radar for crustal deformation analysis, with application to Volcán Alcedo, Galápagos, J. Geophys. Res., 112, B07407, doi:10.1029/2006JB004763.

Jones, F. E., & Harris, G. L. (1992). ITS-90 density of water formulation for volumetric standards calibration. J. Res. Natl. Inst. Stand. Technol., 97(3), 335-340.

Jung H S, Lee C W, Pork J W, Kim K D and Won J S (2008). Improvement of small baseline subset (SBAS) algorithm for measuring time-series surface deformations from differential SAR interferograms. Korean Journal of Remote Sensing, 2008,24, 165-177. (in Korean)

Jung J., Kim D., Park S.-E.(2014).Correction of Atmospheric Phase Screen in Time Series InSAR using WRF Model for Monitoring Volcanic Activities. IEEE Transactions on Geoscience and Remote Sensing, vol. 52, issue 5, pp. 2678-2689. DOI: 10.1109/TGRS.2013.2264532

Kingsbury N.G. (1998). The Dual-tree Complex Wavelet Transform: A new technique for shift invariance and directional filters. In *IEEE Digital Signal Processing Workshop* (Vol. 86, pp. 120-131). Bryce Canyon.

Lu, Z. (2007). InSAR imaging of volcanic deformation over cloudprone areas—Aleutian Islands. Photogrammetric Engineering & Remote Sensing, 73, 245–257. DOI: 10.14358/PERS.73.3.245

Marín J.C., Pozo D., Mlawer E., Turner D.D., Curé M. (2013). Dynamics of Local Circulations in Mountainous Terrain during the RHUBC-II Project. Monthly Weather Review, Vol.141, 3641-3656, DOI: 10.1175/MWR-D-12-00245.1

Massonnet D., Briole P., Arnaud A. (1995). Deflation of Mount Etna monitored by spaceborne radar interferometry. Nature, 375, 567-570. doi:10.1038/375567a0

Mateus, P., Nico, G., & Catalão, J. (2013). Can spaceborne SAR interferometry be used to study the temporal evolution of PWV?. Atmospheric Research, 119, 70-80. doi:10.1016/j.atmosres.2011.10.002

Matthews S. J., Jones A. P., Gardeweg M. C. (1994b) Lascar Volcano, northern Chile; evidence for steady-state disequilibrium. Journal of Petrology, 35, 401-432. doi:10.1093/petrology/35.2.401

Matthews S. J., Gardeweg M. C., Sparks R. S. J. (1997) The 1984 to 1996 cyclic activity of Lascar Volcano, Northern Chile; cycles of dome growth, dome subsidence, degassing and explosive eruptions. Bulletin of Volcanology 1997;59:72-82. doi:10.1007/s004450050176

Matthews S. J., Sparks R. S. J., & Gardeweg M. C. (1999). The Piedras Grandes–Soncor eruptions, Lascar volcano, Chile; evolution of a zoned magma chamber in the central Andean upper crust. *Journal of Petrology*, *40*(12), 1891-1919. doi:10.1093/petroj/40.12.1891

Menard, G., Moune, S., Vlastélic, I., Aguilera, F., Valade, S., Bontemps, M., & González, R. (2014). Gas and aerosol emissions from Lascar volcano (Northern Chile): Insights into the origin of gases and their links with the volcanic activity. *Journal of Volcanology and Geothermal Research*, *287*, 51-67. doi:10.1016/j.jvolgeores.2014.09.004

Nann, S., & Riordan, C. (1991). Solar spectral irradiance under clear and cloudy skies: Measurements and a semiempirical model. Journal of Applied Meteorology, 30(4), 447-462. DOI:10.1175/1520-0450(1991)030<0447:SSIUCA>2.0.CO;2

Oppenheimer C., Francis P. W., Rothery D. A., Carlton R. W., & Glaze L. S. (1993). Infrared image analysis of volcanic thermal features: Lascar Volcano, Chile, 1984–1992. Journal of Geophysical Research: Solid Earth (1978–2012), 98(B3), 4269-4286. doi:10.1029/92JB02134

Otárola A., Holdaway M., Nyman L-A., Radford S.J.E, Butler B.J. (2005) Atmospheric transparency at Chajnantor: 1973-2003. ALMA Memo #512. http://www.alma.cl/almamemos/100538/Memo512.pdf

Pavez, A., Remy, D., Bonvalot, S., Diament, M., Gabalda, G., Froger, J. L., ... & Moisset, D. (2006). Insight into ground deformations at Lascar volcano (Chile) from SAR interferometry, photogrammetry and GPS data: Implications on volcano dynamics and future space monitoring. Remote Sensing of Environment, 100(3), 307-320. doi:10.1016/j.rse.2005.10.013

Penman, H. L. (1948). Natural evaporation from open water, bare soil, and grass, Proc. R. Soc. London, A193, 120–146.

Pichelli E., Ferretti R., Cimini D., Perissin D., Montopoli M., Marzano F.S., Pierdicca N. (2010). Water vapour distribution at urban scale using high-resolution numerical weather model and spaceborne SAR interferometric data. Nat. Hazards Earth Syst. Sci., 10, 121–132, 2010. doi:10.5194/nhess-10-121-2010

Platt, U. and Stutz, J. (2008). Differential Optical Absorption Spectroscopy – Principles and Applications. Springer-Verlag Berlin Heidelberg. DOI: 10.1007/978-3-540-75776-4

Plate, E. J. and A. A. Quraishi (1965) Modeling of Velocity Distributions Inside and Above Tall Crops. J. Appl. Meteor., 4, 400–408. doi: 10.1175/1520-0450(1965)004<0400:MOVDIA>2.0.CO;2

Remy D., Bonvalot S., Briole P., Murakami M. (2003). Accurate measurements of tropospheric effects in volcanic areas from SAR interferometry data: application to Sakurajima volcano (Japan). Earth and Planetary Science Letters 213 (2003) 299-310. doi:10.1016/S0012-821X(03)00331-5

Rosen P.A., Henley S., Zebker H.A., Webb F.H., Fielding E.J. (1996). Surface deformation and coherence measurements of Kilauea volcano, Hawaii, from SIR-C radar interferometry. Journal Of Geophysical Research, Volume 101, Issue E10: 23109-23125, 25 October 1996. DOI:10.1029/96JE01459

Rosen P., S. Hensley, I.R. Joughin, F.K. Li, S.N. Madsen, E. Rodriguez, and R.M. Goldstein (2000). Synthetic aperture radar interferometry. Proceedings of the IEEE, 88:333–380. DOI:10.1109/5.838084

Rüeger, J.M., 2002. Refractive index formulae for radio waves. FIG XXII International Congress, Washington, D.C. USA, April 19-26 2002

Saastamoinen J. (1972) Introduction to practical computation of astronomical refraction. Bulletin Géodésique 106, 383-397. DOI:10.1007/BF02522047

Selesnick I. W., R. G. Baraniuk, N. C. Kingsbury (2005). The dual-tree complex wavelet transform. IEEE Signal Processing Magazine, Volume 22, Issue 6, pp 123-151. DOI:10.1109/MSP.2005.1550194

Shinohara H., Aiuppa A., Guidice G., Gurrieri S., Liuzzo M. (2008). Variation of H_2O/CO_2 and CO_2/SO_2 ratios of volcanic gases discharged by continuous degassing of Mount Etna volcano, Italy. J. Geophys. Res., 113, B09203, doi:10.1029/2007JB005185.

Smith E. K. and S. Weintraub (1953) The Constants in the Equation for Atmospheric Refractive Index at Radio Frequencies. Proceedings of the IRE, Volume 41 , Issue 8, pp1035 - 1037. DOI:10.1109/JRPROC.1953.274297

Sonntag, D. (1990). Important new values of the physical constants of 1986, vapor pressure formulations based on the ITS-90, and psychrometer formulate. Z. Meteorol., 70(5), 340-344.

Sparks RSJ (2003) Dynamics of magma degassing. *Geological Society, London, Special Publications 2003,* v. 213, p. 5-22. doi: 10.1144/GSL.SP.2003.213.01.02

Stern CR (2004) Active andean volcanism: its geologic and tectonic setting. Revista Geológica de Chile, 31 (2):161–206. DOI:10.4067/S0716-02082004000200001

Tait, Stephen, Jaupart, Claude, Vergniolle, Sylvie (1989) Pressure, gas content and eruption periodicity of a shallow, crystallising magma chamber. Earth and Planetary Science Letters, 92 (1989) 107-123. doi:10.1016/0012-821X(89)90025-3

Tassi et al (2009) - The magmatic- and hydrothermal-dominated fumarolic system at the active crater of Lascar volcano, northern Chile. Bulletin of Volcanology, Volume 71, Issue 2 , pp 171-183. DOI:10.1007/s00445-008-0216-z

Ulmer, Franz-Georg (2015) Cinderella: Method Generalisation of the Elimination Process to Filter Repeating Patterns. In: 2015 IEEE International Conference on Digital Signal Processing (DSP), Seiten 1001-1005. IEEE Xplore. IEEE International Conference on Digital Signal Processing 2015, 21-24 July 2015, Singapore. DOI: 10.1109/ICDSP.2015.7252028.

Ulmer, Franz-Georg (2015) Cinderella: Method Generalisation of the Elimination Process to Filter Repeating Patterns. In: 2015 IEEE International Conference on Digital Signal Processing (DSP), Seiten 1001-1005. IEEE Xplore. IEEE International Conference on Digital Signal Processing 2015, 21-24 July 2015, Singapore. DOI: 10.1109/ICDSP.2015.7252028.

Ulmer, Franz-Georg und Adam, Nico (2015) A Synergy Method to Improve Ensemble Weather Predictions and Differential SAR Interferograms. ISPRS Journal of Photogrammetry and Remote Sensing (109), Seiten 98-107. Elsevier. DOI: 10.1016/j.isprsjprs.2015.09.004. ISSN 0924-2716.

Ulmer, Franz-Georg (2016) On the accuracy gain of electromagnetic wave delay predictions derived by the digital filter initialization technique. Journal of Applied Remote Sensing, 10 (1), 016007-1-016007-7. SPIE digital library. DOI: 10.1117/1.JRS.10.016007. ISSN 1931-3195.

Ulmer, Franz-Georg und Adam, Nico (2015) A Synergy Method to Improve Ensemble Weather Predictions and Differential SAR Interferograms. ISPRS Journal of Photogrammetry and Remote Sensing (109), Seiten 98-107. Elsevier. DOI: 10.1016/j.isprsjprs.2015.09.004. ISSN 0924-2716.

Vandaele AC, Simon PC, Guilmot JM, Carleer M, Colin R (1994) SO_2 absorption cross section measurement in the UV using a Fourier transform spectrometer. J Geophys Res 99 (D12): 25,599-25,605. DOI: 10.1029/94JD02187

Voigt S, Orphal J, Bogumil K, Burrows JP (2001) The temperature dependence (203-293K) of the absorption cross sections of O_3 in the 230-850 nm region measured by Fourier-transform spectroscopy. Journal of Photochemistry and Photobiology A: Chemistry 143:1-9. DOI: 10.1016/S1010-6030(01)00480-4

Vuille M. (1999). Atmospheric circulation over the Bolivian Altiplano during dry and wet periods and extreme phases of the Southern Oscillation. Int. J. Climatol. 19: 1579–1600. doi:10.1002/(SICI)1097-0088(19991130)19:14<1579::AID-JOC441>3.0.CO;2-N

Wadge, G., P. W. Webley, I. N. James, R. Bingley, A. Dodson, S. Waugh, T. Veneboer, G. Puglisi, M. Mattia, D. Baker, S. C. Edwards, S. J. Edwards, and P. J. Clarke (2002). Atmospheric models, GPS and InSAR measurements of the tropospheric water vapour field over Mount Etna. Geophys. Res. Lett., 29(19), 1905. doi:10.1029/2002GL015159

Wadge,G., G.S. Mattioli, R.A. Herd (2006). Ground deformation at Soufrière Hills Volcano, Montserrat during 1998–2000 measured by radar interferometry and GPS. Journal of Volcanology and Geothermal Research, Volume 152, Issues 1–2, pp.157–173. doi:10.1016/j.jvolgeores.2005.11.007

Watson, I.M., C. Oppenheimer, B. Voight, P.W. Francis, A. Clarke, J. Stix, A. Miller, D.M. Pyle, M.R. Burton, S.R. Young, G. Norton, S. Loughlin, B. Darroux, MVO Staff (2000). The relationship between degassing and ground deformation at Soufriere Hills Volcano, Montserrat. Journal of Volcanology and Geothermal Research 98 (2000) 117–126. doi:10.1016/S0377-0273(99)00187-0

Wooster M. J., & Rothery D. A. (1997). Thermal monitoring of Lascar Volcano, Chile, using infrared data from the along-track scanning radiometer: a 1992–1995 time series. Bulletin of Volcanology, 58(7), 566-579.

Wooster M. J. (2001). Long-term infrared surveillance of Lascar Volcano: Contrasting activity cycles and cooling pyroclastics. Geophysical Research Letters, 28(5), 847-850.

Zebker H., Rosen P., and Hensley S. (1997). Atmospheric effects in interferometric synthetic aperture radar surface deformation and topographic maps. Journal of Geophysical Research, 102, 7547–7563. DOI: 10.1029/96JB03804

APPENDIX

Acquisition, evaluation and processing of scanning Mini-DOAS data

APPENDIX

Acquisition, evaluation and processing of scanning Mini-DOAS data

A1. Scan-DOAS equipment and software

Continuous long-term monitoring of SO_2-fluxes in this work has been conducted using permanent stationary NOVAC version 1 scan-DOAS instruments (Chapters II-IV and VI), which were developed in the framework of the so-called NOVAC project (Galle et al., 2010; Network for the Observation of Volcanic and Atmospheric Change). In addition a portable version of this instrument, which was developed for the rapid temporary deployment (Conde et al., 2014), has been used during several measurement campaigns in Northern Chile as detailed in Chapter V (Tamburello et al., 2014). Evaluation of the scan-DOAS data was done using a dedicated observatory software package, called the NOVAC program, which allows performing fully automated near-real time SO_2-flux monitoring, and provides standardized evaluation routines in order to produce consistent datasets which facilitates intercomparison of measurements from different instruments (Johansson 2009).

The NOVAC version 1 scan-DOAS instrument consists of a single- or a dual-channel S2000 Ocean Optics© UV spectrometer, and a scanning device with an incorporated telescope, which is connected to the spectrometer via optical fibers. A rotating mirror located in front of the telescope redirects the incoming scattered sunlight to the telescope, which enables the UV spectrometer to stepwise scan across the sky above, and to measure the intensity of the incident sunlight at different elevation angles of a scan, yielding cross-sections of the volcanic gas plume, which are perpendicularly aligned to the direction of transport. Each scan is preceded by the acquisition of two reference spectra, in order to be able to characterize the on-site measurement conditions. A solar radiation spectrum measured at the zenith position of the scanner is being used as sky light reference, and for the automatic determination and adjustment of the exposure time used for the subsequent collection of spectra at each scan angle of the measured plume cross section. Automatic adjustment of exposure times entails highly variable acquisition durations of the scans, especially in unstable weather situations, which can range between 3 and 15 minutes per scan throughout the measurement series of a day. In order to correct for instrumental noise, additionally a dark current spectrum is being measured at the nadir position of the scanner, where sunlight is inhibited to reach the sensor.

SO_2 differential column densities (SCDs) were retrieved from the measured sunlight spectra by means of differential optical absorption spectroscopy (DOAS, Platt & Stutz, 2008) using the fully automated DOAS evaluation routine of the NOVAC program. Evaluation was performed in the wavelength range 310-325 nm using the two on-site measured reference spectra and four laboratory reference spectra, which were all convolved to the spectral resolution of the instrument. The laboratory reference spectra comprise absorption cross sections of SO_2 (Fig. 1; Vandaele et al., 1994), and O_3 (Voigt et al., 2003). In addition, a ring spectrum and a solar spectrum were included in the DOAS-fit, in order to correct for scattering effects due to the so-called ring effect (Grainger & Ring, 1962), and to account for SO_2-contaminated background sky reference spectra, which were recorded by the instrument before each scan.
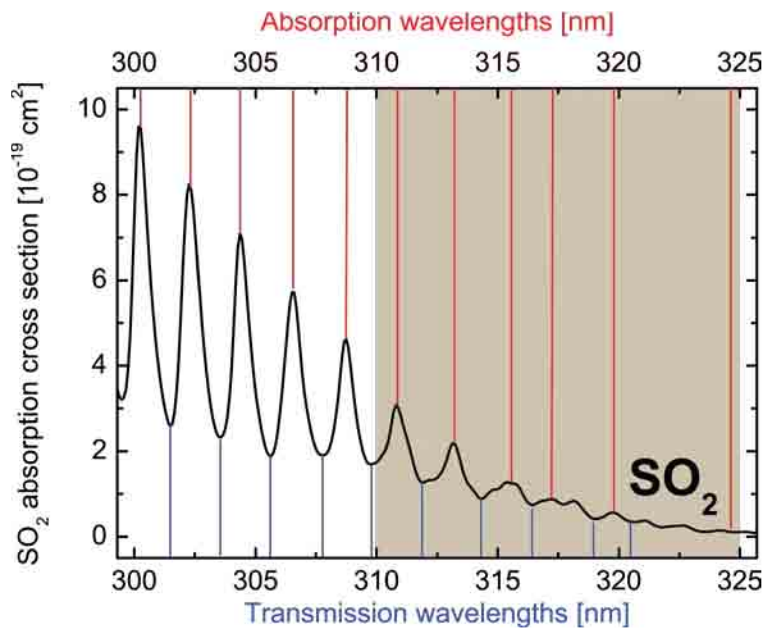
Fig.1 Absorption cross-section of SO₂ showing its specific narrow band absorption and transmission wavelengths indicated by red and blue lines respectively. The shaded area indicates the wavelength range of 310-325 nm, which was commonly used for DOAS evaluation in this work, because broad band scattering effects and the interference with the absorption structures of ozone (O_3) is minor in this range than at shorter wavelengths.

A2. Installation of permanent scan-DOAS instruments for the purpose of long-term monitoring

Scan-DOAS instruments are typically deployed in the range of the most common wind directions downwind of a volcano, as to best cover the prevailing direction of plume transport. An appropriate location for the permanent installation of such an instrument can easily be found by means of a careful analysis of the wind field in the area of the volcano. Wind fields aloft mountainous terrain are commonly characterized by systematic diurnal variations in prevalent wind directions, which govern the direction of plume transport. Best monitoring results are obtained, if the instrument is roughly standing below the plume during the measurements, and if the scanner of the instrument is well aligned with respect to the emission source, i.e. the instrument is scanning perpendicular to the direction of plume transport. Additionally the instrument requires free lines of sight towards the horizon, for which the morphology of the target volcano and the terrain surrounding the volcano needs to be taken into account. Gas emissions from well exposed solitary steep volcanic cones that significantly overtop the surrounding landscape are typically much easier to be measured by means of scan-DOAS, than those of flat and/or more complex cones, with adjacent obstacles of same size (e.g. other volcanoes), since the morphology influences crosswind dispersion of the plume, and the instruments have to be located considerably below the plume, in order to capture the entire gas emission. Errors due to scattering effects generally increase with increasing distance from the plume (Mori et al., 2006). Thus a reasonable distance of the instrument from the emission source has to be chosen, which is always a compromise between being too close to the emission source and being too far way, since the strength of the emission source may vary a lot, resulting in very dilute plumes during periods of quiescence or turbulent transport conditions, which interchange with optically opaque plumes during eruptive events.

A3. Determination of plume location, geometry and transport speed

Calculation of SO₂-fluxes from scan-DOAS measurements demands knowledge of the measurement geometry, comprising the height at which the plume crosses the scanning surface of the scan-DOAS, and the velocity and direction of plume transport. Under favourable conditions these parameters can be obtained

154

from simultaneous measurements of at least two individual scan-DOAS instruments whose scan ranges overlap significantly (Johansson et al., 2009). Direction and plume height are determined by triangulation between simultaneous scans of the two scanners, demanding that both instruments see the center of mass of the plume, which should preferably not be located too close to the horizons of the instruments. Plume speed measurements require one of the instruments to stop scanning, i.e. to stop measuring fluxes and to record time series of the variations in the gas column using both channels of the S2000 Ocean Optics© spectrometer instead. The two channels of the spectrometer point into different directions, with a fixed angular separation of 6.9 degrees between the optical axes and thus one channel is looking further upwind, while the other channel is viewing further downwind. Such dual-channel recordings are preferably conducted when the plume is located directly above the instrument, enabling to determine the wind speed via cross-correlation between the recordings of the two channels, while the other instrument is scanning the plume as usual, in order to measure SO_2-fluxes. Such favourable conditions and redundancy of two instruments are however rarely found, which is why plume transport velocities and directions are typically obtained from numerical weather predictions, or weather stations located on the summit of the volcanoes for most of the DOAS scans (Fig.2).
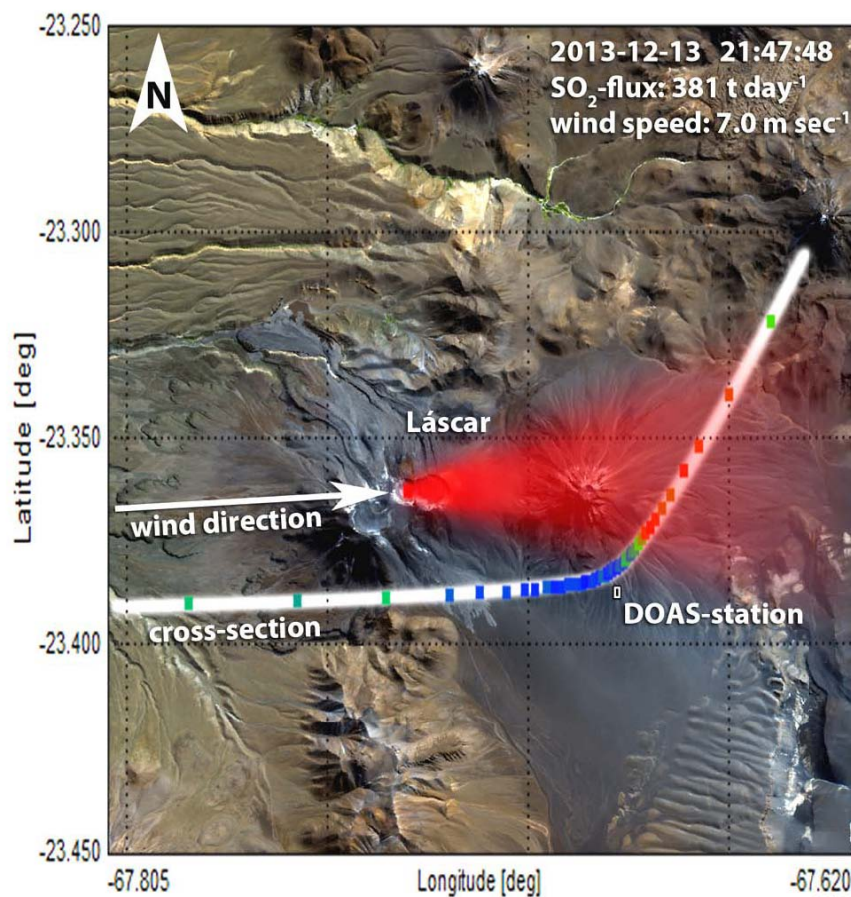
Fig.2 Projection of a plume cross-section obtained from a stationary scan-DOAS instrument at Láscar volcano showing the spatial extent of the volcanic gas plume. The trace of the cross section is highlighted by the thick white line. Gas concentrations, respectively SO_2 column densities measured along the section are depicted by a RGB-color code: red squares - high gas concentrations, green squares - medium gas concentrations, and blue squares - low gas concentrations. For the SO_2-flux calculation the plume height was assumed to be equal to summit height. Plume speed was assumed to be equal to the wind speed at summit altitude obtained from hindcasts of the Global Forecast System (GFS) and plume direction was geometrically calculated by combining plume height and the scan angle corresponding to the position of the center of mass in the concentration profile of the volcanic plume.

_____

A4. Archived weather data

In this work we generally used archived weather data of the Global Forecast System (GFS), which is run by the National Centers for Environmental Prediction (NCEP). The NCEP datasets are archived by the Air Resources Laboratory (ARL) at the National Oceanic and Atmospheric Administration (NOAA), which are made available for download in the form of 3-dimensional gridded meteorological datasets, or 1-dimensional vertical atmospheric profiles, respectively soundings for a specific forecast location.

Atmospheric soundings obtained from the Global Data Assimilation System one-degree archive (GDAS1) provide fairly reliable information on weather conditions at various levels above ground surface at a temporal resolution of 1 sounding every 3 hours. GDAS1 sounding data has to be downloaded manually from NOAA's Real-time Environmental Applications and Display sYstem (READY) at https://ready.arl.noaa.gov/READYamet.php , since NOAA ARL denies access to computers found to be using automated methods to request data. The amount of data that can be downloaded per request is limited to 84 hours of subsequent data, thus each file contains data for at most half a week, which is arranged in a format that was designed to be compatible for the use with the Hybrid Single Particle Lagrangian Integrated Trajectory Model (HYSPLIT), an atmospheric transport and dispersion modeling system that is also provided by NOAA.

The structure of the GDAS1 sounding data is as follows. The archive data files contain the data in synoptic time sequence, and at each time period an index record (containing date and time of the prediction) is always the first record, followed by single-level surface data, and then all data in each pressure level from the ground up to the top of the model. Measures of atmospheric stability comprising time series of skew-T/log-P diagrams and Theta-e (Equivalent Potential Temperature) data are appended at the end of the file, if these were requested too. Single-level and multi-level data thus require some rearrangement, in order to obtain time series, since these data files do not contain the data in a proper time series format.

A5. Pre-processing of GDAS1 sounding data

In order to automate rearrangement of GDAS1 sounding data, a lightweight JavaScript based standalone software, called the NOVAC Tools was developed, which exclusively runs on Windows operating systems and requires a Java Runtime Environment to be installed on your computer (concept by Stefan Bredemeyer; programming and design by Jürgen Bredemeyer; 2012). The software considerably speeds up the time series construction from GDAS1 sounding data, which was essential for the processing of weather data used in Chapters II, V and VI, and enables to assign the plume height information obtained from the NOVAC program to the wind field information at corresponding pressure levels of the GDAS1 soundings.

The user interface of the NOVAC Tools software is kept very simple, and consists of a number of buttons arranged in chronological order suggested for processing, which enable to process single or multiple data files with only a few mouse clicks (Fig.3). The buttons are divided into two processing groups, *Step 1* and *Step 2*.

Buttons of the first processing group *Step 1 "Split GDAS1 Sounding Files"* enable to split up the contents of text files containing the GDAS1 sounding data according to three different topics (sounding data, surface data, and atmospheric stability data) and rearrange the data to a proper time series format, by assigning the index records containing date and time of the GFS hindcasts to the corresponding weather data. The results are written into 3 separate tab-delimited text files, each containing the time series data of only one of the above mentioned topics. The file names of each of the generated text files are created by appending the names of the respective topics to the file name of the original text file, and the generated files are being saved into the same directory, where also the original text file is located.

The buttons in the second processing group *Step 2 "Combine (Post)Geometry Log and Press Data Files"* serve to merge GDAS1 sounding data with calculated plume-heights from the Geometry log files that were generated by the NOVAC program from simultaneous scans of two or more NOVAC instruments.
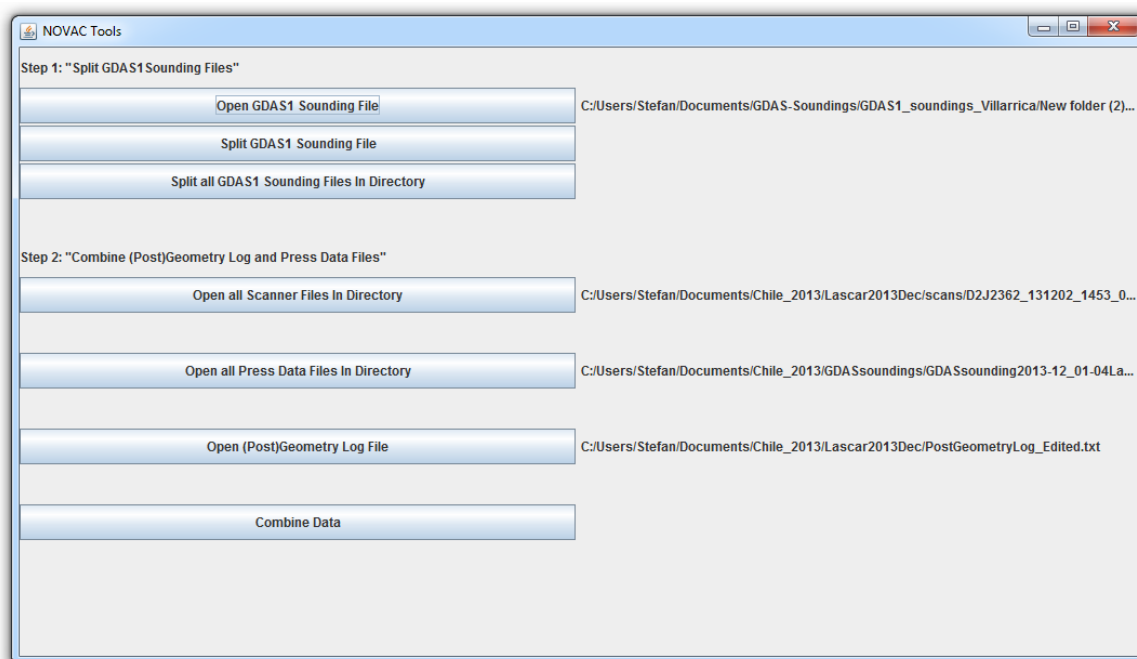
Fig.3 User interface of the NOVAC Tools software showing the two processing groups for time series construction and assignment of plume height information to corresponding weather data.

A6. SO$_2$-flux calculation from scan-DOAS data

SO$_2$-fluxes were calculated by manual selection and input of evaluation parameters (plume height, speed and direction) into the NOVAC program, which was done for each of the scans, aiming to exploit the collected data more efficiently than is possible with the automatic batch flux calculation routine implemented in the NOVAC program (Johansson, 2009). The NOVAC program automatically assesses the quality of each DOAS scan by inferring the plume geometry from the measured plume cross sections in order to determine how well a scan covers the whole extent of the plume, and by this means derives a measure of plume completeness. Based on this estimate the NOVAC program automatically discards any scan, which does not seem to capture more than 50 % of the plume. Under certain weather conditions this pre-selection can result in undesirably huge data gaps in the otherwise continuous gas emission record. Manual selection and input of evaluation parameters enables to evaluate also those DOAS scans, which were not accepted by the batch flux calculation of the NOVAC program, i.e. all scans in which the software was not able to detect a plume signature, respectively to determine the center of mass and extent of the volcanic plume (Fig.4).

Examination of each single DOAS scan and comparison with previous and subsequent scans revealed that many of the discarded scans yield reasonable SO$_2$-flux measurements, which are in the range of accepted previous and subsequent scans. The manual evaluation allows for choosing the best available information on plume position for each scan, since it enables to take into account the evolution of plume positions determined for previous and following scans, which is time consuming, but facilitates to make a good decision regarding the choice of the parameters used for calculation (plume height, wind speed and wind direction). This manual approach thus significantly improved the temporal coverage of the resulting time series, which was of particular importance for the examination of strongly dispersed gas emissions, which commonly occur at weakly degassing volcanoes, such as Llaima volcano, and during stormy periods with wind speeds larger than 15 meters per second also affect strong gas emitters, such as Láscar or Villarrica volcanoes (Chapters II, IV, V). Plume cross sections recorded during periods with strong winds are often characterized by strongly perturbed column density distributions along the measured plume cross-sections, which can be attributed to rapid meandering of the plume at speeds larger than the scan duration.
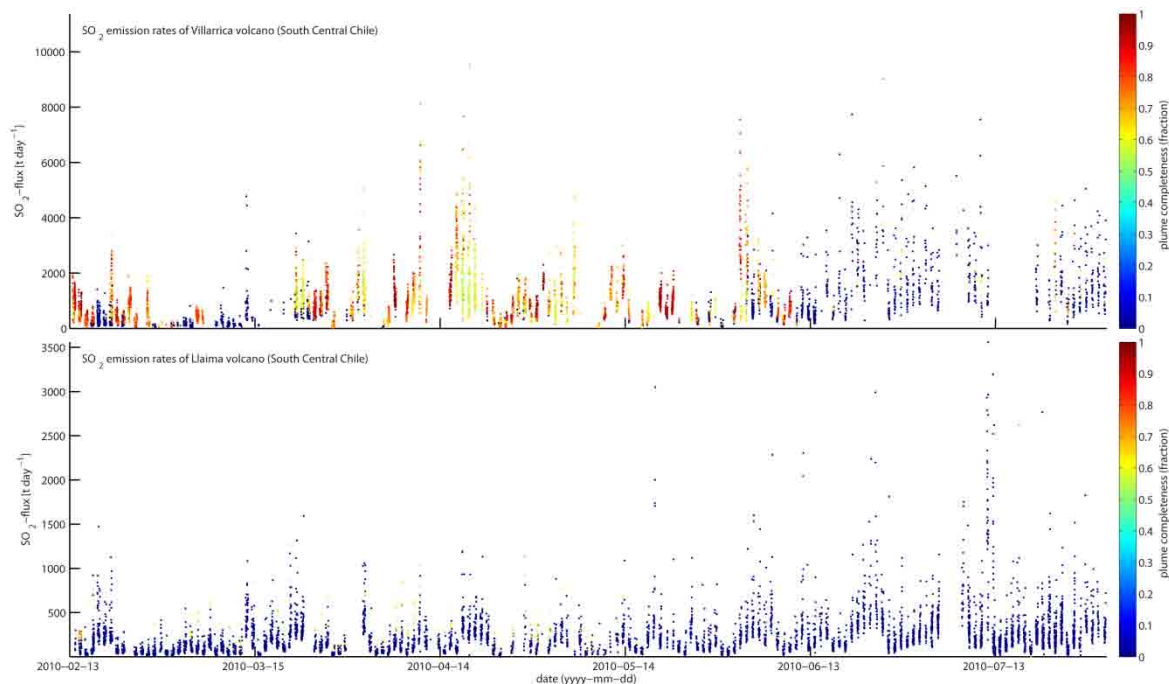
Fig.4 Scatter plot of single measurements of the SO_2-flux time series from Villarrica and Llaima volcanoes, which were used to calculate the hourly averaged time series presented in Chapter II (Bredemeyer & Hansteen 2014). Single measurements are colored by the plume completeness estimate of the NOVAC program. Dark blue dots correspond to measurements which would have been skipped by the automatic SO_2-flux calculation routine of the NOVAC program.

A7. SO_2-flux time series processing

SO_2-flux data obtained from NOVAC instruments involves working with highly non-equidistant time series, since automatic adjustment of exposure times and variations in the length of the day result in highly irregular sampling rates. The SO_2-flux data additionally commonly is characterized by strong short-term variations, resulting in measurement noise, which however can slightly be reduced by time averaging, respectively down sampling of the SO_2-flux data, provided that the data density is sufficiently high. Achieving better exploitation of the data directly led to the possibility to work with hourly average data, which significantly de-noised our SO_2-flux data at short timescales, and enabled to obtain equidistant time series with a higher temporal resolution than the daily averages commonly used in previous works on the grounds that the data would be too noisy otherwise. Using hourly average time series enabled us to identify pronounced diurnal and semidiurnal variations in the SO_2 emission rates (Chapter II: Bredemeyer & Hansteen 2014). These strong natural variations are responsible for the large standard deviations typically reported for daily averaged SO_2-fluxes. For this reason long term trends in the data can better be observed, when the data is down sampled to daily averages, which we obtain from hourly averaged data, in order to avoid propagation of the bias caused by the uneven sampling, and to further stabilize the statistics.

References

Bredemeyer S, Hansteen T (2014) Synchronous degassing patterns of the neighbouring volcanoes Llaima and Villarrica in southcentral Chile: the influence of tidal forces. Int J Earth Sci (Geol Rundsch) 103(7):1999–2012. doi:10.1007/s00531-014-1029-2

Conde, V., Nilsson, D., Galle, B., Cartagena, R., & Muñoz, A. (2014). A rapid deployment instrument network for temporarily monitoring volcanic SO_2 emissions-a case study from Telica volcano. Geoscientific Instrumentation, Methods and Data Systems, 3(2), 127. DOI:10.5194/gid-4-191-2014

Galle B, Johansson M, Rivera C, Zhang Y, Kihlman M, Kern C, Lehmann T, Platt U, Arellano S, Hidalgo S (2010) Network for observation of volcanic and atmospheric change (NOVAC)—a global network for volcanic gas monitoring: network layout and instrument description. J Geophys Res 115:D05304. doi:10.102 9/2009JD011823

Grainger, J. F. and Ring, J. (1962). Anomalous Fraunhofer line profiles. Nature, 193, 762. doi:10.1038/193762a0

Johansson, M., Galle, B., Zhang, Y., Rivera, C., Chen, D., & Wyser, K. (2009). The dual-beam mini-DOAS technique—measurements of volcanic gas emission, plume height and plume speed with a single instrument. Bulletin of volcanology, 71(7), 747-751. DOI:10.1007/s00445-008-0260-8

Johansson, Mattias E.B. (2009) Application of Passive DOAS for Studies of Megacity Air Pollution and Volcanic Gas Emissions [Doctoral thesis] Chalmers University of Technology (Department of Radio and Space Science, Optical Remote Sensing), 2009. ISBN: 978-91-7385-238-8.

Mori, T., Mori, T., Kazahaya, K., Ohwada, M., Hirabayashi, J. I., & Yoshikawa, S. (2006). Effect of UV scattering on SO_2 emission rate measurements. Geophysical research letters, 33(17). DOI:10.1029/2006GL026285

Platt, U., & Stutz, J. (2008). Differential absorption spectroscopy. In Differential Optical Absorption Spectroscopy (pp. 135-174). Springer Berlin Heidelberg. ISBN 978-3-540-21193-8

Tamburello, G., T. H. Hansteen, **S. Bredemeyer**, A. Aiuppa, F. Tassi (2014). Gas emissions from five volcanoes in northern Chile and implications for the volatiles budget of the Central Volcanic Zone. *Geophys Res Lett*, Volume 41, Issue 14, 28 July 2014, pp. 4961–4969. DOI: 10.1002/2014GL060653

Vandaele AC, Simon PC, Guilmot JM, Carleer M, Colin R (1994) SO_2 absorption cross section measurement in the UV using a Fourier transform spectrometer. J Geophys Res 99 (D12): 25,599-25,605. . DOI: 10.1029/94JD02187

Voigt S, Orphal J, Bogumil K, Burrows JP (2001) The temperature dependence (203-293K) of the absorption cross sections of O_3 in the 230-850 nm region measured by Fourier-transform spectroscopy. Journal of Photochemistry and Photobiology A: Chemistry 143:1-9. DOI: 10.1016/S1010-6030(01)00480-4

_____

ACKNOWLEDGEMENTS

CURRICULUM VITAE

Stefan Bredemeyer

Date of birth: November 09, 1975

Place of birth: Kiel, Germany

Nationality: German

ACADEMIC EDUCATION

2010-2016	Post-graduate studies (Doctoral program) in the field of geosciences at the University of Kiel (CAU: Christian-Albrechts-Universität zu Kiel) and GEOMAR Helmholtz Centre for Ocean Research Kiel, Germany
1996-2004	Diploma studies of geology, palaeontology, and mineralogy/crystallography with focus on petrology/petrography, geochemistry and economic geology at the University of Kiel (CAU: Christian-Albrechts-Universität zu Kiel), Germany

LIST OF PUBLICATIONS

ARTICLES IN PREPARATION

Bredemeyer, **S.**, F.-G. Ulmer, T.H. Hansteen, E. De Zeeuw van Dalfsen, N. Richter, T. Walter (in prep.). Radar path delay effects in volcanic gas plumes: The case of Láscar Volcano, Northern Chile.

Bredemeyer, S., M. Zimmer, J. Salzer, G. Tamburello, C. Kujawa, T.H. Hansteen, T. Walter (in prep.), Daily variations in volcanic activity.

ARTICLES IN A SCIENTIFIC JOURNAL (PEER_REVIEWED)

Conde, V., **S. Bredemeyer**, J.A. Saballos, Bo Galle, T.H. Hansteen (2014). Linking SO_2 emission rates and seismicity by continuous wavelet transform: implications for volcanic surveillance at San Cristóbal volcano, Nicaragua. *Int J Earth Sci (Geol Rundsch)*, pp 1-13. DOI 10.1007/s00531-015-1264-1

Tamburello, G., T. H. Hansteen, **S. Bredemeyer**, A. Aiuppa, F. Tassi (2014). Gas emissions from five volcanoes in northern Chile and implications for the volatiles budget of the Central Volcanic Zone. *Geophys Res Lett*, Volume 41, Issue 14, 28 July 2014, pp. 4961–4969. DOI: 10.1002/2014GL060653

Bredemeyer, S., T.H. Hansteen (2014). Synchronous degassing patterns of the neighbouring volcanoes Llaima and Villarrica in south-central Chile: the influence of tidal forces. *Int J Earth Sci (Geol Rundsch)*, Volume 103, Issue 7, pp. 1999-2012. DOI 10.1007/s00531-014-1029-2

Bredemeyer, S., T.H. Hansteen (2014). Erratum to: Synchronous degassing patterns of the neighbouring volcanoes Llaima and Villarrica in south-central Chile: the influence of tidal forces. *Int J Earth Sci (Geol Rundsch)*, Volume 103, Issue 7, pp. 2013-2013. DOI 10.1007/s00531-014-1037-2

Conde, V., **S. Bredemeyer**, E. Duarte, J.F. Pacheco, S. Miranda, Bo Galle, T.H. Hansteen (2013). SO_2 degassing from Turrialba Volcano linked to seismic signatures during the period 2008–2012. *Int J Earth Sci (Geol Rundsch)*, Volume 103, Issue 7, pp 1983-1998. DOI 10.1007/s00531-013-0958-5

Mora-Stock, C., M. Thorwart, T. Wunderlich, **S. Bredemeyer**, T.H. Hansteen, W. Rabbel (2012). Comparison of seismic activity for Llaima and Villarrica volcanoes prior to and after the Maule 2010 earthquake. *Int J Earth Sci (Geol Rundsch)*, Volume 103, Issue 7, pp. 2015-2028. DOI 10.1007/s00531-012-0840-x

CONFERENCE PRESENTATIONS

Conde, V., **S. Bredemeyer**, B. Galle, A. Saballos, J. Álvarez (2014). Cross-Correlation between SO_2 flux and seismicity from San Cristobal volcano during the period 2012-2014 [Talk] In: 12. Gas Workshop, Commission on the Chemistry of Volcanic Gases (CCVG) - IAVCEI, 16.11.-24.11.2014, Atacama, Chile.

Zimmer, M., **S. Bredemeyer**, T.H. Hansteen, C. Kujawa, C. Bucarey, J. Erzinger (2014). Thermal and gas chemical monitoring at Lastarria, Láscar and El Tatio [Talk] In: 12. Gas Workshop, Commission on the Chemistry of Volcanic Gases (CCVG) - IAVCEI, 16.11.-24.11.2014, Atacama, Chile .

Tamburello, G., Agusto, M., Aiuppa, A., **Bredemeyer, S.**, Capaccioni, B., Chiodini, G., Calabrese, S., Cardellini, C., Caselli, A.T., Hansteen, T.H., La Canna, G., Ripepe, M., Tassi, F., Vaselli, O. (2014). Volcanic degassing in the Southern-Central Volcanic Zone (Southern Andes) [Poster] In: 12. Gas Workshop, Commission on the Chemistry of Volcanic Gases (CCVG) - IAVCEI, 16.11.-24.11.2014, Atacama, Chile.

Tamburello, G., Hansteen, T.H., **Bredemeyer, S.**, Aiuppa, A., Guidice, G. (2013). Gas fluxes and compositions of two active volcanoes in Northern Chile: Lastarria and Láscar [Poster] In: AGU Fall Meeting 2013, 09.12.-13.12.2013, San Francisco, California, USA .

Hansteen, T.H., G. Tamburello, **S. Bredemeyer**, A. Aiuppa, (2013). Gas compositions and fluxes at Lascar and Lastarria volcanoes, Northern Chile: Preliminary results from the field measurements in November –

December 2012 [Report] Report for the DCO, Reservoirs and Fluxes Directorate Research carried out within the framework of the DECADE project, February 2013.

Mora-Stock, C., Thorwart, M., Wunderlich, T., **Bredemeyer, S.**, Rabbel, W. and Hansteen, T.H. (2012). Multiparameter surveillance of the Llaima and Villarrica volcanoes (Southern Chile): The near real-time approach [Talk] In: The Lübeck Retreat, Collaborative Research SFB 574 Volatiles and Fluids in Subduction Zones: Climate Feedback and Trigger Mechanisms for Natural Disasters, 23.-25.05.2012, Lübeck . The Lübeck Retreat: final colloquium of SFB 574; May 23-25, 2012: program & abstracts ; p. 21 .

Mora-Stock, C., Thorwart, M., Wunderlich, T., **Bredemeyer, S.**, Hansteen, T.H. and Rabbel, W. (2012). Comparison of volcano-seismic activity in Llaima and Villarrica before and after the Maule M8.8 earthquake in Southern Chile [Poster] In: The Lübeck Retreat, Collaborative Research SFB 574 Volatiles and Fluids in Subduction Zones: Climate Feedback and Trigger Mechanisms for Natural Disasters, 23.-25.05.2012, Lübeck . The Lübeck Retreat: final colloquium of SFB 574; May 23-25, 2012: program & abstracts ; p. 20 .

Hansteen, T.H., **Bredemeyer, S.**, Mora-Stock, C., Dzierma, Y., Thorwart, M., Rabbel, W., Garofalo, K. and Gil Cruz, F. (2012). Strong variations in degassing rates at Villarrica Volcano (Southern Chile): Consequences for deep-seated processes [Talk] In: The Lübeck Retreat, Collaborative Research SFB 574 Volatiles and Fluids in Subduction Zones: Climate Feedback and Trigger Mechanisms for Natural Disasters, 23.05-25.05.2012, Lübeck . The Lübeck Retreat: final colloquium of SFB 574; May 23-25, 2012: program & abstracts ; p. 11 .

Bobrowski N., Vogel L., Platt U., Arellano S., Galle B., Hansteen T.H., **Bredemeyer S.** (2012). Bromine monoxide evolution in early plumes of Mutnovsky and Gorely (Kamchatka, Russia) [Poster] In: European Geosciences Union General Assembly, Geophysical Research Abstracts Vol. 14, EGU2012, Vienna, Austria, April 2012.

Mora-Stock, C., Thorwart, M., Wunderlich, T., **Bredemeyer, S.**, Rabbel, W. (2012). Volcano-seismic activity before and after the Maule 2010 Earthquake (Southern Chile): a comparison between Llaima and Villarrica volcanoes [Talk] In: EGU General Assembly 2012, held 22-27 April, 2012 in Vienna, Austria., Vol 14, p.169.

Bredemeyer, S., Hansteen, T.H., Garofalo, K., Mora-Stock, C., Rabbel, W. and Gil Cruz, F. (2011). Remote sensing of thermal emission and degassing at Villarrica Volcano, Chile [Talk] In: AGU Fall Meeting 2011, 05.12.-09.12.2011, San Francisco, California, USA, abstract #V44C-02 .

Arellano, S., Galle, B., Hansteen, T.H., **Bredemeyer, S.**, Melnikov, D. (2011). Ground-based optical remote sensing measurements of SO_2 gas emissions from volcanoes of Kamchatka during September 2011 [Report] Report for the IAVCEI-CCVG, Department of Earth and Space Sciences, Chalmers University of Technology, Gothenburg, Sweden, November 2011.

Hansteen, T.H., **Bredemeyer, S.**, Garofalo, K., Pena, P., Rüpke, L., Mora-Stock, C., Dzierma, Y., Rabbel, W., Bataille, K. and Gil Cruz, F. (2011). The influence of earthquakes on degassing at Villarrica Volcano, Chile [Poster] In: AGU Fall Meeting 2011, 05.12.-09.12.2011, San Francisco, California, USA, abstract #V53E-2681 .

Hansteen, T.H., **Bredemeyer, S.**, Garofalo, K., Mora-Stock, C., Rabbel, W., Dzierma, Y., Bataille, K., Pena, P. and Gil Cruz, F. (2011). Gas monitoring and seismicity at Villarrica Volcano, South-Central Chile [Talk] In: 11. Gas Workshop, Commission on the Chemistry of Volcanic Gases (CCVG) - IAVCEI, 01.09.-10.09.2011, Kamchatka, Russia .

Garofalo, K., Pena, P., Dzierma, Y., Hansteen, T.H., Rabbel, W., Gil, F. and **Bredemeyer, S.** (2010). Multiparameter surveillance of Villarrica volcano [Talk] In: SFB 574 Subduction Workshop, 04.-07.11.2010, Pucon, Chile .